The acquisition of Hyperspectral Digital Surface Models of crops from UAV snapshot cameras

Inaugural-Dissertation

zur

Erlangung des Doktorgrades

der Mathematisch-Naturwissenschaftlichen Fakultät

der Universität zu Köln

vorgelegt von

Helge Aasen

aus Rheine

Köln 2016

Berichterstatter: Prof. Dr. Georg Bareth

Prof. Dr. Karl Schneider

Prof. Dr. Natascha Oppelt

Tag der mündlichen Prüfung: 28.06.2016

ABSTRACT

In order to meet the global food demand in a sustainable way, agricultural crop production must diminish its environmental footprint. Increasing cropping efficiency based on site-specific management practices can help to reduce the use of resources by utilizing the right management at the right place and at the right time. For an operational success, accurate data about the crop's status is needed. Today, a great variety of remote sensing systems exist, which enables to capture spectral or 3D information. Within the last few years, unmanned aerial vehicles (UAVs) have been widely adapted as flexible remote sensing platforms. In combination with appropriate sensors they become powerful sensing systems. Recently lightweight hyperspectral snapshot cameras have been developed that can be carried by UAVs and allow spectral information to be captured as two dimensional images.

This thesis develops a new approach to capture information about agricultural crops by utilizing advances in the field of robotics, sensor technology, computer vision and photogrammetry: Hyperspectral digital surface models (HS DSMs) generated with UAV snapshot cameras are a representation of a surface in 3D space linked with hyperspectral information emitted and reflected by the objects covered by that surface. The overall research aim of this thesis is to evaluate if HS DSMs are suited for supporting a site-specific crop management. Based on six research studies, three research objectives are discussed for this evaluation.

The first three studies focus on methodological aspects in the context of the generation of HS DSMs. First, the method to generate HS DSMs from UAV snapshot camera data is introduced, which is based on the computer vision technique *Structure from Motion*. Additionally, a method is introduced to trace the properties of each individual pixel within an HS DSM. Based on this method, the angular properties of the spectral data within HS DSMs are investigated and differences to data from field spectroscopy are highlighted. Additionally, a method to investigate the anisotropy of canopies based on an UAV goniometer is introduced. Using this technique the anisotropy of a wheat canopy is characterized. The other three studies focus on potential applications of HS DSMs, but use data that is not captured by hyperspectral snapshot cameras. HS DSMs contain spectral and 3D spatial information. To investigate the potential of a combination of spectral data and plant height for the estimation of biomass of barley, an RGB camera flown on an UAV and a terrestrial laser scanner were used to derive plant height. This data was combined with vegetation indices derived from hyperspectral data acquired by a field-spectrometer. In both studies, plant height was found to be the best predictor for dry green biomass, while a combination of spectral and plant height data could slightly increase the prediction of fresh biomass. The last study introduces a new method to use large multi-temporal spectral libraries to improve the prediction of biomass of rice within individual and across multiple growth stages. The results show that the optimal spectral bands for the prediction differ between the growth stages. Most

data within this thesis was acquired at a plant experimental-plot experiment in Klein-Altendorf, Germany, with six different barley varieties and two different fertilizer treatments in the growing seasons of 2013 and 2014. In total, 22 measurement campaigns were carried out in the context of this thesis. These campaigns also include four flights with the hyperspectral snapshot camera *Cubert UHD 185-Firefly* (UHD).

To address the overall research aim of this thesis, firstly the influences of environmental effects, the sensing system and data processing of the spectral data within HS DSMs are discussed. Secondly, the comparability of HS DSMs to data from other remote sensing methods is investigated and thirdly their potential to support site-specific crop management is evaluated. The results show that angular effects resulting from the measurement geometry of the system in combination with the surface anisotropy exert a major influence on the spectral data. Within the data acquired by the UHD, angular effects were approximated to account for a variation of up to 25%. Furthermore, the current measurement protocol was found to be prone to errors during the calibration procedure and cannot compensate for varying illumination conditions. Additionally, the comparison of the hyperspectral snapshot camera and field-spectrometry data revealed discrepancies due to the different reflectance quantities measured by the two systems. Similarly, the 3D data was also found to be influenced by the measurement conditions. Parameters such as image overlap and camera configuration influenced the generation of 3D information. A comparison with data from a terrestrial laser scanning system revealed that the different measurement techniques also influenced the retrieved 3D information. In addition, the different processing workflows had an impact on the estimation of the plant height.

Despite these challenges, great potential of HS DSMs acquired with hyperspectral snapshot cameras was found for practical applications. The combination of UAVs and the UHD allowed data to be captured at a high spatial, spectral and temporal resolution. The spatial resolution allowed detection of small-scale heterogeneities within the plant population. Additionally, with the spectral and 3D information contained in HS DSMs, plant parameters such as chlorophyll, biomass and plant height could be estimated within individual, and across different growing stages. The techniques developed in this thesis therefore offer a significant contribution towards increasing cropping efficiency through the support of site-specific management.

ZUSAMMENFASSUNG

Für eine dauerhafte und nachhaltige Deckung des Nahrungsmittelbedarfs der Welt muss der ökologische Fußabdruck der Landwirtschaft verkleinert werden. In diesem Zusammenhang kann ein teilschlagspezifisches Management der Ackerfläche, welches Bewirtschaftungsmaßnahmen an die aktuelle Beschaffenheit des Feldes anpasst, helfen, den Einsatz von Ressourcen zu reduzieren. Dafür werden Informationen über den aktuellen Zustand der Pflanzen benötigt. Verschiedene Fernerkundungssensoren können Informationen über die spektrale Reflexion oder die 3D Geometrie von Objekten erfassen. Außerdem werden seit einigen Jahren zunehmend unbemannte Luftfahrzeuge (engl.: Unmanned aerial vehicles, UAVs) als Fernerkundungsplattformen eingesetzt. In Kombination mit entsprechenden Sensoren stellen diese leistungsfähige Fernerkundungssysteme dar. Ein Beispiel für diese Sensoren sind neuartige leichtgewichtige hyperspektrale Snapshotkameras, welche von UAVs transportiert werden können und Spektralinformationen als zweidimensionales Bild erfassen.

Diese Dissertation stellt einen neuen Ansatz vor, der aktuelle Entwicklungen aus den Bereichen der Robotik, Sensortechnologie, visuellen Bildverarbeitung und Photogrammmetrie kombiniert, um Informationen über Agrarfrüchte zu erfassen: Hyperspektrale digitale Höhenmodelle (engl.: Hyperspectral digital surface models, HS DSMs) sind eine dreidimensionale Repräsentation einer Oberfläche, die mit Informationen über ihre spektralen Reflexions- und Emissionseigenschaften verknüpft ist. Grundlage dieser HS DSMs ist die Datenerfassung mit Hilfe von UAVs und hyperspektralen Snapshotkameras. Das Ziel dieser Dissertation ist eine Bewertung, ob HS DSMs ein teilschlagspezifisches Management unterstützen können. Grundlage für diese Bewertung sind drei Diskussionspunkte, welche auf Basis von sechs Forschungsstudien erörtert werden.

Die ersten drei Studien beschäftigen sich mit methodischen Aspekten im Zusammenhang mit der Generierung von HS DSMs. Darin wird zuerst die Methodik zur Erfassung von HS DSMs vorgestellt, welche auf dem *Structure from Motion* Verfahren aus der visuellen Bildverarbeitung beruht. Weiterhin wird eine Methodik eingeführt, die es erlaubt, Eigenschaften von einzelnen Pixels innerhalb des HS DSMs nachzuvollziehen. Basierend auf dieser Methode werden die speziellen Eigenschaften der spektralen Informationen innerhalb des HS DSMs untersucht und Unterschiede zu Feldspektrometerdaten herausgestellt. Zusätzlich werden die Daten eines UAV Goniometers hinsichtlich der angularen Reflexionseigenschaften eines Weizenbestandes analysiert. Die weiteren drei Studien betrachten das Potential der in HS DSMs enthaltenen Spektral- und 3D-Daten, verwenden jedoch Daten anderer Sensorsysteme. Der Fokus der Studien liegt auf einer Abschätzung des Potentials für die Erfassung von Biomasse. Dazu wird mit Hilfe von einem UAV-getragenen RGB Kamerasystem und einem terrestrischen Laserscanner die Pflanzenhöhe eines Gerstenbestandes abgeleitet und jeweils mit Spektraldaten eines Feldspektrometers kombiniert. Die Untersuchungen zeigen, dass die

besten Schätzungen des Trockengewichtes der Biomasse allein mit Hilfe der Pflanzenhöhe erzielt werden können. Die Schätzungen des Feuchtgewichts der Biomasse können jedoch durch die Kombination mit Vegetationsindizes, abgeleitet aus den Spektraldaten, leicht verbessert werden. Die letzte Studie führt eine Methode ein, wie mit Hilfe von multi-temporalen Spektralbibliotheken und an die Wachstumsperiode angepassten Vegetationsindizes die Schätzung von Biomasse in Reis verbessert werden kann. Mit Ausnahme dieser letzten Studie wurden die verwendeten Daten in einem Züchtungsexperiment auf dem Campus Klein-Altendorf in der Nähe von Bonn während den Wachstumsperioden 2013 und 2014 erfasst. Insgesamt werden in dieser Dissertation Daten von 22 Messkampagnen verwendet. Darin eingeschlossen sind vier Flüge mit der hyperspektralen Snapshotkamera *Cubert UHD 185-Firefly* (UHD).

Bei der abschließenden Bewertung des Potentials von HS DSMs werden drei Aspekte betrachtet: Erstens wird der Einfluss der natürlichen Bedingungen, des Sensorsystems und des Messprotokolls sowie der Datenverarbeitung auf die Spektralinformation innerhalb von HS DSMs diskutiert. Zweites wird die Vergleichbarkeit von HS DSMs mit Daten von anderen Fernerkundungssystemen untersucht. Drittens wird das Potential der HS DSMs für ein teilschlagspezifisches Management abgeschätzt. Dabei zeigt sich, dass winkelabhängige Effekte, hervorgerufen durch die Messgeometrie und die angularen Reflexionseigenschaften des Pflanzenbestandes, das erfasste spektrale Signal in einer Größenordnung von bis zu 25% beeinflussen. Darüber hinaus ist das in den Studien verwendete Messprotokoll anfällig für Fehler während der Kalibrierung. Außerdem können Beleuchtungsunterschiede während den Messungen nicht korrigiert werden. Zusätzlich zeigt der Vergleich von Daten der UHD mit denen eines Feldspektrometers, dass die unterschiedlichen Sichtbereiche der Sensoren einen Einfluss auf die Ergebnisse haben. Die 3D Daten werden durch Aufnahmefaktoren wie zum Bespiel Bildüberlappung und die Bildauflösung beeinflusst. Durch einen Vergleich der durch *Structure from Motion* erhaltenen Daten mit denen eines terrestrischen Laserscanners werden zusätzlich systematische Unterschiede aufgrund der unterschiedlichen Messprinzipien herausgestellt. Daneben haben auch die unterschiedlichen Datenverarbeitungsverfahren einen Einfluss auf die Ableitung der Pflanzenhöhe.

Auch wenn, wie oben beschrieben, noch Forschungsbedarf besteht, haben HS DSMs, generiert mit hyperspektralen Snapshotkameras, ein großes Potential für die praktische Anwendung. Die Kombination aus UAV und UHD erlaubt es, Daten in einer hohen räumlichen, spektralen und zeitlichen Auflösung zu erfassen. Die räumliche Auflösung erlaubt es kleinflächige Heterogenität innerhalb eines Bestandes zu erkennen. Die in HS DSMs enthaltenen spektralen und 3D Informationen können genutzt werden, um Pflanzenparameter wie Chlorophyllgehalt, Biomasse und Pflanzenhöhe für einzelne Termine und über die Wachstumsperiode hinweg abzuleiten und so Aussagen über den Zustand der Pflanzen zu treffen. Daher sind die Erkenntnisse dieser Dissertation ein wichtiger Beitrag auf dem Weg zu einem reduzierten Einsatz von Ressourcen innerhalb der Nahrungsmittelproduktion.

ACKNOWLEDGMENTS

After such an intensive and exciting time it is almost impossible to acknowledge all of the great friends, support and experiences that have made it so amazing. First of all, I want to thank my supervisor Georg Bareth for providing me with the chance, the freedom and the outstanding support to develop my scientific interests and undertake the research which has led to this thesis. I also want to thank Andreas Bolten for his constant generous support from the server room in the basement to 100 m above ground altitude. I want to thank Arko Lucieer for being an important advisor in the course of this thesis and a welcoming host. I sincerely also thank Karl Schneider for consenting to act as the second examiner of this thesis and Bülent Tezkan for chairing the examination committee. Additionally, I would like to acknowledge Sam Works for proof reading, Rene Michels for his support with the camera and the people of Campus Klein-Altendorf for their support with the field experiment. I also acknowledge the financial support I have received in support for my research. In particular, I want to thank the Graduate School of Geosciences at the University of Cologne and the Gesellschaft für Erdkunde zu Köln e.V.

Moreover, I am most thankful to have had the chance to meet interesting people, find new and deepen existing friendships during the course of this PhD.

Kristof, my brother,

Nora, part of the experience since the very beginning (almost). The moment one of us has to leave the cave I will cry – but don't tell my mom next time you two chatter. For your deep friendship and support,

Andreas, one day there will be rainbow airships all over the sky,

Juliane, for your support during tough times down under,

But also all the people who supported me during the preparation of this thesis, during the field campaigns or just made work time fun. In particular, Sebastian, Martin, Simon, Janis, Jonas, Silas, Sven, Markus, Max, Ulrike, Hannes, Melanie, Georgina and all the other of the AG Bareth and the Institute of Geography at the University of Cologne,

And to my friends and family, I have no words.

Thank you

TABLE OF CONTENT

Abstract I

Zusammenfassung III

Acknowledgments V

Table of Content VI

Figures XI

Tables XVII

Abbreviations XX

1. Introduction 1

1.1 Remote sensing in support for site-specific crop management 1

1.2 Diversification in remote sensing 2

1.3 Complexity of spectral remote sensing of vegetation 5

1.4 Research objectives and outline 8

1.4.1 Influences on the spectral information 9

1.4.2 Comparability of hyperspectral digital surface models 11

1.4.3 Potentials of hyperspectral digital surfaces models 12

2. Background 14

2.1 Spectral remote sensing of vegetation 15

2.1.1 Angular effects 15

2.1.2 Reflectance quantities 16

2.1.3 Principles of spectroscopy 19

2.1.4 Snapshot imaging spectroscopy 22

2.2 3D remote sensing 23

2.2.1 Structure from Motion 24

2.2.2 Terrestrial laser scanning 25

2.3 Sensing systems used in this study 26

2.4 Plant growth of barley 28

2.5 Study site 29

3. Generating 3D Hyperspectral Information with Lightweight UAV Snapshot Cameras for Vegetation Monitoring: From Camera Calibration to Quality Assurance 32

3.1 Introduction 33

3.2 Materials 37

3.2.1 Carrier platform 37

3.2.2 Image capturing system 37

3.2.3 Field study 39

3.2.4 Invasive sampling 39

3.2.5 Flight planning and conditions 39

3.3 Methods 40
3.3.1 Radiometric calibration 40
3.3.1.1 Noise correction 40
3.3.1.2 Radiometric response 41
3.3.1.3 Radiometric registration 42
3.3.1.4 Quality Assurance 43
3.3.2 Hyperspectral 3D information generation 43
3.3.2.1 Hyperspectral band preparation 43
3.3.2.2 Point cloud generation 44
3.3.2.3 Hyperspectral digital surface model preparation 45
3.3.3 Plant parameter extraction 46
3.3.3.1 Plant height 46
3.3.3.2 Hyperspectral vegetation indices 47
3.4 Results 48
3.4.1 Radiometric calibration 48
3.4.1.1 Dark current 48
3.4.1.2 Flat fielding and radiometric response 49
3.4.1.3 Radiometric correction and registration 50
3.4.1.4 Quality assurance information 51
3.4.2 Hyperspectral 3D information 53
3.4.2.1 Plant height 53
3.4.2.2 Hyperspectral vegetation indices 53
3.5 Discussion 55
3.5.1 Radiometric calibration and quality assurance information 55
3.5.2 Hyperspectral 3D information 57
3.6 Conclusion 59
3.7 References 60
4. Multi-temporal monitoring of agricultural crops with high-resolution 3D hyperspectral digital surface models in comparison with ground observations 66
4.1 Introduction 67
4.2 Materials and methods 69
4.2.1 Field experiment 69
4.2.2 Field-spectrometer data collection and processing 70
4.2.3 Hyperspectral digital surface generation 71
4.2.3.1 UAV sensing system 71
4.2.3.2 Hyperspectral snapshot camera data processing 71
4.2.4 Spectral data properties of hyperspectral digital surface models 72
4.2.4.1 Measurement extent 72
4.2.4.2 Specific field of view 73
4.2.4.3 Processing mode 75
4.2.4.4 Radiometric calibration 76
4.2.5 Multi-temporal chlorophyll retrieval 76
4.2.6 Multi-temporal canopy height monitoring 77
4.2.6.1 Canopy height model generation 77
4.2.6.2 Plant height evaluation 78

4.3 Results and Discussion 78
4.3.1 Spectral data properties of HS DSMs 78
4.3.1.1 Measurement extent 79
4.3.1.2 Specific field of view 80
4.3.1.3 Processing mode 82
4.3.1.4 Radiometric calibration conditions 83
4.3.2 Multi-temporal chlorophyll retrieval 85
4.3.3 Multi-temporal canopy height monitoring 88
4.3.3.1 Canopy height model generation 88
4.3.3.2 Plant height evaluation 91
4.4 Conclusion 92
4.5 References 95
5. Angular Dependency of Hyperspectral Measurements over Wheat Characterized by a Novel UAV Based Goniometer 100
5.1 Introduction 101
5.2 Material and Methods 103
5.2.1 Flight Pattern 104
5.2.2 Accuracy of the unmanned aerial vehicle Goniometer 105
5.2.3 Field Campaign 105
5.2.4 Data Preprocessing 106
5.2.5 Vegetation Indices 107
5.2.6 Data Visualization 107
5.2.7 Radiative transfer model comparison 108
5.3 Results 109
5.3.1 Accuracy Assessment of the UAV Goniometer 109
5.3.2 Full Spectrum Analysis 110
5.3.3 Vegetation Indices 112
5.3.4 Diurnal Variations of angular effects 113
5.3.5 Flying goniometer vs. radiative transfer model 115
5.4 Discussion 116
5.5 Conclusions 119
5.6 References 121
6. Fusion of Plant Height and Vegetation Indices for the Estimation of Barley Biomass 125
6.1 Introduction 126
6.2 Methods 128
6.2.1 Field measurements 128
6.2.1.1 Terrestrial laser scanning 130
6.2.1.2 Field-spectrometer measurements 131
6.2.2 Post-processing 132
6.2.2.1 TLS data 132
6.2.2.2 Spectral data 133
6.2.3 Biomass regression models 135

6.3 Results ... 136
6.3.1 Acquired plant parameters ... 136
6.3.2 Biomass estimation ... 139
6.3.2.1 Bivariate models ... 141
6.3.2.2 Multivariate models ... 143
6.4 Discussion ... 145
6.4.1 TLS-derived plant height ... 145
6.4.2 Biomass estimation from plant height ... 147
6.4.3 Biomass estimation from vegetation indices ... 147
6.4.4 Biomass estimation with fused models ... 149
6.5 Conclusion and outlook ... 151
6.6 Appendix ... 154
6.7 References ... 156
7. Combining UAV-based plant height from Crop Surface Models, Visible, and Near Infrared Vegetation Indices for Biomass Monitoring in Barley ... 162
7.1 Introduction ... 163
7.2 Materials and Methods ... 164
7.2.1 Test Site ... 164
7.2.2 Biomass Sampling and BBCH Measurements ... 164
7.2.3 UAV-based Data Collection ... 165
7.2.4 Field-spectroradiometer Measurements ... 166
7.2.5 Plant Height Generation from CSM ... 166
7.2.6 Vegetation Indices ... 167
7.2.6.1 Near Infrared Vegetation Indices ... 167
7.2.6.2 Visible Band Vegetation Indices ... 168
7.2.7 Statistical Analyses ... 169
7.3 Results ... 169
7.3.1 Plant Height and Biomass Samples ... 169
7.3.2 Biomass Modelling ... 170
7.3.2.1 Model Development ... 170
7.3.2.2 Model Application ... 171
7.4 Discussion ... 173
7.5 Conclusions and Outlook ... 175
7.6 References ... 177
8. Automated hyperspectral vegetation index retrieval from multiple correlation matrices with HyperCor ... 181
8.1 Introduction ... 181
8.2 Study site and data ... 183
8.2.1 Study site and experiment design ... 183
8.2.2 Hyperspectral data collection ... 183
8.2.3 Destructive plant parameter samples ... 184

8.3 Methods 184
8.3.1 Spectral library 184
8.3.2 Vegetation indices 185
8.3.3 HyperCor 186
8.3.3.1 Data pre-processing 186
8.3.3.2 Identifying substantial and redundant bands 188
8.3.3.3 Calculation of the correlation matrices and identification of potential hyperspectral vegetation indices 188
8.3.4 Multi-correlation matrix strategy 189
8.4 Results 190
8.5 Discussion 193
8.5.1 HyperCor 193
8.5.2 Multi-correlation matrix strategy 194
8.6 Conclusion and outlook 196
8.7 References 197
9. Overall Discussion 200
9.1 Influences on the spectral information along the path from particle to pixel 200
9.1.1 Interactions with the environment 200
9.1.2 Sensing system and measurement protocol 204
9.1.3 Data processing 206
9.1.4 Conclusion on the spectral data quality 207
9.2 Comparability of hyperspectral digital surface models to data from other sensing systems 211
9.2.1 Spectral data 211
9.2.2 Digital surface model 215
9.2.3 Canopy height 219
9.2.4 Destructive measurements 223
9.2.5 Conclusions on the comparability of hyperspectral digital surface models 224
9.3 Potentials of hyperspectral digital surface models acquired with UAV snapshot cameras 227
9.3.1 For crop parameter estimation 227
9.3.2 For site-specific crop management 232
9.3.3 Prospects for hyperspectral snapshot cameras 236
10. Conclusion 237
11. References 239
Appendix A: Eigenanteile i
Appendix B: Erklärung iii

FIGURES

Figure 1.1 Number of publications on remote sensing in combination with UAV or SfM and computer vision in the Web of Science. 4

Figure 1.2 The concept of this thesis. The three research objectives (RO) are motivated by the introductory chapters and discussed based on the research studies. The discussion of subsequent RO is supported by the insights from the previous research objective (RS denotes remote sensing). 8

Figure 1.3 The path of information from particle to pixel: The information about a particle within an environment is modified at different stages. Its acquisition is influenced by environmental conditions and their interaction with the sensing systems. The transformation within the sensing system of the signal of a particle to data and its conversion into information during the data processing also influences how the particle is represented within the pixels (respectively voxels for 3D data) of the final data product. 9

Figure 2.1 Schematical drawing of the relationship of the NDVI with different plant parameters. Solid arrows indicate a more direct functional relationship while dotted lines indicate a more indirect relationship (adapted from Jones and Vaughan, 2010).....14

Figure 2.2 Specular (A), Lambertian (B), asymmetrical scattering of a canopy (C; adapted from Jones and Vaughan, 2010) and hotspot within an RGB image of a winter wheat field (D; Burkart et al., 2015, Chapter 5). 16

Figure 2.3 Illustration of beam geometries within the concept of directional reflectance measurements. θ and ϕ denotes the zenith and azimuth angles, respectively, for the incident (i) and reflected (r) radiance (Suomalainen et al., 2009). 17

Figure 2.4 Schematic drawing of the field of view (FOV), instantaneous field of view (IFOV), ground instantaneous field of view (GIFOV) and ground sampling distance with point spread function of an airborne line scanner (left). Towards the edges of the swath, the ground sampling distance increases as a function of the oblique viewing angle and increased path length through the atmosphere. At the same time, the viewing geometry of every pixel changes slightly with every pixel (right; adapted from Jones and Vaughan, 2010).....21

Figure 2.5 Proportions of the image cube collected during a single detector integration period for scanning (a) and snapshot (b) devices (Hagen et al., 2012). X and y denote the spatial dimensions, while λ denotes the spectral dimension. 22

Figure 2.6 Different principles of data acquisition. Line-scanning devices record individual image-lines along one spatial dimension. Movement of the sensing system is needed to create a 2D scene (A). Snapshot cameras record image cubes with two spatial dimensions with every exposure. Thus, movement generates overlapping image cubes (B). 23

Figure 2.7 Growth of barley with BBCH-scale and typical periods of fertilization and plant protection (modified from Munzert and Frahm, 2005). 28

Figure 2.8 Dry matter accumulation in spring wheat in connection with photosynthetically active radiation (PAR) and green area index (modified from Fischer et al., 2014). 29

Figure 2.9 Climate diagram (long-term average 1956 - 2014) for Klein-Altendorf (Tilly, 2015).....29

Figure 2.10 Map of the CROP.SENSe.net experiment at Campus Klein-Altendorf in 2014 with plot number (large numbers) and cultivar (small numbers). The cultivar-wise colored squares indicate the destructive measurement part. The destructively sampled plots are framed with a solid rectangle. Positions of the ground control points (GCPs) and terrestrial laser scanning positions (TLS) are given. 31

Figure 3.1 Carrier Platform (CP) MikroCopter Okto XL with Gimbal and image capturing system (ICS) with UHD 185-Firefly and the single board computer (SBC) Pokini Z. 37

Figure 3.2 Full width at half maximum (FWHM) at each sampling wavelength as given by the manufacturer. 38

Figure 3.3 Scheme of the image cube after pre-processing of the spectral bands and merging with the grayscale image and pixel position band. 44

Figure 3.4 Generation of the hyperspectral 3D information with image pre-processing (dark current (DC) removal and radiometric calibration with reference image cube (IC (REF))) and merge to the grayscale image (PAN)) and the pixel position band (PPB) with MATLAB. Point cloud generation and georeferencing with ground control points (GCPs) with PHOTOSCAN. For the individual orthorectified image cubes the optimal cover area is calculated with Thiessen polygons, a mosaic is created and an orthomosaic is exported with ArcGIS. Since the spectral information is linked to the spatial information while the point cloud is generated the result is a hyperspectral digital surface model (HS DSM). 46

Figure 3.5 Histogram of the dark current values for the entire image cube between 466 (band 5) and 926 nm (band 120) (left) and dark current of band 5 (right). 48

Figure 3.6 Minimum (min), median and maximum (max) DN from 450 (band 1) to 926 nm (band 120) (left) and the intensity of 466 nm (band 5) relative to the maximum DN of the band (right) of a Zenith LiteTM panel on a sunny day. These values define the actual radiometric resolution for each band and individual pixel. 50

Figure 3.7 Image with reference targets as grayscale image (left), at 726 nm before (middle) and after (right) the radiometric correction and registration. 50

Figure 3.8 Comparison of spectra derived from the UHD (solid), an ASD (dashed) and their difference (dotted) for four reference panels with 5, 18, 43 and 58 percent reflectance. Additionally, a spectrum of the adjacent meadow grass is shown in light green. 51

Figure 3.9 Pixel distance in x (A) and y (B) direction from the image center of the original images. An absolute value of 25 correspond to pixels at the image edge, 1 to pixels closest to the image center. Radiometric precision (C) of the spectral information at 466 nm (band 5) and image overlap (D) of the scene. The dots represent the image capturing positions. 52

Figure 3.10 Map of the crop surface height. The spectrally measured non-invasive plot parts are marked in black with their plot number. Green points represent the ground control points while red ones represent the extraction points for the interpolation of the bare surface (left). Scatterplot of the averaged crop surface height for 26 plots compared to the manual ruler measurements of the marked 26 experimental plots (right). 53

Figure 3.11 3D visualization of the HS DSM with the BGI2 calculated from the hyperspectral data clipped to the extent of the experimental plots. The spectral sample areas are marked with black rectangles (left). The scatterplot shows the averaged BGI2 values per plot and the invasive measured chlorophyll values for the 36 plots (right). 54

Figure 4.1 RGB orthomosaic of the field experiment at 70 days after seeding. The black squares represent the non-destructive measurement parts while the white squares represent the destructive sampling parts. Unmarked plots were not measured by the ground-based measurements 70

Figure 4.2 Schematic drawing of the concept of the specific field of view (SFOV) of an area of interest (AOI) within a hyperspectral digital surface model generated from snapshot cameras. Each pixel within an image is recorded with different angular properties. The same surface area may be captured by several pixels with different angular properties (as denoted by the zenith reflectance angles $\theta r \; and \; \theta r'$ for one pixel. For clarity, the azimuth angles are omitted). The SFOV describes the pixels and their angular properties which are used to characterize an AOI (excerpt top right). Additionally, the field of views (FOVs) of two images and an instantaneous field of view (IFOV) of one pixel is shown. 75

Figure 4.3 Plant height extraction from the hyperspectral digital surface model (HS DSM). A digital terrain model (DTM) is created and subtracted from the digital surface model. The result is a canopy height model (CHM). 77

Figure 4.4 Ratio of the reflectance retrieved from the HS DSM and the FS3 averaged over all plots for DAS 56, 70 and 84 (solid line) with standard deviation (ribbon). Additionally, the ratio of plot 52 (upper black dotted line) and plot 20 (lower black dotted line) at DAS 56 is shown. 78

Figure 4.5 RGB image of plot 20 and 52 at DAS 56. The black frame marks the area measured within the HS DSM. The blue circles exemplary show six measurement positions of the FS3 within one plot. 79

Figure 4.6 Comparison of the 25° FOV of the FS3 (gray) and 20° of the UHD (orange) and their footprint from the same height (left and center). For plot 4 at DAS 70 the specific field of view (SFOV) within the hyperspectral digital surface is shown (right). The plot is characterizedi' by spectral information from two images (image A and B). The colors indicate how many pixels are taken from a particular position within the images. Additionally, the resulting along track SFOV is shown in light blue (left). 80

Figure 4.7 Relative difference between blending mode ‘average’ and ‘disabled’ of spectral data at 670 nm (left), and pixel position as distance from the image center in the original images in the y- (center) and x-direction (right). 82

Figure 4.8 Measurements of a Zenith Light reference panel under clear sky conditions (reference), with a person behind the panel in the principle plane (person pp.), person perpendicular to the principle plane (person), with a UAV above the panel held by a person within the principle plane (UAV pp.) and a UAV held from a person perpendicular to the principle plane (UAV). Additionally, a measurement under cloudy conditions with a UAV held by a person within the principle plane relative to a measurement under cloudy conditions without obstacles (cloudy pp.). 84

Figure 4.9 Maps of the red-edge inflection point (REIP) derived from the hyperspectral digital surface model of DAS 56, 70, 84 and 96. Please note that the data for DAS 56 is biased by the calibration under cloudy conditions (c.f. section 3.1.4). 86

Figure 4.10 Evolution of the canopy surface model for DAS 70: A) Map of image overlap, B) digital surface model (DSM), C) digital terrain model (DTM) interpolated from the DTM extraction points, and D) canopy height model resulting from the substraction of DTM from the DSM. The DSM and DTM show the ‘bowl-effect’ outside the covered ground control points. 88

Figure 4.11 Canopy height models of DAS 56, 70, 84 and 96. For DAS 70 to 96 some areas were excluded due to missing data. Remotely measured parts of the plots are marked with the number of the plot. Additionally, digital terrain model (DTM) extraction and ground control points are indicated. 90

Figure 4.12 Scatterplot of the ruler and HS DSM derived plant heights for the individual four measurement dates (red, yellow, blue, azure), and DAS 70 without plot 46 – 54 (green) and all dates together (pink). The one to one line is shown in gray. 92

Figure 5.1 Graphical user interface of the mAngle software with input fields for the desired waypoint pattern. By setting radius, number of desired waypoints as well as starting angle and other parameters, a distinct goniometric flight pattern can be generated. A draft of the waypoint pattern is visualized in the right box of the program window. 104

Figure 5.2 Wheat (Triticum aestivum) at the study site Merzenhausen, Germany, at the time of the multiangular flights, 18 June 2013. Ears were fully developed but still green. 105

Figure 5.3 Example Red-Green-Blue (RGB) images with tilt angles of 20°, 66° and 90°. These images were acquired at the Merzenhausen site at approximately 13:30 following a multiangular flight path identical to the spectrometer flights. The Field-Of-View (FOV) of the RGB camera is 73.7° × 53.1° (compared to the 12° FOV of the airborne spectrometer) and allows observing multiangular effects within a single image–the bright hotspot with the shadow of the unmanned aerial vehicle in the center, located in the lower left corner of the 90° image is an example..... 106

Figure 5.4 Reflectance of wheat at 480 nm measured at all 25 waypoints shown as a circular graph, or polar plot. Each “slice” represents a heading while each ring represents a sensor tilt angle. Spectral reflectance magnitude is color coded from low values of light blue, to high values in bright red. The angular position of the sun is depicted by the sun-symbol. In this figure no interpolation between waypoints is performed. 108

Figure 5.5 Camera orientation: Heading (azimuth) of the spectral measurements expressed in angular degrees from north. To assume a view angle of 0°, the UAV will hover north of the centeroid and aim the spectrometer at 180°. Tilt: 0° = horizontal and 90° = nadir view. 109

Figure 5.6 The spectrometer of the unmanned aerial vehicle goniometer was triggered three times at each waypoint. This figure shows the overall variation of the three spectra measured at each waypoint as average for the MERZ1 dataset. 110

Figure 5.7 To present the angular influence at different waypoints on the full spectrum the normalized nadir anisotropy factor (ANIF) of 66° tilt for all headings at MERZ1 from 400 to 823 nm is plotted as example. By using the ANIF notation spectral deviation of single waypoints is referred to the nadir waypoint and thus can be relatively compared. A waypoint with the same spectrum as nadir would remain at an ANIF of 1 throughout all wavelengths. The legend on the right represents the color of each ANIF curve and depicts their respective heading angle. The azimuth position of the sun (155°) is visualized by the sun symbol. 111

Figure 5.8 Top: Absolute values for the NDVI, TCARI and REIP compared to the nadir value (center of the polar plot) for all waypoints of MERZ1. The range of values is chosen with nadir as center value, respectively, for each plot. Figure 5.5 details the angular arrangement depicted here. Bottom: Relative differences for NDVI and TCARI compared to the nadir value. 113

Figure 5.9 Reflection of MERZ1 and MERZ2 for 5 wavelengths of interest. The color legend of reflection for each horizontal pair was scaled to the occurring reflectance wavelength range. Figure 5.5 details the angular arrangement depicted here. Waypoint (20°, 225°) is missing in MERZ2 and coded in this graphic in grey. 114

Figure 5.10 Comparison of modeled angular reflectance Soil-Canopy-Observation of Photosynthesis and the Energy balance (SCOPE) with the unmanned aerial vehicle (UAV) measured values for MERZ1. Shown are two exemplary wavelengths, which are scaled to the present range of values. 115

Figure 6.1 Instrumental set-up: (A) terrestrial laser scanner Riegl LMS-Z420i; (B) tractor with hydraulic platform; (C) ranging pole with reflective cylinder. 131

Figure 6.2 Workflow for the calibration and validation of the biomass regression models and distinction of cases for each model. 135

Figure 6.3 Maps of four plots from the last six and five campaigns of 2013 and 2014, respectively. One plot of each N fertilizer level of the barley cultivar Trumpf is shown for each year (∅: Plot mean height). 137

Figure 6.4 Regression of the mean CSM-derived and manual measured plant heights (2012: n = 131; 2013: n = 196; 2014: n = 180). 138

Figure 6.5 Scatterplots of measured vs. estimated dry biomass for one validation data set for NDVI, RGBVI, REIP, and GnyLi (exponential model). Pre-anthesis: crosses and solid green line; whole observed period: circles and dashed black line; 1:1 line: light grey. 142

Figure 6.6 Scatterplots of measured vs. estimated fresh biomass for one validation data set for NDVI, RGBVI, REIP, and GnyLi (exponential model). Pre-anthesis: crosses and solid green line; whole observed period: circles and dashed black line; 1:1 line: light grey. 143

Figure 6.7 Scatterplot for one validation data set for the pre-anthesis (green) and for the whole observed period (black) of the bivariate BRM of PH (circles and solid regression line) and multivariate BRM of PH and GnyLi (crosses and dashed regression line) for dry biomass (top) and fresh biomass (bottom) (all exponential models); 1:1 line: light grey. 144

Figure 7.1 Test site: spring barley experiment at Campus Klein-Altendorf agricultural research station in 2013 (Bendig et al., 2014) with ground control points (GCPs) used for crop surface model (CSM) generation. 165

Figure 7.2 Workflow for VIRGB calculation. (AOI = old and new cultivars in Figure 7.1) 169

Figure 7.3 'All data' class cross-validation scatter plots for observed dry biomass versus predicted biomass derived from validation datasets listed in Table 7.4; $p < 0.0001$ for all R^2. 172

Figure 7.4 'Pre-heading' class cross-validation scatter plots for observed dry biomass versus predicted biomass derived from validation datasets listed in Table 7.4; $p < 0.0001$ for all R^2. 173

Figure 8.1 Graphical user interface of HyperCor (left) with band exclusion table (right). 186

Figure 8.2 Spectral reflectance curves before (top) and after the pre-processing (bottom) with resulting correlogram for biomass. 187

Figure 8.3 Data processing and analysis with HyperCor. 189

Figure 8.4 Scheme of the multi-correlation matrix strategy with input correlation matrix CM1, CM2 … CMn and the resulting matrix f(CM1,CM2 … CMn) after applying a function. 189

Figure 8.5 Plot of biomass against the NDI for the MCMS (dashed) and standard approach (dotted) and the derived prediction model for tillering, stem elongation and heading (left). The corresponding correlograms of the mean coefficient of determination (R^2) for the years 2007 to 2009 for tillering, stem elongation and heading (right). 192

Figure 8.6 Plot of the predicted and observed biomass from the MCMS (dashed) and direct approach (dotted) for the validation dataset for tillering, stem elongation and heading. 193

Figure 9.1 The same plot extracted from different positions within six images (IC1 - IC6) seen at 670 nm (A), 798 nm (B) and as NDVI (C). The across-track pixel position is cropped at pixel 35. Additionally, the average relative change in reflectance at the two wavelengths and the NDVI along the average along-track position of the images is shown (D). The along-track pixel positions are almost parallel to the solar principal plane and pixels at lower pixel positions have a more acute angle to the sun. Since the sun's elevation is about 60°, the hotspot is at a zenith angle of about 30°. The along-track pixel position corresponds to the zenith angle of 10° towards the sun (pixel position 0) and 10° towards the sun averted side (pixel position 50). 202

Figure 9.2 Two images taken within seconds of each other at Campus Klein-Altendorf on 5 June 2014. The impact of wind gusts on the canopy is apparent. 203

Figure 9.3 Field of view of the FS3 (gray), UHD (yellow) and of multiple pixels within an HS DSM used to characterize an area (SFOV (light blue), c.f. Figure 4.6) with sparse vegetation (A) and dense vegetation (B). Towards a nadir viewing geometry beams from the soil are more likely to reach the sensor. The spectral data within the HS DSM is composed by pixels with a close-to-nadir viewing geometry captured from multiple positions. 212

Figure 9.4 Properties of single flight lines of the pushbroom camera micro-Hyperspec NIR (MHS) flown at the University of Tasmania after preliminary orthorectification (03/20/2014 unpublished data, left) and the HSC UHD flown at the Campus Klein-Altendorf (2014 DAS 70, right). For the MHS, digital numbers (DN) at 1025 nm and the across-track pixel position (pix pos) are shown. For the UHD, the reflectance (refl) at 544 nm and the corresponding across-track and along-track pixel positions are shown. Within the UHD data, some processing artifacts due to the exclusion of the other flight lines are visible. 213

Figure 9.5 Transects through point clouds of winter wheat plots derived with the software packages Pix4D, Sure and Photoscan (Grenzdörffer, 2014). 216

Figure 9.6 The maps at the top show the density of a point cloud within 0.1 m by 0.1 m cells derived by a terrestrial laser scanning system (TLS), the UHD and the GX1 camera flown on a UAV at almost the same date (around DAS 70, 2014). The color represents the point density per square decimeter (a histogram equalizer is applied to the color scheme to emphasize the different patterns). Additionally, the scan and the image capturing positions are shown in light green and light blue, respectively. The histogram at the bottom shows the distribution of densities for the three point clouds. 217

Figure 9.7 Schematic drawing of canopy height estimation with terrestrial laser scanning (blue), Structure from Motion (green) and manual ruler measurements (red) with the resulting average height (left). The shaded part of the canopy (gray background) can barely be captured by image-based approaches. 219

Figure 9.8 Oblique images (facing north) of the CROP.SENSe.net experiment at booting (top), heading (center) and development of fruit stage (bottom). Images are captured from the crop monitoring station (for details please refer to Brocks et al., in review). 222

Figure 9.9 Ratio of the leaf and stem dry biomass of barley at different days after seeding (DAS) with standard deviation. Generated from data of the CROP.SENSe.net experiment in 2013. No stem was developed for dates prior to DAS 49. 228

Figure 9.10 The upper triangular matrix shows the coefficient of determination (R^2) of all UHD band combinations with chlorophyll for DAS 70. The lower triangular matrix shows the difference of the result with spectral information of FS3 resampled to the UHD bands (rUHD) and the UHD data (rUHD - UHD). 230

TABLES

Table 2.1 Summary of the spectral and RGB sensing systems used in this study with relevant technical details such as the field of view (FOV) and instantaneous field of view (IFOV), typical above ground altitude (AGA), ground sampling distance (GSD) at typical above ground altitude, coverage (per time or scene) and full width half maximum (FWHM). 27

Table 2.2 Summary of the campaigns carried out with the terrestrial laser scanner (TLS), field-spectrometer (FS3), UAV RGB and UAV UHD in the context of this thesis in 2013 and 2014. The campaign dates are sorted by the day after seeding (DAS). For the manual sampling dates of the plant parameters (PP), the average BBCH-scale is given. 30

Table 3.1 Categorization of image-frame spectral cameras by the type of spectral information captured and the capturing procedure with some examples. Both categories are hierarchically structured: as hyperspectral cameras are multispectral cameras, so are snapshot cameras image-frame cameras. 35

Table 3.2 VIs used in this study and their formula. Some wavelength are slightly adjusted to align with the band configuration of the UHD. 48

Table 3.3 Coefficients of determination (R^2) and absolute and relative root mean square error (RMSE) of vegetation indices with chlorophyll, Leaf Area Index (LAI) and green biomass (green BM). 54

Table 4.1 Summary of the dates with corresponding days after seeding (DAS), parameters and environmental conditions during the UHD campaigns. Additionally, the date of the field-spectrometer (FS3) measurements and plant parameter (PP) extraction are shown. 72

Table 4.2 Coefficients of determination (R^2) of different vegetation indices for the prediction of chlorophyll for the individual dates and across the DAS 70 – 96 and 84 – 96 from the HS DSM and FS3 data. 87

Table 4.3 Quantitative comparison of the ruler measured and the HS DSM derived plant heights. 91

Table 5.1 Local time and duration with the corresponding sun angle parameters for the two hyperspectral flights performed over wheat field in Merzenhausen, Germany. 106

Table 5.2 Vegetation indices used in this study and their underlying formulas. 107

Table 5.3 Soil-Canopy-Observation of Photosynthesis and the Energy balance model (SCOPE) input parameters: Leaf Area Index (LAI), Leaf Inclination (LIDFa), Chorophyll A/B (Cab) content in µg/cm2, Leaf Thickness Parameter (N), Leaf water equivalent layer (Cw) in cm, Dry matter content (Cdm) in g/cm2, Senescent material fraction (Cs), Variation in leaf inclination (LIDFb). Default values were used for all other SCOPE input parameters. 108

Table 5.4 Accuracy of the unmanned aerial vehicle (UAV) heading and spatial positioning calculated by structure from motion using 75 high-resolution images. Nine images were unusable due to motion induced “blur” and excluded from processing. Heading and tilt columns represent the deviation of the cameras actual pointing direction to the programmed angle. Altitude, X- and Y-position describe the deviation of the UAVs position as calculated from the differential-GPS ground-referenced structure from motion approach compared to the programmed waypoints. 110

Table 5.5 Normalized nadir anisotropy factor (ANIF) values for five characteristic wavelengths in the blue (480 nm), green (550 nm), red (680 nm) spectral bands; red-edge-inflection-point (REIP) (733 nm) and near-infrared (NIR) (780 nm) for 20°, 43° and 66° tilt, as well as all headings together with their average values. Values greater than 1 (blue bar) represent spectral reflectance measurements greater than nadir; values below 1 (red bar) represent measurements less than nadir. The suns azimuth was 155° and elevation 66°. 111

Table 5.6 Correlation of modeled data with measured data for different tilt angles. 116

Table 5.7 Correlation of modeled data with measured data for all tilt angles at specific wavelengths. 116

Table 6.1. Dates of the terrestrial laser scanning (TLS) and spectrometer (S) campaigns listed as day after seeding (DAS). Averaged codes for the developmental steps are given for the dates of manual plant parameter measurements (BBCH). For some dates BBCH codes were not determined (N/A). 129

Table 6.2. Principal growth stages of the BBCH scale. 130

Table 6.3. Vegetation indices(VIs) used in this study. 134

Table 6.4. Statistics for the plot-wise averaged CSM-derived plant heights and destructively taken biomass for the reduced data sets of 2013 and 2014 (n: number of samples; x: mean value; min: minimum; max: maximum; SD: standard deviation). 139

Table 6.5. Statistics for the model calibration as mean values of the four subset combinations (R^2: coefficient of determination; SEE: standard error of the estimate). 140

Table 6.6. Statistics for the model validation as mean values of the four subset combinations (R^2: coefficient of determination; RMSE: root mean square error (g/m²); d: Willmott's index of agreement). 141

Table 7.1 Near infrared vegetation indices (VINIR) used in this study where R = reflectance (%), RR = red (630-690 nm), Ri = reflectance in a narrow band e.g. R1220 = 1220 nm, L = constant (Huete, 1988). 167

Table 7.2 Visible band vegetation indices (VIRGB) used in this study where R = reflectance (%), RR = red, RG = green, RB = blue. Red, Green and Blue are the DN values in the respective channels extracted from the orthophotos. 168

Table 7.3 Coefficient of determination (R^2) and root mean square error (RMSE) for regression between dry biomass and either CSM derived plant height (PHCSM) or near infrared (VINIR) or visible band (VIRGB) vegetation indices where n = number of samples; ER = exponential regression and LR = linear regression. 170

Table 7.4 Cross-validation relationships between observed and predicted biomass (kg/m²) for selected vegetation indices, PHCSM respectively and combinations of both; ER = exponential regression; MLR = multiple linear regression, LR = linear regression; MNLR = multiple non-linear regression; n = number of samples; SE = standard error; R^2 = coefficient of determination; RMSE = root mean square error; RE = relative error. 171

Table 8.1 Overview of the three spectrometers and their configurations. 184

Table 8.2 Descriptive statistics of the biomass with number of samples (#), mean, standard deviation (std) and coefficient of variation (cv) separated by year and stages tillering (t), stem elongation (se) and heading (h). 185

Table 8.3 Summary of the results of MCMS and direct approach with the correlation of calibration and validation. 191

Table 9.1 Sources of influence along the path from particle to pixel with an approximated potential impact on the information relative to the signal. 210

Table 9.2 Summary of the issues related to the comparability of the data contained in HS DSMs to data from other sensing systems and destructive in-field measurements. 226

Table 9.3 Coefficient of determination (R^2) of the plant height (PH) and the optimized combination of spectral and PH data for the estimation of fresh and dry biomass at different dates after seeding (DAS). 229

Table 9.4 Coefficients of determination (R^2) of different vegetation indices (VIs) with chlorophyll at different days after seeding (DAS) for the same combinations of datasets as in Aasen and Bolten (in review, Chapter 4). UHD denotes the results of an optimized combination of UHD bands (denoted with its wavelength in nm), rUHD for FS3 data resampled to UHD bands, VI for the best performing published VIs used in Aasen and Bolten (in review, Chapter 4) and VIS for the spectral data resampled to the RGB bands in WorldView-3 configuration. 231

Table 9.5 Quality of the retrieval (o: $0.48 < R^2 < 0.7$) of different plant parameters from HS DSMs acquired with the UHD and potential applications in precision agriculture. 234

ABBREVIATIONS

As used in Chapter 1, 2 and 9.

AGA	Above ground altitude
ANIF	Anisotropy factor
APEX	Airborne prism experiment
BBCH	Scale to characterize the phenological stage of crops. Developed by the Biologische Bundesanstalt (German Federal Biological Research Centre for Agriculture and Forestry), Bundessortenamt (German Federal Office of Plant Varieties), and chemische Industrie (chemical industry)
BRDF	Bidirectional reflection distribution function
BRF	Bidirectional reflectance factor
CIR	Color infrared
DAS	Day after seeding
DN	Digital number
DSM	Digital surface model
DTM	Digital terrain model
FOV	Field of view
FS3	Field-spectrometer 3
FWHM	Full width at half maximum
GCP	Ground control point
GIFOV	Ground instantaneous field of view
GSD	Ground sampling distance
HCRF	Hemispherical-conical reflectance factor
HDRF	Hemispherical-directional reflectance factor
HS DSM	Hyperspectral digital surface model
HSC	Hyperspectral snapshot camera
IFOV	Instantaneous field of view
LAI	Leaf area index
LiDAR	Light detection and ranging
MHS	Micro-Hyperspec NIR
NDVI	Normalized difference vegetation index
NIR	Near infrared
PAR	Photosynthetic active radiation
PH	Plant height
PP	Plant parameter
REIP	Red-edge inflection point
RGB	Red, green, blue bands
SfM	Structure from Motion
SFOV	Specific field of view
SIFT	Scale invariant feature transform operator
SWIR	Short wave infrared
TLS	Terrestrial laser scanning
UAV	Unmanned aerial vehicle
UAV-STS	UAV-Goniometer
UHD	UHD-185 Firefly
VI	Vegetation index
VIS	Visible (part of light spectrum)

Abbreviations are generally introduced once. Still, for an improved understanding of the text, they might be spelled out at several places.

1. INTRODUCTION

Global agriculture faces enormous challenges. The world's population is growing and large parts of it are changing their diet to an increased consumption of high-protein and energy-dense food such as meat (Pingali, 2007). At the same time, there are approximately 870 million people worldwide who are undernourished (FAO, 2012). Thus, global crop production will need to be doubled by 2050 (Tilman et al., 2011). While early agricultural revolutions involved the expansion of agricultural land (Pretty and Bharucha, 2014), continuing such expansions is a threat to biodiversity (Balmford et al., 2005). Moreover, much of the remaining reserves of cultivable cropland is under valuable forests or in protected areas (Ramankutty et al., 2002). Besides, most of the increase in total yield of major crops such as maize, rice and wheat in the past 40 years has been driven by an intensification of agricultural production within the *green revolution* (Foley et al., 2011; Pingali, 2012). Along with the introduction of high yield seeds, this development is largely based on an increasing use of chemical fertilizers and pesticides, mechanization and irrigation. As an example, the global nitrogen fertilizer use increased by about 600% since 1960 (Matson, 1997) and in 2005, agricultural production accounted for 10 – 12% of the total anthropogenic greenhouse gas emissions (Burney et al., 2010). Besides, over the last 50 years more than 40% of the increase in food production has come from irrigated areas, which have doubled in size (FAO and OAA, 2011) and are the primary users of diverted water in some regions of the world (Fereres and Soriano, 2006). Overall, agricultural systems are concurrently degrading land, water, biodiversity and climate. In light of the planet's limited resources and increasing global population, a turn is needed towards more sustainable growth in agricultural production while simultaneously diminishing its environmental footprint (Foley et al., 2011).

1.1 Remote sensing in support for site-specific crop management

One approach towards more sustainable crop production is increasing the cropping efficiency (Foley et al., 2011). This can be accomplished by dividing agricultural areas into management zones that receive customized management inputs based on crop requirements as they vary in the field, such that resources are used in the right place at the right time. Such practices are called *site-specific crop management* (Pinter et al., 2003; Whelan and Taylor, 2013) and are part of *precision agriculture* (Mulla, 2013). With current agricultural machinery, such as the Leeb GS (HORSCH Maschinen GmbH, 2016), crop treatments can be applied with a spatial precision of about 0.25 m. At the same time farmers can control their machinery in near real time with farm information systems such as the Operation Center (John Deere GmbH & Co. KG, 2016). However, the operational success of variable applications of fertilizer or other management actions requires accurate data to produce maps of crop growth, weeds, insect infestations, nutrient and water deficiencies and other crop and soil conditions (Moran et al., 1997). But also the timeliness of that information is important. Phenomena such as plant diseases are

highly dynamic and require short revisit times (Voss et al., 2010). For other applications such as the monitoring of phenology, crop vigor or yield a revisit time of 5 to 10 days can be determined as appropriate on a local to sub-national scale (Justice and Becker-Reshef, 2007).

Spectral (Yao et al., 2012) and other remote sensing techniques (Lee et al., 2010) can provide timely and accurate information (Atzberger, 2013) about important parameters for agricultural applications (Clevers and Jongschaap, 2003). Satellites cover wide areas and as the spatial and spectral resolution of satellite imagery has improved, their suitability for precision agricultural applications has increased (Mulla, 2013). However, for optical satellites, cloud cover compromises the necessary revisit times. A study by Claverie et al. (2012) on the estimation of biomass from Formosat-2 data reported that for the study area in southwest France no cloud-free images could be obtained from February 11 to June 19 in 2008, which is the major growing period of several crops in central Europe (Munzert and Frahm, 2005). Radar systems could circumvent this problem but are not yet operational for systematic crop monitoring purposes (Nelson et al., 2014). Satellite systems are also lagging behind in comparison with the spatial precision of current agricultural machinery. Presently, systems such as Sentinel-2 provide free spectral data in a spatial resolution of up to 10 m (ESA, 2016). Commercial systems such as WorldView-3 provide spectral information with a spatial resolution of about 1.3 m (DigitalGlobe, 2016), but their usability is limited by the costs and availability of a scene. Additionally, the spectral resolution of most satellite systems is too coarse compared to a suggested bandwidth of less than 10 nm for an adequate mapping of agricultural crops (Thenkabail et al., 2012). Current operational airborne systems, such as the Airborne Prism EXperiment (APEX), provide data in a high spectral resolution and a spatial resolution of 1 – 2 m at their typical flying altitude (Schaepman et al., 2015). However, long turnaround times combined with the high volume of data processing and high operational costs, due to the lack of cost-effective products from private companies, have limited the use of airborne sensors to research activities (Berni et al., 2009).

Overall, it can be concluded that the demand for timely information (revisit time of 5 – 10 days) in very high spatial (~ 0.25 m) and spectral resolution (< 10 nm) in support of more sustainable crop production through efficient site-specific crop management cannot be met by current remote sensing solutions. However, due to recent technical innovations, remote sensing is in transition and this may be about to change.

1.2 Diversification in remote sensing

Remote sensing is “the acquisition of physical data of an object without touch or contact”. Since this definition was posed by Lintz and Simonett (1976), the field has undergone several phases of transition. After an era where aerial photography was mostly used in military applications, Evelyn Pruitt coined

the term 'remote sensing' in the 1960s in an appreciation of the many forms of imagery that was collected (Campbell and Wynne, 2011; Jones and Vaughan, 2010). By the 1990s, satellites designed to acquire global coverage to monitor changes in the world's ecosystem were launched (Mather et al., 1992). But until the first decade of the 21st century, remote sensing was the work of specialists who produced specialized data products for other specialists. With the introduction of tools like Google Earth, geospatial data became available for a wider public audience (Campbell and Wynne, 2011). Still, this data was mostly generated using specialized instruments attached to platforms such as airplanes or satellites, and provided by a few specialists or specialized organizations. Due to the combination of developments in the fields of robotics, sensor technology, photogrammetry and computer vision, the way how remote sensing data is created is in transition.

The first important development is coming from advancements in the field of robotics. Unmanned Aerial Vehicles (UAVs), also known as 'Unmanned Aerial Systems' or 'Remotely-Piloted Aerial Systems', have infiltrated the field of remote sensing as a new sensing platform (Figure 1.1). While in 2004 the Congress of the *International Society for Photogrammetry and Remote Sensing* had only three UAV related papers, the last congress in 2012 held already nine sessions with a total of around 50 papers on UAV and remote sensing related papers (Colomina and Molina, 2014). Journals such as *Remote Sensing* (MDPI RS) or *Photogrammetric Engineering and Remote Sensing* (PE & RS) have published and announced issues specifically for or with major contributions on remote sensing with UAVs – of which two were also specifically related to vegetation and agricultural crops. This might result from the potential of M-class UAVs with a takeoff weight of less than 5 kg (for a classification of UAVs please refer to Eisenbeiß (2009). In the course of this thesis the term UAV will implicitly refer to UAVs of the M-class). These UAVs are rather low-cost platforms and operationally flexible (Berni et al., 2009), which makes them suitable for a number of applications including precision farming (for a comprehensive overview please refer to Colomina and Molina, 2014; Pajares, 2015; Salamí et al., 2014). Additionally, they can fly slowly at low altitudes and are able to acquire spatial information in high resolution (Pajares, 2015). Together with specialized sensors, they are becoming powerful sensing systems.

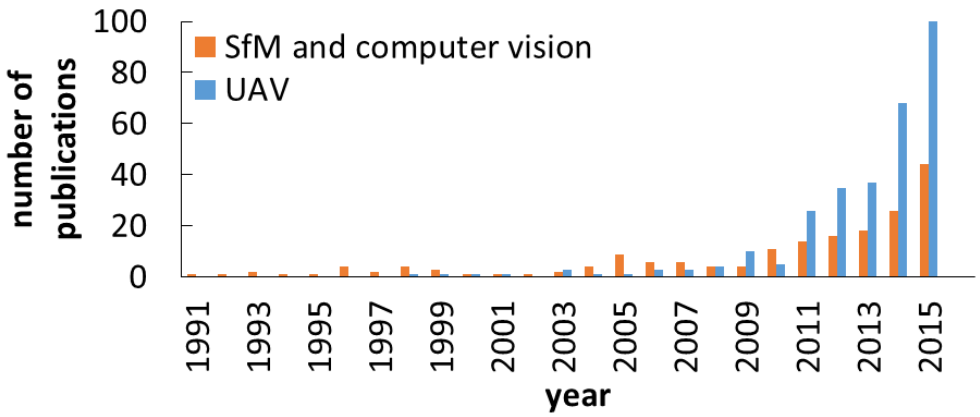

Figure 1.1 Number of publications on remote sensing in combination with UAV[1] or SfM and computer vision[2] in the Web of Science.

The second important development currently taking place is in the field of sensor technologies. Remote sensing systems are becoming available for a broader range of use and to a wider audience. Active systems such as laser scanners can be used to create dense point clouds with millions of points in a very short time (Vosselman and Maas, 2011). Airborne laser scanning systems have been applied since the 1970s (Lillesand et al., 2008). Within the last 20 years also ground based systems were introduced. These have been rapidly developed to achieve higher ranges and measurement rates and more and more systems appear on the market. Additionally, recently these systems are accompanied by low cost and light weight systems, which are potentially accessible to more users (Large and Heritage, 2009; Tilly, 2015) and are suitable for new applications (e.g. on UAVs, see Wallace et al., 2012).

Passive systems such as spectral radiometers measure the intensity of radiometric radiation within a defined spectral range (Jones and Vaughan, 2010). Since Goetz (1975) described the first portable radiometer to be applied in the field, spectral sensing systems have continued to shrink in size and weight. With the development of sensors like the Mini-MCA (TETRACAM Inc, 2015) and the Headwall Micro-Hyperspec (Headwall Photonics Inc, 2015) these systems are now suitable for mounting on UAVs (Berni et al., 2009; Kelcey and Lucieer, 2012; Zarco-Tejada et al., 2012). Within the last three years, a great variety of spectral sensing systems for UAVs have become available and have been applied to remote sensing. These systems can be distinguished by the spatial dimensionality of the data they record. While whisk- and pushbroom systems record individual pixels or image lines, hyperspectral snapshot cameras (HSCs) record hyperspectral data in two spatial dimensions within a single integration period (Hagen et al., 2012). This brings a significant advantage: similar to common RGB cameras, their 2D images contain information about the shape and position of the objects within their

[1] Web of Science search on “TS=("remote sensing") and TS=("UAV*" or "UAS*" or "RPAS*" or "Remotely-Piloted Aerial System*" or "Unmanned Aerial System*" or "Unmanned Aerial Vehicle*")”, 2016-04-18

[2] Web of Science search on “TS=("computer vision" or "SfM" or "structure from motion") and TS=("remote sensing")”, 2016-04-18

field of view (FOV). Recently, these systems have been miniaturized and systems such as the UHD-185 Firefly (UHD; Cubert GmbH, 2016) can now be flown onboard UAVs.

The third important development comes from the coalescence of the fields of photogrammetry and computer vision. With photogrammetric algorithms overlapping 2D images can be aligned and the 3D geometry of an object can be reconstructed by using the mathematical model of central projection imaging (Luhmann et al., 2014). Particularly important for UAV remote sensing was the development of the Structure from Motion (SfM) technique within the field of computer vision and its combination with digital photogrammetry (Colomina and Molina, 2014; Eltner and Schneider, 2015). Advances of the latter in image matching (Gruen, 2012), orientation (Remondino et al., 2012) and the process of dense 3D point cloud generation allow the reconstruction of surfaces in very high resolution (Haala, 2013). Several implementations of these algorithms exist, some of them with the ability to exploit today's computing powers through parallel processing on multi-core central processing and graphical processing units (Remondino et al., 2014). These developments have fundamentally changed the photogrammetric recording process. Together with software tools with simple interfaces, they allow even non-experts to apply these methods (Luhmann et al., 2014). Consequently, these methods are increasingly used by the remote sensing community (Figure 1.1).

In summary, the combination of these developments have opened up the way for a new phase in remote sensing, where more and more sensors become available and a wide range of users have the ability to collect and generate data based on their specific needs. This diversification of sensing systems and methods also opens up new opportunities for precision agriculture applications. However, spectral remote sensing of vegetation is not a trivial task, as will be seen in the next section.

1.3 Complexity of spectral remote sensing of vegetation

Natural factors such as atmospheric and illumination conditions (Damm et al., 2015; Ishihara et al., 2015; Rasmussen et al., 2016) and topographic effects (Richter and Schläpfer, 2002) influence the remote sensing signal. Additionally, natural properties of the surface such as its anisotropy may affect the signal (Schläpfer et al., 2015; Weyermann et al., 2014). In remote sensing, errors associated with data acquisition, processing, analysis, conversion, and final product presentation can have a significant impact on the confidence of the decisions made using the data, since they accumulate during the processing steps (Lunetta et al., 1991). Therefore, assessing the quality of the data and accuracy of its analysis is crucial to understanding the reliability of the information.

The literature on the assessment of the accuracy of data analysis techniques is comprehensive[3]. Although subject to discussion (Foody, 2002; Pontius and Millones, 2011), the assessment of the quality of classifications of remotely sensed data has been well established for decades (e.g. Congalton, 1991). Additionally, many articles have been published on assessing the accuracy of quantitative retrieval methods to estimate specific plant parameters such as pigment content (Ustin et al., 2009), biomass, leaf area index (LAI; Hansen and Schjoerring, 2003) and other plant traits (Homolová et al., 2013). Increasingly, state-of-the-art machine learning methods such as Gaussian Processes are being used in remote sensing applications and provide uncertainty measures inherently (Verrelst et al., 2012).

In comparison, the literature on the assessment of the quality of the data acquisition and processing of raw data from remote sensing sensors is rather limited[4] and often sensor-specific, although undertaken in great detail by the involved researchers. During the acquisition process the sensing system, as well as the applied measurement protocol, influence the data. Thus, comprehensive calibration and validation procedures are continuously carried out to characterize the performance of established satellite (e.g. EO-1 Hyperion: Datt et al., 2003) and airborne (e.g. AVIRIS: Green et al., 1998; APEX: Schaepman et al., 2015) sensing systems. These procedures are complex, as seen in Schaepman et al. (2015), where the results of 10 individual validation studies are summarized to fully describe the specifications and corresponding performances for just the APEX sensor. This effort is needed since most users expect the data to be in standardized reflectance quantities. But standardization of spectral remote sensing data is a very difficult task due to the existence of different types of reflectance quantities (c.f. Subsection 2.1.2) and the interaction of the sensing system with the properties of the surface and the environment. For vegetated surfaces, the latter is mostly driven by the anisotropy of the canopy and its interaction with the incident irradiance field and the viewing direction of the sensing system described by the framework of the bidirectional reflection distribution function (BRDF) of a surface (Nicodemus et al., 1977; Schaepman-Strub et al., 2006). It highly influences imaging spectroscopy data and needs to be regarded for all measurements (Schläpfer et al., 2015; Weyermann et al., 2014). BRDF effects are a major source of uncertainty (Richter and Schläpfer, 2002) and only a small scientific community explicitly addresses the issue for space, airborne and ground-based observations[5]. This is particularly interesting, since almost all remote sensing textbooks address the issue (Campbell and Wynne, 2011; Jensen, 2007; Jones and Vaughan, 2010), but it has not yet been 'solved', even for well-developed sensing systems such as Landsat (Nagol et al., 2015).

[3] Web of Science search on "TS = (hyperspectral and (retrieval or classification) and accuracy)" yields 1489 matches, 2016-04-18

[4] Web of Science search on "TS = (hyperspectral and sensor and (calibration or "data acquisition"))" yields 244 matches, 2016-04-18

[5] Web of Science search on "TS = ("*directional effect*" or "brdf") and TS= ("correction" and "reflectance") not TS=("atmospheric correction")" yields 69 matches, 2016-04-18

The minor interest in issues related to data collection, calibration and standardization may be due to two reasons: first, according to information theory, data on higher processing levels is more meaningful and has a higher number of potential users (Rowley, 2007). Second, as outlined in Section 1.2, until recently only a few air- and spaceborne imaging spectroscopy systems collected the data for almost the whole scientific community and the associated mission team was responsible for the data quality. However, with the diversification in remote sensing, individuals, research teams or companies can start to collect their own imaging spectroscopy data. While this drastically improves the flexibility of the process of data collection, the burden of data quality assurance is also on individual users of these sensing systems. Thus, knowledge is needed on how to calibrate hyperspectral sensors so that they provide reliable data, and how this could be accomplished by 'normal' researchers who do not have access to advanced calibration facilities.

The diversification in remote sensing emphasizes the importance of more than just data quality concerns. The advent of new sensors with different sensing techniques, their application in a variety of settings, and data processing done by different users with different processing workflows, raises the issue of comparability. As an example within the domain of field-spectroscopy, studies found differences due to the technical design (Mac Arthur et al., 2012) and the specifications of instruments (Julitta et al., 2016) as well as due to different operation and sampling modes (Anderson et al., 2011; Mac Arthur and Robinson, 2015). Results from different scales, such as ground and UAV observations, and different types of sensors, such as imaging and non-imaging sensors, may also differ (Bareth et al., 2015a; von Bueren et al., 2015). Such considerations are specifically important for sensor systems that are also suitable for UAVs, since their biggest advantage is also a challenge: the miniaturization of sensors is usually a compromise between size, weight, specifications and cost. Thus, such systems tend to produce data with reduced radiometric, spectral and geometrical quality in comparison to systems on manned aircrafts (Zarco-Tejada et al., 2014).

But comparative studies on the retrieval of 3D data in forest environments have also disclosed differences between different sensing techniques, such as airborne laser scanning and SfM (Dandois and Ellis, 2013; Lisein et al., 2013; White et al., 2015), and between different processing tools and illumination conditions for SfM (Dandois et al., 2015). For cereal canopies, a study by Grenzdörffer (2014) confirmed the influence of the processing tools, but other sources of influences have not been investigated yet. These results demonstrate that the findings of one campaign are hard to extend to other campaigns if the comparability of the sensing system and sensing circumstances have not been investigated and thus, systematic differences have not been identified. Therefore, besides an assessment of the data quality of a data product, information about its comparability is also important. Thus, both issues will be addressed in the course of this thesis.

1.4 Research objectives and outline

Enabled by the current diversification in remote sensing, this thesis explores new approaches to address the demand for timely information in high spatial and spectral resolution to support site-specific crop management. The focus is placed on hyperspectral digital surface models (HS DSMs) – a representation of the surface in 3D space linked with hyperspectral information emitted and reflected by the objects covered by this surface (Aasen et al., 2015, Chapter 3) –, which are developed within this thesis. Their generation is based on data acquired by novel lightweight HSCs carried by UAVs and data processing based on SfM. The overall aim is to evaluate whether HS DSMs of crops are suitable to support a site-specific crop management. This evaluation is based on the discussion of three research objectives, which are motivated by the complexity of the remote sensing of vegetation (Section 1.3), a diversification of sensing systems and processing workflows (Section 1.2) and the demands of site-specific crop management (Section 1.1). The concept of this thesis is that each research objective supports the discussion of the next research objective until the overall research aim is reached (Figure 1.2).

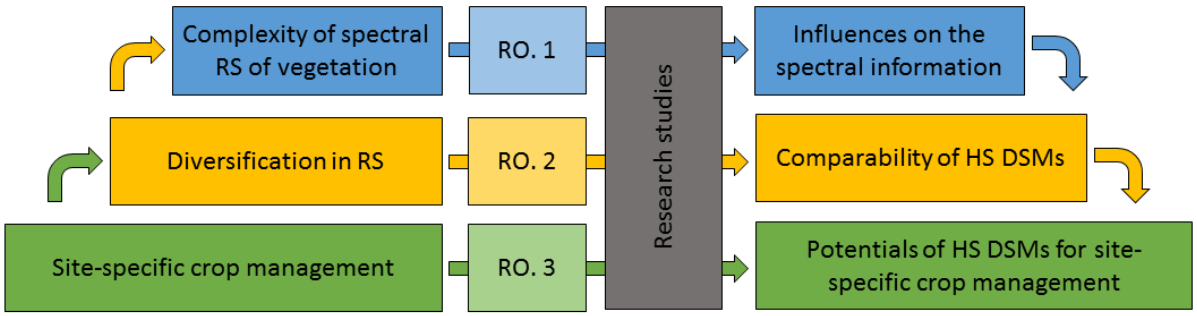

Figure 1.2 The concept of this thesis. The three research objectives (RO) are motivated by the introductory chapters and discussed based on the research studies. The discussion of subsequent RO is supported by the insights from the previous research objective (RS denotes remote sensing).

The discussion of the research objectives is based on the six research studies (Chapters 3 to 6) within this thesis. The first three studies focus on rather methodological aspects in the context of hyperspectral measurements with UAVs: Aasen et al. (2015, Chapter 3) introduces the method to generate HS DSMs with HSCs and to trace the properties of individual pixels. Aasen and Bolten (in review, Chapter 4) uses this method and investigates the special properties of the spectral data within HS DSMs. Burkart et al. (2015, Chapter 5) investigates the influence of different viewing geometries within spectral data acquired from UAVs. The other three studies focus on potentials of HS DSMs for precision agriculture applications, but use data which is not captured by HSCs: Tilly et al. (2015, Chapter 6) and Bendig et al. (2015, Chapter 7) combine spectral and plant height (PH) data acquired with terrestrial laser scanning (TLS) and an RGB camera system to estimate the biomass of barley. Aasen et al. (2014, Chapter 8) introduce a new method to use large multi-temporal spectral libraries to improve

the prediction of the biomass of rice. Chapter 2 complements the content of the research studies to provide the necessary background for the discussion of the three research objectives (Chapter 9), which are described in the following.

1.4.1 Influences on the spectral information

The first research objective is motivated by the complexity of spectral remote sensing of vegetation (Section 1.3). The process of gathering information about plant particles (plant compounds such as pigments or cells) is complex. At each step of the remote sensing process (c.f. Campbell and Wynne, 2011), from the creation of a signal by these particles to its representation within a data product, the information is prone to many sources of influence. Already the data acquisition is influenced by environmental conditions and their interaction with the sensing system. But the transformation of the signal to digital data within the sensing system and its conversion into information during the data processing also influences how the particle is represented within the pixels of the final data product. This transformation of the signal to information will be called 'the path of information from particle to pixel' and is outlined in Figure 1.3. In this context it should be noted that processes such as scattering within the plant also influence its absorption, reflectance and transmittance (Kumar et al., 2003). However, the influences of these processes are beyond the scope of this thesis.

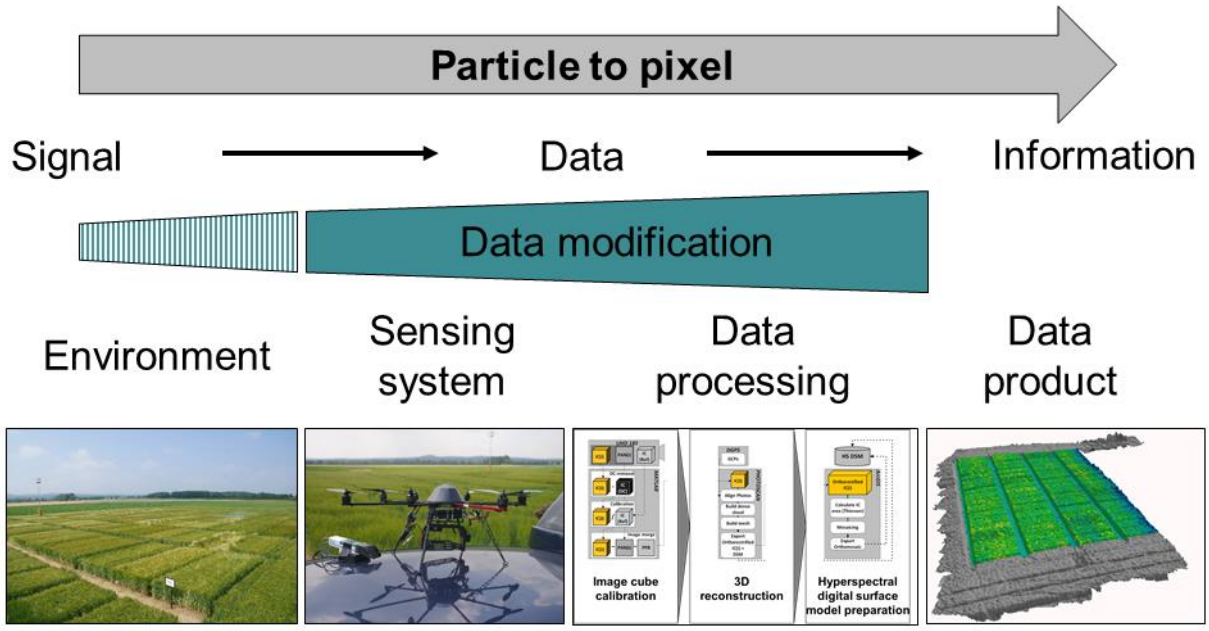

Figure 1.3 The path of information from particle to pixel: The information about a particle within an environment is modified at different stages. Its acquisition is influenced by environmental conditions and their interaction with the sensing systems. The transformation within the sensing system of the signal of a particle to data and its conversion into information during the data processing also influences how the particle is represented within the pixels of the final data product.

As Section 1.3 highlighted, information about the data quality as well as knowledge about the appropriate methods to derive the data is important. Thus, the first research objective of this thesis evaluates and discusses the spectral data quality derived from HSCs and the introduced method to derive HS DSMs. In order to be able to assess the quality of remotely sensed data, it is necessary to appreciate the errors that may enter at all stages of the process (Jones and Vaughan, 2010). Thus, in Section 9.1 the path from particle to pixel is traced to investigate and discuss the following potential sources of influence during the generation of HS DSMs:

Subsection 9.1.1 Interactions with the environment

Subsection 9.1.2 Sensing system and measurement protocol

Subsection 9.1.3 Data processing

These aspects are investigated and discussed in as follows: in Burkart et al. (2015, Chapter 5) a novel approach is used to investigate the interaction of the environmental illumination conditions with a cereal crop canopy and the sensing system. The impact of angular effects (i.e. the interaction of the measurement geometry of a sensing system and the anisotropy of a surface) on the hyperspectral signal and vegetation parameter retrieval by means of vegetation indices (VIs) are quantified for a wheat canopy at two different times of the day with an UAV goniometer. In Aasen et al. (2015, Chapter 3), a novel method is developed to trace these angular effects in imaging spectroscopy data captured by HSCs. Based on these two chapters, the potential influence of angular effects on imaging spectroscopy data from HSCs is approximated and discussed in Subsection 9.1.1. Additionally, other environmental sources of influence are identified.

Right before the start of this thesis in April 2013, a prototype of the HSC system "UHD 185-Firefly" arrived at our research group. In Aasen et al. (2015, Chapter 3) this HSC system is characterized and a radiometric calibration procedure is developed. In Subsection 9.1.2, the results of this characterization are used to estimate and discuss the influences resulting from the technical aspects of the sensing system on the level of individual pixels. This discussion is complemented by results of Aasen and Bolten (in review, Chapter 4) where the calibration protocol is investigated. Aasen and Bolten (in review, Chapter 4) also investigates the special data properties within the spectral data of HS DSMs. Additionally, the influence of different processing schemes on the final data product are investigated. The results of these investigations are set in context to potentially desired data products and discussed in Subsection 9.1.3.

Overall, this first research objective is focused on the spectral data derived by HSCs. For each source of influence, the influenced data entity level (pixel, image, scene) is identified and, where possible, the magnitude of the impact is approximated. Thus, the results of this first research objective are a characterization and evaluation of the spectral data within the HS DSMs. Not only does this provide

the necessary information to assess the quality of the data, but it is also the basis for an appropriate interpretation of the results of subsequent analysis procedures. Additionally, it provides the necessary background to compare the spectral data contained in HS DSMs with the data from other sensing systems, which is part of the discussion in the second research objective.

1.4.2 Comparability of hyperspectral digital surface models

The second research objective is motivated by the advent of new sensing systems and an increasing variability of data processing workflows (Section 1.2) and the challenges associated with this development (Section 1.3). It discusses the comparability of the HS DSMs to remotely sensed data of other instruments and destructive in-field measurements. Information about the comparability of a new method is important to investigate systematic differences, which must be regarded if results from different studies are compared. Additionally, this can lead to insights into the suitability of a new method to substitute or complement an established method. With the ongoing diversification in remote sensing and the appearance of new sensing systems, the need for such information becomes increasingly important as can be seen also within this thesis. In total, five different sensors with different processing workflows were used in the studies to gather information about crop canopies. The data and insights gained in these studies provide the basis to discuss the comparability of HS DSMs in Section 9.2 with regard to:

Subsection 9.2.1	Spectral data from other sensing systems
Subsection 9.2.2	DSMs derived from SfM, with different tools and different settings, and TLS
Subsection 9.2.3	Different canopy height estimations
Subsection 9.2.4	Destructive in-field measurements

These aspects are discussed as follows: in Subsection 9.2.1 the results of Aasen and Bolten (in review, Chapter 4) are generalized in a discussion on the comparability of the spectral data within HS DSMs to other types of spectral data. Additionally, the established data processing workflow introduced in Aasen et al. (2015, Chapter 3) is reviewed with regards to its ability to produce data comparable to data products of established sensing platforms. Here aspects of the first research objective are picked up and differences in the measurement geometry and data processing of pushbroom and snapshot systems will be examined. Lastly, the comparability of uncalibrated RGB data, as used in Bendig et al. (2015, Chapter 7), to the spectral data used in Aasen et al. (2015, Chapter 3) and Aasen and Bolten (in review, Chapter 4), is discussed.

In Subsection 9.2.2 and 9.2.3 investigate the comparability of DSMs. Within this thesis, DSMs are derived from 3D point clouds generated by SfM applied to images from an HSC (Aasen et al., 2015, Chapter 3; Aasen and Bolten, in review, Chapter 4) and an RGB camera (Bendig et al., 2015, Chapter

7). These two cameras not only differ by the type of information they record, but also by their images' specifications. Additionally, TLS is used to derive DSMs (Tilly et al., 2015, Chapter 6). This raises the question of whether the DSMs derived by these different approaches are comparable. This can only be answered by understanding how the DSMs are generated. Therefore this research objective starts with investigating systematic differences within the point clouds of these approaches. Similar to in the first research objective, the path of particle to pixel is followed but now for the 3D data. As a first step, the influence of different image capturing conditions (such as the flight pattern, image specifications and illumination conditions) and different implementations of the SfM method on the derived point cloud is discussed based on observations made during this thesis and supplemented by important aspects from the literature. As a second step, the differences between SfM and TLS and their implications on the derived point clouds, and consequently on the DSMs, are discussed. In a third step, the extent to which the height of the canopy represented in the DSMs and manual ruler measurements can be compared is examined.

As a last aspect Subsection 9.2.4 discusses the comparability of HS DSMs to destructive in-field measurements. In the studies Aasen et al. (2015, Chapter 3), Aasen and Bolten (in review, Chapter 4), Tilly et al. (2015 Chapter 6) and Bendig et al. (2015, Chapter 7), spatially resolved remote sensing data is compared to destructive in-field measurements of plant parameters. To evaluate the issues of comparability between these two types of measurements, the outcomes of the studies are evaluated with regards to the spatial heterogeneity within the experimental plots. Insights into the spectral data retrieval of the previous chapters are also related to the issue.

1.4.3 Potentials of hyperspectral digital surfaces models

After the data quality and the comparability of the HS DSMs has been discussed, this last research objective evaluates the potentials of the HS DSMs acquired with UAV HSCs to support decision making in precision agriculture. The discussion in Section 9.3 is based on the requirements that have to be met by remote sensing approaches for site-specific crop management (Section 1.1). Additionally, the results of Chapter 4 and 6 to 8 are picked up and related to the HS DSMs generated with the UHD. In particular, the evaluation is based on a discussion on:

- Subsection 9.3.1 Crop parameter estimation
- Subsection 9.3.2 Site-specific crop management
- Subsection 9.3.3 HSC systems

Within this thesis different studies investigate the potential of HS DSMs for the retrieval the three plant parameters PH, biomass and chlorophyll based on data from other sensors. Bendig et al. (2015; Chapter 7) and Tilly et al. (2015, Chapter 6) investigate the retrieval of PH and biomass across several

growth stages using SfM and TLS, respectively. Aasen et al. (2014, Chapter 8) investigates if the same spectral information can be used to estimate biomass in different growth stages. Aasen and Bolten (in review, Chapter 4) investigate the retrieval of chlorophyll and compare the results from spectral data captured by the UHD with spectral data captured by a field-spectrometer. Based on the results of these studies and the investigation of the comparability of the different systems in the second research objective, the generality of the obtained results and the potential of the data within HS DSMs is discussed in Subsection 9.3.1. In some cases, the results are complemented by additional analysis carried out with the tool HyperCor, introduced in Aasen et al. (2014, Chapter 8). HyperCor investigates a dataset for the best combination of two variables to predict a plant parameter based on different formulas. For example, it derives the best two bands from a hyperspectral dataset to be used with an NDVI-type VI to predict biomass. Although developed for spectral data, PH can be included into the analysis as an additional variable by considering it as an additional band. To exemplify the potentials of HS DSMs derived by HSCs, the discussion uses the data acquired with the UHD in 2014.

The insights of Subsection 9.3.1 also help to discuss the potentials of HS DSMs of crops acquired with UAV snapshot cameras for site-specific crop management. After it is evaluated if the approach meets the demands defined in Section 1.1, Subsection 9.3.2 discusses how the three plant parameters can support fertilization and stress protection. In a last step, the potentials of HS DSMs acquired with UAV snapshot cameras are set in context to existing approaches in precision agriculture. The chapter is completed with Subsection 9.3.3, which highlights the potentials of HSC systems to further support the development of sensing systems for precision agriculture and other applications. Here the focus is widened in an anticipation of current developments and an outlook towards new ways to explore the data derived by HSCs is given.

2. BACKGROUND

For a site-specific management it is important to know about the current status of the crop. Conventionally, management decisions are made on the basis of crop walking or a limited number of observations. By measuring the leaf nitrogen or water content, a farmer can adapt the management to the needs of the plants (Jones and Vaughan, 2010). Plant parameters such as PH and chlorophyll can indicate biotic and abiotic stresses (Mahlein, 2016; Samarah et al., 2009; Zarco-Tejada et al., 2012). Besides, biomass has a connection to yield (Boukerrou and Rasmusson, 1990; Kren et al., 2014). In recent years, efforts have been undertaken to derive plant parameters by using remote sensing techniques in support of a site-specific crop management (Pinter et al., 2003). These parameters directly or indirectly relate to important variables for precision agricultural applications as exemplarily shown for the Normalized Differenced Vegetation Index (NDVI) in Figure 2.1.

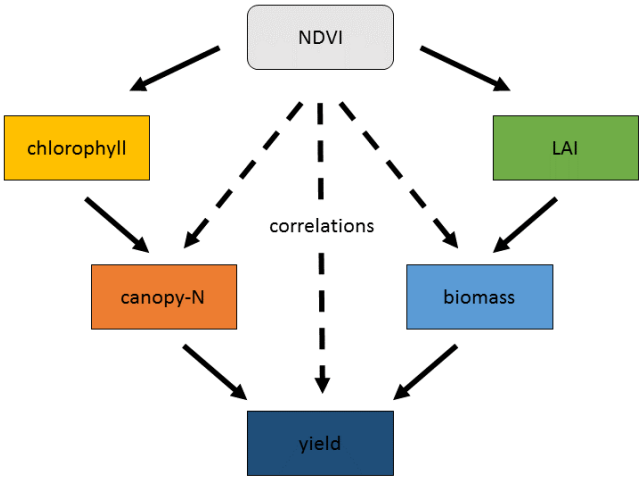

Figure 2.1 Schematical drawing of the relationship of the NDVI with different plant parameters. Solid arrows indicate a more direct functional relationship while dotted lines indicate a more indirect relationship (adapted from Jones and Vaughan, 2010).

The situation is complicated by the phenology of the plants. The growing stage influences the chemical compounds of the plants as well as their geometrical structure (Nobel, 2005). This in turn is also influencing the remote sensing signal. Therefore growth stage specific models need to be developed (Gnyp et al., 2014b; Küster et al., 2014; Li et al., 2010). Within this thesis, spectral and 3D remote sensing techniques are applied to estimate the plant parameters PH, chlorophyll and biomass. The basic principles of these sensing techniques are well understood and can be found in almost every remote sensing textbook (e.g. Campbell and Wynne, 2011; Jones and Vaughan, 2010). Thus, in this section only the information about the sensing principles and theory is summarized that is necessary for the understanding of this thesis. This also includes the introduction of snapshot imaging spectroscopy, which cannot yet be found in textbooks because of its novelty. Additionally, the specifications of the sensing systems used in this thesis are outlined. The methodical introduction is

followed by a summary on the growth of spring barley, since most of the research studies were carried out in this species. The last sections of this chapter present the CROP.SENSe.net study site at Campus Klein-Altendorf.

2.1 Spectral remote sensing of vegetation

When incident sunlight hits a canopy it interacts with its components, such as leafs or stems, and may be reflected, transmitted or absorbed. The proportion by which the light is reflected or transmitted depends on the biophysical and biochemical compounds within the plant and the wavelength of the incident light, since different compounds absorb light in different wavelengths. A comprehensive overview of these absorption bands can be found in Kumar et al. (2003). A fraction of the absorbed light energy is used to drive electron transport and photosynthetic carbon assimilation. Besides, a small fraction (1 – 2%) of the energy is emitted at a longer wavelength as chlorophyll fluorescence (Jones and Vaughan, 2010). Although fluorescence is of minor relevance for this thesis, it should be noted that this signal also is part of the spectral signature received by a sensing system, which motivated the inclusion of 'emitted' into the definition of HS DSMs. Besides of the compounds within the plant, also the canopy structure influences the signature that is received by a sensor.

2.1.1 Angular effects

Vegetated surfaces appear different when viewed from different directions. This results from the scattering behavior of vegetation and its interaction with the irradiance field and the view angle of the sensor during the measurement, also known as the measurement geometry (Jones and Vaughan, 2010). In the following, this interaction will be referred to as 'angular effects'. Reflection from a surface varies from specular reflectance, where surface irregularities are small in relation to the incident radiation wavelength, to perfectly diffuse *Lambertian scattering*, where the light is scattered uniformly over the hemisphere. Typically, plant canopies show an anisotropic asymmetric scattering behavior with a maximum apparent reflectance in the opposite direction of the incident light. Since this area appears brightest in aerial images it is called the *hotspot* (Jones and Vaughan, 2010). Figure 2.2 A, B and C schematically show the different scattering behaviors. Additionally an RGB image of a winter wheat field with the hotspot feature to the bottom left is shown. In the center of the hotspot the shadow of the UAV from which the image was taken is visible.

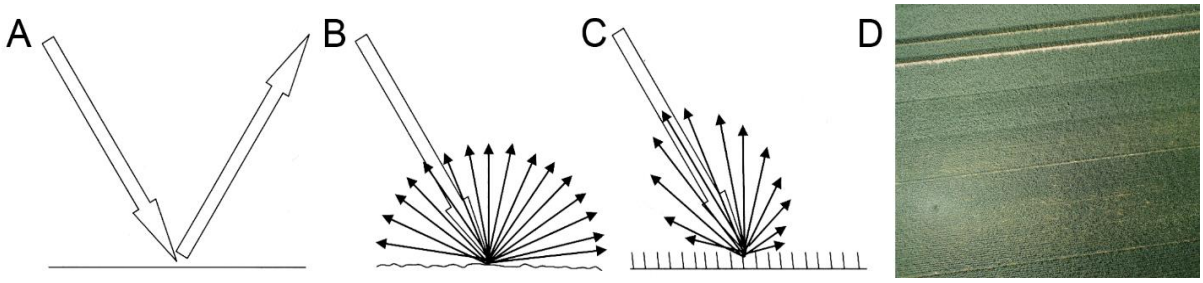

Figure 2.2 Specular (A), Lambertian (B), asymmetrical scattering of a canopy (C; adapted from Jones and Vaughan, 2010) and hotspot within an RGB image of a winter wheat field (D; Burkart et al., 2015, Chapter 5).

The asymmetric scattering behavior of vegetation is caused by structural properties such as the leaf angle distribution. Also the illumination play an important role. The proportion of shadow seen at a specific spot within an image depends on the sun's position relative to the surface and the observer position. Such structural and optical properties of the surface, including multiple scattering, mutual shadowing, transmission, reflectance and absorption, influence the apparent reflectance perceived by a sensor (Gatebe, 2003; Jones and Vaughan, 2010). The anisotropy of a surface can be quantified by multi-angular measurements. In this thesis, the angular setting under which a measurement is carried out is called the measurement geometry and implicitly defines the angular properties of that measurement (which is pixel specific in the case of imaging devices). It comprises the viewing geometry of a sensing system relative to the surface and its relation to the sun's position and the irradiance field.

2.1.2 Reflectance quantities

The irradiance field describes the composition of the direct incident radiation from the sun and the diffuse radiation scattered by the atmosphere onto a specific point in space. The BRDF is the theoretical framework to express the angular dependencies of the scattering of this radiation by a surface. It describes the reflectance of a target as a function of illumination geometry and viewing geometry (measurement geometry), and hence carries information about the anisotropy of the surface (Gatebe, 2003). A variety of measurable quantities and inconsistent use of nomenclature in association with BRDF are present throughout the remote sensing community. In an effort to improve the ambiguous usage of reflectance terms, Schaepmen-Strub et al. (2006) suggested a standardized terminology of reflectance products based on the work of Nicodemus et al. (1977). In the following, the important aspects for this thesis in the context of BRDF are summarized. The nomenclature used is illustrated in Figure 2.3.

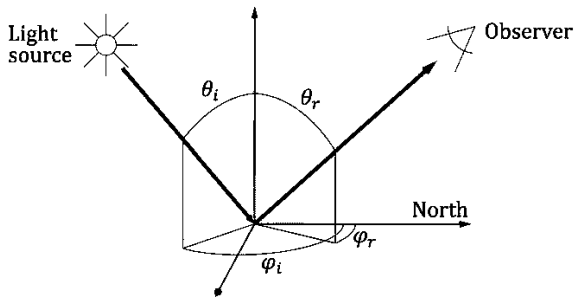

Figure 2.3 Illustration of beam geometries within the concept of directional reflectance measurements. θ and ϕ denotes the zenith and azimuth angles, respectively, for the incident (i) and reflected (r) radiance (Suomalainen et al., 2009).

The BRDF is described by the zenith and azimuth angle of the infinitesimally small solid angle of the incident and reflected radiance. Each beam of incident light from one direction of the hemisphere is scattered into another direction of the hemisphere (Eq. 2.1). This relation describes the intrinsic reflectance properties of a surface and facilitates the derivation of many other relevant quantities (e.g. conical and hemispherical reflectance factors) by integrating over the corresponding finite solid angles. It should be noted that the BRDF is generally wavelength dependent (Schaepman-Strub et al., 2006). However, for reasons of clarity the spectral dependence is omitted throughout this section.

$$BRDF = f(\theta_i, \phi_i; \theta_r, \phi_r) = \frac{dL_r(\theta_r, \phi_r; \theta_i, \phi_i)}{dE_i(\theta_i, \phi_i)} [sr^{-1}] \quad \text{(Eq. 2.1)}$$

θ_i and ϕ_i	incident radiance zenith and azimuth angles
θ_r and ϕ_r	reflected radiance zenith and azimuth angles
dE_i and dL_r	incident and reflected directional spectral radiance for infinitesimally small view and incident angels in steradiant (sr).

When reflectance properties of a surface are measured, the reflected radiance is usually compared to a reference. The result is the bidirectional reflectance factor (BRF), which is the ratio of the radiance reflected by a surface in a given direction to a standard surface, often Lambertian (lossless and diffuse), in the same beam geometry (Nicodemus et al., 1977; Schaepman-Strub et al., 2006). Since the reflectance of a Lambertian surface is view-angle independent its notation can be omitted (Eq. 2.2; Schaepman-Strub et al., 2006).

$$BRF = R(\theta_i, \phi_i, \omega_i; \theta_r, \phi_r, \omega_r) = \frac{d\Phi_r(\theta_i, \phi_i, \omega_i; \theta_r, \phi_r, \omega_r)}{d\Phi_r^{id}(\theta_i, \phi_i)} \quad \text{(Eq. 2.2)}$$

θ_i and ϕ_i	incident radiance zenith and azimuth angles
θ_r and ϕ_r	reflected radiance zenith and azimuth angles
$d\Phi_r$ and $d\Phi_r^{id}$	radiant flux [W] of the target and Lambertian reference
ω_i , $\omega_r \approx 0$	incident and reflected radiance cone is infinitesimal small

The concept of BRF assumes one light source that radiates from a specific direction. However, under field conditions light is also received indirectly from the hemisphere in addition to the directed

irradiance from the sun. To normalize for variances in the ratio of diffuse and direct irradiation, the direct and diffuse incident radiation is integrated over the whole hemisphere. The resulting quantity is the hemispherical-directional reflectance factor (HDRF; Eq. 2.3).

$$HDRF = R(\theta_i, \phi_i, 2\pi; \theta_r, \phi_r, \omega_r) \quad \text{(Eq. 2.3)}$$

θ_i and ϕ_i	incident radiance zenith and azimuth angles
θ_r and ϕ_r	reflected radiance zenith and azimuth angles
$d\Phi_r$ and $d\Phi_r^{id}$	radiant flux [W] of the target and ideal Lambertian reference
$\omega_i = 2\pi$	incident radiance cone of hemispherical extent
$\omega_r \approx 0$	reflected radiance cone is infinitesimal small

BRDF, BRF and HDRF all have in common that they assume an infinitesimally small solid view angle. However, these do not exist (Schaepman-Strub et al., 2006). Thus in reality the measured quantity can most precisely be described as hemispherical-conical reflectance factor (HCRF) and the reflection is integrated over a solid angle around the reflected zenith and azimuth angle (Eq. 2.4).

$$HCRF = R(\theta_i, \phi_i, 2\pi; \theta_r, \phi_r, \omega_r) \quad \text{(Eq. 2.4)}$$

θ_i and ϕ_i	incident radiance zenith and azimuth angles
θ_r and ϕ_r	reflected radiance zenith and azimuth angles
$\omega_i = 2\pi$	incident radiation cone of hemispherical extent
$\omega_r \equiv IFOV$	reflected radiance cone corresponding to an instantaneous field of view (c.f. Section 2.1.3) of a sensor

A different normalization concept is used by the anisotropy factor (ANIF). The ANIF describes the anisotropy of a target in comparison to its nadir reflectance (Sandmeier et al., 1999). Similar to the HDRF and HCRF it is a function of hemispherical illumination conditions, viewing angle and solid cone. Also it is wavelength dependent. However, instead of the normalization by a Lambertian surface, the nadir reflectance of the same target is used (Eq. 2.4).

$$ANIF = f(\theta_i, \phi_i, 2\pi; \theta_r, \phi_r, \omega_r) = \frac{d\Phi_r(\theta_i, \phi_i, 2\pi; \theta_r, \phi_r, \omega_r)}{d\Phi_{nadir}(\theta_i, \phi_i, 2\pi; 0, \phi_-, \omega_r)} \quad \text{(Eq. 2.5)}$$

θ_i and ϕ_i	incident radiance zenith and azimuth angles
θ_r and ϕ_r	reflected radiance zenith and azimuth angles.
ϕ_-	Since the reference measurement is acquired from nadir, the zenith angle of the measurement is zero and the azimuth is arbitrary
2π	incident radiation cone of hemispherical extent
$\omega_r \equiv IFOV$	solid angle resulting from a non-infinitesimally small instantaneous field of view (IFOV)

Within Burkart et al. 2015 (Chapter 5) a simplified version of Eq. 2.5 is presented which assumes that the incident zenith and azimuth angles stay the same during each measurement campaign. Also, the solid angle is not regarded since it stays the same for all measurements. Besides, in the following the

measured reflectance factors will be denoted as reflectance as long as a differentiation is not required for the understanding.

2.1.3 Principles of spectroscopy

Generally, optical sensing systems can record the optical signature of a canopy in discrete bands. This information is called spectral when the radiometric response of these bands is known and the bands have been spectrally characterized by a center wavelength and a bandwidth, described by the full width at half maximum (FWHM). Technically the FWHM defines the spectral resolution of a sensor, since it defines the narrowest spectral interval that can be resolved. The spacing of the center wavelength is called sampling interval (Campbell and Wynne, 2011). Sometimes this information is resampled to a regular spacing and then stated as spectral resolution of a sensor or a data product. Spectral sensors can be differentiated by the number and spacing of the bands they record. If many continuous bands are recorded, a sensor is called hyperspectral (HS; Goetz, 2009; Goetz et al., 1985), else they are called multispectral. Most consumer-grade RGB cameras record information in three uncharacterized bands within the red, green and blue range. All these sensors transform the incoming light into an electrical signal recorded as digital numbers (DNs). The precision of this transformation is given by the radiometric resolution. It refers to the number of intensity levels (expressed in DN) that can be resolved by the sensor and is usually denoted as the bit depth (e.g. 256 for 8-bit, 4096 for 12-bit). To derive the spectral signature of an object, these DNs are transformed to physically traceable units by radiometric calibration. The result is a measure of the radiation reflected or emitted from an objects as a function of the wavelength as spectral radiance (= the radiant flux density emanating from the surface; W m^{-2} sr^{-1} nm^{-1}) or reflectance. Depending on the technical design of a sensor, it may record the signal in different spectral domains (Jones and Vaughan, 2010). In this thesis, it will be differentiated between the visible (VIS; 450 – 700 nm), near infrared (NIR; 700 – 1300 nm) and short wave infrared (SWIR; 1300 – 2500 nm). Additionally, the VIS can be divided into the blue (400 – 500 nm), green (500 – 600 nm) and red (600 – 700 nm). Nevertheless, these borders should only be considered as reference points.

In principle the process of spectral-radiometric (spectral) measurements can be divided in non-imaging and imaging spectroscopy. Non-imaging spectroscopy can be described as a method to characterize the spectral radiometric properties of a surface within the FOV of a spectrometer as a spectrally resolved but spatially integrated signal. Consequently, every measurement creates one spectral signature (Campbell and Wynne, 2011; Jones and Vaughan, 2010). Commonly, ground-based spectral measurements are carried out with field-spectrometers to study “the interrelationships between the spectral characteristics of objects and their biophysical attributes in the field environment“ to “act as a bridge between laboratory […] and field situations” and “provide a tool for the development,

refinement and testing of models relation biophysical attributes to remotely-sensed data" (Milton, 1987). Although this description is more than two and a half decades old, it is still a very appropriate description of the use of field-spectrometers today. Field-spectrometers have been mounted on moveable platforms to cover large areas and static structures, like flux towers, for continuous measurements (Milton et al., 2009). At the same time, more customized non-imaging spectrometers have been developed that have a higher spectral resolution (e.g. to measure fluorescence: Cogliati et al., 2015) or are more lightweight so that they can be carried by new platforms (e.g. UAVs: Burkart et al., 2014). Additionally, non-imaging spectrometers have been used in field-goniometers to characterize the anisotropy of vegetated (Sandmeier et al., 1999) and non-vegetated surfaces (Suomalainen et al., 2009). Within this thesis, non-imaging spectroscopy are mostly used as ground validation (Aasen et al., 2015, Chapter 3; Aasen and Bolten, in review Chapter 4) and for proximal sensing of vegetation properties (Aasen et al., 2014, Chapter 8; Bendig et al., 2015, Chapter 7; Tilly et al., 2015, Chapter 6). Additionally, angular reflectance properties of vegetation are estimated with an UAV-goniometer, based on a lightweight spectrometer (Burkart et al., 2015, Chapter 5).

Imaging spectroscopy generates a representation of the spectral properties of a surface in two spatial dimensions. Most imaging systems scan the surface point- (whiskbroom) or line-wise (pushbroom). In both cases, a 2D representation of the surface is built up while the sensor is moving across the surface (or an object is moved by the sensor, e.g. on a conveyer belt). During that process the light reflected or emitted towards the instantaneous field of view (IFOV) of a detector element is recorded. The projected area on the ground of the IFOV is called the ground IFOV (GIFOV). The combined IFOV of all detector elements of a sensor is called its FOV and defines the footprint on the ground which is covered by the sensor. For non-imaging devices the IFOV equals the FOV (it has to be noted that the footprint of different bands might differ slightly as shown by Mac Arthur et al., 2012. However, for simplicity this will be neglected during the course of this thesis.). Within the GIFOV different parts may contribute differently to the value recorded by the detector, which is described by the point spread function. The spacing between the centers of the GIFOVs is called ground sampling distance (GSD). The width that is covered by one scan-line of an imaging line-scanner, usually perpendicular to the longitudinal axis of the plane or along track direction, is commonly called swath (Figure 2.4, left). Every measurement within this swath has its own IFOV and is looking into a slightly different direction. The direction of the surface normal is called nadir (Jones and Vaughan, 2010). The solid angle (mentioned in the context of reflectance quantities described in Subsection 2.1.2) is defined by the IFOV of a detector. Thus, from a strict physical point of view, field-spectrometers as well as most common satellite and airborne systems measure HCRFs. While the former typically have a FOV of approx. 25°, when no fore optic is used, the IFOV of space-based instruments (e.g. WorldView-3, Sentinel-2) correspond to a much smaller cone. Thus, data products of the latter are often referred to as HDRF and BRF under the

assumption that the HDRF is constant over the full cone angle of the IFOV (Schaepman-Strub et al., 2006). Besides, since every IFOV of an imaging spectrometer is pointing in a slightly different direction, each measurement by a detector element has slightly different angular properties. Additionally, also the ground sampling distance towards the edges of the swath relatively increases because of the view-angle effect (Figure 2.4, right).

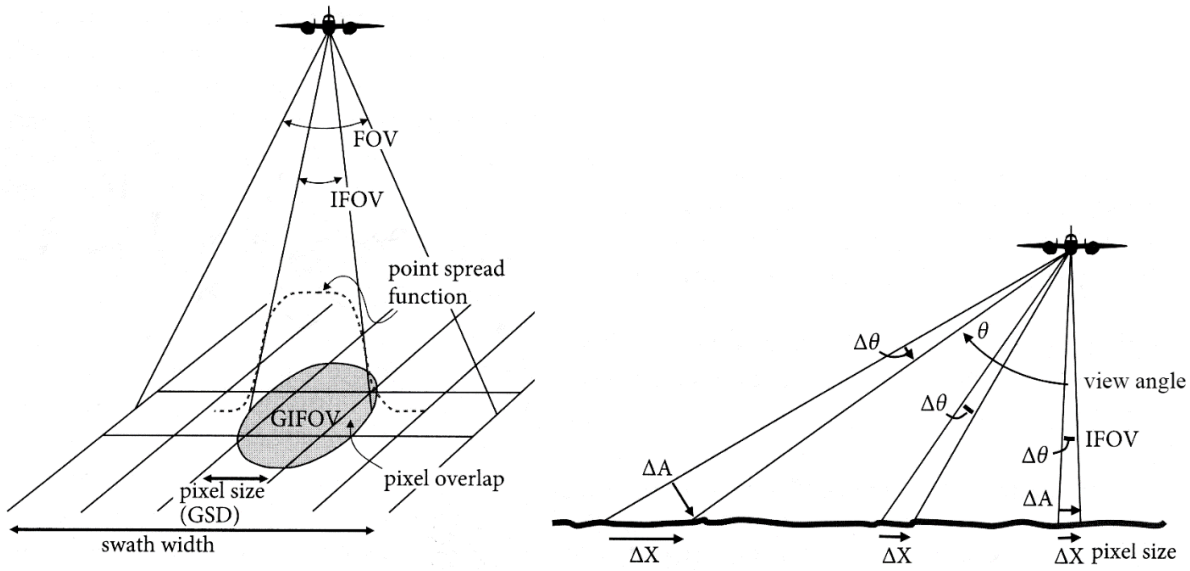

Figure 2.4 Schematic drawing of the field of view (FOV), instantaneous field of view (IFOV), ground instantaneous field of view (GIFOV) and ground sampling distance (GSD) with point spread function of an airborne line scanner (left). Towards the edges of the swath, the ground sampling distance increases as a function of the oblique viewing angle and increased path length through the atmosphere. At the same time, the viewing geometry of every pixel changes slightly with every pixel (right; adapted from Jones and Vaughan, 2010).

Commonly information by imaging spectrometers is geometrically corrected and reprojected to a regular grid during post-processing in a way that it can be represented as pixels within a raster dataset (Jones and Vaughan, 2010). However, this process is prone to problems since it has to be defined how the irregular spaced spectral information from individual measurements of the sensing system is assigned to the pixels. The complexity of this problem has led Fisher (1997) to call “the pixel: a snare and a delusion”. While a comprehensive and interesting discussion of the topic can be found in Cracknell (1998), this topic will become important within Aasen and Bolten (in review, Chapter 4), where it is discussed how to assign a spectral signature to a specific pixel seen in overlapping images. Additionally, it should be noted that an ambiguous use of the term “spatial resolution” is found within the literature. In this thesis, the spatial resolution of a sensor refers to the pixels of its image, while the spatial resolution of a data product (e.g. a remote sensing scene) refers to the spacing of the pixels in the units of its global reference system (also referred to as the ground sampling distance).

Imaging systems have been developed by different agencies and research facilities around the world and applied to manned aircrafts. Within Europe, the two most prominent ones are APEX (Itten et al., 2008; Schaepman et al., 2015) and the novel HyPlant specified to measure sun-induced fluorescence (Rascher et al., 2015). But miniaturized hyperspectral pushbroom scanners have also been mounted on UAVs (Lucieer et al., 2014; Zarco-Tejada et al., 2012). Regardless of the carrier platform or the size of the sensor, scanning devices need a movement of the sensor relative to the surface and precise orientation and positioning information for every measurement to compose an image cube of the 2D scene. Recently, hyperspectral snapshot cameras were introduced for remote sensing applications, which record data in a different way.

2.1.4 Snapshot imaging spectroscopy

Hyperspectral snapshot cameras (HSCs) record spectral information in two spatial dimensions within a single exposure and therefore without any scanning process (Hagen et al., 2012). In contrast to whisk- or pushbroom spectrometers, snapshot cameras (also called central perspective imagers) capture the whole of a scene at one instant of time from the viewpoint of the camera lens (Jones and Vaughan, 2010). Consequently in case of spectral snapshot cameras the full image cube is recorded within one integration of the sensor (Figure 2.5).

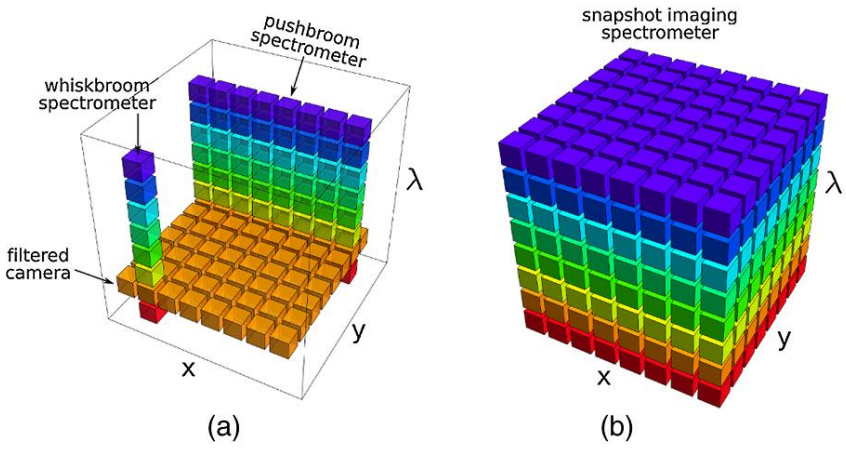

Figure 2.5 Proportions of the image cube collected during a single detector integration period for scanning (a) and snapshot (b) devices (Hagen et al., 2012). X and y denote the spatial dimensions, while λ denotes the spectral dimension.

Different advantages of snapshot systems have been stated in the non-remote sensing literature. Due to the elimination of the scanning process, snapshot systems do not require moving elements and are therefore more rugged. At the same time, they can record dynamic events of two dimensional scenes (Descour and Dereniak, 1995). Additionally, snapshot systems have an advantage in light collection compared to scanning devices. Hagen et al. (2012) identifies this as the “snapshot advantage”. For remote sensing, on one hand the spatial two dimensionality of the data at first brings additional

complexity. While objects at the center of the scene are viewed with a nadir geometry, those towards the edge are viewed obliquely. In comparison to whisk- and pushbroom systems this complicates the interpretation of the data with regard to angular effects (c.f. Subsection 2.1.1), since more dimensions have to be regarded (Jones and Vaughan, 2010). On the other hand, the movement of the sensing system can be used to create multiple overlapping image cubes (Figure 2.6).

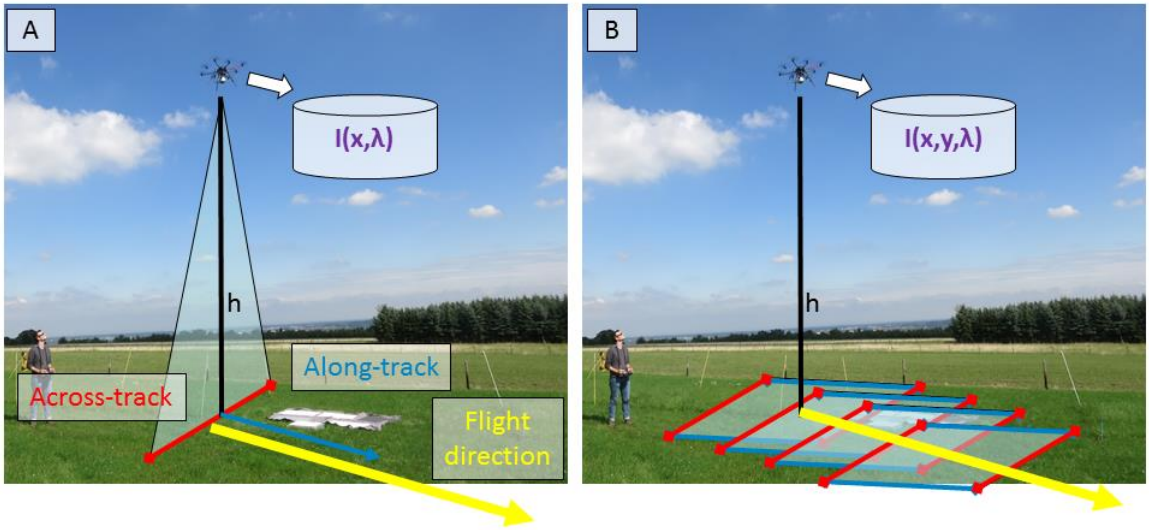

Figure 2.6 Different principles of data acquisition. Line-scanning devices record individual image-lines along one spatial dimension. Movement of the sensing system is needed to create a 2D scene (A). Snapshot cameras record image cubes with two spatial dimensions with every exposure. Thus, movement generates overlapping image cubes (B).

Taxonomy wise, snapshot cameras are a special case of image-frame cameras. Image-frame cameras such as Fabry–Pérot interferometers (e.g. Honkavaara et al., 2013), also record spectral information in two spatial dimensions. However, since only individual bands or band packages are recorded, the generation of an image cube requires a scanning process through the spectral dimension. The elimination of any scanning process with snapshot cameras has the benefit to omit the spatial co-registration process of the spectral data, which simplifies the remote sensing process. Thus, the data can also be considered as hyperspectral images. Nevertheless, to capture larger areas the relative orientation and position of these images need to be reconstructed and potential spatial distortions need to be corrected. Fortunately, recent developments in computer vision and photogrammetry provide a solution for this and even more, can use the spatial information within these images to reconstruct the 3D geometry of the scene.

2.2 3D remote sensing

Non-contact methods to derive 3D information about a surface include methods such as X-ray, SAR, photogrammetry and laser scanning (Remondino and El-Hakim, 2006). These techniques generate a set of points with 3D coordinates (x, y, z) to describe a surface. This information is commonly referred

to as 3D surface points or a 3D point cloud. From this information a digital surface model (DSM) can be created with triangular mesh generation. The resulting DSM may have a reduced dimensionality where only one z-value is assigned to every (x, y)-coordinate within a grid spacing (Eq. 2.6). Such surfaces are known as 2.5D surfaces (Luhmann et al., 2014).

$$f(x, y) = z \qquad \text{(Eq. 2.6)}$$

In remote sensing such 2.5D surfaces are commonly found describing a digital elevation model. It is defined as a file or database containing elevation points over a contiguous area. Digital elevation models can further be divided into DSMs, which contain the elevation information of all features in the landscape, and digital terrain models (DTMs), which contain the information about the bare soil surface without features in the landscape such as vegetation (Jensen, 2007). New applications and technologies led to modifications of this terminology for specific purposes. Terminologies such as canopy height models (Dandois and Ellis, 2013; Lisein et al., 2013), crop surface models (Bendig et al., 2014; Geipel et al., 2014; Tilly et al., 2014) or canopy height (Friedli et al., 2016; Nakai et al., 2010) have been used to specifying the height of vegetation. Additionally, the PH has been used to denote the difference between a DTM and a DSM on vegetated surfaces (Bendig et al., 2014; Tilly et al., 2014). In this thesis, the latter is adapted (c.f. Subsection 4.2.6.1). Additionally, a DSM will denote the 2.5D height information assigned to a raster grid cell (pixel) based on the 3D information of the point cloud in the corresponding area. In this thesis, a photogrammetric approach and TLS are used to derive 3D information about the barley canopy. Both techniques will be introduced in the following.

2.2.1 Structure from Motion

The term 'Structure from Motion' originates from visual motion perception and describes "how the 3D structure and motion of objects can be inferred from a 2D transformation of their projected images" (Ullman, 1979). During the last decade, advances in computer vision and photogrammetry have allowed a new way to exploit this procedure – and in combination with flying platforms such as UAVs – to gather 3D information of a landscape. The combination of advances in image and dense matching algorithms allow to reconstruct the 3D topography of a scene in very-high resolution from multiple images captured by an UAV. Although SfM technically only refers to the image matching technique, the entire process of image and dense matching is commonly referred to as SfM. This nomenclature will also be used in this thesis. Image matching calculates the relative position of a series of images by identifying identical object features (points, patterns, edges) in the overlap of the images and reconstruction their 3D topology (Luhmann et al., 2014). Various approaches have been developed to identify corresponding features, among them the Scale Invariant Feature Transform operator (SIFT; Lowe, 2004). After these features have been identified, a bundle adjustment is carried out to merge

the individual images to a global model. Bundle adjustment is the process of refining a visual reconstruction to produce jointly optimal 3D structure and viewing parameter (camera pose and/or calibration) estimates (Triggs et al., 2000). During that process the orientation and position of the images and the 3D coordinates of the identified points are calculated. Different software tools can be used to carry out the bundle adjustment, e.g. Bundler (Snavely, 2016; Snavely et al., 2008). Optionally, the connection to a global coordinate system can be established by providing a set of reference points such as the georeferenced ground control points (GCPs) used in this thesis. The result of this process is a representation of the surface as a point cloud (Luhmann et al., 2014). Generally, the density of the point cloud after the bundle adjustment is quite sparse (Harwin and Lucieer, 2012). To increase the point density, dense matching techniques are used that use the output of a bundle adjustment to densify the sparse point cloud. The process is very computationally intensive and algorithms have been developed to exploit parallel computing and graphics processing units (Remondino et al., 2014). Among these dense matching algorithms, semi-global matching represents a computational efficient method. However, in comparison to multi-view techniques it only uses stereo pairs of images and the depth maps are fused (Hirschmuller, 2008; Luhmann et al., 2014). As a result a dense 3D point cloud is created that corresponds to the ground sampling of the original images (Haala, 2013). Within the SfM process, the image matching is the most problematic step since its success in matching directly depends on the shape and form of the objects in the scene (Luhmann et al., 2014). Thus, a sufficient image overlap (Szeliski, 2011) and sufficient scene texture is required (Remondino and El-Hakim, 2006). In case of aerial photography an overlap of 60% side and 80% forward overlap is suggested (Agisoft LLC, 2016).

In this thesis, the SfM software Photoscan was used. Only vague information about the algorithms within the software are known. In a forum post by an Agisoft employee, it was disclosed that the feature matching is based on a similar approach as SIFT and the solving of the image orientation parameters has “many things in common with Bundler” (Semyonov, 2011). Besides, Remondino et al. (2014) state that the implemented image-matching algorithm seems to be a method similar to stereo semi-global matching. Since SfM can be used with almost every camera, it is increasingly adapted by the remote sensing community (Figure 1.1). Examples from the remote sensing of vegetation are the estimation of PH in forest (Dandois and Ellis, 2013, 2010; White et al., 2015) and agricultural crops (Bareth et al., 2015b; Bendig et al., 2014, 2013; Geipel et al., 2014).

2.2.2 Terrestrial laser scanning

Light detection and ranging (LiDAR) is an active remote sensing technique. LiDAR systems send out very short pulses of a very narrow beam of coherent light and record the time delay until the signal returns from a reflective object. Since the beam is traveling with the speed of light, the distance to the object can be calculated. Depending on the beam width and the structure of the object, one pulse may be

reflected multiple times on its path. LiDAR systems can be divided into discrete return and full-waveform LiDAR systems, depending on how the return signal is recorded. Discrete LiDAR systems record a certain number of returned pulses, while full-waveform LiDARs record the full shape of the intensity of the returning pulse as a function of time after emission. Along with the received signal reflected from an object the angle of each pulse is stored. Together with the position and orientation of the LiDAR system this information can be used to derive a 3D point cloud for each return of the beam (i.e. the discretized points of waveform). Thus advanced LiDAR systems, which penetrate through vegetation and record multiple returns, allow the mapping of multiple layers of the canopy and ground at the same time (Jones and Vaughan, 2010). LiDAR systems have been deployed on several platforms and applied to a multitude applications. A comprehensive review of crop monitoring approaches can be found in Tilly et al. (2015, Chapter 6).

TLS are static LiDAR systems equipped with a scanning mechanism such as a rotation mirror and thus sweep along a surface and create a (vertical) profile. Additionally, the system is rotated around the axis of its mounting tripod to capture the second (horizontal) dimension (Petrie and Toth, 2009; Tilly, 2015). Within this thesis, the TLS system Riegl LMS-Z420i was used. The sensor operates with a near-infrared laser beam, has a beam divergence of 0.25 mrad, and a measurement rate of up to 11,000 points/sec. In addition, its field of view is up to 80° in the vertical and 360° in the horizontal direction (RIEGL GmbH, 2010). The position of the scanner was tracked by the RTK-DGPS system HiPer Pro (TOPCON, 2004). By establishing a reference station the relative position of the entire TLS setup used in this study was determined to be approximately 0.01 m (Tilly et al., 2015, Chapter 6).

2.3 Sensing systems used in this study

Different sensors have been used in this study to derive RGB, spectral and 3D information. A detailed description of these systems can be found in the following sections: Subsection 3.2.2 introduces the UAV snapshot camera system UHD, Section 5.2 introduces the UAV-Goniometer (UAV-STS), Subsection 6.2.1.1 introduces the TLS system, Subsection 7.2.3 introduces the RGB camera GX1 and the FS3 field-spectrometer is introduced in Subsection 8.2.2. A summary of the technical details relevant for this thesis can be found in Table 2.1. In the overall discussion, these sensing systems are compared to the airborne sensing system APEX (Schaepman et al., 2015). Thus, also the technical details of this sensing systems can be found in Table 2.1. Besides, a detailed description of the M-class rotary-wing UAV MK-OktoXL which was used as the carrier platform for the UHD and GX1 can be found in Subsection 3.2.1. The UAV used for the UAV-STS can be found in Section 5.2.

Table 2.1 Summary of the spectral and RGB sensing systems used in this study with relevant technical details such as the field of view (FOV) and instantaneous field of view (IFOV), typical above ground altitude (AGA), ground sampling distance (GSD) at typical above ground altitude, coverage (per time or scene) and full width half maximum (FWHM). Additionally, the specifications of the Airborne Prism EXperiment (APEX) are shown.

sensor	AGA	GSD[3]	spatial resolution	coverage	number of bands (range)	FOV	IFOV	sensor type	FWHM	detailed information
UHD	30 m	HS: 0.2 m gray: 0.01 m	50 x 50 px 1000 x 990 px	12 m x 12 m (1500 m² in 14 min)[2]	95 (466 nm - 850 nm)[1]	20° x 20°	0.4°	snapshot	5 (at 466 nm) - 25.6 (at 850 nm)	Subsection 3.2.2
UAV-STS	16 m	9 - 30 m² depending on tilt	1	-	256 (338 nm - 823 nm)	12°	-	non-imaging	3 nm	Section 5.2
FS3	1 m	0.15 m²	1	36 plots x 6 samples in 1 - 2h[4]	VNIR: 650 (350 nm - 1000 nm) SWIR1 and SWIR 2: 800 (1000-2500)	25°	-	non-imaging	3 (at 700 nm) 10 (at 1400 nm)	Subsection 8.2.2
GX1	50 m	0.01 m	4608 × 3464 px	41.5 m x 31.2 m (>1500 m² in 5 min)²	3 RGB (non-spectral)	55.8° × 38.9°	0.012°	RGB snapshot	-	Subsection 7.2.3
APEX	60 - 7620 m	1-2 m	1000 px	-	VNIR: 114 (372 nm -1015 nm) SWIR: 198 (940 nm - 2540 nm)	28.1°	0.028°	Pushbroom	6 nm (at 760 nm)	Schaepman et al. (2015)

1 Recommended bands by Aasen et al. (2015)
2 In 2014 configuration. Depends on the flight pattern and flight speed
3 For non-imaging devices the footprint size is given
4 Depends on the stability of the illumination conditions

2.4 Plant growth of barley

In most areas, spring barley is cultivated to produce high-quality malting barley. After being sown in late March or early April, the growing period is about 110 to 130 days. Several nomenclatures exits to describe the current growth stage of the plants. In this thesis, the BBCH-scale (Meier, 2001) is used. It divides the growth into several growth stages denoted with two digit numbers from 0 to 99, of which the first denotes the principle growth stage and the second the within stage development (Figure 2.7). The most important growth stages for management practices, such as fertilization and plant protection, are within the vegetative phase from leaf development (BBCH < 10) to stem elongation (BBCH < 39; Munzert and Frahm, 2005).

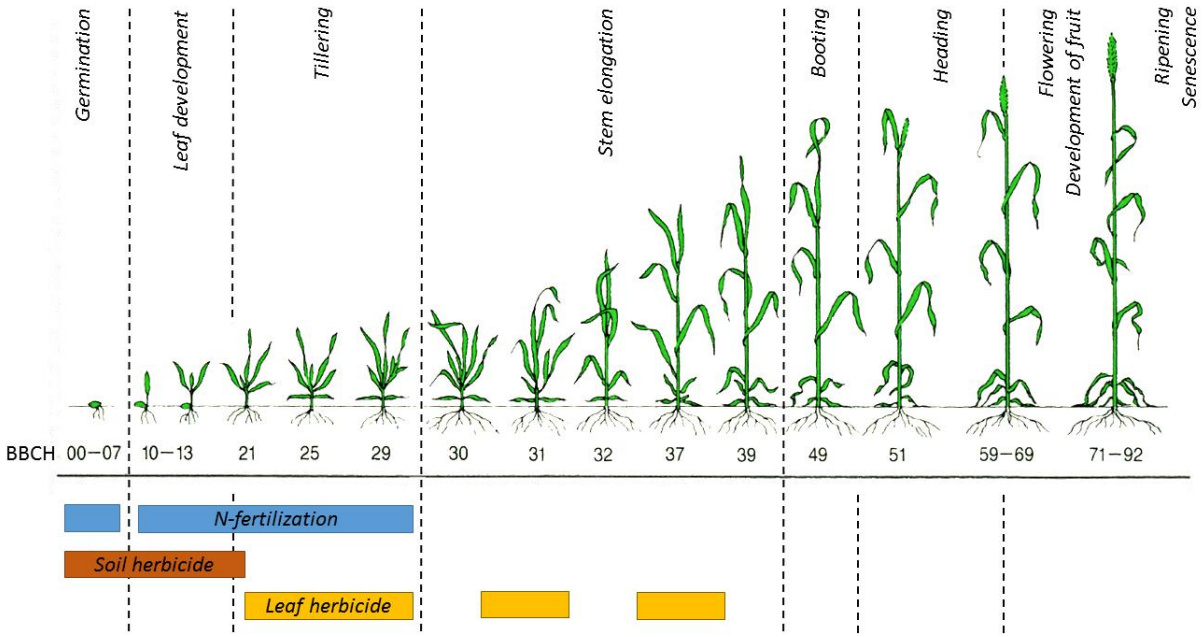

Figure 2.7 Growth of barley with BBCH-scale and typical periods of fertilization and plant protection (modified from Munzert and Frahm, 2005).

During the different development stages different parts of the plant grow. Dry matter in cereals is first accumulated in leafs until they intercept almost 100% of the photosynthetic active radiation (PAR). PAR excites the electrons in the chlorophyll molecules in the chloroplasts of the plant and drives the process of photosynthesis (Fischer et al., 2014; Jones and Vaughan, 2010). After the tillering, biomass is mostly accumulated in the stem and later in the spike and grains (Figure 2.8). The exact pattern of the plant growth depends on the climate and soil conditions of the growing area as well as the management of the field.

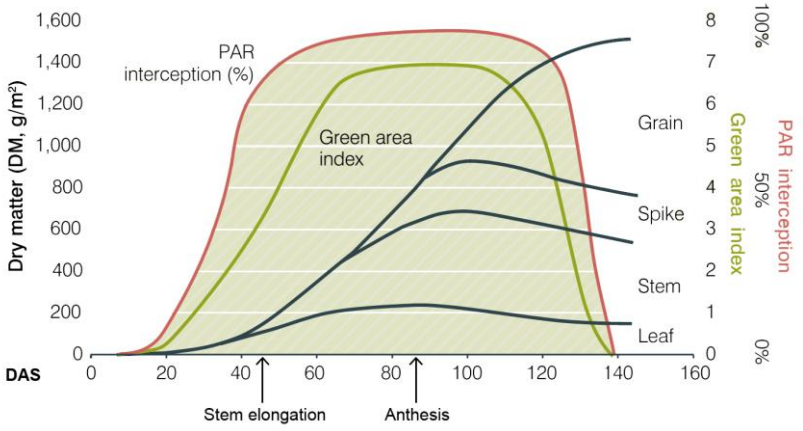

Figure 2.8 Dry matter accumulation in spring wheat in connection with photosynthetically active radiation (PAR) and green area index (modified from Fischer et al., 2014).

2.5 Study site

Most studies within in this thesis were carried out at the research station Campus Klein-Altendorf (50° 37'51"N, E 6°59'32") of the University of Bonn (https://www.cka.uni-bonn.de/) within the interdisciplinary research project CROP.SENSe.net (www.cropsense.uni-bonn.de). Due to the crop rotation, the experiments were placed at different fields each year. Nevertheless, the overall soil and climate were the same. The soil was a clayey silt luvisol. The campus-owned weather station reported a long-term average precipitation of 600 mm and a daily average temperature of 9.3 °C for 2014 (Figure 2.9; Campus Klein-Altendorf, 2010).

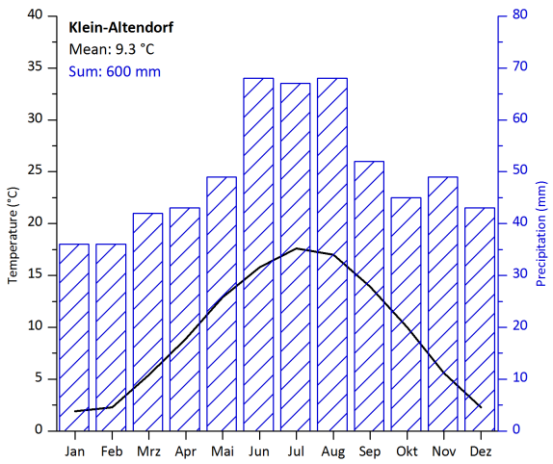

Figure 2.9 Climate diagram (long-term average 1956 - 2014) for Klein-Altendorf (Tilly, 2015).

In total, 22 campaigns were carried out at the CROP.SENSe.net experiment in the context of this thesis in 2013 and 2014. In conjunction with these campaigns, manual plant height and destructive samplings of fresh and dry biomass, divided by plant organs, and laboratory based chlorophyll, carbon and nitrogen measurements were carried out (Table 2.2). Each year, 36 plots of different spring barley

cultivars were sampled. Half of them were treated with a farmer's common rate of 80 kg/ha nitrogen (N) fertilizer and the other half with 40 kg/ha N. In 2013, one repetition of 18 cultivars (Barke, Wiebke, Beatrix, Eunova, Djamila, Streif, Ursa, Victoriana, Sissy, Perun, Apex, Isaria, Trumpf, Pflugs Intensiv, Heils Franken, Ackermanns Bavaria, Mauritia and Sebastian) per fertilizer treatment was sampled, while in 2014 six cultivars (Barke, Beatrix, Eunova, Trumpf, Mauritia and Sebastian) in three repetitions were sampled. The map of the experiment of 2014 is shown in Figure 2.10. Each plot was divided into a non-destructive part for the remote sensing and plant height measurements, and a destructive measurement part where the biomass and chlorophyll measurements were carried out. The seeding days were 9 April 2013 and 13 March 2014.

Table 2.2 Summary of the campaigns carried out with the terrestrial laser scanning system (TLS), field-spectrometer (FS3), UAV RGB and UAV UHD in the context of this thesis in 2013 and 2014. The campaign dates are sorted by the day after seeding (DAS). For the manual sampling dates of the plant parameters (PP), the average BBCH-scale is given.

DAS	**2013**			**2014**		
	date	**sensor**	**PP (BBCH)**	**date**	**sensor**	**PP (BBCH)**
15				3/28/2014	TLS	
20	4/29/2013	TLS, FS3				
34	5/13/2013	TLS				
35	5/14/2013	FS3, RGB	18			
41				4/23/2014	TLS, FS3	29
49	5/28/2013	TLS, FS3, RGB	30			
54				5/6/2014	FS3, UHD	
56				5/8/2014	TLS	31
63	6/11/2013	RGB				
64	6/12/2013	TLS, FS3	41			
68				5/20/2014	UHD	
70				5/22/2014	TLS, FS3	49
78	6/26/2013	TLS, FS3	57			
80	6/28/2013	RGB				
82				6/3/2014	FS3	
84				6/5/2014	TLS, UHD	56
91	7/9/2013	FS3, RGB	68	6/12/2014	UHD	
92	7/10/2013	TLS				
96				6/17/2014	UHD	74
97				6/18/2014	TLS, FS3	
104	7/22/2013	TLS, FS3, RGB	81			

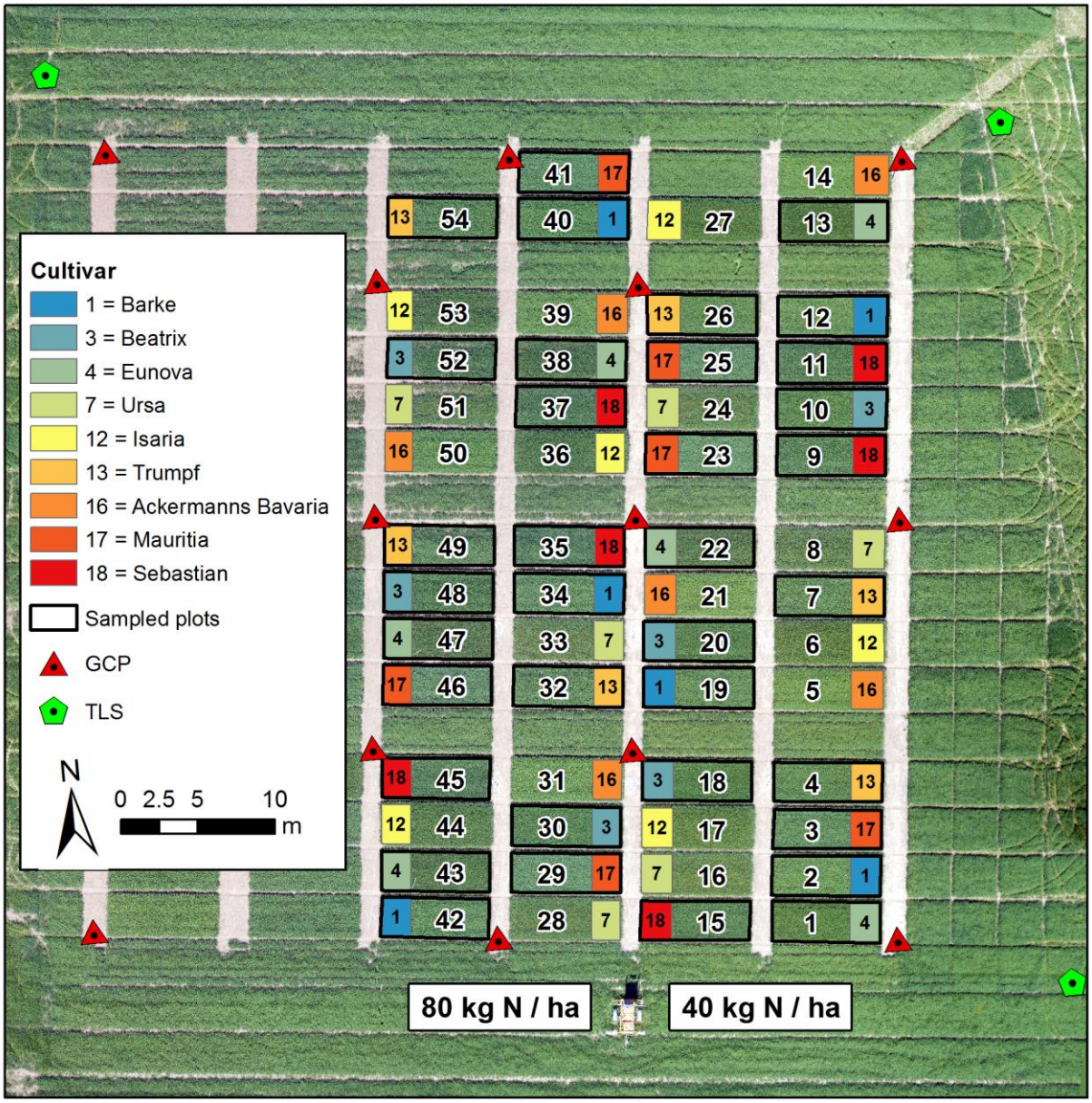

Figure 2.10 Map of the CROP.SENSe.net experiment at Campus Klein-Altendorf in 2014 with plot number (large numbers) and cultivar (small numbers). The cultivar-wise colored squares indicate the destructive measurement part. The destructively sampled plots are framed with a solid rectangle. Positions of the ground control points (GCPs) and terrestrial laser scanning positions (TLS) are shown. The two plot rows to the left were treated with a farmer's common rate of 80 kg/ha nitrogen (N) fertilizer and the other half with 40 kg/ha N.

Besides, for Aasen et al. (2014, Chapter 8) data from field campaigns in rice from a study site at Jiansanjiang (47.2°N, 132.8°E) in the Heilongjiang Province of Northeast China was used. The details about this experiment can be found in Subsection 8.2.1.

3. GENERATING 3D HYPERSPECTRAL INFORMATION WITH LIGHTWEIGHT UAV SNAPSHOT CAMERAS FOR VEGETATION MONITORING: FROM CAMERA CALIBRATION TO QUALITY ASSURANCE

*HELGE AASEN [1, *], ANDREAS BURKART [2], ANDREAS BOLTEN [1], GEORG BARETH [1]*

Published in: ISPRS Journal of Photogrammetry and Remote Sensing, 80, 785-796

DOI: 10.1016/j.isprsjprs.2015.08.002

Formatting and orthography of the manuscript is adapted to the dissertation style.

[1] University of Cologne, Department of Geoscience, Institute of Geography, GIS and RS research group, 50923 Cologne, Germany (helge.aasen; andreas.bolten; g.bareth@uni-koeln.de)

[2] Institute of Bio- and Geosciences, IBG-2: Plant Sciences, Jülich GmbH, 52428 Jülich, Germany (an.burkart@fz-juelich.de)

* Corresponding author: Tel.: +49 221 470 6265; Email: helge.aasen@uni-koeln.de

Abstract: This paper describes a novel way to derive 3D hyperspectral information from lightweight snapshot cameras for unmanned aerial vehicles for vegetation monitoring. The Cubert UHD 185-Firefly collects a full hyperspectral image cube with 125 bands from 450 to 950 nm with two spatial dimensions during one exposure. First we describe and apply methods to radiometrically characterize and calibrate snapshot cameras. Then, we introduce our processing chain to derive 3D hyperspectral information from the calibrated image cubes based on structure from motion. The approach includes a novel way for quality assurance of the data. Latter is used to assess the quality of the hyperspectral data for every single pixel in the final data product. The result is a hyperspectral digital surface model as a representation of the surface in 3D space linked with hyperspectral information emitted and reflected by the objects covered by the surface. We apply the approach to data from a flight campaign in a barley experiment with different varieties to demonstrate the feasibility for vegetation monitoring in the context of precision agriculture and derive chlorophyll, LAI, green biomass and plant height from the hyperspectral 3D data. The radiometric calibration yield good results with less than one percent offset in reflectance compared to an ASD FieldSpec 3 for most of the spectral range. The quality assurance information show that the radiometric precision is better than 0.15 percent for the derived data product. The plant parameters retrieved from the data product correspond to in-field measurements of a single date field campaign for plant height ($R^2 = 0.7$), chlorophyll ($R^2 = 0.52$), LAI (R^2

= 0.31) and biomass (R^2 = 0.29). Our approach can also be applied for other image-frame cameras as long as the individual bands of the image cube are spatially co-registered beforehand.

Keywords: hyperspectral digital surface model, image-frame camera, radiometric calibration, quality assurance information, precision agriculture

3.1 Introduction

In the context of vegetation monitoring for agricultural applications up-to-date information is critical for in-time decision making (Atzberger, 2013). It can help optimize the inputs of fertilizers, herbicides, seed and fuel by doing the right management practice at the right place and the right time (Mulla, 2013) and thus save resources within the needed intensification of agricultural production (Foley et al., 2011). In the last years unmanned aerial vehicles (UAVs), also known as unmanned aircraft systems or remotely piloted aircraft systems, are increasingly adopted as remote sensing platforms (Colomina and Molina, 2014). These include rotary-wing (Bendig et al., 2013; Berni et al., 2009; Honkavaara et al., 2013; Lucieer et al., 2014; Suomalainen et al., 2014a) and fixed-wing platforms (Büttner and Röser, 2014; Hruska et al., 2012; Zarco-Tejada et al., 2012). Compared to proximal ground-based systems UAV platforms can survey areas faster and without distracting the surface cover (Burkart et al., 2015). They can provide remote sensing data in higher temporal, spatial and spectral resolution and are more flexible than plane and satellite based sensors. Additionally, they are considerably cheaper, can be deployed where and when needed and fly below the clouds which makes them a promising tool for frequent observations (Berni et al., 2009). When combined with sensors they become sensing platforms to gather the needed up-to-date information for vegetation monitoring.

Hyperspectral (HS) sensors have shown great potential to derive information about the biophysical (Aasen et al., 2014b; Erdle et al., 2011; Gnyp et al., 2013; Haboudane et al., 2004; Hansen and Schjoerring, 2003; Thenkabail et al., 2000) and biochemical parameters (Haboudane et al., 2002; Li et al., 2010; Thenkabail et al., 2011; Yu et al., 2013b) of vegetation and agricultural crops as well as to detect environmental stress or plant diseases (Delalieux et al., 2007; Mahlein et al., 2013; Stagakis et al., 2012; Yu et al., 2013a). Traditionally, HS data is acquired with field-spectrometers, airborne sensors or satellites (Itten et al., 2008; Milton et al., 2007; Pearlman et al., 2003). Recently, HS sensors have been shrinking in size and weight and have thus become feasible for use onboard of UAVs. Burkart et al. (2014) introduced an ultra-light weight spectrometer mounted on an UAV for field spectroscopy feasible of acquiring HS point measurements with adjustable angles. Several line scanners are available for UAVs and have been flown on fixed- and rotary-wing UAVs for vegetation studies (Büttner and Röser, 2014; Lucieer et al., 2014; Suomalainen et al., 2014b; Zarco-Tejada et al., 2012). Line scanners

record one spatial dimension and are depended on the movement of the imaging system or the object to generate an HS image cube with two spatial dimensions.

Lately, a new type of HS cameras has been introduced to UAV remote sensing: HS image-frame (IF) cameras like the Cubert UHD 185-Firefly (http://cubert-gmbh.de/), the Rikola FPI (http://www.rikola.fi) or the IMEC SM5X5 (http://www2.imec.be) record HS information with two spatial dimension. Several nomenclatures are used for these cameras (Bareth et al., 2015a; Honkavaara et al., 2013). In an effort to structure these we identified two parameters by which IF cameras can be categorized. The first category refers to the type of spectral data the camera records. Here we divide into multispectral (MS) and hyperspectral (HS) cameras. Following the core definition of imaging spectroscopy by Goetz et al. (2009; 1985) HS cameras have to record many continues, registered (characterized), spectral bands. Other devices are categorized multispectral (MS) as long as their channels are spectrally and radiometrically characterized. In particular the spectral response curve of the individual channels should be quantified to make results intercomparable. Thus, MS would include MS IF cameras as the Mini-MCA (http://www.tetracam.com/) or the MicaSense RedEdge (http://www.micasense.com/) but also characterized standard or modified RGB (CIR: modified RGB camera with NIR filter removed) cameras capturing RAW images without automatic color balance (e.g. Hunt et al.(2010)). A third category are IF cameras, which have not been spectrally characterized. These include (modified) RGB cameras. The second parameter for the categorization refers to the way the images are acquired. Here, we separate IF and snapshot camera systems. If all bands are synchronously captured, e.g. within the same exposure and thus, the full image cube is recorded without a scanning process, the cameras are referred to as snapshot cameras (Hagen, 2012). On the other hand, if bands or band packages are recorded sequentially or unsynchronized as two dimensional IF and thus, the image cube needs to be created by band co-registration, these cameras are referred to as IF cameras. This categorization is summarized in Table 3.1. Both categories are hierarchical structured: as HS cameras are MS cameras, so are snapshot cameras IF cameras. Additionally, the cameras can be characterized by other typical parameters like spatial and spectral resolution, FWHM and spectral domain.

Because IF cameras record 2D spatial information, they provide the opportunity to derive additional vegetation parameters like plant height from 3D data complementary to HS data. So far, mostly LiDAR is used to derive 3D information to monitor growth of individual trees (Jaakkola et al., 2010), forests (Koch, 2010) and agricultural crops (Tilly et al., 2014). For the latter Hoffmeister et al. (2010) introduced the concept of crop surface models to monitor crop canopy growth in 3D over time. More recently, structure from motion (SfM) algorithms are used to reconstruct the 3D geometry from 2D images: When images are collected with a sufficient overlap, SfM can calculate the relative position and

orientation information by matching features within the individual images (Szeliski, 2011) as long as the scene shows sufficient texture (Remondino and El-Hakim, 2006). Some studies demonstrate the feasibility of images acquired from UAV platforms with SfM to derive plant growth: Bendig et al. (2013) generated multi-temporal crop surface models to monitor plant growth of barley with very high resolution < 0.05 m from a rotary-wing UAV flying at 30 m. Zarco-Tejada et al. (2014) quantified tree height in orchards from a fixed-wing UAV flying at 200 m with the same resolution.

Table 3.1 Categorization of image-frame spectral cameras by the type of spectral information captured and the capturing procedure with some examples. Both categories are hierarchically structured: as hyperspectral cameras are multispectral cameras, so are snapshot cameras image-frame cameras.

		RGB / CIR	**spectral**	
		uncharacterized bands	**several characterized bands (multispectral)**	**many characterized, continues bands (hyperspectral)**
Image-frame (IF)	bands or band packaged (sequentially) captured as two dimensional image frames		Mini-MCA, MicaSense RedEdge	Rikola hyperspectral camera
Snapshot (S)	all bands simultaneously captured as two dimensional image frames covering the same area	(modified) RGB cameras	characterized (modified) RGB cameras	UHD, SM5X5

For the combined analysis HS and 3D information are co-register from several sources in most studies. These demonstrate the advantages of combining the two types of information: With the combined data accuracy of vegetation mapping can be increased (Alonzo et al., 2014; Hladik et al., 2013), estimation of biomass is improved (Clark et al., 2011) and stress is detected (Swatantran et al., 2011). All these studies used LiDAR to derive the structural information. Recently, also SfM is used: Bendig et al. (2015) combined the plant height derived from crop surface models and VIs from field-spectrometer data to improve the accuracy of biomass estimation in barley. Suomalainen et al. (2014b) developed a bundle of an HS push broom scanner and a RGB camera to map HS data simultaneously to digital surface models (DSM) with SfM from a rotary-wing UAV platform. However, fusion of data from different sensors, eventually mounted on different platforms and collected at different times, may become challenging (Avbelj et al., 2014). Very few studies so far have used color intensity and 3D data created from a single cameras system: Geipel et al. (2014) and Bareth et al. (2015b) used plant height and uncalibrated RGB information from UAV-borne cameras to increase grain yield prediction accuracy and derive spatial information of grassland ecosystems, respectively. Diaz-Varela et al. (2014) used a CIR to identify agricultural terraces. To collect HS and structural information with the same system Honkavaara et al. (2013) used a Fabry Perot interferometer-based HS IF camera on a small helicopter

UAV flying at 140 m to derive a DSM together with spectral information with a resolution of about 0.2 m to estimate plant height and biomass of cereals. A different approach to collect HS and structural data with the same instrument was developed by Suomalainen et al. (2011) who created an active HS LiDAR. To the authors knowledge the latter two studies are the only ones which used a single instrument to monitor HS and 3D information at the same time for vegetation monitoring.

In the context of remote sensing of vegetation the importance of spectral sensor calibration and characterization has to be underlined. In order to make quantitative remote sensing studies, accurate radiometric and spectral calibrations of HS imaging data are necessary (Gao et al., 2004) and improves consistency between datasets by reducing temporally a spatially variable environmental effects (Kelcey and Lucieer, 2012). Such metadata information support the interpretation of scientific data, in general, help to ensure long-term usability and provide a basis for the assessment of data quality and possibility of data sharing between scientists (Hueni et al., 2009). For imaging systems data quality might be pixel dependent. Thus, satellite systems such as MODIS (Roy et al., 2002) and airborne spectral systems as APEX provide per-pixel quality information directly linked to the image (Itten et al., 2008). For lightweight HS imaging systems such information has not yet become a standard. Additionally, multi-sensor studies become more frequent (Atzberger, 2013). To compare results from different campaigns or transfer between different systems sensors should be carefully characterized and properly calibrated to the current environment (von Bueren et al., 2015). While comprehensive calibration studies exist for individual lightweight UAV IF sensors (Kelcey and Lucieer, 2012) there is still a need to adapt calibration procedures to new systems with different sensing techniques (Bareth et al., 2015a).

The scope of this contribution is to introduce an innovative way to create a data product containing HS 3D information from images captured by a novel HS snapshot camera based on available software without co-registration of 3D and HS information. Thus, we describe the full process including i) camera characterization and calibration, ii) 3D HS data product generation, iii) pixel wise quality assurance information. The result is a hyperspectral digital surface model as a representation of the surface in 3D space linked with hyperspectral information emitted and reflected by the objects covered by the surface accompanied by quality assurance information for every pixel. In a last step we demonstrate how to derive plant parameters for vegetation monitoring of agricultural crops from this data product.

3.2 Materials

3.2.1 Carrier platform

Our carrier platform MK-OktoXL (http://www.mikrokopter.de) is a rotary-wing UAV with a maximum payload of 2.5 kg (Figure 3.1). The total weight is less than 5 kg. Depending on the payload and the batteries, the flight time varies from 15 to 30 min. The altitude, speed and position is controlled during the flight and logged to an on-board memory card. The flight path is controlled by the autopilot Flight Ctrl. 2.1 following predefined waypoints configured in the MikroKopterTool. The payload is mounted on a gimbal. We use the MK HiSight SLR2 gimbal which compensates for pitch and roll movement during the flight by using the UAV's on-board gyroscopes. The compensation allows to maintain a nadir orientation of the sensor. The weight of the gimbal is about 280 g.

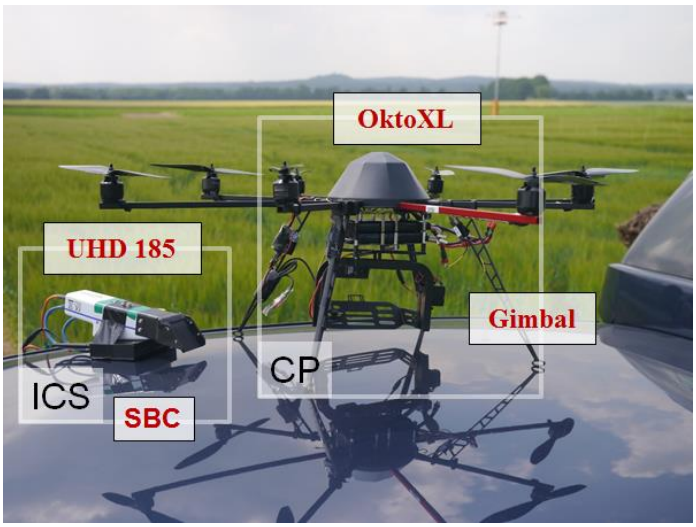

Figure 3.1 Carrier Platform (CP) MikroCopter Okto XL with Gimbal and image capturing system (ICS) with UHD 185-Firefly and the single board computer (SBC) Pokini Z.

3.2.2 Image capturing system

Our image capturing system consists of the Cubert UHD 185-Firefly (UHD) HS snapshot camera and the small single board computer (SBC) Pokini Z (http://www.pokini.de/). The UHD simultaneously captures 138 spectral bands with a sampling interval of 4 nm. From these bands the camera's manufacturer recommends the use of 125 bands between 450 and 950 nm. The FWHM of the bands are shown in Figure 3.2 and increases from about 4 nm at 450 nm to about 26 nm at 850 nm.

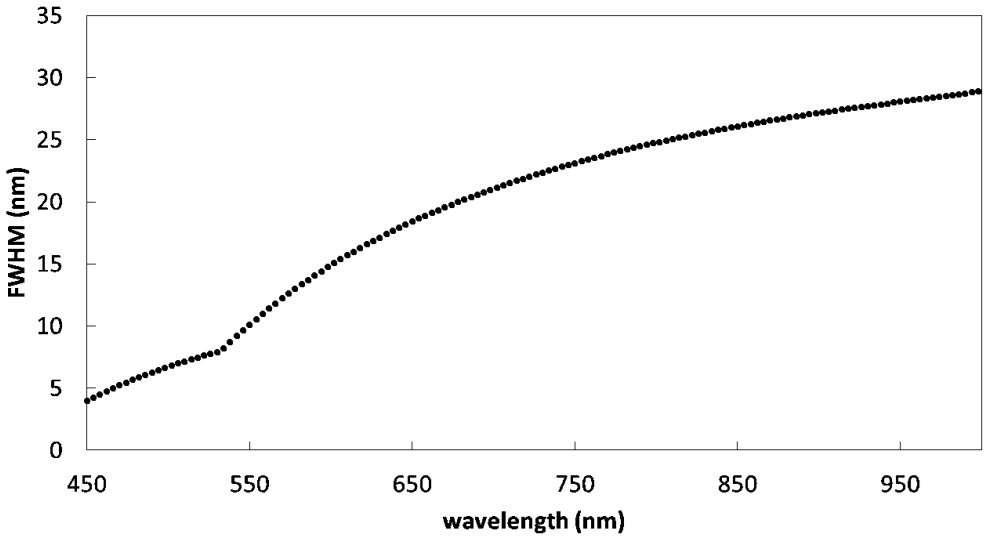

Figure 3.2 Full width at half maximum (FWHM) at each sampling wavelength as given by the manufacturer.

For each band a 50 by 50 pixel image with 12 bit (4096 DN) dynamic range is created. Inside the camera, this is done by projecting the different bands to different parts of a charged coupled device (CCD). Technically, the pixels on the CCD correspond to different bands and spatial pixels of the image cube. Nevertheless, in this contribution we use the nomenclature on the data level such that the term pixel will refer to the pixels within one image band and bands will refer to the spectral bands. At the same time as the HS image is recorded a grayscale image with a resolution of 990 by 1000 pixel is captured. We use a lens with a focal length of 16 mm resulting in an across track field of view (FOV) of approximately 20°. Since the camera's housing is elongated with the lens looking forward a mirror is fixed at the front to capture nadir images (Figure 3.1). The ground resolution at 30 m flying height is about 21 cm for the HS pixels and 1 cm for the grayscale image. With the software of the camera the HS resolution may be pan-sharpened to the grayscale images resolution. Latter is not used in our study. The total weight of the Camera is about 470 g. and its housing is about 28 by 6.5 by 7 cm.

The camera is controlled by a SBC. It is connected to the camera with two gigabit ethernet cables and runs a server application which controls the camera and receives and stores the data to the SBC's flash drive. The configuration is done remotely via WiFi from a control application run on a different computer. Within the WiFi range a live view may be transmitted to the control application and measurements may be triggered manually. Additionally, a sequence of images with defined frequency and duration can be recorded. The performance of the SBC allows to capture HS image cubes with a frame rate of about 0.6 hertz. The typical integration time under cloudless conditions is 1 ms, increasing to about 6 ms under cloud covered conditions. The whole image capturing system together with a three cell lithium polymer battery weighs about 1 kg.

3.2.3 Field study

The field experiment was carried out at the research station Campus Klein-Altendorf (50° 37', 51 N; 6° 59', 32 E) of the University of Bonn within the CROP.SENSe.net project (http://www.cropsense.uni-bonn.de/). In total nine varieties of barley were planted and treated with two nitrogen treatments (40 kg/ha, 80 kg/ha) in three repetitions in an experimental plot layout. Each plot had an extent of three by seven meters and was divided into an invasive and non-invasive sampling part. This way the plants in the non-invasive area could grow undisturbed. For this study samples from a single date (03rd June 2014) were evaluated: We collected plant samples from all repetitions of six varieties in the invasive sampling part. Additionally, we captured the area of approximately 0.15 ha with in total 320 UHD images with the UHD carried by the UAV in two flights within approximately 20 min.

3.2.4 Invasive sampling

To estimate the average height within each plot we manually measured the plan height with a ruler at ten random positions within the non-invasive sampling part of the plot. The measurements were averaged to represent the plant height per plot. To measure the chlorophyll (Chl) content we collected four times three stamps with a radius of 3 mm from leafs at the top layer of the canopy within the invasive sampling part of the plot. These were instantly frozen with liquid nitrogen inside a dryshipper to preserve the samples. Later the Chl content of three stamps a time were measured with the DMSO-Method (Blanke, 1992) at the Institute of Crop Science and Resource Conservation (INRES), University of Bonn. The four samples for each plot were averaged. The biomass was measured by extracting all plants within a 20 by 20 cm square in the invasive sampling area of the plot. The roots were cut off and the plants were stored in a cooler and transported to the laboratory. There, the samples were cleaned from mud, divided by the plant organs and weighed. The LAI was measured with a leaf area meter (LI-3100C, http://www.licor.com/).

3.2.5 Flight planning and conditions

To define the flight path we measured eight GPS positions on the south and nine on the north side with a distance of two meters from the experimental plots. For the measurement the internal navigation grade GPS of the UAV was used. Due to an unexpected shutdown of the SBC two flights had to be carried out immediately consecutively. The flights was conducted during an opening in cloud cover on a partly cloudy day under sunny conditions. A close by weather station recorded no change in global radiation during the flights. The take-off time of the first flight was 12:50 PM and each flight lasted about 10 minutes. Before the flight ground control points (GCPs) were mounted on positions previously

measured with a differential GPS with a relative sub centimeter accuracy. The heading of the UAV was set such that the camera orientation stayed constant during the flight.

3.3 Methods

In the following we give a brief introduction to the effects influencing the signal inside an IF camera, how to quantify them and approaches to correct them. The process is applied to our camera and the results are quantified in section 3.4. Additionally, we describe the generation of the HS digital surface model (HS DSM) and a method for quality assurance of the derived data product. The entire process is implemented in MATLAB (Version R2011b, www.mathworks.de). The last part of this section describes the extraction of the plant parameters from the HS DSM. In our calibration procedure spectral calibration was not included, since it the center wavelength and FWHM was delivered with the camera. For a detailed description of a spectral calibration procedure of HS UAV sensors one can refer to e.g. Lucieer et al. (2014).

3.3.1 Radiometric calibration

The raw HS image cubes recorded by the UHD consist of a three dimensional matrix where two dimensions represent the spatial extent of the FOV and the third dimension represent the HS bands. The pixels within each band contain a DN value which is created by the CCD corresponding to the electronic charge present within the pixel array at time of the readout. However, these do not necessarily represent the real radiation reflected or emitted by the objects within the sensors FOV. Artifacts introduced by the cameras optical system and its electronic components influence the signal and have to be corrected. Then, the signal has to be transformed to registered units (e.g. reflectance or radiance) to make them comparable and useful for analysis purposes.

3.3.1.1 Noise correction

In theory, a CCD sensor proportionally transforms the incoming luminous energy of each point of a scene into an electrical signal (Mansouri et al., 2005). During the process of translating radiation into digital numbers (DN) noise is added to the signal. The noise becomes obvious when the camera is triggered under perfect dark conditions. Theoretically, the image DN values should be zero. Mostly, this is not the case due to the dark current (DC). The DC consists of a readout noise and thermal noise. Latter is depending on the detectors temperature and the integration time.

Typically, the read out noise can be measured with very short integration times (Mansouri et al., 2005). The thermal noise influencing a measurement can be estimated by blocking the lens under the same

conditions (temperature and integration time) as the subsequent measurements (Mansouri et al., 2005). For changing conditions the DC should be frequently measured during the acquisition process, as it is common in field-spectroscopy (Aasen et al., 2014b; Gnyp et al., 2014), or empirically modelled after careful assessment of its dependency on the integration time and sensor temperature (Burkart et al., 2014; Kuusk, 2011). Most lightweight UAV sensors do not provide the possibility to physically block incoming light and thus, do not allow DC measurements during the flight. Additionally, some do not track the sensor's temperature during the image acquisition.

Since latter is the case for the UHD, we implement a DC correction assuming virtually stable conditions after sufficient sensor heat up time. To estimate the DC we covered the lens and place the UHD into a closed case in a dark room laboratory. Then we measure 30 images every 10 minutes starting three minutes after the sensor is switched on. For each time step the 30 measurements are averaged per pixel for each band. Additionally, we measure the DC in the field by carefully covering the lens.

3.3.1.2 Radiometric response

Besides of the noise the incoming radiance is altered during its path through the optical system of a sensor and during transformation into an electronic signal by the CCD. The most prominent influence of the optical system is the vignetting effect. Vignetting is defined as a spatially dependent light intensity fall-off that results in a radial reduction in brightness towards the image edges. It can account for 30 to 40 percent of the intensity even for high-quality fixed focal length lenses (Goldman, 2010a). It results from different reasons which can be found in Goldman (2010b) and Kim and Pollefeys (2008).

Vignetting may be corrected by modelling the optical pathway or by image-based techniques. We used the latter approach since it is both simpler and more accurate (Yu, 2004). It is based on the generation of per pixel per band coefficients to correct the illumination fall-off. This can be done by pointing the sensor at a perfect homogeneous, lambertian surface (flat-field).

After the radiation has passed the optical system, it liberates electrons inside the photosensitive cells of the CCD which then create the electric signal (Mansouri et al., 2005). The precision of this signal is defined by the theoretical dynamic range based on the bit depth of the sensor. However, the response of photosensitive cells is not necessarily linear. Thus, the same amount of light may resulting in different readings in different wavelengths and different cells. Specifically, the quantum efficiency of a CCD is effected by saturation effects under high light intensities. Thus, the radiometric response function is not linear for the entire theoretical dynamic range of a CCD and the integration time should be adjusted such that the maximum intensity of the signal stays within the linear range.

To quantify these effects we use an integration sphere (Labsphere CSTM-USS-1200C-SL, http://www.labsphere.com) placed in the spectral laboratory at the IBG-2 at the research center Forschungszentrum Jülich GmbH, Germany. The inside of the sphere is coated with Spectraflect® to provide a homogenous illumination. The light intensity is measured by a silicone and an InGaAS detector inside the sphere. After the sensor and the integration sphere is preheated we capture 30 images at one ms integration time, which is typical for a measurement campaign under clear sky conditions around noon. We then average the measurements per pixel. For each band the median value of all pixels is evaluated and used as a reference to generate coefficients for each pixel to equalize irradiance differences. Similarly, we carry out the same measurement outside under clear sky conditions with a Zenith Lite™ panel. Here, the sensor is mounted on a gimbal to ensure a nadir view.

Additionally, we adjust the light intensity inside the sphere until the sensor was clearly saturating. We then compare the DN values of the image to the readings from the silicone light sensor inside the sphere and quantify the ratio of the two values. As long as the ratio stays constant the response of the sensor is within the linear range.

3.3.1.3 Radiometric registration

In general two different types of transformation can be used to calibrate DN values to physical units. During the flat-field acquisition in the sphere the light intensities are measured. Since the radiometric response curve of the sphere is known this curve can be used to transform the flat-fielded images to radiance. In a second step, the solar illumination at the target area at the time of the measurements has to be estimated to correct the signal for illumination changes. This can be done by modelling the atmosphere (Zarco-Tejada et al., 2012) or by (continuously) measuring the incoming radiance (Burkart et al., 2014). A more direct approach is the empirical line method. Here one or more well characterized reference targets on the ground are used. Then the spectra of these are extracted from the image data and correction coefficients for each band are estimated (Smith and Milton, 1999). In our case we use a simple one point calibration empirical line method, where only one reference target is measured (James Burger, 2005). Before the flight, the sensor is pointed towards a well characterized homogenous (near) lambertian reference target (REF) on the ground and a reference image is taken. Latter is then used to transform the images to reflectance. Careful assessment of the sensor-sun-REF geometry is critical (Schaepman-Strub et al., 2006). During the calibration the sensors view orientation should be the same as during the flight, the plane of the REF should be parallel to the surface and shadows on the REF should be avoided and stray light minimized. Additionally, the calibration should be carried out with the same heading as in the flight. Latter minimizes the influence of bidirectional reflectance effects.

In our case we use a 50 cm by 50 cm Zenith Lite™ panel as REF with a reflectance of approximately 96 percent and perform the reference image acquisition as described above. To ensure a stable sensors view orientation the camera is mounted on the CP and the gimbal is calibrated to nadir. The whole system is kept about 1.5 meters above the REF during the reference acquisition.

3.3.1.4 Quality Assurance

Careful characterization of a sensor and robust calibration procedures are critical to generate reliable data. At the same time, information about the data quality needs to be embedded to the data to help users to evaluate their results based on the data. As mentioned in 3.3.1.1 and 3.3.1.2 the signal is influenced in different ways by the sensor system depending on the position of the pixel within the image. Thus, the image quality (e.g. radiometric resolution) differ within the image cube. Additionally, all pixels recorded by imaging sensors have different sun-object-sensor geometries which is related to bidirectional reflectance effects. Thus, we encode the pixel position of the original image into an additional pixel position band and append it to the image cube. With the help of this information pixel depending properties of the final data product can be looked up from the camera characterization and considered during the analysis. In our case we demonstrate the potential of the pixel position band to disclose the actual radiometric resolution of each individual pixel, which corresponds to the minimal change (or distinct levels) of intensity depicted by the dynamic range of a certain pixel under actual conditions (e.g. illumination conditions).

3.3.2 Hyperspectral 3D information generation

3.3.2.1 Hyperspectral band preparation

To process the HS images we import the image cubes in their native resolution of 50 by 50 pixels together with the corresponding grayscale images into a self-developed program written in MATLAB. The program automates the entire image processing. After the selection of the reference image the program calibrates the image cubes to reflectance and appends the pixel position band. For the spectral bands, the DC is removed by subtracting it pixel and band wise from the DN values. To transform these values to reflectance, each pixel value is divided by the value of the reference target subtracted by the corresponding DC. Then the values are multiplied by a correction factor (REF_b) per band, which is the inverse of the reflectance of the REF, to correct for the not 100 percent reflectance of the REF (Eq. 3.1).

$$IC_{b,i,j} = \frac{DN_{b,i,j} - DC_{b,i,j}}{REF_{b,i,j} - DC_{b,i,j}} * REF_b \qquad \text{(Eq. 3.1)}$$

The calibrated HS bands are than appended to the grayscale image. Latter has the dimensions of 1000 by 990 pixels due to an unidirectional optical distortion (personal correspondence, Cubert GmbH). To match the HS data to the gray image we resample the image cube to the gray images resolution with the nearest neighbor algorithm to preserve the original HS values. The resulting HS bands have blocks of 20 by 20 and 20 by 19 pixels with the same value. In the resulting image cube the first band then corresponds to the grayscale image, followed by the HS bands and the pixel position band (Figure 3.3). Thus, it has a resolution of 1000 by 990 by (number of bands + two). Too preserve the theoretical 12 bit precision of the sensor but limit the file size we resample and save the image cube as 16 bit TIFF. Optionally, to reduce processing time and file size the processing can be limited to specific bands. For this study 320 image cube were generated with 19 spectral bands.

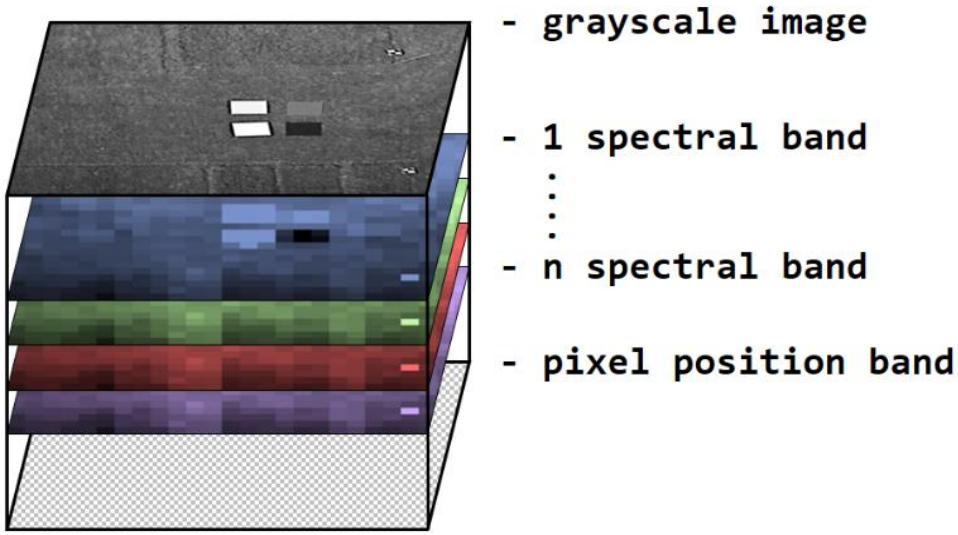

Figure 3.3 Scheme of the image cube after pre-processing of the spectral bands and merging with the grayscale image and pixel position band.

3.3.2.2 Point cloud generation

With the SfM approach the 3D structure of a scene can be reconstructed from 2D images. Different photogrammetric algorithms can be used to match feature points in overlapping images to compute the relative camera orientation and position and derive the 3D structure of the image pixels (Szeliski, 2011). Different software packages exist that incorporate SfM algorithms for 3D structure reconstruction (Harwin and Lucieer, 2012). We use Agisoft Photoscan (Version 1.0.4. http://www.agisoft.com/) since it showed good results in a previous study (Turner et al., 2014). The 320 image cubes are imported and the first channel containing the grayscale image is set as master channel. The first step for the data processing in Photoscan is initial low quality photo alignment. It estimates both internal and external camera orientation parameters, including nonlinear radial distortions. In total nine GCPs are placed in the point cloud to georeference it. After optimizing the

model a dense point cloud in ultra-high resolution is processed and a mesh for the surface type height field is built based on the dense cloud (Figure 3.3). Surface type height field is chosen since it is recommended for rather planar type surfaces (Agisoft LLC, 2014). At this stage an HS dense point cloud is created. Although the entire 3D reconstruction process for multi tiffs is based on the master channel each of the points derived from grayscale image implicitly defines the position of the HS information contained in the other bands. The entire processing time in Photoscan on a an Intel Core i7-3740QM with four (eight virtual) cores at 2.7 GHz, 16 GB ram and NVIDIA NVS 5200M is about four hours.

3.3.2.3 Hyperspectral digital surface model preparation

Unfortunately, Photoscan does only allow the export of point clouds with “color” information of up to three bands. Thus, we export the spatial and spectral information separately. The created spatial information is exported as DSM (export DEM in the software) with the suggested pixel size of 0.93 cm in a geographic projection (WSG 84, UTM zone 32N). The easiest way to export the spectral information would be to export it as an orthophoto. However, we discovered that despite the manual states that the mosaic mode “does not mix image details of overlapping photos but uses most appropriate photo (i.e. the one where the pixel in question is located within the shortest distance from the image center)” (Agisoft LLC, 2014) - it does. Latter was confirmed by Agisoft (personal correspondence, Agisoft LLC, 06.11.2014). Thus, to preserve the original spectral information, we export each orthorectified image cube separately with the same projection and pixel size as the DSM.

As described in section 3.3.1.2 the signal quality generally decreases towards the image edges. Thus, it is beneficial to use the spectral information from the center pixels of the original images for the final data product. Therefore, we import the orthorectified image cubes into a mosaic dataset in ArcGIS (Version 10.2.2, www.arcgis.com). We fit the footprint to the pixels containing real data to exclude no data pixels, calculate the center points of these footprints and create Thiessen polygons based on these. Then, the images are mosaicked based on the Thiessen polygons. The resulting scene contains the spectral information closest to the center of the original image cubes. At the same time, the pixels still spatially correspond to the pixels of the DSM. With this spectral information and the spatial information we have created a representation of the surface in 3D space linked with HS information emitted and reflected by the objects covered by the surface in 3D space. Thus, we name the resulting data product hyperspectral digital surface model (HS DSM). Figure 3.4 summarizes the data pre-processing and HS 3D information generation. The resulting data product has an extent of 7455 by 8409 pixels.

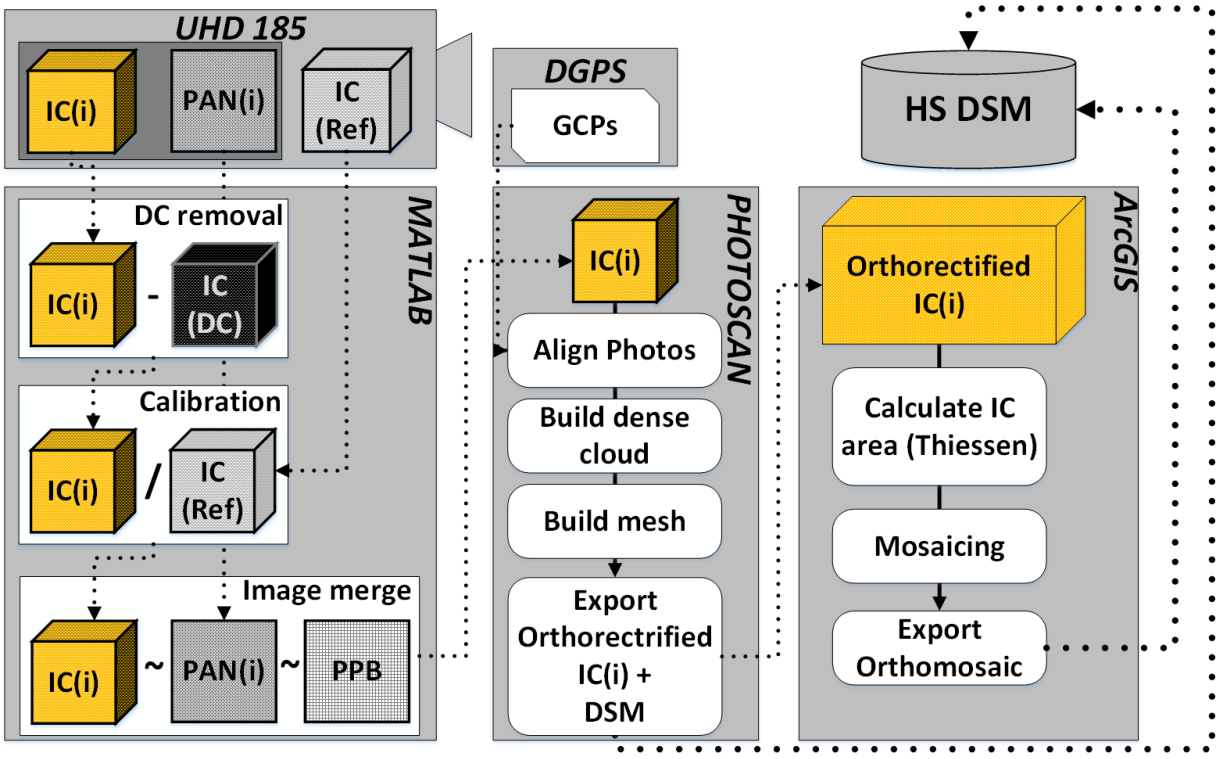

Figure 3.4 Generation of the hyperspectral 3D information with image pre-processing (dark current (DC) removal and radiometric calibration with reference image cube (IC (REF))) and merge to the grayscale image (PAN)) and the pixel position band (PPB) with MATLAB. Point cloud generation and georeferencing with ground control points (GCPs) with PHOTOSCAN. For the individual orthorectified image cubes the optimal cover area is calculated with Thiessen polygons, a mosaic is created and an orthomosaic is exported with ArcGIS. Since the spectral information is linked to the spatial information while the point cloud is generated the result is a hyperspectral digital surface model (HS DSM).

3.3.3 Plant parameter extraction

As described above the applied goal of this study is to derive plant parameters for each plot of the experimental fields. To extract the plant parameters from the HS DSM we use ArcGIS. From the corners of the plots measured with a DGPS during the field campaign we subtract a 40 cm buffer from the edges to exclude border effects and create plot shapes. For each plot zonal statistics are computed to extract the parameters described in the following. Additionally, maps can be produced in 2D (ArcGIS) and 2.5D (ArcScene).

3.3.3.1 Plant height

Plant height is a proxy for biomass estimation (Bendig et al., 2014; Tilly et al., 2014) and an important factor to distinguish plant cultivars, phonological stages, crop treatments and stress (Bendig et al., 2013). Additionally, it is an important input for growth models to assess canopy structure (Pronk et al., 2003), yield losses and potentials (Evans, 1993; Sterling et al., 2003).

To extract the absolute plant height the difference between the DSM and the bare soil surface has to be calculated. Bendig et al. (2014, 2013) created the digital terrain model (DTM) from a flight campaign before the growing period. In our case we use a similar approach as (Geipel et al., 2014): Since the paths between the experimental plots are not covered with vegetation, we extract the surface heights from points from an almost regular grid within the paths. From these 28 points a DTM is interpolated. Unfortunately, neither the path nor the GCPs on the east side of the experimental area is covered. Thus, for the last row no DTM can be created and Plot 1 to 13 are excluded from the height analysis. To extract the plant height we use the raster calculator in ArcGIS and subtract the DTM from the DSM. Based on the plot shapes we perform zonal statistics for each plot. We then compare these values to the manual ruler measurements.

3.3.3.2 Hyperspectral vegetation indices

In this study we use previously published VIs for the detection of Chl content, green biomass and LAI. To detect the Chl content we apply the Transformed Chlorophyll Absorption Reflectance Index (TCARI), the Optimised Soil-Adjusted Vegetation Index (OSAVI) and the ratio of both, as well as the Blue Green Pigment Index 2 (BGI2) which have shown good results in previous studies (Haboudane et al., 2004; Quemada et al., 2014; Rondeaux et al., 1996; Zarco-Tejada et al., 2005). Additionally, we use the modified Photochemical Reflectance Index (PRI) sensitive to plant pigments (Hernández-Clemente et al., 2011). As estimators for vegetation greenness and LAI we apply the Normalized Difference Vegetation Index (NDVI, (1974)) and the Reformed Difference Vegetation Index (RDVI) as estimators for the absorbed photosynthetically active radiation (Roujean and Breon, 1995). Additionally, we apply the Modified Chlorophyll Absorption Ratio Index 2 (MCARI2) which showed good performance in Haboudane et al. (2004). For some VIs the original wavelength were slightly adjusted to fit the UHD bands (Table 3.2). To derive the VI values per plot we calculate the VI pixel wise for the entire area and extract the average value with the zonal statistics on basis of the plot shapes. These values are then compared with the invasive samples to assess the VIs for their predictability for Chl, LAI, and green biomass.

Table 3.2 VIs used in this study and their formula. Some wavelength are slightly adjusted to align with the band configuration of the UHD.

BGI2	$R454/R550$	(Zarco-Tejada et al., 2005)
NDVI	$(R798 - R670)/(R798 + R670)$	(Rouse Jr. et al., 1974)
RDVI	$(R798 - R670)/\left(\sqrt{R798 + R670}\right)$	(Roujean and Breon, 1995)
TCARI	3[(R702 − R670) − 0.2(R702 − R550)/(R702/R670)]	(Haboudane et al., 2002)
OSAVI	(1 + 0.16) × (R798 − R670)/(R798 + R670 + 0.16)	(Rondeaux et al., 1996)
TCARI/OSAVI	TCARI/OSAVI	(Haboudane et al., 2002)
MCARI2	$\frac{1.5[2.5(R798 - R670) - 1.3(R798 - R550)]}{\sqrt{(2\,R798 + 1)^2 - \left(6\,R800 - 5\sqrt{R670}\right) - 0.5}}$	(Haboudane et al., 2004)
PRI(514, 530)	(R514 − R530)/(R514 + R530)	(Hernández-Clemente et al., 2011)

3.4 Results

3.4.1 Radiometric calibration

3.4.1.1 Dark current

When the sensor heats up the average DC of all bands increase from 0.52 DN at 13 min to 2.66 DN at 63 min. Since the sensor does not provide a temperature reading the response to temperature changes cannot be exactly quantified. Thus, we additionally evaluated the DC measurements from four field campaigns. Figure 3.5 (left) shows the histogram of the DC for all pixel of all bands after 33 min heat up time, which corresponds to the in-field measurements. The average DC is about 1 DN. The minimum DC is 0.03 and the maximum DC is 2.9 DN. Figure 3.5 (right) shows the pattern of the DC at 466 nm (band 5). The pattern is similar for all bands.

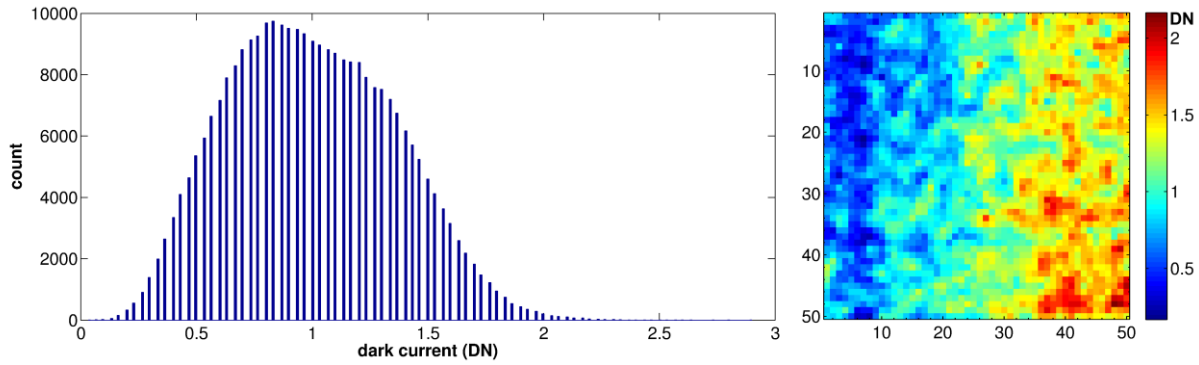

Figure 3.5 Histogram of the dark current values for the entire image cube between 466 (band 5) and 926 nm (band 120) (left) and dark current of band 5 (right).

3.4.1.2 Flat fielding and radiometric response

To determine the linearity of the radiometric response of the sensor we compare the readings of the silicone light sensors inside the sphere with the DN values measured by the sensor. Latter increase similar with the light intensity as long as the DN values stay below 3600 DN. For higher values the sensors readings do not increase linearly with the illumination change. Thus, 3600 DN is determined as a maximum intensity for the linear response.

When we look at the results of the flat-field images a spherical decrease of the DN values towards the edges of the image is visible. Additionally, the decrease is superimposed by an undulated pattern (Figure 3.6, right). This pattern is visible for all bands with varying intensity. For 466 nm (band 5) these effects decrease the signal up to 86 percent. However, for most of the pixels the signal is decreased less than 50 percent. Similar results are acquired in the laboratory and the outdoor measurements, although the intensities vary. To compare the performance of a flat-field calibration based on the laboratory measurements (Aasen et al., 2014a) and the simple in-field one point empirical line method calibration described in section 3.3.1.3 we applied both approaches, normalized for the light intensity, to different in-field measurements of a calibration panel from several campaigns. While the vignetting effect is corrected comparably, the in-field calibrations performs better for the undulated pattern. Based on that result we include the in-field calibration procedure into our processing chain.

Figure 3.6 (left) shows the minimum, median and maximum DN values from 450 to 926 nm acquired outside under sunny conditions around noon in June from a Zenith Lite^{TM} panel with one ms integration time. The maximum DN is 3563 (678 nm, band 58). From here it decreases towards lower and higher wavelength. Since the maximum DN of the image cube is exploiting nearly all of the possible linear dynamic range of the sensor, the DN shown in Figure 3.6 (left) represent the maximum values which can be achieved under field conditions. Theoretically, the sensor has a 12 bit radiometric resolution which results in 4096 digital counts to represent the reflectance. But as stated above, this is practically decreased to about 3600 DN where the sensor behaves linear. Because of the sensors sensitivity and the suns spectrum this is further decreased band and pixel dependently as shown in Figure 3.6 (left). This leaves 111 DN to express 100 percent reflectance for 466 nm (band 5) in the worst case (for the pixel with lowest DN value). Thus, the radiometric resolution has a minimum precision of 0.9 percent reflectance at 466 nm (band 5). Below 466 nm (band 5) the precision drops below one percent reflectance. On the other side of the spectrum 866 nm (band 105) is the last band where the precision is above one percent reflectance for all pixels. For the best pixel in band 678 (band 58) the precision is above 0.03 percent.

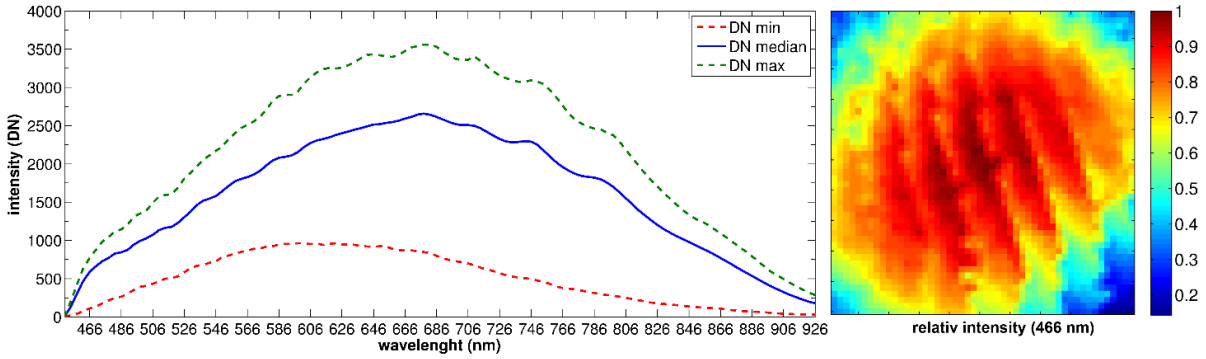

Figure 3.6 Minimum (min), median and maximum (max) DN from 450 (band 1) to 926 nm (band 120) (left) and the intensity of 466 nm (band 5) relative to the maximum DN of the band (right) of a Zenith Lite™ panel on a sunny day. These values define the actual radiometric resolution for each band and individual pixel.

3.4.1.3 Radiometric correction and registration

To evaluate the results of the radiometric registration we flew at 30 m above ground level over four 80 cm by 80 cm reference panels placed on a meadow. Each target was homogenously painted with a different grey hue corresponding to approximately 58, 43, 18 and 5 percent reflectance. Figure 3.7 shows the scene at 726 nm (band 70) before and after the radiometric correction and registration with the in-field procedure described in section 3.3.1.3. In the un-calibrated image the vignetting effect and the overlying undulated pattern are visible. In the calibrated image these are not visible anymore. Additionally, the reference panel with 18 percent reflectance, which was hardly visible in the uncalibrated image, is now visible.

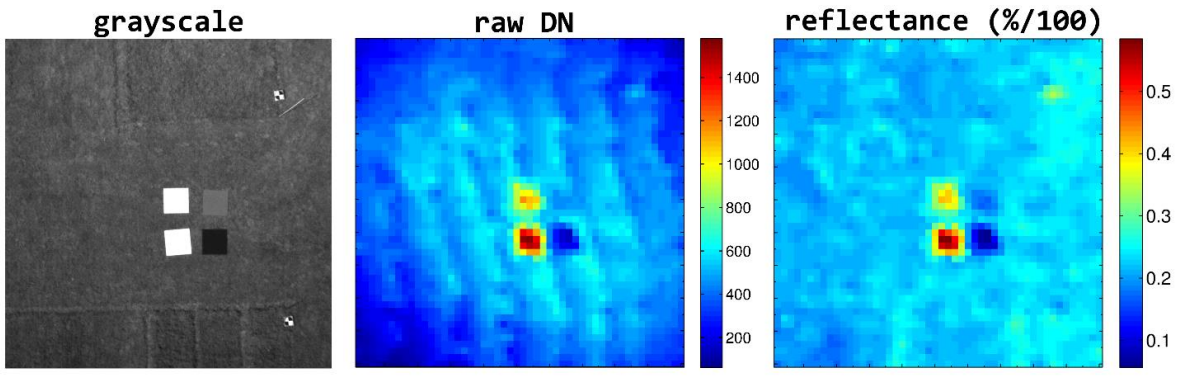

Figure 3.7 Image with reference targets as grayscale image (left), at 726 nm before (middle) and after (right) the radiometric correction and registration.

To evaluate the spectral quality of the calibration we measured the targets with an ASDI FieldSpec 3 (http://www.asdi.com/) and resampled the spectra to the UHDs band configuration with EXELIS Envi (version 5.0, http://www.exelisvis.com). From the scene captured by the UHD we extracted the spectrum of the center pixel of each panel. The spectra and their difference are shown in Figure 3.8.

For 466 nm (band 5) to 806 nm (band 90) the ASD and UHD spectra differ by less than one percent. Only the spectra measured at the 43 percent reference panel differs up to two percent below 482 nm (band 9) and above 782 nm (band 85). Below 466 nm (band 5) and above 850 nm (band 100) the offset increases rapidly. For the panels, where the reflectance is below the reflectance of the adjacent meadow, the UHD tent to have lower reflectance than the ASD and vice versa.

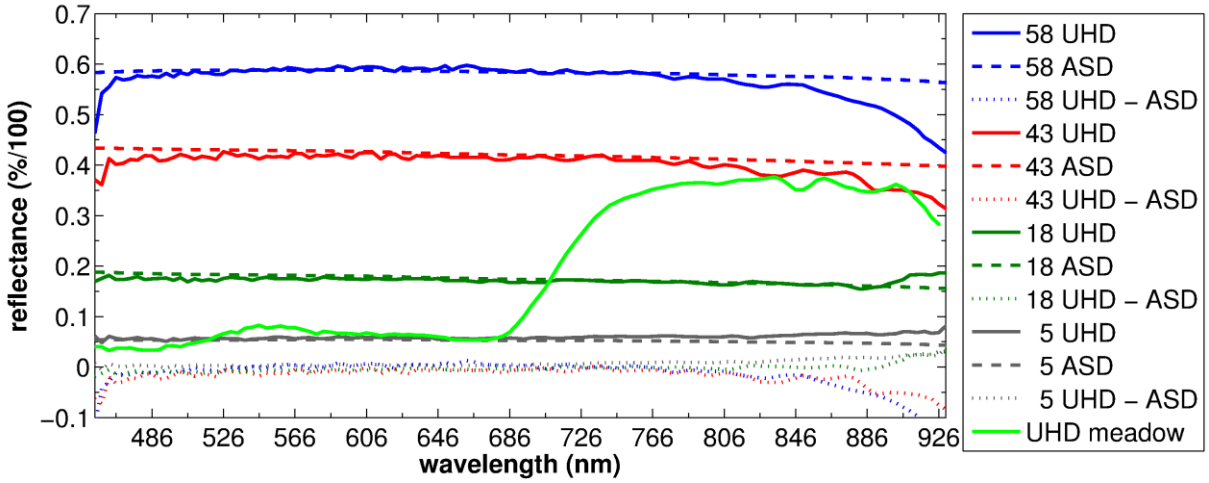

Figure 3.8 Comparison of spectra derived from the UHD (solid), an ASD (dashed) and their difference (dotted) for four reference panels with 5, 18, 43 and 58 percent reflectance. Additionally, a spectrum of the adjacent meadow grass is shown in light green.

3.4.1.4 Quality assurance information

As shown above the quality of the spectral information depends on both the band and pixel position. Thus, we integrate the x and y pixel position of the original image into an additional band. In the final HS DSM we can extract this information to look up the properties for each pixel from each band from the camera characterization. Figure 3.9 (A, B) shows the pixel position in the original images of the pixel. -1 and 1 represent the pixel closest to the middle, -25 and 25 the pixels at the edges of the original image in the x (A) and y (B) direction. Thus, yellow colors in the map symbolize pixels taken from the image center while green and red symbolize pixels towards the edges of the original image.

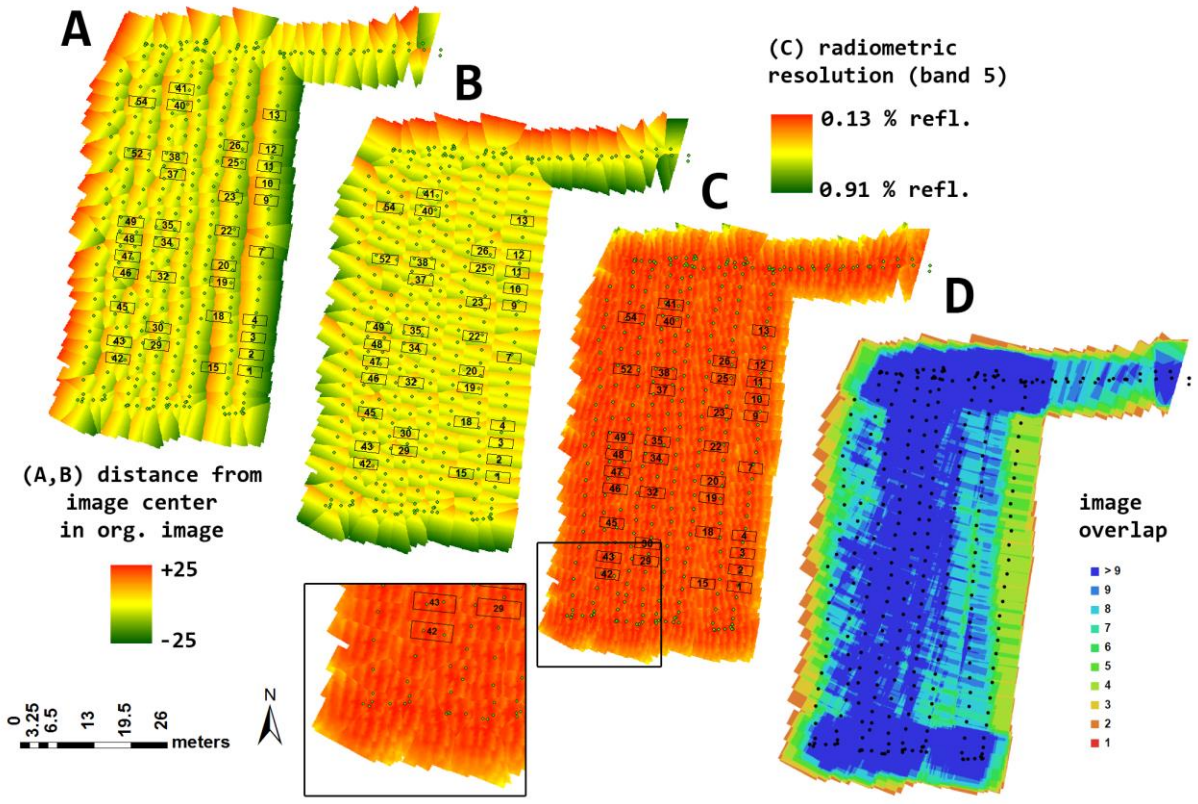

Figure 3.9 Pixel distance in x (A) and y (B) direction from the image center of the original images. An absolute value of 25 correspond to pixels at the image edge, 1 to pixels closest to the image center. Radiometric precision (C) of the spectral information at 466 nm (band 5) and image overlap (D) of the scene. The dots represent the image capturing positions.

The pixel towards the edges of the entire scene are derived from peripheral pixels of the original images. Additionally, pixel values between the flight lines, respectively the image positions, are taken towards the edges of the original images (Figure 3.9, A, B). The lower the overlap of the images, the more pixels are taken from the image edges since the area which is covered by each image is increasing (Figure 3.9, A, B).

To demonstrate one possible application of the pixel position information we generated a map of the maximal precision of the HS information for 466 nm (band 5) (Figure 3.9, C). The radiometric resolution is a function of the sensor, band and spatial position of the pixel. Thus, the x and y position in the original image defines the radiometric resolution of each pixel in the output scene: Towards the edges of the scene the radiometric precision decreases. For most of the scene the pixels are taken from the inner area of the original images and have a high pixel precision. Additionally, the pattern described in section 3.4.1.2 is visible (Figure 3.9, C magnification). The maximum precision within the entire scene is 0.13 percent reflectance. The minimum precision is 0.91 percent. Thus, results of the analysis carried out in regions of the latter precisions cannot be more precise than 0.91 percent reflectance. However, 95 percent of the scene have a precision of more than 0.2 percent. For the pixels within the

experimental plots the minimum average precision is 0.15 and the average plot precision is 0.14 percent (std. < 0.002 percent).

3.4.2 Hyperspectral 3D information

3.4.2.1 Plant height

Figure 3.10 shows a map of the crop surface height (left) and a scatterplot of the average height of 26 plots compared to the manual ruler measurements (right). The alignment of both measurements is R^2 = 0.7. The UHD measurements constantly underestimate the plant height by about 0.19 m (std. 0.03 m). Only the height of plot 52 shows a significant higher offset with 0.3 m. Plot 19 and 23 show the smallest difference with less than 0.15 m.

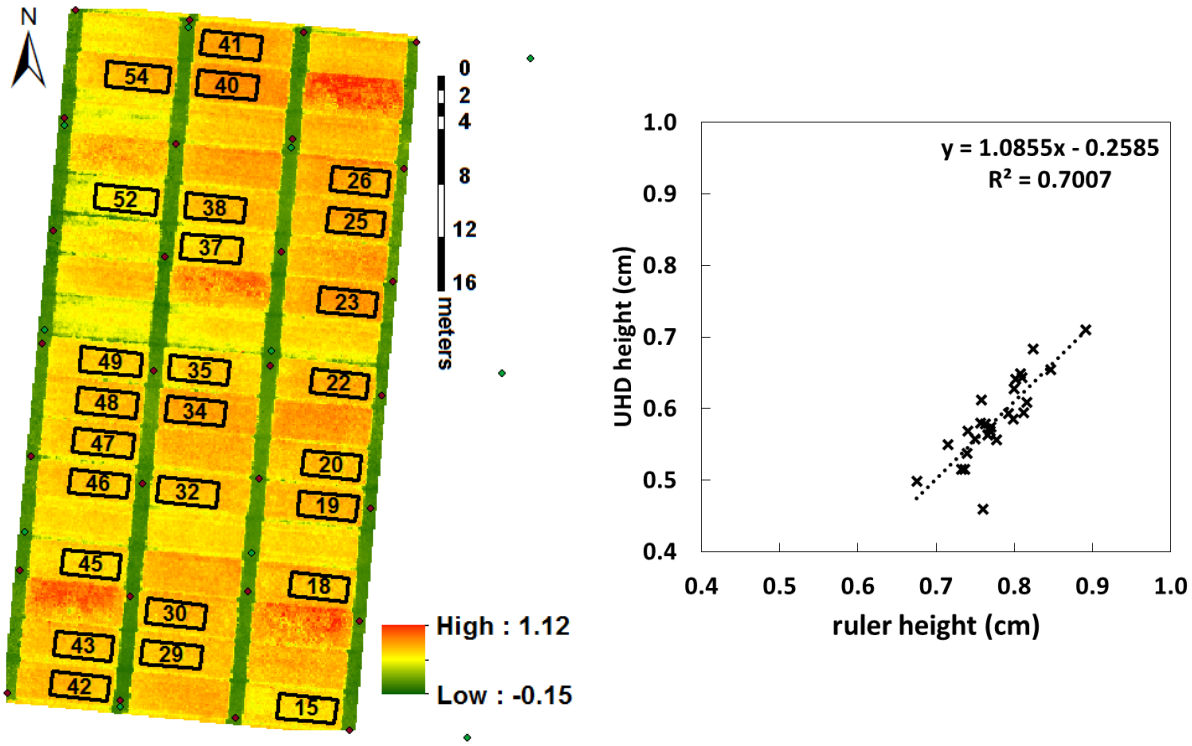

Figure 3.10 Map of the crop surface height. The spectrally measured non-invasive plot parts are marked in black with their plot number. Green points represent the ground control points while red ones represent the extraction points for the interpolation of the bare surface (left). Scatterplot of the averaged crop surface height for 26 plots compared to the manual ruler measurements of the marked 26 experimental plots (right).

3.4.2.2 Hyperspectral vegetation indices

Table 3.3 shows the relationship of the VIs with the Chl, LAI and green biomass derived from the HS DSM. For Chl the BGI2 and PRI show the best results with an R^2 = 0.51 and 0.44, respectively. For LAI the RDVI performs best with R^2 = 0.32. Only the RDVI supplies significant results. For green biomass

the RDVI shows the best results, too. For Chl all VIs have a relative RMSE of about 10 to 13 percent of the average Chl value. For LAI and green biomass the relative RMSE is up to 24 and 22 percent, respectively.

Table 3.3 Coefficients of determination (R^2) and absolute and relative root mean square error (RMSE) of vegetation indices with chlorophyll, Leaf Area Index (LAI) and green biomass (green BM).

	Chlorophyll			LAI			Green BM		
	R^2	RMSE	(%)	R^2	RMSE	(%)	R^2	RMSE	(%)
BGI2	0.51	5.35	(10)	0.09	293.17	(23)	0.10	22.28	(21)
MCARI2	0.34	5.83	(11)	0.02	304.01	(24)	0.01	23.38	(22)
TCARI/OSAVI	0.26	6.16	(12)	0.02	303.42	(24)	0.04	23.08	(22)
RDVI	0.20	6.39	(12)	0.32	254.11	(20)	0.29	19.76	(19)
PRI(514, 530)	0.44	5.35	(10)	0.17	280.46	(22)	0.18	21.23	(20)
NDVI(798, 670)	0.12	6.73	(13)	0.11	289.59	(23)	0.18	21.33	(20)
param. mean		53.24			1266.38			106.73	

Figure 3.11 shows a visualization of HS DSM with the BGI2 values shown for the area of the experimental plots and a scatterplot of the averaged BGI2 values per plot and the invasive measured chl values. The paths between the plots and the bare soil in the north can be identified. Different plots can be distinguished by their BGI2 value. Besides of the differences between the cultivars very low BGI2 values to the very east edge of the scene can be seen.

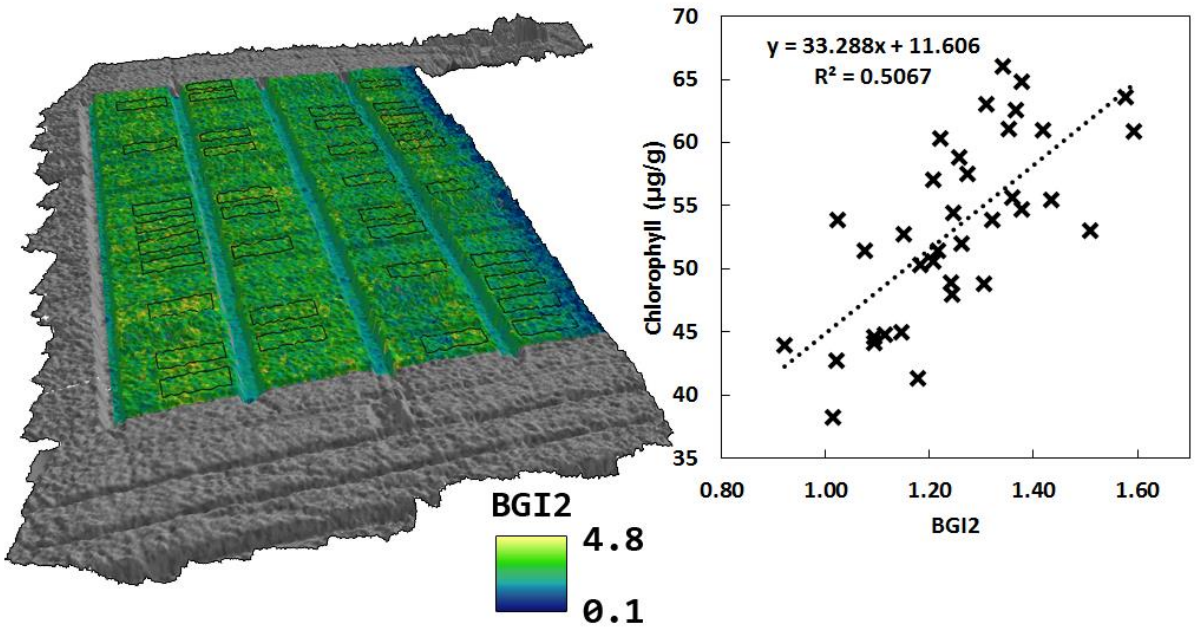

Figure 3.11 3D visualization of the HS DSM with the BGI2 calculated from the hyperspectral data clipped to the extent of the experimental plots. The spectral sample areas are marked with black rectangles (left). The scatterplot shows the averaged BGI2 values per plot and the invasive measured chlorophyll values for the 36 plots (right).

3.5 Discussion

In this paper we describe a way to derive HS 3D information from images captured by a novel HS snapshot camera based on available software. It can also be used for data from IF cameras if the bands have been previously spatially co-registered to image cube with bands of the same spatial extend. Snapshot (and IF) cameras provide two key advantages for remote sensing applications compared to traditional line scanners: With current photogrammetric algorithms the relative position and orientation of images can be determined without any other information. To georeference the resulting scenes only a few GCPs are needed. This saves payload onboard the UAV compared to line scanning devices, which need very precise orientation and positioning information to orthorectify the individual image lines, and thus, increases flight time. Moreover, the complex process of data stream synchronization from GPS, IMU and image lines can be omitted. The second advantage is that IF cameras capture 2D spatial information. Thus, individual image bands can be used for the reconstruction of 3D information with SfM algorithms. Thereby, considering the limitations of SfM mentioned in Remondino and El-Hakim (2006), multispectral or HS image frame and snapshot cameras allow to capture spectral and structural information at the same time. This significantly reduces the complexity and costs compared to approaches were multiple sensor systems are used. The procedure introduced in this study allows to capture both 3D and HS information at the same time, with the same sensor, through the same lens and thus, without co-registration. Although not demonstrated here, this data can now be used for combined data analysis approaches as has been shown in other studies (Alonzo et al., 2014; Bendig et al.,2015; Clark et al., 2011; Hladik et al., 2013; Swatantran et al., 2011).

3.5.1 Radiometric calibration and quality assurance information

Before a new camera system can be used, it should be carefully characterized to ensure the validity of resulting data products. We describe the important radiometric calibration steps for IF cameras and apply them to assess the UHD for HS remote sensing applications: The camera has a very low average DC of less than one DN per band. The highest DC for a single pixel is below three DN under operational conditions. Ideally, the DC of a sensor should be modeled as a function of sensor temperature and integration time. Unfortunately, this is not possible with the current version of the UHD, since temperature information is not available. Thus, we had to estimate it with an empirical approach of unknown precision. Future sensor systems should provide temperature readings for a better estimation. Nevertheless, since the overall maximum DC is very low (for most of the bands below one percent of the minimal intensity) it has minor influences on the final data product.

On the contrary the flat-field analysis revealed a strong influence of the optical system on the images. Especially the undulated pattern caused significant challenges. With the help of the manufacturer a

coating on a beam splitter could be identified as the reason for the pattern. Additionally, the lab calibration failed because the mechanically stability of the camera was not strong enough. Thus, the optical path was slightly altered when the camera was mounted differently. In future versions of the camera this effect will be significantly reduced (personal correspondence, Cubert GmbH). The now chosen approach of in-field calibration compensated the undulated pattern well and showed very good results with less than one percent offset compared to ASD measurements of reference targets. However, compared to a lab calibration approach, it complicates the in-field measurement procedure and is more exposed to errors. Besides, the method cannot adapt for illumination changes during the flight. Especially for remote sensing applications in areas where constant illumination conditions cannot be guaranteed ground or UAV based measurements of the suns irradiance (Burkart et al., 2014; Hakala et al., 2013) or based on radiometric block adjustment (Honkavaara et al., 2013) should become a standard to increase the flexibility of spectral measurements. For very precise measurements spectrally resolved irradiance measurement techniques for onboard use of UAVs should be developed.

Even with very well calibrated sensors (Hyper-) spectral remote sensing of plants is challenging: plants have relatively low reflection in the VIS compared to the NIR. At the same time already small changes in reflectance may point out important changes in the plants status. Additionally, the suns irradiance is not homogenous throughout the spectrum. Combined with the efficiency fall-off of detector towards its sensitivity borders and, for imaging sensors the decreased intensity towards the edges of the image (-lines), the precision of the spectral information for a certain pixel within a certain band might be strongly limited. We think that regardless of the size of the sensor or the carrier platform quality information should be included in every data product. Thus, we developed a method to trace the pixel position from the original image which was used to derive the spectral information of the final data. This information together with the characterization of the sensor provides good quality assurance information for every pixel in the final data product. With this information we showed that the radiometric precision was very good for most of the area mapped in this study. As expected the precision decreases between image positions and towards the edges of the entire scene. This can be explained by the decrease of signal intensity towards the edges of the original images. Still, with the quality information we can assure that the precision in most of the area of interest is sufficient for quantitative analysis. Only to the very east of the scene the precision decreases (Figure 3.9). Here the pixels are taken from the edges of the original images since center pixels are not available. Additionally, Figure 3.11 shows that the BRI2 values decrease strongly in the same area. This could result from the different sun-object-sensor geometries of pixels from different positions of the original images, leading to BRDF effects which have been shown to have significant influences on HS data collected by UAVs (Burkart et al., 2015). As for every analysis we recommend that the data quality information of a data

product should be carefully assessed if it is sufficient for the desired purpose. Thus, it should accompany the data. For the current version of the camera we recommend to limit the use from 466 to 850 nm (band 5 to 100) because of the radiometric resolution and spectral quality. Additionally, the integration time should be set to limit the maximum DN value to less than 3600.

During the development of the described methodology we discovered that Photoscan is interpolating the color information although it is stated otherwise in the manual (section 3.3.2.3). This introduces a non-traceable modification of the spectral data and makes the pixel position information unusable. Thus, we had to develop the described rather laborious workaround of mosaicking the individual image cubes in ArcGIS. Studies, which use interpolated color or spectral information need to investigate the influence on the data quality since the impact on the results might depend on several factors as image overlap, spatial resolution and the purpose of the study.

3.5.2 Hyperspectral 3D information

With the SfM approach 3D information can be derived from 2D images. The main advance of this method compared to laser scanning approaches is the considerable lower cost for the equipment (Remondino and El-Hakim, 2006). However, since the technique is not able to penetrate through vegetation it is not suited to generate structural information below the canopy but well suited for canopy monitoring (Dandois and Ellis, 2010; Harwin and Lucieer, 2012). Thus, we use a similar approach as Bendig et al. (2013) used to create crop surface models from the derived 3D information. However, since we additionally have HS information linked to every pixel of the DSM and the methodology is not limited to crops we name the data product HS DSM referring to a digital surface model as a representation of the elevation of the earth's surface and its covering objects linked with hyperspectral information. Since all data is captured through the same lens, at the same time, during the same exposure and of the same area no co-registration is needed. Nevertheless, since the spatial resolution of the HS bands is lower than the gray image's we scale it with a nearest neighbor interpolation. Due to the unidirectional optical distortion, and the resulting slightly non-quadratic shape of the gray image, the merging introduces a spatial uncertainty of one percent in one direction. We think that for UAV studies with a spatial resolution as the present, this is acceptable. However, for studies which require more precise spatial allocation it should be further evaluated.

From the created data product we derive several important plant parameters for vegetation monitoring applications. The correlation of the height derived from the SfM approach with manually measured plant heights show good results and is comparable to other studies (Bendig et al., 2013). The almost constant offset of 0.19 m might be explained by different factors: Before this study several other sampling campaigns were carried out within the same experimental plots. Thus, the soil on the

paths between the plots was significantly compressed and lower than the soil below the actual plots. Unfortunately, at time of the data analysis the absolute lowering was not ascertainable any more. Additionally, the manual ruler measurements might not be the best ground truth since it is prone to many errors in itself. As also mentioned in other studies (Geipel et al., 2014) ideally the results should be validated with perfectly co-registered high resolution laser scanning data. However, such data is currently not available for this measurement campaign. Besides, it has to be noted that the algorithms used in Photoscan are not publically known. Thus, it is not entirely clear how very complex surfaces like plants (e.g. with single high rising stems and ears) are handled.

With the additional spectral information we derive biochemical and biophysical plant parameters. The BGI2 and PRI archive the best results for Chl with correlations comparable to other studies (Quemada et al., 2014; Yu et al., 2013a). For the biophysical parameters LAI and green biomass the RDVI, which is related to the absorbed photosynthetically active radiation, performs best. In many previous studies the NDVI has shown good results for LAI and biomass. However, most studies were carried out over more than one sampling date. In this study only a single measurement date was evaluated. Thus, temporal effects which usually expand the feature space – and often improve the correlations (Aasen et al., 2014b; Gnyp et al., 2014) - did not influence the results. For precision agriculture applications, where in-time information is critical, this effect should be further investigated. Reliable HS UAV data provides a great opportunity to support that. Additionally, it has to be noted that although VIs are still very common in vegetation studies, they may disregard the full potential of HS data as shown in comparative studies with other statistical approaches (Atzberger et al., 2010; Yu et al., 2013b).

Besides, the invasive sampled plant parameters have been measured from the plants leafs. Unfortunately, the spatial resolution of the UHD is too coarse to sample HS signatures on the leaf level when flown on an UAV. By sampling signatures on the canopy level all organs of the plants, possibly background signals from the soil, the canopy structure, multi-scatter and shadow effects influence the spectra. Latter could be addressed by including canopy structural elements into the analysis but goes beyond this study. Additionally, it could be addressed by higher resolution data which allows sampling on the leaf level. However, when working with multispectral or HS sensor systems onboard of UAVs we face the challenge of spectral resolution versus spatial resolution versus coverage: Because of the size and weight limitations a trade-off between spectral and spatial resolution of a sensor has to be made. When applying the sensor the latter can be compensated by adapting the flight plan to the desired ground resolution – but this comes with a decrease in coverage because of the limited flight time. Thus, future studies should investigate the resolution needed for specific applications. Besides, the sensor technology is evolving fast. We are confided that the spatial resolution of the HS information of current HS image frame and snapshot cameras will further increase. Thus, besides of technical

developments for sensor systems and carrier platforms, advances in data management and automated processing will be needed to make use of the increasing volume of data.

3.6 Conclusion

In this study we introduced a novel way to derive 3D hyperspectral information from a lightweight UAV snapshot camera for vegetation monitoring. Since the camera captures all information through the same lens at the same time with the same spatial extend no spatial co-registration is needed. The derived data product combines the 3D surface with hyperspectral information emitted and reflected by the objects covered by the surface and is thus named hyperspectral digital surface model. It has a spatial resolution of approximately 1 cm for the spatial and 21 cm for the hyperspectral information. The radiometric characterization of the camera demonstrates the feasibility for vegetation monitoring: The hyperspectral information has a sufficient accuracy (> one percent reflectance) from 466 to 850 nm compared to an ASD field-spec 3.The radiometric precision of the spectral data in the area of interest is evaluated based on quality assurance information included in the created data product and is better than 0.13 percent reflectance. The derived plant parameters from a single date (3rd June 2014) field campaign in barley show significant correlations with invasive measurements of the plant height (R^2 = 0.7), chlorophyll (BGI2, PRI: R^2 = 0.51, 0.44), LAI (RDVI: R^2 = 0.32), biomass (RDVI: R^2 = 0.29).

Acknowledgements

We thank the students Simon Bennertz, Janis Broscheit, Silas Eichfuss and Sven Ortloff very much for their outstanding engagement in the fieldwork and the people of Campus Klein-Altendorf (University of Bonn) for maintaining the field experiment. Moreover, we thank Edelgard Schölgens (Forschungszentrum Jülich), Ira Kurth and Mauritio Hunsche (INRES, University of Bonn) for the access to the laboratory and the measurements of the plant parameters. Also, we are thankful to Rene Michels and Rainer Ganser of the Cubert GmbH for their support with the UHD185-Firefly camera and the constructive discussions. Besides, we thank Arco Lucieer and Zbynek Malenovsky for the idea for the reference panels. The authors acknowledge the funding of the CROP.SENSe.net project in the context of the Ziel 2-Programms NRW 2007–2013 “Regionale Wettbewerbsfähigkeit und Beschäftigung” by the Ministry for Innovation, Science and Research (MIWF) of the state North Rhine Westphalia (NRW) and European Union Funds for regional development (EFRE) (005-1103-0018).

3.7 References

Aasen, H., Bendig, J., Bolten, A., Bennertz, S., Willkomm, M., Bareth, G., 2014a. Introduction and preliminary results of a calibration for full-frame hyperspectral cameras to monitor agricultural crops with UAVs. Int. Arch. Photogramm. Remote Sens. Spat. Inf. Sci. Vol. XL-7 2014 ISPRS Tech. Comm. VII Symp. XL, 8. doi:10.5194/isprsarchives-XL-7-1-2014

Aasen, H., Gnyp, M.L., Miao, Y., Bareth, G., 2014b. Automated Hyperspectral Vegetation Index Retrieval from Multiple Correlation Matrices with HyperCor. Photogramm. Eng. Remote Sens. 80, 785–795. doi:10.14358/PERS.80.8.785

Agisoft LLC, 2014. Agisoft PhotoScan User Manual: Professional Edition, version 1.0.

Alonzo, M., Bookhagen, B., Roberts, D. a., 2014. Urban tree species mapping using hyperspectral and LiDAR data fusion. Remote Sens. Environ. 148, 70–83. doi:10.1016/j.rse.2014.03.018

Atzberger, C., 2013. Advances in remote sensing of agriculture: Context description, existing operational monitoring systems and major information needs. Remote Sens. doi:10.3390/rs5020949

Atzberger, C., Guérif, M., Baret, F., Werner, W., 2010. Comparative analysis of three chemometric techniques for the spectroradiometric assessment of canopy chlorophyll content in winter wheat. Comput. Electron. Agric. 73, 165–173. doi:10.1016/j.compag.2010.05.006

Avbelj, J., Iwaszczuk, D., Müller, R., Reinartz, P., Stilla, U., 2014. Coregistration refinement of hyperspectral images and DSM: An object-based approach using spectral information. ISPRS J. Photogramm. Remote Sens. doi:10.1016/j.isprsjprs.2014.05.010

Bareth, G., Aasen, H., Bendig, J., Gnyp, M.L., Bolten, A., Jung, A., Michels, R., Soukkamäki, J., 2015a. Low-weight and UAV-based Hyperspectral Full-frame Cameras for Monitoring Crops: Spectral Comparison with Portable Spectroradiometer Measurements. Photogramm. - Fernerkund. - Geoinformation 2015, 69–79. doi:10.1127/pfg/2015/0256

Bareth, G., Bolten, A., Hollberg, J., Aasen, H., Burkart, A., Schellberg, J., 2015b. Feasibility study of using non-calibrated UAV-based RGB imagery for grassland monitoring : Case study at the Rengen Long-term Grassland Experiment (RGE), Germany, in: DGPF Tagungsband 24/2015. Cologne, pp. 1–7.

Bendig, J., Bolten, A., Bareth, G., 2013. UAV-based Imaging for Multi-Temporal, very high Resolution Crop Surface Models to monitor Crop Growth Variability. Photogramm. - Fernerkund. - Geoinformation 2013, 551–562. doi:10.1127/1432-8364/2013/0200

Bendig, J., Bolten, A., Bennertz, S., Broscheit, J., Eichfuss, S., Bareth, G., 2014. Estimating Biomass of Barley Using Crop Surface Models (CSMs) Derived from UAV-Based RGB Imaging. Remote Sens. 6, 10395–10412. doi:10.3390/rs61110395

Bendig, J., Yu, K., Aasen, H., Bolten, A., Bennertz, S., Janis, B., Gnyp, M.L., Bareth, G., 2015. Combining UAV-based Crop Surface Models, Visible and Near Infrared Vegetation Indices for Biomass Monitoring in Barley. Int. J. Appl. Earth Obs. Geoinformation accepted.

Berni, J.A.J., Member, S., Zarco-tejada, P.J., Suárez, L., Fereres, E., 2009. Thermal and Narrowband Multispectral Remote Sensing for Vegetation Monitoring From an Unmanned Aerial Vehicle 1–17.

Blanke, M., 1992. Determination of chlorophyll using DMSO. Wein-Wiss. 47, 32–35.

Burkart, A., Aasen, H., Alonso, L., Menz, G., Bareth, G., Rascher, U., 2015. Angular Dependency of Hyperspectral Measurements over Wheat Characterized by a Novel UAV Based Goniometer. Remote Sens. 7, 725–746. doi:10.3390/rs70100725

Burkart, A., Cogliati, S., Schickling, A., Rascher, U., 2014. A Novel UAV-Based Ultra-Light Weight Spectrometer for Field-spectroscopy. IEEE Sens. J. 14, 62–67. doi:10.1109/JSEN.2013.2279720

Büttner, A., Röser, H.-P., 2014. Hyperspectral Remote Sensing with the UAS "Stuttgarter Adler" – System Setup, Calibration and First Results. Photogramm. - Fernerkund. - Geoinformation 2014, 265–274. doi:10.1127/1432-8364/2014/0217

Clark, M.L., Roberts, D. a., Ewel, J.J., Clark, D.B., 2011. Estimation of tropical rain forest aboveground biomass with small-footprint LiDAR and hyperspectral sensors. Remote Sens. Environ. 115, 2931–2942. doi:10.1016/j.rse.2010.08.029

Colomina, I., Molina, P., 2014. Unmanned aerial systems for photogrammetry and remote sensing: A review. ISPRS J. Photogramm. Remote Sens. doi:10.1016/j.isprsjprs.2014.02.013

Dandois, J.P., Ellis, E.C., 2010. Remote Sensing of Vegetation Structure Using Computer Vision. Remote Sens. 2, 1157–1176. doi:10.3390/rs2041157

Delalieux, S., van Aardt, J., Keulemans, W., Schrevens, E., Coppin, P., 2007. Detection of biotic stress (Venturia inaequalis) in apple trees using hyperspectral data: Non-parametric statistical approaches and physiological implications. Eur. J. Agron. 27, 130–143. doi:10.1016/j.eja.2007.02.005

Diaz-Varela, R. a, Zarco-Tejada, P.J., Angileri, V., Loudjani, P., 2014. Automatic identification of agricultural terraces through object-oriented analysis of very high resolution DSMs and multispectral imagery obtained from an unmanned aerial vehicle. J. Environ. Manage. 134, 117–26. doi:10.1016/j.jenvman.2014.01.006

Erdle, K., Mistele, B., Schmidhalter, U., 2011. Comparison of active and passive spectral sensors in discriminating biomass parameters and nitrogen status in wheat cultivars. Field Crops Res. 124, 74–84. doi:10.1016/j.fcr.2011.06.007

Evans, L.T., 1993. Crop Evolution, Adaptation and Yield. Cambridge Univ. Press, Cambridge.

Foley, J. a, Ramankutty, N., Brauman, K. a, Cassidy, E.S., Gerber, J.S., Johnston, M., Mueller, N.D., O'Connell, C., Ray, D.K., West, P.C., Balzer, C., Bennett, E.M., Carpenter, S.R., Hill, J., Monfreda, C., Polasky, S., Rockström, J., Sheehan, J., Siebert, S., Tilman, D., Zaks, D.P.M., 2011. Solutions for a cultivated planet. Nature 478, 337–42. doi:10.1038/nature10452

Gao, B.C., Montes, M.J., Davis, C.O., 2004. Refinement of wavelength calibrations of hyperspectral imaging data using a spectrum-matching technique. Remote Sens. Environ. 90, 424–433. doi:10.1016/j.rse.2003.09.002

Geipel, J., Link, J., Claupein, W., 2014. Combined Spectral and Spatial Modeling of Corn Yield Based on Aerial Images and Crop Surface Models Acquired with an Unmanned Aircraft System. Remote Sens. 6, 10335–10355. doi:10.3390/rs61110335

Gnyp, M.L., Miao, Y., Yuan, F., Ustin, S.L., Yu, K., Yao, Y., Huang, S., Bareth, G., 2014. Hyperspectral canopy sensing of paddy rice aboveground biomass at different growth stages. Field Crops Res. 155, 42–55. doi:10.1016/j.fcr.2013.09.023

Gnyp, M.L., Yu, K., Aasen, H., Yao, Y., Huang, S., Miao, Y., Bareth, C.& G., 2013. Analysis of Crop Reflectance for Estimating Biomass in Rice Canopies at Different Phenological Stages.

Photogramm. - Fernerkund. - Geoinformation 2013, 351–365. doi:10.1127/1432-8364/2013/0182

Goetz, A.F.H., 2009. Remote Sensing of Environment Three decades of hyperspectral remote sensing of the Earth : A personal view. Remote Sens. Environ. 113, S5–S16. doi:10.1016/j.rse.2007.12.014

Goetz, A.F.H., Vane, G., Solomon, J.E., Rock, B.N., 1985. Imaging Spectrometry for Earth Remote Sensing 228.

Goldman, D.B., 2010a. Vignette and exposure calibration and compensation. IEEE Trans. Pattern Anal. Mach. Intell. 32, 2276–88. doi:10.1109/TPAMI.2010.55

Goldman, D.B., 2010b. Vignette and exposure calibration and compensation. IEEE Trans. Pattern Anal. Mach. Intell. 32, 2276–88. doi:10.1109/TPAMI.2010.55

Haboudane, D., Miller, J.R., Pattey, E., Zarco-tejada, P.J., Strachan, I.B., 2004. Hyperspectral vegetation indices and novel algorithms for predicting green LAI of crop canopies : Modeling and validation in the context of precision agriculture 90, 337–352. doi:10.1016/j.rse.2003.12.013

Haboudane, D., Miller, J.R., Tremblay, N., Zarco-Tejada, P.J., Dextraze, L., 2002. Integrated narrow-band vegetation indices for prediction of crop chlorophyll content for application to precision agriculture. Remote Sens. Environ. 81, 416–426. doi:10.1016/S0034-4257(02)00018-4

Hagen, N., 2012. Snapshot advantage: a review of the light collection improvement for parallel high-dimensional measurement systems. Opt. Eng. doi:10.1117/1.OE.51.11.111702

Hakala, T., Honkavaara, E., Saari, H., Mäkynen, J., Kaivosoja, J., Pesonen, L., Pölönen, I., 2013. Spectral Imaging From Uavs Under Varying Illumination Conditions. ISPRS - Int. Arch. Photogramm. Remote Sens. Spat. Inf. Sci. XL-1/W2, 189–194. doi:10.5194/isprsarchives-XL-1-W2-189-2013

Hansen, P.M., Schjoerring, J.K., 2003. Reflectance measurement of canopy biomass and nitrogen status in wheat crops using normalized difference vegetation indices and partial least squares regression 86, 542–553. doi:10.1016/S0034-4257(03)00131-7

Harwin, S., Lucieer, A., 2012. Assessing the Accuracy of Georeferenced Point Clouds Produced via Multi-View Stereopsis from Unmanned Aerial Vehicle (UAV) Imagery. Remote Sens. 4, 1573–1599. doi:10.3390/rs4061573

Hernández-Clemente, R., Navarro-Cerrillo, R.M., Suárez, L., Morales, F., Zarco-Tejada, P.J., 2011. Assessing structural effects on PRI for stress detection in conifer forests. Remote Sens. Environ. 115, 2360–2375. doi:10.1016/j.rse.2011.04.036

Hladik, C., Schalles, J., Alber, M., 2013. Salt marsh elevation and habitat mapping using hyperspectral and LIDAR data. Remote Sens. Environ. 139, 318–330. doi:10.1016/j.rse.2013.08.003

Hoffmeister, D., Bolten, A., Curdt, C., Waldhoff, G., Bareth, G., 2010. High resolution Crop Surface Models (CSM) and Crop Volume Models (CVM) on field level by terrestrial laser scanning. SPIE Proc. 7840, 78400E–78400E–6. doi:10.1117/12.872315

Honkavaara, E., Saari, H., Kaivosoja, J., Pölönen, I., Hakala, T., Litkey, P., Mäkynen, J., Pesonen, L., 2013. Processing and assessment of spectrometric, stereoscopic imagery collected using a lightweight UAV spectral camera for precision agriculture. Remote Sens. 5, 5006–5039. doi:10.3390/rs5105006

Hruska, R., Mitchell, J., Anderson, M., Glenn, N.F., 2012. Radiometric and Geometric Analysis of Hyperspectral Imagery Acquired from an Unmanned Aerial Vehicle. Remote Sens. 4, 2736–2752. doi:10.3390/rs4092736

Hueni, a., Nieke, J., Schopfer, J., Kneubühler, M., Itten, K.I., 2009. The spectral database SPECCHIO for improved long-term usability and data sharing. Comput. Geosci. 35, 557–565. doi:10.1016/j.cageo.2008.03.015

Hunt, E.R., Dean Hively, W., Fujikawa, S.J., Linden, D.S., Daughtry, C.S.T., McCarty, G.W., 2010. Acquisition of NIR-green-blue digital photographs from unmanned aircraft for crop monitoring. Remote Sens. 2, 290–305. doi:10.3390/rs2010290

Itten, K.I., Dell'Endice, F., Hueni, A., Kneubühler, M., Schläpfer, D., Odermatt, D., Seidel, F., Huber, S., Schopfer, J., Kellenberger, T., Bühler, Y., D'Odorico, P., Nieke, J., Alberti, E., Meuleman, K., 2008. APEX - The hyperspectral ESA airborne prism experiment. Sensors 8, 6235–6259. doi:10.3390/s8106235

Jaakkola, A., Hyyppä, J., Kukko, A., Yu, X., Kaartinen, H., Lehtomäki, M., Lin, Y., 2010. A low-cost multi-sensoral mobile mapping system and its feasibility for tree measurements. ISPRS J. Photogramm. Remote Sens. 65, 514–522. doi:10.1016/j.isprsjprs.2010.08.002

James Burger, P.G., 2005. Hyperspectral NIR image regression part I: calibration and correction. J. Chemom. 19, 355–363. doi:10.1002/cem.938

Kelcey, J., Lucieer, A., 2012. Sensor Correction of a 6-Band Multispectral Imaging Sensor for UAV Remote Sensing. Remote Sens. 4, 1462–1493. doi:10.3390/rs4051462

Kim, S.J., Pollefeys, M., 2008. Robust radiometric calibration and vignetting correction. IEEE Trans. Pattern Anal. Mach. Intell. 30, 562–76. doi:10.1109/TPAMI.2007.70732

Koch, B., 2010. Status and future of laser scanning, synthetic aperture radar and hyperspectral remote sensing data for forest biomass assessment. ISPRS J. Photogramm. Remote Sens. 65, 581–590. doi:10.1016/j.isprsjprs.2010.09.001

Kuusk, J., 2011. Dark Signal Temperature Dependence Correction Method for Miniature Spectrometer Modules. J. Sens. 2011, 1–9. doi:10.1155/2011/608157

Li, F., Miao, Y., Hennig, S.D., Gnyp, M.L., Chen, X., Jia, L., Bareth, G., 2010. Evaluating hyperspectral vegetation indices for estimating nitrogen concentration of winter wheat at different growth stages. Precis. Agric. 11, 335–357. doi:10.1007/s11119-010-9165-6

Lucieer, A., Malenovský, Z., Veness, T., Wallace, L., 2014. HyperUAS-Imaging Spectroscopy from a Multirotor Unmanned Aircraft System. J. Field Robot. 31, 571–590. doi:10.1002/rob.21508

Mahlein, A., Rumpf, T., Welke, P., Dehne, H., Plümer, L., Steiner, U., Oerke, E., 2013. Remote Sensing of Environment Development of spectral indices for detecting and identifying plant diseases. Remote Sens. Environ. 128, 21–30. doi:10.1016/j.rse.2012.09.019

Mansouri, a., Marzani, F.S., Gouton, P., 2005. Development of a Protocol for CCD Calibration: Application to a Multispectral Imaging System. Int. J. Robot. Autom. doi:10.2316/Journal.206.2005.2.206-2784

Milton, E.J., Schaepman, M.E., Anderson, K., Fox, N., 2007. Progress in field-spectroscopy. Remote Sens. Environ. 113, 92–109. doi:10.1016/j.rse.2007.08.001

Mulla, D.J., 2013. Twenty five years of remote sensing in precision agriculture: Key advances and remaining knowledge gaps. Biosyst. Eng. 114, 358–371. doi:10.1016/j.biosystemseng.2012.08.009

Pearlman, J.S., Barry, P.S., Segal, C.C., Shepanski, J., Beiso, D., Carman, S.L., 2003. Hyperion, a space-based imaging spectrometer. IEEE Trans. Geosci. Remote Sens. 41, 1160–1173. doi:10.1109/TGRS.2003.815018

Pronk, a. a., Goudriaan, J., Stilma, E., Challa, H., 2003. A simple method to estimate radiation interception by nursery stock conifers: a case study of eastern white cedar. NJAS - Wagening. J. Life Sci. 51, 279–295. doi:10.1016/S1573-5214(03)80020-9

Quemada, M., Gabriel, J., Zarco-Tejada, P., 2014. Airborne Hyperspectral Images and Ground-Level Optical Sensors As Assessment Tools for Maize Nitrogen Fertilization. Remote Sens. 6, 2940–2962. doi:10.3390/rs6042940

Remondino, F., El-Hakim, S., 2006. Image-based 3D Modelling: A Review. Photogramm. Rec. 21, 269–291. doi:10.1111/j.1477-9730.2006.00383.x

Rondeaux, G., Steven, M., Baret, F., 1996. Optimization of soil-adjusted vegetation indices. Remote Sens. Environ. 55, 95–107. doi:10.1016/0034-4257(95)00186-7

Roujean, J.-L., Breon, F.-M., 1995. Estimating PAR absorbed by vegetation from bidirectional reflectance measurements. Remote Sens. Environ. 51, 375–384. doi:10.1016/0034-4257(94)00114-3

Rouse Jr., J.W., Haas, R.H., Schell, J.A., Deering, D.W., Rouse, W., Haas, H., Deering, W., 1974. Monitoring vegetation systems in the Great Plains with ERTS, in: NASA SP-351, 3rd ERTS-1 Symposium. Washington, DC, pp. 309 – 317.

Roy, D.P., Borak, J.S., Devadiga, S., Wolfe, R.E., Zheng, M., Descloitres, J., 2002. The MODIS Land product quality assessment approach. Remote Sens. Environ. 83, 62–76. doi:10.1016/S0034-4257(02)00087-1

Schaepman-Strub, G., Schaepman, M.E., Painter, T.H., Dangel, S., Martonchik, J. V, 2006. Reflectance quantities in optical remote sensing-definitions and case studies. Remote Sens. Environ. 103, 27–42. doi:10.1016/j.rse.2006.03.002

Smith, G.M., Milton, E.J., 1999. The use of the empirical line method to calibrate remotely sensed data to reflectance. Int. J. Remote Sens. 20, 2653–2662. doi:10.1080/014311699211994

Stagakis, S., González-Dugo, V., Cid, P., Guillén-Climent, M.L., Zarco-Tejada, P.J., 2012. Monitoring water stress and fruit quality in an orange orchard under regulated deficit irrigation using narrow-band structural and physiological remote sensing indices. ISPRS J. Photogramm. Remote Sens. 71, 47–61. doi:10.1016/j.isprsjprs.2012.05.003

Sterling, M., Baker, C.., Berry, P.., Wade, A., 2003. An experimental investigation of the lodging of wheat. Agric. For. Meteorol. 119, 149–165. doi:10.1016/S0168-1923(03)00140-0

Suomalainen, J., Anders, N., Iqbal, S., Roerink, G., Franke, J., Wenting, P., Hünniger, D., Bartholomeus, H., Becker, R., Kooistra, L., 2014a. A Lightweight Hyperspectral Mapping System and Photogrammetric Processing Chain for Unmanned Aerial Vehicles. Remote Sens. 6, 11013–11030. doi:10.3390/rs61111013

Suomalainen, J., Anders, N., Iqbal, S., Roerink, G., Franke, J., Wenting, P., Hünniger, D., Bartholomeus, H., Becker, R., Kooistra, L., 2014b. A Lightweight Hyperspectral Mapping System and Photogrammetric Processing Chain for Unmanned Aerial Vehicles. Remote Sens. 6, 11013–11030. doi:10.3390/rs61111013

Suomalainen, J., Hakala, T., Kaartinen, H., Räikkönen, E., Kaasalainen, S., 2011. Demonstration of a virtual active hyperspectral LiDAR in automated point cloud classification. ISPRS J. Photogramm. Remote Sens. 66, 637–641. doi:10.1016/j.isprsjprs.2011.04.002

Swatantran, A., Dubayah, R., Roberts, D., Hofton, M., Blair, J.B., 2011. Mapping biomass and stress in the Sierra Nevada using LiDAR and hyperspectral data fusion. Remote Sens. Environ. 115, 2917–2930. doi:10.1016/j.rse.2010.08.027

Szeliski, R., 2011. Computer Vision, Texts in Computer Science. Springer London, London. doi:10.1007/978-1-84882-935-0

Thenkabail, P.S., Lyon, J.G., Huete, A., 2011. Advances in hyperspectral remote sensing of vegetation and agricultural crops, in: Thenkabail, P.S., Lyon, J.G., Huete, A. (Eds.), Hyperspectral Remote Sensing of Vegetation. CRC Press- Taylor and Francis group, Boca Raton, London, New York, pp. 3–29.

Thenkabail, P.S., Smith, R.B., De Pauw, E., 2000. Hyperspectral vegetation indices and their relationships with agricultural crop characteristics. Remote Sens. Environ. 71, 158–182. doi:10.1016/S0034-4257(99)00067-X

Tilly, N., Hoffmeister, D., Cao, Q., Huang, S., Lenz-Wiedemann, V., Miao, Y., Bareth, G., 2014. Multitemporal crop surface models: accurate plant height measurement and biomass estimation with terrestrial laser scanning in paddy rice. J. Appl. Remote Sens. 8, 083671. doi:10.1117/1.JRS.8.083671

Turner, D., Lucieer, A., Wallace, L., 2014. Direct Georeferencing of Ultrahigh-Resolution UAV Imagery. IEEE Trans. Geosci. Remote Sens. 52, 2738–2745. doi:10.1109/TGRS.2013.2265295

von Bueren, S., Burkart, A., Hueni, A., Rascher, U., Tuohy, M., Yule, I., 2015. Deploying four optical UAV-based sensors over grassland: challenges and limitations. Biogeosciences. doi:10.5194/bg-12-163-2015

Yu, K., Leufen, G., Hunsche, M., Noga, G., Chen, X., Bareth, G., 2013a. Investigation of leaf diseases and estimation of chlorophyll concentration in seven barley varieties using fluorescence and hyperspectral indices. Remote Sens. 6, 64–86. doi:10.3390/rs6010064

Yu, K., Li, F., Gnyp, M.L., Miao, Y., Bareth, G., Chen, X., 2013b. Remotely detecting canopy nitrogen concentration and uptake of paddy rice in the Northeast China Plain. ISPRS J. Photogramm. Remote Sens. 78, 102–115. doi:10.1016/j.isprsjprs.2013.01.008

Yu, W., 2004. Practical anti-vignetting methods for digital cameras. IEEE Trans. Consum. Electron. 50, 975–983. doi:10.1109/TCE.2004.1362487

Zarco-Tejada, P.J., Berjon, A., Lopezlozano, R., Miller, J., Martin, P., Cachorro, V., Gonzalez, M., Defrutos, A., 2005. Assessing vineyard condition with hyperspectral indices: Leaf and canopy reflectance simulation in a row-structured discontinuous canopy. Remote Sens. Environ. 99, 271–287. doi:10.1016/j.rse.2005.09.002

Zarco-Tejada, P.J., Diaz-Varela, R., Angileri, V., Loudjani, P., 2014. Tree height quantification using very high resolution imagery acquired from an unmanned aerial vehicle (UAV) and automatic 3D photo-reconstruction methods. Eur. J. Agron. 55, 89–99. doi:10.1016/j.eja.2014.01.004

Zarco-Tejada, P.J., González-Dugo, V., Berni, J.A.J., 2012. Fluorescence, temperature and narrow-band indices acquired from a UAV platform for water stress detection using a micro-hyperspectral imager and a thermal camera. Remote Sens. Environ. 117, 322–337. doi:10.1016/j.rse.2011.10.007

4. MULTI-TEMPORAL MONITORING OF AGRICULTURAL CROPS WITH HIGH-RESOLUTION 3D HYPERSPECTRAL DIGITAL SURFACE MODELS IN COMPARISON WITH GROUND OBSERVATIONS

HELGE AASEN [1,], ANDREAS BOLTEN [1]*

Under review: Remote Sensing of Environment

DOI: N.A.

Formatting and orthography of the manuscript is adapted to the dissertation style.

[1] University of Cologne, Department of Geoscience, Institute of Geography, GIS and RS Research Group, 50923 Cologne, Germany (helge.aasen, andreas.bolten@uni-koeln.de)

* Corresponding author: Tel.: +49 221 470 6265; Email: helge.aasen@uni-koeln.de

Abstract: In order to reduce the unsustainable use of resources in agricultural areas while keeping up with global demand for food, timely and high-resolution remote sensing data is needed. In this context, unmanned aerial vehicles (UAVs) with specialized sensors become powerful sensing systems. This study evaluates novel high-resolution hyperspectral digital surface models (HS DSMs) derived from UAV snapshot cameras for the multi-temporal acquisition of crops growth on canopy scale. HS DSMs are a representation of the surface in 3D space linked with hyperspectral information emitted and reflected by the objects covered by the surface.

To investigate their potential for multi-temporal monitoring of agricultural crops, four field campaigns were carried out under different illumination conditions at a barley experiment with different cultivars and nitrogen fertilizer treatments during the 2014 growing season. Chlorophyll was estimated from the spectral HS DSM data by means of vegetation indices. In the heading and development of fruit stage and across several growth stages, good agreements were found with destructive laboratory measurements ($R^2 = 0.50 – 0.64$). At the same time, significantly different correlations were found with estimations from field-spectrometer measurements.

Thus, the special properties of the hyperspectral information within HS DSMs are investigated with an emphasis on the theoretical description and quantitative approximation of systematic differences resulting from the different measurement extents, directional reflectance effects and data processing schemes of imaging and non-imaging data. In this context, the concept of a specific field of view is introduced as a composition of pixels used to characterize a specific area of interest within a scene. Additionally, the impact of the illumination conditions during the radiometric in-field calibration is estimated.

The different measurement extent and angular properties accounted for up to 33% of the difference between the spectral imaging and non-imaging measurements. The results of the different processing schemes for the spectral imaging data differed by up to 29%. The radiometric calibration of the spectral data showed a significant impact of up to 14%, depending on the calibration procedure and illumination conditions.

Besides challenges in the multi-temporal retrieval of the 3D information in conjunction with image overlap, ground control point placement and spatial coverage are highlighted. The comparison of the 3D information with manually measured plant heights showed good correspondence for most of the individual dates and across several growth stages (R^2 = 0.45, 0.70 – 0.98).

Keywords: specific field of view, unmanned aerial vehicle (UAV), precision agriculture, BRDF, angular properties, field-spectroscopy, imaging spectroscopy, low-altitude remote sensing, radiometric calibration, mosaicking, plant height, chlorophyll, canopy scale

4.1 Introduction

In recent decades, the vegetated environment has changed its appearance. Today, croplands and pastures cover about 40% of the land surface (Foley, 2005). Since the human population and its food consumption is increasing, agricultural production needs to be roughly doubled by 2050 (Ray et al., 2013). However, extending agricultural areas has far-reaching effects on the ecosystem (Foley, 2005) and much of the remaining land is unsuitable for agricultural production (Ellis et al., 2010). Thus, agricultural production needs to intensify while reducing the unsustainable use of resources (Foley et al., 2011).

One approach is to use in-time knowledge to optimize management decisions about where, when and how much action to take (Mulla, 2013). In this context, remote sensing can provide timely and accurate information about vegetation status and stress (Atzberger, 2013). An additional approach is to breed cultivars which show strong resilience against biotic and abiotic stresses and maximize yield per unit of resource use (Araus and Cairns, 2014; Rascher et al., 2011). Both approaches benefit from high spatial resolution data to identify plant traits in the field. The timeliness and precision required in these agricultural applications make them an ideal field to evaluate remote sensing techniques for frequent high-resolution environmental monitoring approaches.

In recent years, unmanned aerial vehicles (UAVs) have become an increasingly used platform for photogrammetry and remote sensing (Colomina and Molina, 2014; Pajares, 2015). Particularly when combined with specialized sensors, they become powerful sensing systems for gathering up-to-date information about vegetation. Their low flying altitude allows them to capture data in very high spatial

resolution. The advent of small and lightweight sensors has boosted this development as demonstrated by several studies: metrics from dense point clouds have been used to estimate tree height and biomass (Dandois and Ellis, 2010; Jaakkola et al., 2010; Puliti et al., 2015; Zarco-Tejada et al., 2014) or pruning (Wallace et al., 2014) in forest environments but also to monitor microtopography of Antarctic moss beds (Lucieer et al., 2014b). For precision agriculture applications, crop growth has been monitored with high-resolution canopy height models to estimate crop biomass (Bendig et al., 2014) and yield (Geipel et al., 2014). High-resolution spectral data has been used to detect biotic (Calderón et al., 2013; Näsi et al., 2015) and abiotic stress (Malenovský et al., 2015; Zarco-Tejada et al., 2012), chlorophyll content (Berni et al., 2009; Elarab et al., 2015), biomass (Honkavaara et al., 2013) and nitrogen uptake (Quemada et al., 2014). However, until recently spectral and 3D spatial data needed to be acquired separately.

Lightweight hyperspectral (HS) snapshot cameras have overcome this limitation. They distinguish themselves from other spectral sensors by recording a two-dimensional hyperspectral image cube within a single exposure and thus without any scanning process. With recent photogrammetric algorithms based on structure from motion (SfM) the 3D geometry of a scene can be reconstructed from 2D images as long as the scene shows sufficient texture and the images are recorded with a sufficient overlap (Remondino and El-Hakim, 2006; Szeliski, 2011). Aasen et al. (2015) adapted this technique for hyperspectral snapshot cameras and introduced a method to derive hyperspectral digital surface models (HS DSMs), a representation of the surface in 3D space linked with HS information emitted and reflected by the objects covered by this surface. With this method, HS and 3D information can now be derived at the same time with only one camera system. This allows new analysis approaches which combine spatial and spectral data (Marshall and Thenkabail, 2015; Tilly et al., 2015).

Although HS imaging data is becoming more and more common, non-imaging devices such as field-spectrometers are still widely used at ground level (Milton et al., 2009). They have a long history in crop characterization (Mulla, 2013; Thenkabail et al., 2012). To name just a few examples, HS data can help estimate biophysical plant parameters such as biomass (Aasen et al., 2014; Gnyp et al., 2013; Hansen and Schjoerring, 2003; Marshall and Thenkabail, 2015), LAI (Haboudane et al., 2004), and biochemical parameters such as chlorophyll (Gitelson and Merzlyak, 1994; Haboudane et al., 2002; Yu et al., 2014).

However, vegetated areas are anisotropic surfaces. Thus, differences in the field of view (FOV), sensor to canopy distance and viewing geometry have an influence on the apparent reflectance derived by a sensor (Zhao et al., 2015). Additionally, the interaction between the sun's position and sensor orientation introduces directional effects which influence the reflectance perceived by a sensor

(Burkart et al., 2015; Schaepman-Strub et al., 2006; Verrelst et al., 2008). Therefore the question arises of how non-imaging ground observations compare to imaging data. Only a few studies have included such a comparison for vegetated areas (Bareth et al., 2015; von Bueren et al., 2015). However, the appearance of crop canopies become increasingly complex with smaller pixel sizes (Damm et al., 2015).This becomes even more important with the recent advent of low-flying sensing systems capable of collecting very high-resolution data. Moreover, low flying altitudes require wider FOVs to cover the same area. Therefore, the variety of viewing geometries within a scene also increases.

So far, no study has evaluated HS DSM containing 3D and HS information derived from a single sensor for frequent crop monitoring. Moreover, multi-temporal studies that investigate and explain differences of these novel data products with ground-based measurement approaches do not exist. However, with the tremendous potential and increasing use of novel snapshot cameras onboard UAVs, both topics are highly relevant for the field of remote sensing. Thus in this study high-resolution HS DSMs derived from UAV snapshot cameras are evaluated as an innovative approach to monitor agricultural crops in comparison with established in-field observations. Within the multi-temporal setting of this study, significant differences become apparent. For the spectral data, the common theory for imaging spectroscopy is advanced by the specific field of view (SFOV) to describe important data properties of HS DSMs. In comparison to field-spectrometer measurements, the influence of the different measurement extents and angular properties within the data are discussed. Additionally, the influence of two different processing schemes and the radiometric calibration are investigated. The influence of the differences on biochemical parameter retrieval is demonstrated by estimating chlorophyll by means of vegetation indices (VIs). For the 3D data, challenges in conjunction with image overlap, ground control point placement and spatial coverage and their implications for multi-temporal parameter retrieval are investigated. As an example, plant height data is estimated from the 3D data.

4.2 Materials and methods

4.2.1 Field experiment

The field campaigns were carried out on a barley experiment at the University of Bonn's research station, Campus Klein-Altendorf (50°37,51' N; 6°59,32' E), within the CROP.SENSe.net project (www.cropsense.uni-bonn.de/) in 2014. In total, nine varieties of barley were cultivated with two nitrogen treatments (40 kg/ha, 80 kg/ha) three times. In this study, six different varieties in 32 plots were considered. The size of each experimental plot was 3 x 7 m. Each plot was divided into two parts: in one part, destructive measurements of biomass and chlorophyll were carried out. In the remaining part, non-destructive remote sensing measurements were taken. To exclude border effects and tractor tracks a 0.8 m distance to the plot border was kept. The plots were separated by paths of bare soil for

management purposes. Within these paths ground control points (GCPs) were placed as references and measured with a differential GPS (TOPCON Hiper Pro, www.topcon.eu) with a precision of approximately 1 cm. Figure 4.1 shows the layout of the field experiment.

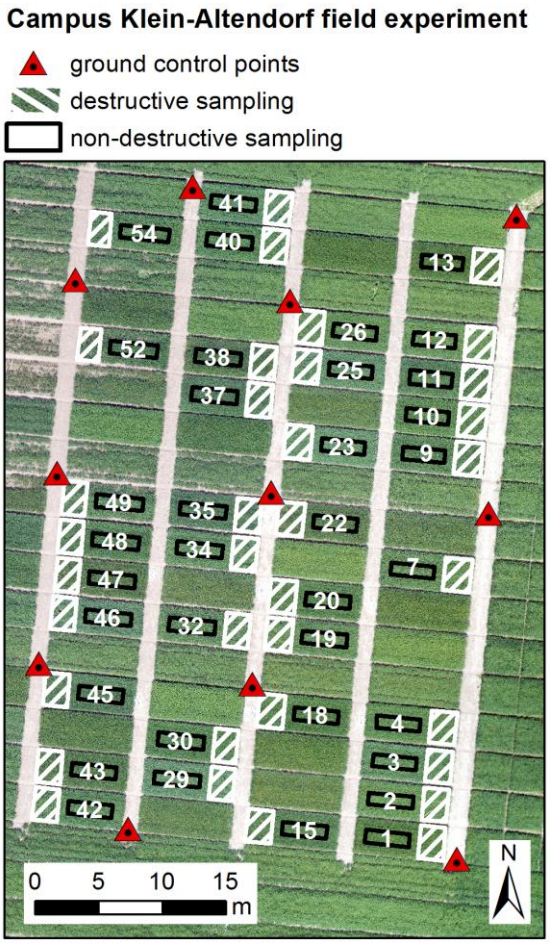

Figure 4.1 RGB orthomosaic of the field experiment at 70 days after seeding. The black squares represent the non-destructive measurement parts while the white squares represent the destructive sampling parts. Unmarked plots were not measured by the ground-based measurements.

4.2.2 Field-spectrometer data collection and processing

The FieldSpec3 (FS3; ASD Inc., www.asdi.com) is a field-spectrometer with a spectral range of 350 to 2500 nm with a FWHM of 3 nm (VNIR) to 10 nm (SWIR). The spectra are resampled to 1 nm resolution by the software of the manufacturer. Each measurement spatially integrates one spectrum for the entire FOV. The FS3 was used without a fore optic resulting in a FOV of 25°. Measurements with the FS3 were taken with a common measurement procedure including regular optimization and calibration with a white reference to adapt for illumination changes. For details, please refer to Tilly et al. (2015). Within each plot at six random positions, 10 measurements were taken. After the detector offset was corrected (Aasen et al., 2014) the measurements were averaged so that each plot was represented by one spectrum.

4.2.3 Hyperspectral digital surface generation

4.2.3.1 UAV sensing system

The UHD 185-Firefly (UHD; Cubert GmbH, www.cubert-gmbh.de) is a hyperspectral snapshot camera that records 138 spectral bands from 450 to 950 nm with a spatial resolution of 50 x 50 pixels within one integration. In total, 2500 spectra per band are recorded at the same time. The FWHM ranges from approximately 5 to 25 nm. Additionally, a grayscale image with 1000 x 990 pixels is recorded simultaneously to the hyperspectral image. The FOV of the camera is 20° across and along track. At 30 m above ground flying altitude, this results in a spatial ground resolution of the hyperspectral information of approximately 20 cm and 1 cm for the grayscale image. The instantaneous field of view (IFOV) for every pixel is approximately 0.4°. The camera is mounted on a gimbal (MK HiSight SLR2, www.mikrokopter.de), which compensates for pitch and roll movement and therefore ensures a nadir orientation of the camera. A single board computer controls the camera and records the data. The camera and single board computer are carried on a multirotor UAV (MK OktoXL 2, www.mikrokopter.de). For details on the image capturing system and the UAV please refer to Aasen et al. (2015).

4.2.3.2 Hyperspectral snapshot camera data processing

Before each flight, a reference image was taken by placing the camera and UAV above a white calibration panel (Zenith Lite). After dark current correction, this image was used to convert the raw digital numbers of each image taken during the flight to reflectance. This spectral information was merged with the high-resolution grayscale image into an image cube and information about the pixel position within the image was appended as introduced by Aasen et al. (2015). The individual image cubes were loaded into Photoscan (Professional Edition, version 1.1.6, www.agisoft.com) and processed with the typical workflow: after initial photo alignment, the scene was georeferenced by all GCPs visible in the scene and a dense point cloud (ultra-high) was created. At this stage, an HS dense point cloud was created. Thus, in contrast with traditional approaches, the HS and 3D information is linked inherently throughout the processing and no further post-processing is needed. The hyperspectral and 3D spatial was exported with a spatial resolution of 5 cm. The resulting HS DSM contained a representation of the 3D surface linked with hyperspectral information emitted and reflected by the objects covered by the surface (Aasen et al., 2015). Different blending modes exist in Photoscan, two of which are compared later (section 2.5.3.). For most of this study the blending mode ‘disabled’ was used. In total 294, 198, 353 and 335 images were processed for the campaigns at 56, 70,

84 and 96 days after seeding (DAS), respectively. The measurement parameters and conditions are summarized in Table 4.1.

Table 4.1 Summary of the dates with corresponding days after seeding (DAS), parameters and environmental conditions during the UHD campaigns. Additionally, the date of the field-spectrometer (FS3) measurements and plant parameter (PP) extraction are shown.

UHD	FS3	PP	DAS	growth stage	UHD weather	take off time	image count	sun elevation	sun azimuth
6-May	6-May	8-May	56	stem elongation	cloudy	10:30	294	40.62	117.1
20-May	22-May	22-May	70	booting	sunny	13:30	198	59.35	180.42
5-Jun	2-Jun	5-Jun	84	heading	sunny	12:50	353	60.56	160.57
12-Jun	18-Jun	17-Jun	96	development of fruit	sunny	12:30	335	59.97	150.41

4.2.4 Spectral data properties of hyperspectral digital surface models

The spectral data within HS DSMs have special properties. Compared to non-imaging sensors, the spatial extent and the angular properties of the measurements to characterize an area of interest (AOI) differ. Additionally, the data is influenced by the data processing workflow and the conditions during the radiometric calibration. To highlight the characteristics of hyperspectral data within HS DSMs, the overlying pattern of the difference with the ground-based field-spectrometer observations were evaluated per date and across the dates. For all plots of DAS 56 to 84, the measurements were averaged per date, and then compared by calculating the ratio of the field-spectrometer and HS DSM measurements. Additionally, the standard deviation of the differences between the HS DSM and field-spectrometer derived measurements was calculated for each date. DAS 96 was excluded, since the measurements were taken five days apart. In the following sections, the theoretical background for the discussion of the HS data properties is described and the comparison with ground-based field-spectrometer measurements is outlined.

4.2.4.1 Measurement extent

Imaging systems offer the opportunity to capture several hundreds to thousands of spectra of an AOI. Traditional measurement protocols designed for field-spectrometers use only a few measurements to characterize an AOI. Thus, the data processing schemes for both types of measurements differ. Field-

spectrometer measurements are usually taken at distinct places within an AOI. In this study, measurements were taken at six positions within each plot and then averaged to one spectrum. Since it was intended to estimate vegetation parameters, the measurements were taken at vegetated areas within the non-destructive measurement part of the plot. For the imaging data, the spectrum of each pixel within this part of the plot was extracted from the HS DSM and averaged to a spectrum.

4.2.4.2 Specific field of view

Vegetated areas are anisotropic surfaces. Depending on vegetation properties like leaf angle, leaf area and canopy structure and their interaction with the incident irradiance and illumination regime, light is heterogeneously reflected to the hemisphere. Most vegetated surfaces show a distinct backscatter in the direction of the incident light called the 'hotspot' and a decreased scattering with increasing distance to the incident angle. Thus, the apparent reflectance perceived by a sensing system is dependent on its position and orientation (Qi et al., 1995; Schaepman-Strub et al., 2006; Zhao et al., 2015). For imaging spectroscopy data this becomes even more complex, since the geometric sun-surface-sensor properties are unique for every pixel and depend on the IFOV of that specific pixel.

The conceptual framework used to describe these effects is the bidirectional reflectance distribution function. It describes the scattering of a parallel beam of incident light from one direction of the hemisphere to another and is expressed as the ratio of infinitesimal small quantities (Nicodemus et al., 1977). In remote sensing, the reflectance of a surface is commonly expressed as the ratio of the flux received within the conical (I)FOV of a sensor from the sampled surface and a lossless and Lambertian reference surface in the same beam geometry under natural illumination conditions. Thus, these measurements are precisely referred to as hemispherical conical reflectance factors (HCRF; Schaepman-Strub et al., 2006). This is particularly true for field-spectrometers with a rather wide FOV. The pixels of imaging spectrometers have rather small IFOV, which also results in a rather small measurement cone for each pixel. Therefore their measurements can be considered as an approximation of directional measurements (Schläpfer et al., 2015) and the resulting quantities as hemispherical directional reflectance factors (HDRF). Equation 4.1 gives the formula for the reflectance factor with θ as the zenith and ϕ as the azimuth angle of the incident (i) radiation over the hemisphere (2π) and reflected (r) radiation and the solid angle of the IFOV (ω_r), which for the HDRF case is set (close) to 0. For simplicity, the reflectance factors measured in this study are referred to as reflectance.

$$reflectance\ \ factor\text{:}\quad R(\theta_i, \phi_i, 2\pi, \theta_r, \phi_r, \omega_r) \qquad \text{(Eq. 4.1)}$$
$$HDRF\text{:}\quad \omega_r \approx 0$$

HS DSM are derived from multiple images. Within each of these images, each pixel contains a HDRF measurement with unique angular properties (Figure 4.2). Within an individual image, the angular properties can be calculated as long as the IFOV, the image orientation and position and the surface geometry are known. Within the HS DSM, the images are composed depending on the orientation and position of the individual images defined by the flight trajectory and the capturing position. Depending on the position of an AOI, its area within the HS DSM might be covered by several pixels eventually captured by different images. Thus, a spectrum to characterize this AOI is also composed from multiple pixels and their composition of angular properties. In the following, the composition of pixels and their angular properties within a scene used to characterize a specific AOI is called the specific FOV (SFOV). Figure 4.2 illustrates this concept. The area within the HS DSM is covered by two images. Within these images, each pixel has its own angular properties. Moreover, the same area might be covered by pixels from different images with different angular properties. Depending on the composition of the spectral information within the HS DSM, an AOI is characterized by the SFOV composed of pixels from several images.

With the pixel-tracing technique introduced by Aasen et al. (2015), the pixel position within an image can be traced to the composed HS DSM. This technique can be exploited to comprehend the SFOV of an AOI by extracting the position information of the pixels. Within this study, this information is exemplified by being plotted as a two dimensional histogram showing the distribution of pixel position within the SFOV of plot 4 at DAS 70. The difference between HS DSM derived data and non-imaging data is highlighted by comparing the SFOV with the FOV of the field-spectrometer.

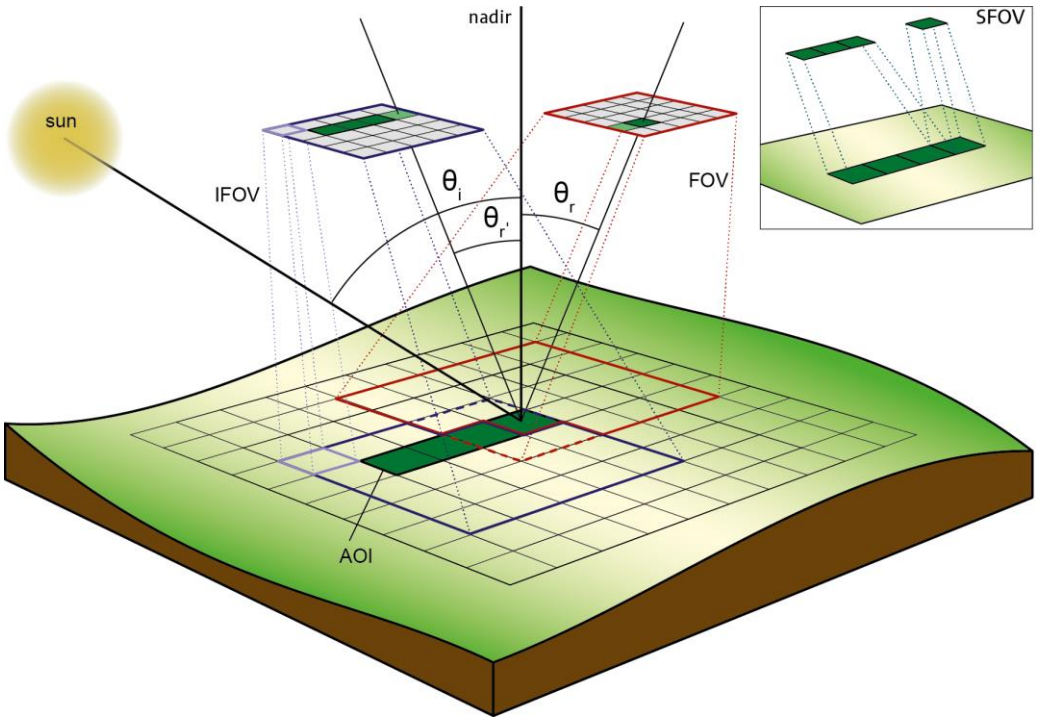

Figure 4.2 Schematic drawing of the concept of the specific field of view (SFOV) of an area of interest (AOI) within a hyperspectral digital surface model generated from snapshot cameras. Each pixel within an image is recorded with different angular properties. The same surface area may be captured by several pixels with different angular properties (as denoted by the zenith reflectance angles θ_r *and* θ_r' *for one pixel. For clarity, the azimuth angles are omitted). The SFOV describes the pixels and their angular properties which are used to characterize an AOI (excerpt top right). Additionally, the field of views (FOVs) of two images and an instantaneous field of view (IFOV) of one pixel is shown.*

4.2.4.3 Processing mode

The HS DSM is generated from multiple overlapping images. Agisoft Photoscan has different processing modes for the spectral information. These include ‘mosaicking’, ‘averaging’ and since version 1.1.3., a blending mode ‘disabled’ (Agisoft LLC, 2015, 2014). The first two modes influence the spectral information by applying a (weighted) average for the calculation of the pixels’ spectral information in the composed scene. In blending mode ‘disabled’, the spectral information is taken from the image whose center is closest to the pixel in the composed scene. Thus, the spectra are not modified and each pixel has the original spectral information. To investigate the influence of the processing mode the HS DSM is processed in blending mode ‘average’ and ‘disabled’ and the resulting hyperspectral information is compared pixel-wise by calculating the ratio of both data products.

4.2.4.4 Radiometric calibration

Due to a mechanical instability of our camera prototype and several maintenances during the year 2014, the camera could not be radiometrically calibrated in a general manner. Additionally, the camera has no irradiance sensor. Thus, a calibration procedure similar to field-spectrometer measurements was applied: before each flight the UHD was pointed towards a reference panel to measure the incoming irradiance. Then this measurement was used to transform the DN values to reflectance. However, this type of calibration is prone to errors. At DAS 56 a significant offset in reflectance was noticed compared to the other dates, which could not be explained by the plant growth. Since the sky was clouded on this date, the influence of the illumination conditions during the calibration was investigated.

To investigate the influence, the FS3 was mounted on a tripod 50 cm above a Zenith Lite calibration panel and the reflected radiation was measured. The UAV was then placed right above the downwards-facing fiber of the FS3 in a similar position as it would be during the in-field calibration and another measurement was taken. The difference represents the influence of the UAV on the radiation reflected from the panel. Accordingly, a sensing system mounted below the UAV will also perceive the influenced radiation instead of the real radiation. Consequently, a reference image taken under these conditions would influence all measurements.

To estimate the influence of the illumination conditions, the measurements were carried out under clear sky and cloudy conditions. In both cases, no direct shadow was cast on the reference panel. Additionally, under the clear sky conditions measurements were taken with the person holding the UAV in and perpendicular to the principle planeof the sun.

4.2.5 Multi-temporal chlorophyll retrieval

To evaluate the prediction of important plant parameters from HS DSMs, canopy chlorophyll was estimated with the widely used VIs TCARI/OSAVI (Haboudane et al., 2002), PRI (Gamon et al., 1992), REIP (Guyot and Baret, 1988) and ND705 (Gitelson and Merzlyak, 1994). For each date maps of the VIs were created. To compare the results to the destructively measured chlorophyll values, all pixels from the non-destructive part of the plot were averaged and a linear regression model was established for each individual date. Additionally, multi-date models were established for DAS 70 – 96 and 84 – 96. The results were compared to the FS3 measurements with the original FS3 data, since a convolution to the UHDs band configuration only showed very minor influence. Only plots which were entirely covered by the HS DSM were considered in the analysis.

4.2.6 Multi-temporal canopy height monitoring

4.2.6.1 Canopy height model generation

The height in the HS DSM represents the absolute height above the ellipsoid. The difference between the DSM and the digital terrain model (DTM), which is the height of the bare soil surface, represents the crop height. To calculate this height a DTM was generated from the non-vegetated paths between the experimental plots for each date: DTM extraction points were placed every 3 m and the height of a circle with a radius of 0.2 m around the points was averaged to minimize small scale differences of the bare soil. Based on these values a DTM was interpolated. From the DSM the generated DTM was subtracted. The result represents the average height of the plants within a pixel. This height will be referred to as canopy or crop height model (CHM). For each plot the average height of the CHM was extracted from the non-destructive measurement part of the plot with a margin of 0.8 m to the plot border to exclude influences of tractor tracks and border effects (Figure 4.3).

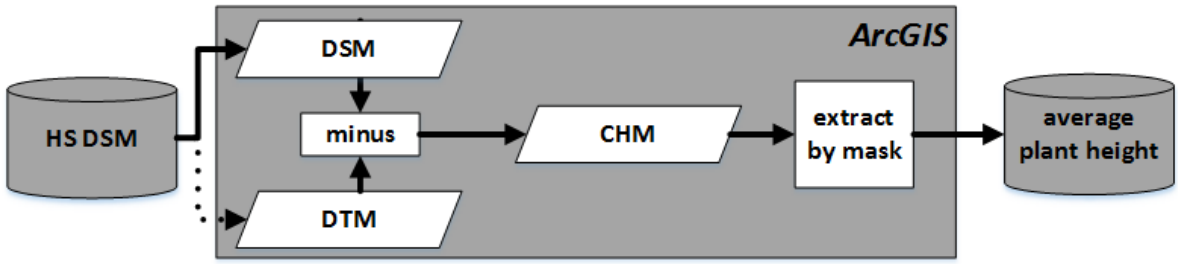

Figure 4.3 Plant height extraction from the hyperspectral digital surface model (HS DSM). A digital terrain model (DTM) is created and subtracted from the digital surface model. The result is a canopy height model (CHM).

Besides the image overlap, the number and placement of GCPs influences the quality of a surface derived from SfM (Harwin and Lucieer, 2012; Mesas-Carrascosa et al., 2015). DSM from SfM are prone to the 'bowl effect' which occurs when the area mapped exceeds the area surrounded by GCPs (Ouédraogo et al., 2014). In our dataset, only the HS DSMs of the first date covered the entire extent of the experimental area. For DAS 70 and DAS 84, the GCPs were missing on the east side of the covered area. To counteract the 'bowl effect', the DTMs were generated individually for each date. Also, plots that were not entirely covered by the generated DTM were excluded. For DAS 70, the most western row was excluded from the analysis as an additional case (DAS 70b), since this area had low image overlap in the HS DSM.

4.2.6.2 Plant height evaluation

The plant height derived from the HS DSM was compared to ruler measured plant heights. Within each plot, the height of ten individual plants was measured and the median was calculated. From the HS DSM the average height per plot was calculated. These estimates where compared for each date and across all dates.

4.3 Results and Discussion

4.3.1 Spectral data properties of HS DSMs

Figure 4.4 shows the ratio of the reflectance extracted from the HS DSM and the FS3 as an average of all plots for DAS 56, 70 and 84 and its standard deviation. Overall, the apparent reflectance of the UHD measurements is higher than for the FS3. For DAS 70 and 84 the ratio is within the same magnitude, while DAS 56 shows an overall higher ratio. All dates show a similar wavelength dependent pattern: in the blue (466 nm) the ratio is at 1.80, 1.37 and 1.55 for DAS 56, 70 and 84, respectively. Towards the green (550 nm) the ratio decreases to 1.39, 1.10 and 1.05. Towards the red (670 nm) the ratio increases to 1.89, 1.29 and 1.33. In the NIR (798 nm) the ratio decreases again to 1.28, 1.03 and 0.92. The standard deviation decreases from DAS 56 to DAS 84.

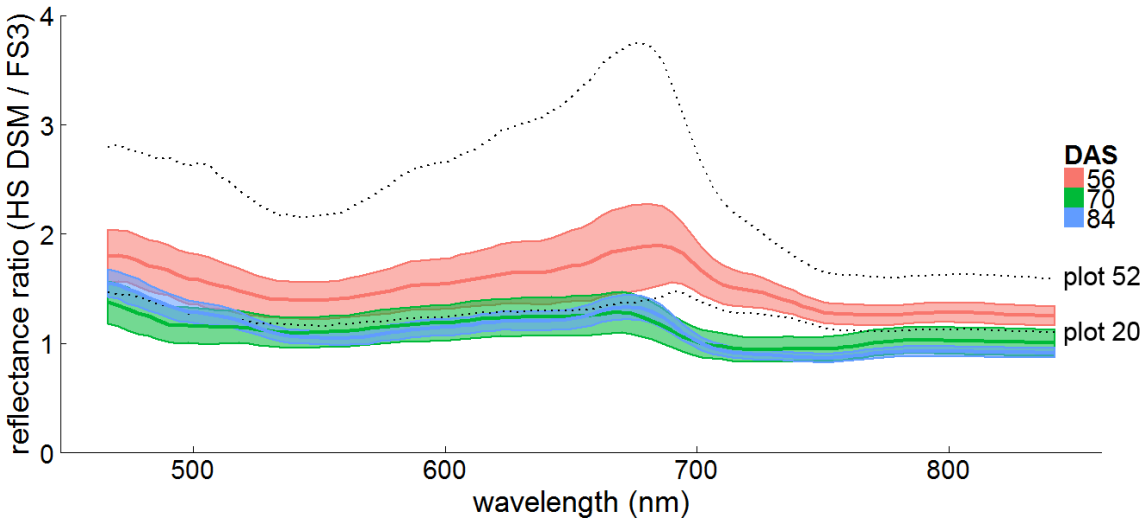

Figure 4.4 Ratio of the reflectance retrieved from the HS DSM and the FS3 averaged over all plots for DAS 56, 70 and 84 (solid line) with standard deviation (ribbon). Additionally, the ratio of plot 52 (upper black dotted line) and plot 20 (lower black dotted line) at DAS 56 is shown.

Three reasons could be identified for these differences: the different measurement extent of the imaging and non-imaging device, the angular properties of the pixels within the measured area and the illumination conditions during the calibration. Additionally, the different spectral data processing schemes for the HS DSM data have an impact on the final data product. These aspects and their

implications for the difference between the HS DSM and field-spectrometer are discussed in the following.

4.3.1.1 Measurement extent

Figure 4.4 shows the ratio of the highest difference (plot 52) and the lowest difference (plot 20) of the imaging and non-imaging data of DAS 56. These two plots are shown in Figure 4.5. The measurement extent of the UHD is framed in black. Additionally, six exemplary measurement positions of the FS3 and their extent are shown for plot 52.

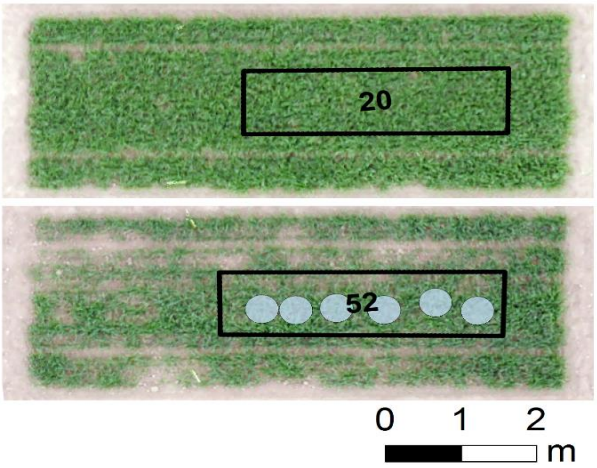

Figure 4.5 RGB image of plot 20 and 52 at DAS 56. The black frame marks the area measured within the HS DSM. The blue circles exemplary show six measurement positions of the FS3 within one plot.

Within plot 52 several patches of bare soil are visible. On the other hand, plot 20 shows an almost homogenous growth and almost closed canopy. Since the spectral information is extracted from the entire measurement area within the HS DSM, it contains more soil areas than the FS3 spectra for plot 52. In plot 20, this is not the case due to the homogeneous growth within the plot. The comparison of the ratio functions for plot 20 and 52 reveal that the HS DSM spectrum of plot 52 is significantly more increased in comparison to the FS3 spectrum. In particular, in the VIS, a very high difference can be seen (Figure 4.4). This is explained by the higher reflectance of soil compared to vegetation in the VIS and lower reflectance in the NIR which influences the HS DSM derived data more than the FS3 measurements. For the averaged spectra, the standard deviation of the difference between the HS DSM and FS3 observations at DAS 56 is higher compared to the other dates. At the later dates, the canopy was closed and the heterogeneity within the plots was reduced. Thus, the standard deviation decreased for DAS 70 and 84.

4.3.1.2 Specific field of view

The ratios between the FS3 and HS DSM derived measurements show a wavelength dependent pattern (Figure 4.4). Both devices have a similar FOV. The FS3 has a circular FOV of approximately 25° while the UHD has rectangular FOV of about 20°. Thus, applied from the same height both instruments cover a similar area. Additionally, if all pixels of the UHD would be averaged, the integration of solid angles of the IFOVs would compose a SFOV similar to the FS3 and therefore the angular properties of the resulting spectra would be similar too. When the UHD is applied on a UAV, the footprint increases with increasing flying altitude. Additionally, the spectrum for a specific area is extracted from the HS DSM, which is composed of multiple images (c.f. section 4.2.4.2). Thus, the angular properties of the SFOV characterize an AOI change too.

Figure 4.6 shows the theoretical across track FOV of the UHD (orange) and FS3 (gray). The FS3 averages the spectral signature of all objects within its circular 25° FOV almost equally by its design (Mac Arthur et al., 2012). The FOV of the UHD is composed by the individual IFOVs of every pixel. During the processing of the HS DSM only pixels from a few location are used to compose the scene. Moreover, the placement of the AOI within the scene defines the SFOV and consequently, also the pixels which are used to spectrally characterize the area. Figure 4.6 (right) shows the number of pixels from each pixel position within the SFOV, which was used to generate the spectrum of plot 4 at DAS 70 from the HS DSM. The purple sections in Figure 4.6 (left) show the resulting section of the along track FOV of the UHD which was used for the area of plot 4. Evidently, just a very small part of the entire FOV is used. As a result the angular properties of the spectrum derived from the FS3 and the HS DSM differ

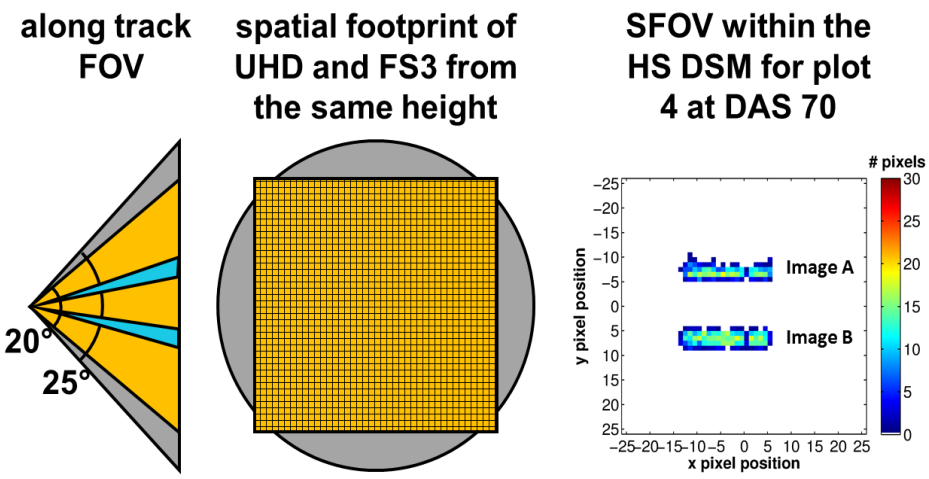

Figure 4.6 Comparison of the 25° FOV of the FS3 (gray) and 20° of the UHD (orange) and their footprint from the same height (left and center). For plot 4 at DAS 70 the specific field of view (SFOV) within the hyperspectral digital surface model is shown (right). The plot is characterized by spectral information from two images (image A and B). The colors indicate how many pixels are taken from a particular position within the images. Additionally, the resulting along-track SFOV is shown in light blue (left).

strongly. In Figure 4.4 it is apparent that the ratio of the HS DSM and FS3 derived spectra is wavelength dependent. The different viewing geometries and their interaction with the sun position, plant structure and the resulting visible features (e.g. soil and green vegetation) have a strong wavelength dependent influence on the apparent spectrum (Burkart et al., 2015; Schaepman-Strub et al., 2006; Verrelst et al., 2008; Zhao et al., 2015). Additionally, they can be very pronounced for certain geometric settings (Küster et al., 2014) and are stronger in the VIS than in the NIR (Burkart et al., 2015; Küster et al., 2014). Due to the integrated FOV of the FS3 some of these effects are averaged. On the contrary, the very narrow SFOV used to derive the spectra from the HS DSM (SFOV) does not average over a wide variety of geometric settings. Mostly, the geometry of the spectral information in the HS DSM is closer to nadir than the integrated information of the FS3 (Figure 4.6, left). Depending on the sun's position and the structural properties of the canopy, this can result in higher or lower apparent reflectance. In this study, most plots have higher apparent reflectance in the HS DSM measurement than in the FS3 measurement. This can be explained since the spectral information within the HS DSM is measured closer to the principle plane and the 'hotspot' of the vegetation in comparison to the information integrated over the wide FOV of the FS3. Additionally, the different angular settings become apparent in the shape of the ratio between the measurements of the two instruments, which are similar to anisotropy factors measured in another studies over wheat (Burkart et al., 2015).

These differences must be kept in mind when data from different sensors are compared. This needs to be considered especially for low-flying imaging systems, since the variety of angular properties within an AOI is considerably increased compared to high-flying platforms. It has also been shown that angular effects influence the retrieval of vegetation properties (Burkart et al., 2015; Verrelst et al., 2008). In general, it can be assumed that an integration over a wider FOV or SFOV is more robust against angular effects (Zhao et al., 2015). On the other hand, well-defined angular properties offer the opportunity to derive additional information about the surface (Schaepman, 2007). In particular, when snapshot cameras capture overlapping images to derive HS DSMs, the same area is measured from multiple positions. Thus, snapshot cameras provide an optimal tool for the derivation of multi-angular properties (Aasen, in review; Hakala et al., 2010; Honkavaara et al., 2014; Koukal et al., 2014). Future studies should exploit this opportunity. At the same time, the gained understanding should be used to further develop and adapt existing methods for the correction of angular effects (e.g. Schlapfer et al., 2015). This is especially important, since high-resolution data increase the apparent heterogeneity of a surface (Damm et al., 2015). In the future, the high-resolution 3D information contained in HS DSMs could support the correction.

4.3.1.3 Processing mode

The spectral data of an HS DSM is composed depending on the processing mode, which is chosen within the photogrammetric software. In the blending mode 'average', all available information from all overlapping images is averaged to one spectral signature per pixel. Consequently, pixels with different angular properties are averaged to produce the pixels in the HS DSM. On the contrary, in the blending mode 'disabled' only the information from one image is taken per pixel in the HS DSM. Figure 4.7 (right) shows the relative difference of the reflectance at 670 nm at a part of the scene at DAS 70 between the processing with blending mode 'average' and 'disabled'. Ratios above 1 represent values, where the averaged reflectance is lower than the one in disabled mode. Additionally, the pixel position as a distance in x- and y-directing from the image center in the original images is shown (Figure 4.7 center and right).

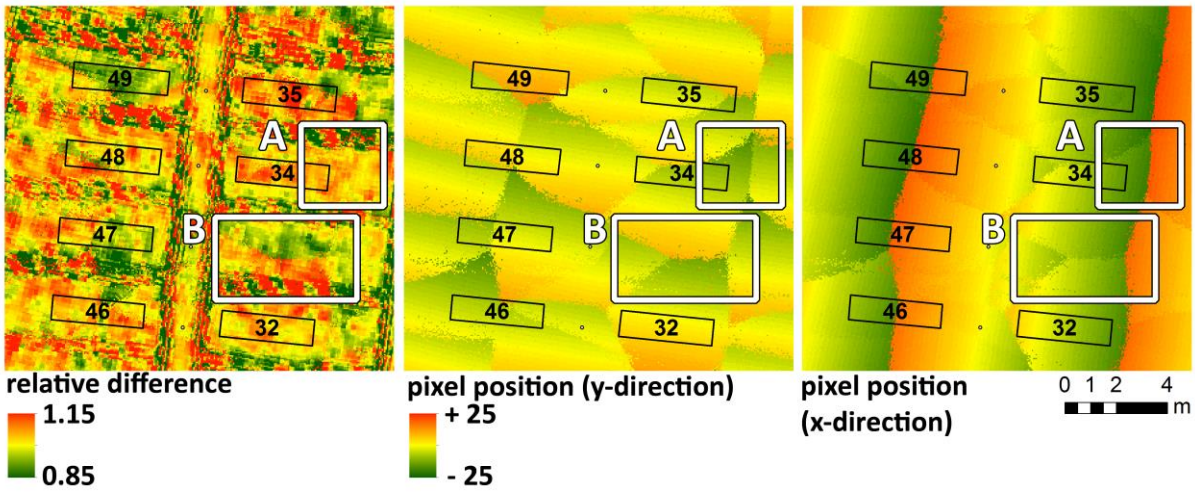

Figure 4.7 Relative difference between blending mode 'average' and 'disabled' of spectral data at 670 nm (left), and pixel position as distance from the image center in the original images in the y- (center) and x-direction (right).

In the entire scene the ratios for individual pixels range from 0.74 to 1.29, while for the shown part the ratios range from 0.85 to 1.15. Within the shown part different patterns can be identified. Within area B an edge of the ratios can be seen in the west-east direction. To the north of this edge the averaged scene shows higher reflectance than the unmodified spectra. Below the edge it is vice versa. These edges align with the transition from one image to another in the y-direction. To the right in area B, a difference in reflectance can be seen at the north-south aligned transition of the images. Here, the pixels on both sides of the transition originate from different pixel positions in the y-direction. Also, area A contains an image transition in the north-south direction, but the apparent reflectance is hardly influenced. The pixel positions show that the position in the y-direction is similar for the images on both sides of the transition.

Although differences are clearly visible between the processing modes, their interpretation is not trivial since angular effects, the structure of the canopy, and the image composition interact. During the flight at DAS 70, the sun had an elevation of approximately 59° and an azimuth angle of 180°. Therefore pixels with a lower pixel position value in the y-direction were captured with a more acute sun angle, closer to the reflection hotspot, resulting in higher reflectance than pixels with a higher pixel position value. On the other hand, the images were approximately aligned with the solar principle plane in the along track direction. Thus, the x-pixel position did not strongly influence the apparent reflectance. These observations align with the theory (Schaepman-Strub et al., 2006), models (Küster et al., 2014) and other measurements of angular effects of vegetation (Burkart et al., 2015).

Both methods have their advantages and drawbacks. While averaging spectral information derived from multiple images and thus with multiple angular properties might approximate an HCRF measurement similar to field-spectrometer measurements, it introduces additional uncertainty as long as it is not possible to trace which parts of which images were overlapping, respectively averaged. Although an approximately uniform flying speed and an along track image overlap of about four images can be assumed (c.f. Figure 4.10 A), it is not guaranteed that similar parts overlapped for all areas of the scene. Additionally, the across track overlap varied significantly. However, without blending stronger angular effects are apparent in the composed scene and might influence the results of retrieval methods. At the same time, they can be traced and included into the analysis.

These results demonstrate the significant impact of the processing mode and viewing geometries on the final data product. Currently, illumination differences resulting from different viewing geometries within an image mosaic are often ignored (Koukal et al., 2014). However, in an applied scenario the UAV trajectory might differ from flight to flight due to wind or other navigational uncertainties. Environmental effects such as the position of the sun might also vary between observations. Thus, in future pixel wise information about the angular properties, the signal quality and the environmental conditions during the acquisition should be incorporated as a standard in the metadata for scientific grade remote sensing data independent from the sensing system.

4.3.1.4 Radiometric calibration conditions

The reflectance at DAS 56 within the HS DSM showed an overall increase in reflectance compared to the field-spectrometer measurements. This difference could not solely be explained by the combination of the different measurement extents and the angular properties. Figure 4.8 shows the reflection of the reference panel under clouded and clear sky conditions when the UAV is held above the panel from a person standing within and perpendicular to the principle plane of the sun.

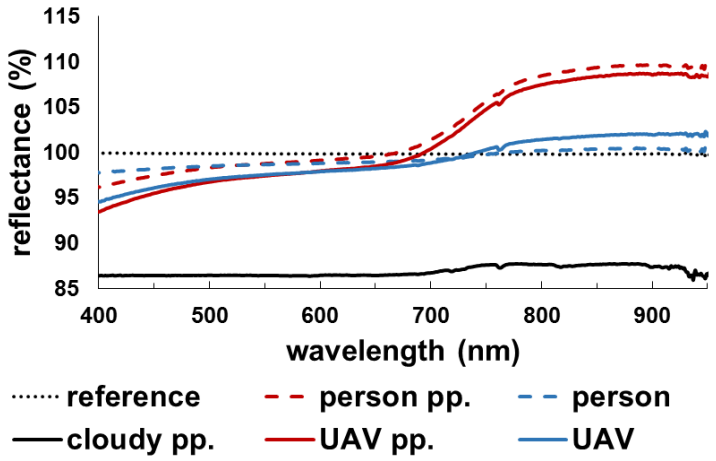

Figure 4.8 Measurements of a Zenith Light reference panel under clear sky conditions (reference), with a person behind the panel in the principle plane (person pp.), person perpendicular to the principle plane (person), with a UAV above the panel held by a person within the principle plane (UAV pp.) and a UAV held from a person perpendicular to the principle plane (UAV). Additionally, a measurement under cloudy conditions with a UAV held by a person within the principle plane relative to a measurement under cloudy conditions without obstacles (cloudy pp.).

The largest difference was introduced by the cloud cover. Under cloudy conditions, the reflectance of the panel was reduced by about 14% reflectance. Depending on the cloud cover and the distance of the panel to the UAV, this value changed (not shown here). Clouds change the illumination regime from a mostly directed illumination under sunny to diffuse illumination conditions, where light is irradiated approximately homogeneously from the whole hemisphere. When a UAV and a person holding the UAV cover large parts of the hemisphere, the illumination of the panel is significantly reduced.

The second largest influence was introduced by the position of the person who is holding the UAV. When the person holding the UAV was standing within the principle plane the reflection in the VIS was decreased by up to 4% (at 466 nm). In the NIR, the reflectance was increased by 8.5%. When the person was standing perpendicular to the principle plane, the influence was significantly reduced in the NIR to an increase of only 1.9% compared to the case without obstacles. In the VIS it was slightly reduced to 3.4%. The presence of the UAV only changed the influence slightly. When the person was standing in the principle plane, the UAV even reduced the difference to the pure reflectance of the reference panel. Similar to the clouded case, the decrease in the VIS can be attributed to the covering of the hemisphere. Since the hemisphere mostly scatters blue light under clear sky conditions, the decrease was most pronounced in this region. As the UAV increased the covered area, the influence was increased. In the NIR, the person and the UAV were scattering light back on the panel. Thus at about 670 nm the reflectance increased. The slight difference of about 1% in the NIR between the case with and without the UAV is most likely explained due to slight differences in the distance to the panel.

Similar results were found by Kimes et al. (1983), who reported errors from 2 to 18% in field-spectrometer measurements depending on the distance and position of a person close to a reference and the color of the clothing worn by the operator.

These results have a great implication for the data quality. Since the measurement of the reference panel is used to transform all image cubes to reflectance, errors will propagate into every measurement. Worse, this error cannot be quantified afterwards. Therefore data calibrated with this approach cannot be directly compared to data captured under different illumination conditions. Although this is particularly true for UAVs or other bulky sensing systems, this might also affect other sensing systems like field-spectrometers, which are calibrated in the same way. Thus, this calibration method should be avoided in the future. For UAVs, robust methods based on laboratory calibrations, characterized ground targets (Lucieer et al., 2014a), and the ability to adapt to changing illumination conditions are necessary to derive more robust scientific grade data. This is particularly important when multi-temporal surveys under different illumination conditions are carried out. However, sensing systems are needed which can record the incident radiation.

4.3.2 Multi-temporal chlorophyll retrieval

Figure 4.9 shows maps of the REIP for DAS 56 to 96 calculated from the HS DSM. At DAS 56, very low REIP values are visible. This can be attributed to the cloud-influenced calibration at that date (c.f. section 2.5.4). The wavelength independent relative overestimation of the reflectance due to the calibration absolutely increases the reflectance in higher wavelengths more than in lower wavelengths. Thus, the slope between the red and NIR increases and the REIP decreases. Still, as for all dates, differences between different cultivars and fertilizer levels and within plots can be seen. For DAS 70 to 96, the differences between the cultivars become more pronounced. Additionally, in some plots the positions of the destructive measurements from the previous dates can be identified (e.g. plot 9). As was already seen in Figure 4.5, the sparse growth around plot 52 can be identified which indicates heterogeneity not introduced by the cultivar but by the management or soil conditions. In DAS 96, the lodging of some plots is visible, similar to within canopy surface models. In DAS 84, the influence of the transition of the images of two flight lines can be seen in the second row from the west, while most other transitions are not as obvious. Here, the images are shifted for about half an image in the y-direction. Thus, the different angular properties become visible (c.f. section 4.3.1.2 and 4.3.1.3) and influence the VI.

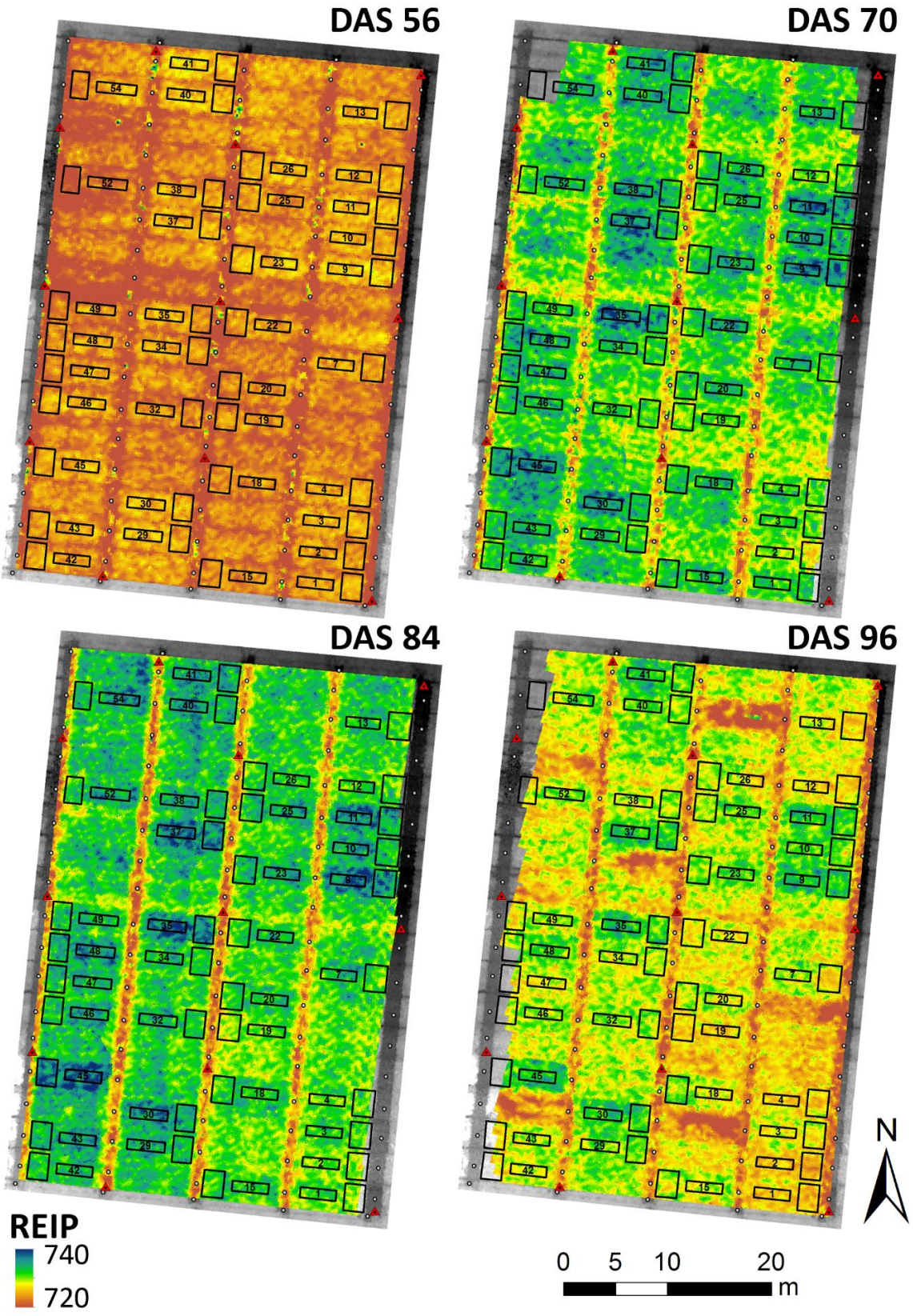

Figure 4.9 Maps of the red-edge inflection point (REIP) derived from the hyperspectral digital surface model of DAS 56, 70, 84 and 96. Please note that the data for DAS 56 is biased by the calibration under cloudy conditions (c.f. section 3.1.4).

In Table 4.2 the coefficient of determination for the estimation of chlorophyll with different VIs from the data of the HS DSM and the FS3 is shown. For DAS 56 and 70, low R^2 were found for both the UHD and the FS3 data. Besides the biased calibration of the UHD, this could be caused by the different illumination conditions at DAS 56, which also affects the retrieval of biophysical properties (Bartlett et al., 1998; Damm et al., 2015). For DAS 84, R^2 of about 0.50 were achieved with MCARI/ OSAVI for both the HS DSM and FS3 data. In DAS 96 and the combined data of DAS 70 – 96 and 84 – 96, the ND705 and REIP from the HS DSM data yielded R^2 between 0.50 and 0.64. The R^2 values were comparable to other studies for single and multi-temporal studies using VIs (Quemada et al., 2014; Yu et al., 2014).

The results from the FS3 and UHD data differed significantly in most cases. Apart from DAS 56, this can be attributed to the different properties resulting from the different measurement extents and angular properties of the spectral data produced by the two approaches (c.f. section 4.3.1). The results show that retrieval techniques as VIs are also influenced by these differences. While the angular sensitivity of VIs have been shown in other studies (Burkart et al., 2015; Verrelst et al., 2008), the influence of a composition of the angular properties has not been explicitly investigated. Interestingly, in most cases the VIs calculated with the HS DSM data performed better than the VIs calculated from the FS3 data. Originally, the REIP and MCARI/OSAVI were developed from modeled data. Although not clearly stated in the original papers (Guyot and Baret, 1988; Haboudane et al., 2002), the VIs might have been developed for a more directional nadir looking narrow FOV case. Thus, the angular properties present in HS DSMs might be better suited for parameter retrieval with those VIs. On the other hand, PRI550 was developed from the data of a spectrometer with a FOV of 15° (Gamon et al., 1992) and in most cases showed better performance for FS3 data. These results suggest that results obtained in one study cannot be transferred to other sensing systems per se. Consequently, more research is needed on the sensitivity of vegetation parameter retrieval techniques from data with different angular properties.

Table 4.2 Coefficients of determination (R^2) of different vegetation indices for the prediction of chlorophyll for the individual dates and across the DAS 70 – 96 and 84 – 96 from the HS DSM and FS3 data.

DAS		**56**	**70**	**84**	**96**	**70 - 96**	**84 - 96**
MCARI / OSAVI	HS DSM	0.07	0.08	0.50	0.37	0.48	0.57
	FS3	0.03	0.28	0.49	0.22	0.35	0.42
ND705	HS DSM	0.04	0.01	0.39	0.60	0.50	0.60
	FS3	0.06	0.12	0.16	0.36	0.39	0.42
PRI550	HS DSM	0.30	0.12	0.11	0.14	0.05	0.23
	FS3	0.10	0.34	0.30	0.31	0.24	0.38
REIP	HS DSM	0.18	0.13	0.44	0.60	0.55	0.64
	FS3	0.13	0.27	0.25	0.49	0.49	0.51

4.3.3 Multi-temporal canopy height monitoring

4.3.3.1 Canopy height model generation

Figure 4.10 shows the evolution of the CSM for DAS 70. Figure 4.10 A) indicates the image overlap of the image cubes captured by the UHD. The dots represent the image centers. Most of the area between the north-south orientated flight lines is well covered by multiple images. The parts at the north and the east side, where the flying speed of the UAV was lower, are very well covered. To the west and the east side the coverage decreases to only a few images. The images of the two most western flight lines only slightly overlap. Figure 4.10 B) shows the DSM created from the images. To the northeast corner of the scene, where the DSM is outside of the GCPs, the elevation decreases towards the edge of the scene. The same effect can also be seen at the center-west side of the scene. This tilting in a model derived from SfM has been referred to as the 'bowl-effect' and can also be seen in DTM extracted from the bare soil in Figure 4.10 C). Since the bare soil to the east side of the scene was not covered by the images, the DTM only extends to the second row from the east. Figure 4.10 D) shows the CHM created from the subtraction of the DTM from the DSM. The decrease towards the northeast corner of the scene is not visible in the CHM. Although not shown here, some small areas between the DTM extraction points showed negative values in the CHM mainly where the tractor tracks crossed the paths.

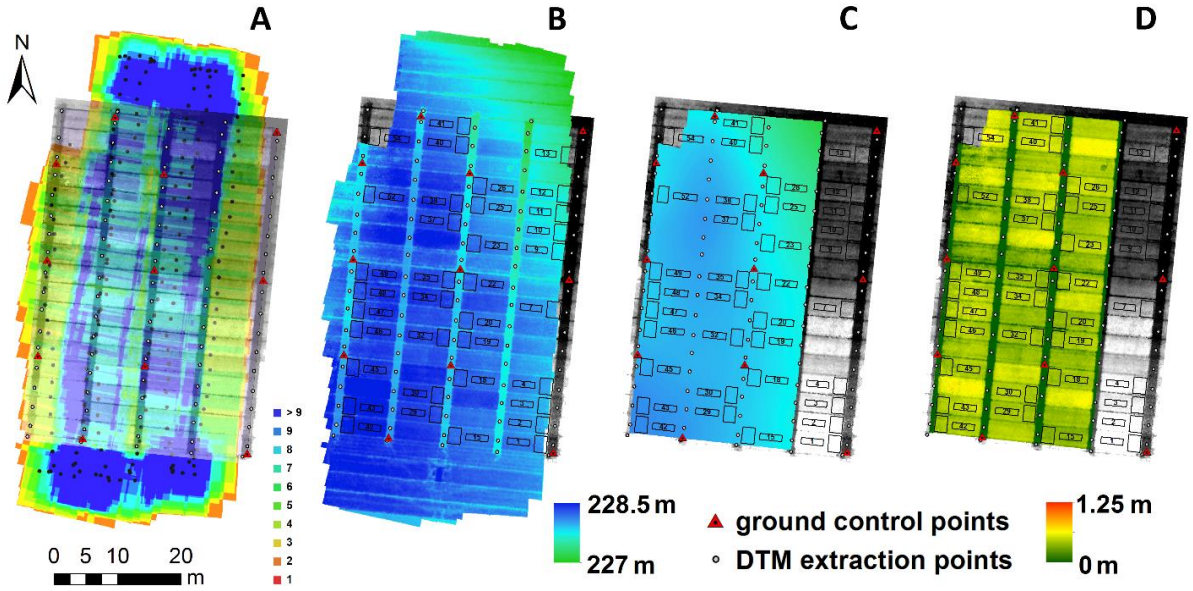

Figure 4.10 Evolution of the canopy surface model for DAS 70: A) Map of image overlap, B) digital surface model (DSM), C) digital terrain model (DTM) interpolated from the DTM extraction points, and D) canopy height model resulting from the substraction of DTM from the DSM. The DSM and DTM show the 'bowl-effect' outside the covered ground control points.

In other studies the DTM was created by surveying the area before the emergence of the plants (Bendig et al., 2014; Tilly et al., 2014). Due to the appearing 'bowl-effect' in some DSMs this approach was not feasible in our case. The 'bowl-effect' seems to result from the low image overlap in some of the scenes and the missing out of some GCPs, since other studies with a similar setting and more image overlap did not report this effect (Bendig et al., 2015, 2014; Geipel et al., 2014). This is also supported by the recommendations of the software manufacturer of 60% across and 80% along track overlap (Agisoft LLC, 2016). Currently, HS snapshot systems onboard UAVs still face the challenge of spectral resolution versus spatial resolution versus coverage (Aasen et al., 2015). The image acquisition of the image capturing system is rather slow (0.6 FPS), the field of view is small (20°) and the hyperspectral spatial resolution is low (50 x 50 px). Additionally, the weight of the image capturing system limits the flight time to under 30 minutes. Thus, to ensure the desired ground resolution of less than 20 cm for the hyperspectral information, an above-ground flying altitude of 30 m was chosen and the optimal overlap recommendations were violated to cover the whole AOI within the flight time. Although the 'bowl-effect' could be compensated for in most parts of the scenes, in the future the across track overlap should be increased and the GCPs should be properly covered to stabilize the 3D information within the HS DSM. This would allow a direct comparison of HS DSMs from different dates.

Figure 4.11 shows the CHM derived from the HS DSM for four dates. Similar to DAS 70, at DAS 84 and DAS 96 the bare soil to the east and west of the plots respectively was also not covered by the images. The color scheme of the maps indicates the plant height for every pixel of the plot. These maps reveal different plant heights for the different cultivars. Differences within the plots are also visible (e.g. DAS 84, plot 52). At DAS 96, four plots have experienced lodging and can be clearly distinguished from the other plots. As well, tractor tracks between and right next to the plot borders are visible. The overall growing pattern indicates strong growth until DAS 84 and only minor differences between DAS 84 and 96, apart from the logged plots. These results demonstrate the feasibility of HS DSMs for high-resolution mapping for agricultural purposes. Additionally, the high spatial resolution of the data allows observations of plot heterogeneity and crop damages from tractor tracks or lodging.

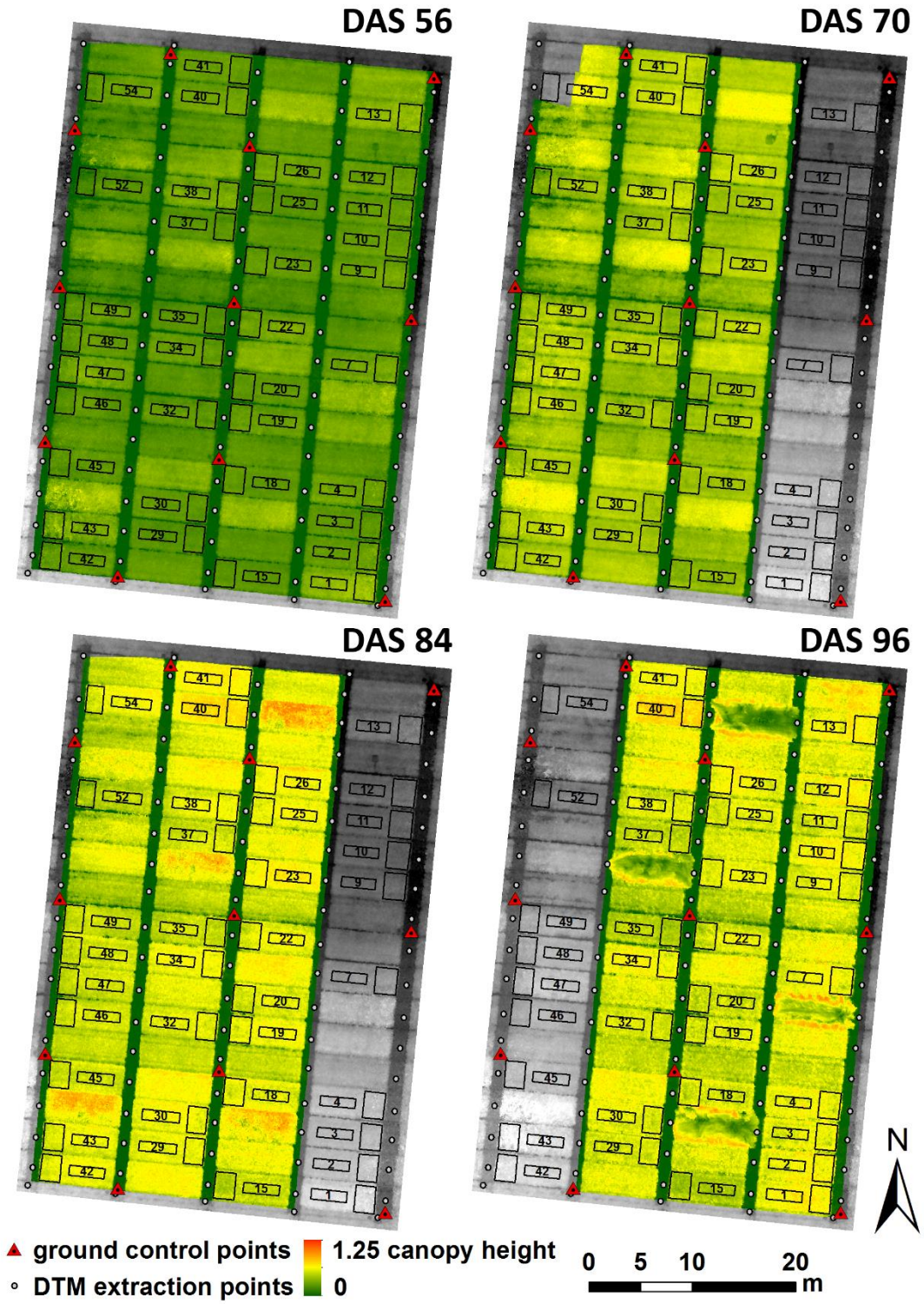

Figure 4.11 Canopy height models of DAS 56, 70, 84 and 96. For DAS 70 to 96 some areas were excluded due to missing data. Remotely measured parts of the plots are marked with the number of the plot. Additionally, digital terrain model (DTM) extraction and ground control points are indicated.

4.3.3.2 Plant height evaluation

The plant height derived from the HS DSM was compared to ruler measured plant heights. Figure 4.12 shows the scatterplot for the individual dates and all dates together. Similar to Figure 4.11 an increase in plant height is visible until DAS 84. The relationships between the ruler measurements and the HS DSM derived plant heights are quantified in Table 4.3.

Table 4.3 Quantitative comparison of the ruler measured and the HS DSM derived plant heights.

DAS	**56**	**70**	**70b**	**84**	**96**	**56 - 84**	**all**
R^2	0.83	0.35	0.70	0.81	0.45	0.98	0.96
RMSE (m)	0.06	0.12	0.08	0.09	0.17	0.12	0.20
RMSE (%)	16	20	13	11	22	20	32
slope	0.66	0.48	0.89	0.89	0.97	0.71	0.75
mean difference	0.11	0.15	0.25	0.26	0.19	0.16	0.17

DAS 56, 84 and the multi-date sets achieve $R^2 > 0.8$. DAS 70 and 96 achieve lower relations. When plots 41 – 54 are excluded from the DAS 70 dataset (DAS 70b) the R^2 increases to 0.7 and the relative RMSE decreases to 12 %. Overall, the RMSE is between 11 and 22% for the single dates and at 32% for all dates together. The slope of the regression line is between 0.66 for DAS 56 and 0.97 for DAS 96. For all dates the HS DSM derived plant height is lower than the ruler measured plant height. The mean difference varies from 0.11 m for DAS 56 to 0.26 m for DAS 84. The quality of the spatial information in the HS DSM also influences the retrieval of the plant height. This can be seen in the significantly increased R^2 and the slope of the regression when the most western row at DAS 70 is excluded. As mentioned above, the image coverage and especially the across track image overlap in this part of the scene was very limited so that the CHM bended downwards at the bare soil path to the west side of the model and upwards in the area of the plot. Thus, these plots showed a higher plant height in the CHM relative to the other plots for the date (Figure 4.12, brown dots).

With the ruler, the heights of individual plants within the plot are measured. On the contrary, the very high resolution point cloud from which the HS DSM is derived does not only represent the highest parts of plants but also reflects heterogeneity in conjunction with the canopy structure. Thus it approximates an average canopy height lower than the ruler derived plant heights. This is also supported by a study by Tilly et al. (2015), where a maximum point filter was used to derive the plant height and a similar offset could not be observed. The slope, close to 1 in most cases, demonstrates the feasibility to estimate the plant height both for individual dates and across several growth stages. However, the best data processing scheme to derive a specific parameter needs further investigation. The latter might also depend on the application, since for some applications the maximum plant height might be

interesting (e.g. stem growth rate), while for others an average canopy height might be beneficial (e.g. biomass estimation).

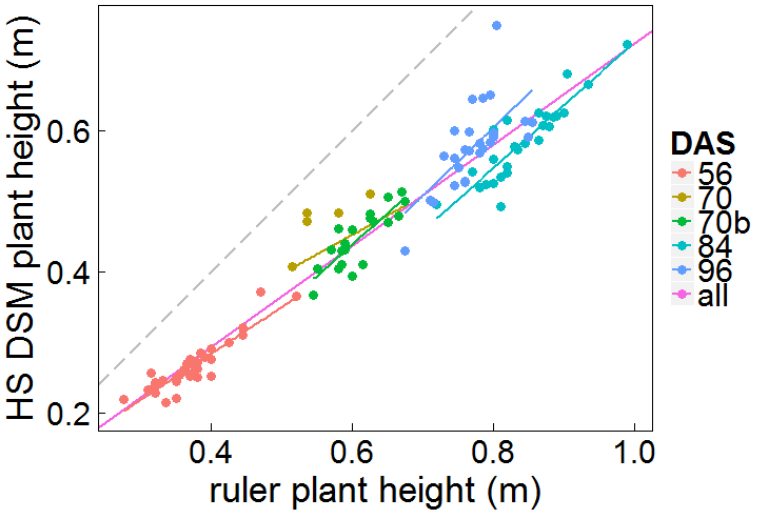

Figure 4.12 Scatterplot of the ruler and HS DSM derived plant heights for the individual four measurement dates (red, yellow, blue, azure), and DAS 70 without plot 46 – 54 (green) and all dates together (pink). The one to one line is shown in gray.

4.4 Conclusion

Low-flying sensing systems can carry out surveys efficiently without disrupting the surface. Unmanned aerial vehicle (UAV)-based hyperspectral snapshot cameras allow the capture of spectral and spatial information at the same time. Within this study, this information was processed to high-resolution hyperspectral digital surface models (HS DSMs) and evaluated for the multi-temporal monitoring of agricultural crops. HS DSMs are a representation of the surface in 3D space linked with hyperspectral information emitted and reflected by the object covered by the surface. The high resolution of the data allows the detection of small-scale variability and impacts on the canopy such as lodging or tractor tracks. Additionally, biophysical and biochemical plant properties could be extracted. Canopy height was well estimated for most individual and across multiple dates (R^2 = 0.45, 0.70 – 0.98). Image overlap, coverage and ground control point distribution were identified as critical factors for the quality of the canopy height. The hyperspectral data used to estimate canopy chlorophyll by means of vegetation indices. Chlorophyll could be well estimated for the individual growth stages heading and fruit development and across the growth stages booting to fruit development (R^2 = 0.50 – 0.64). However, ground-based non-imaging spectral measurements differed from the measurements derived from the HS DSMs. To fully comprehend these differences, the special data properties of HS DSMs were determined.

HS DSMs are generated from many individual images. Each pixel within the HS DSM has its own angular properties with regards to the sensor orientation and the sun's position during the acquisition of each individual image, and the geometry of the sensed surface. This influences the data retrieved from HS DSMs. To comprehend this potential issue, the common theory of imaging spectroscopy was extended by the concept of a specific field of view, which describes the composition of pixels and their angular properties within a scene used to characterize a specific area of interest. Depending on this composition, the measured apparent reflectance might differ. In comparison to non-imaging ground based observations, this resulted in significant differences due to different measurement extents and angular settings of the measurements. Overall, the visible part of the spectrum was more influenced than the near infrared. The different spatial measurement extent and the angular properties accounted for up to 33% increase in reflectance in the red region. In the NIR, only small differences were present. These differences were also reflected in the results for the retrieval of chlorophyll which differed considerably between the imaging and non-imaging data. This questions if models for vegetation parameter retrieval can per se be transferred in-between different sensors. Additionally, different processing schemes for the spectral data within the HS DSM were evaluated and revealed significant differences. Un-modified spectral information differed by up to 29% in comparison with a processing scheme where all available information was averaged for each pixel.

These results highlight the need and opportunity for further research on the understanding of angular effects and its influence on retrieval techniques. In particular, it is likely that similar observations can be made for other imaging devices. Low-flying sensing systems are especially prone to angular effects, since, in comparison with high-flying platforms, wider field of views are needed to cover the same area and thus the variety of viewing geometries increases.

Additionally, cloud cover was found to influence the applied radiometric calibration procedure. One flight was carried out under cloudy conditions and showed considerable difference to the ground based observations, which could not be explained by the different measurement extents and angular properties of the measurements. An approach to quantify the difference showed a wavelength-independent underestimation of the irradiance of approximately 15%. Additionally, the UAV and the position during the calibration introduced additional errors. Thus, the applied pre-flight radiometric calibration should not be used under cloudy conditions and should in general be substituted by more robust methods.

Overall this study demonstrates the feasibility of monitoring agricultural crops with HS DSMs derived from UAV snapshot cameras. They allow the frequent observation of complementary hyperspectral and 3D information at the same time in high resolution. While the angular properties within the

spectral data still need to be better understood, their tracing also offer a great potential for new methods of analysis.

Acknowledgements

We thank Martin Gynp, Jonas Brands, Simon Bennertz, Janis Broscheit, Markus Drahs, Silas Eichfuss, Sven Ortloff and Maximilian Willkomm very much for their outstanding engagement in the field, and the people of Campus Klein-Altendorf (University of Bonn) for maintaining the field experiment. Additionally, we thank Georg Bareth and Nora Tilly for their support during the preparation of the manuscript. Moreover, we thank Ira Kurth and Mauritio Hunsche (INRES, University of Bonn) for the access to and the support in the laboratory. The field measurements were carried out within CROP.SENSe.net project in the context of the Ziel 2-Programms NRW 2007–2013 ‘‘Regionale Wettbewerbsfähigkeit und Beschäftigung” by the Ministry for Innovation, Science and Research (MIWF) of the state North Rhine Westphalia (NRW) and European Union Funds for regional development (EFRE) (005-1103-0018). We acknowledge Agim Ballvora for the management of the barley cluster within this project. Helge Aasen greatly acknowledges the funding through the fellowship grant of the Graduate School of Geosciences (GSGS-2015B-F01), University of Cologne. We acknowledged Sam Work for proofreading of the manuscript.

4.5 References

Aasen, H., in review. Influence of the viewing geometry on hyperspectral data retrieved from UAV snapshot cameras, in: ISPRS Annals of the Photogrammetry, Remote Sensing and Spatial Information Sciences. Presented at the XXIII congress of the International Society for Photogrammetry and Remote Sensing, Prague, Czech Republic.

Aasen, H., Burkart, A., Bolten, A., Bareth, G., 2015. Generating 3D hyperspectral information with lightweight UAV snapshot cameras for vegetation monitoring: From camera calibration to quality assurance. ISPRS J. Photogramm. Remote Sens. 108, 245–259. doi:10.1016/j.isprsjprs.2015.08.002

Aasen, H., Gnyp, M.L., Miao, Y., Bareth, G., 2014. Automated Hyperspectral Vegetation Index Retrieval from Multiple Correlation Matrices with HyperCor. Photogramm. Eng. Remote Sens. 80, 785–795. doi:10.14358/PERS.80.8.785

Agisoft LLC, 2015. Photoscan changelog [WWW Document]. URL http://www.agisoft.com/pdf/photoscan_changelog.pdf (accessed 6.10.15).

Agisoft LLC, 2014. Agisoft PhotoScan User Manual Professional Edition, Version 1.1. St. Petersburg, Russia.

Araus, J.L., Cairns, J.E., 2014. Field high-throughput phenotyping: the new crop breeding frontier. Trends Plant Sci. 19, 52–61. doi:10.1016/j.tplants.2013.09.008

Atzberger, C., 2013. Advances in Remote Sensing of Agriculture: Context Description, Existing Operational Monitoring Systems and Major Information Needs. Remote Sens. 5, 949–981. doi:10.3390/rs5020949

Bareth, G., Aasen, H., Bendig, J., Gnyp, M.L., Bolten, A., Jung, A., Michels, R., Soukkamäki, J., 2015. Low-weight and UAV-based Hyperspectral Full-frame Cameras for Monitoring Crops: Spectral Comparison with Portable Spectroradiometer Measurements. Photogramm. - Fernerkund. - Geoinformation 2015, 69–79. doi:10.1127/pfg/2015/0256

Bartlett, J.S., Ciotti, Á.M., Davis, R.F., Cullen, J.J., 1998. The spectral effects of clouds on solar irradiance. J. Geophys. Res. 103, 31017. doi:10.1029/1998JC900002

Bendig, J., Bolten, A., Bennertz, S., Broscheit, J., Eichfuss, S., Bareth, G., 2014. Estimating Biomass of Barley Using Crop Surface Models (CSMs) Derived from UAV-Based RGB Imaging. Remote Sens. 6, 10395–10412. doi:10.3390/rs61110395

Bendig, J., Yu, K., Aasen, H., Bolten, A., Bennertz, S., Broscheit, J., Gnyp, M.L., Bareth, G., 2015. Combining UAV-based plant height from crop surface models, visible, and near infrared vegetation indices for biomass monitoring in barley. Int. J. Appl. Earth Obs. Geoinformation 39, 79–87. doi:10.1016/j.jag.2015.02.012

Berni, J., Zarco-Tejada, P.J., Suarez, L., Fereres, E., 2009. Thermal and Narrowband Multispectral Remote Sensing for Vegetation Monitoring From an Unmanned Aerial Vehicle. IEEE Trans. Geosci. Remote Sens. 47, 722–738. doi:10.1109/TGRS.2008.2010457

Burkart, A., Aasen, H., Alonso, L., Menz, G., Bareth, G., Rascher, U., 2015. Angular Dependency of Hyperspectral Measurements over Wheat Characterized by a Novel UAV Based Goniometer. Remote Sens. 7, 725–746. doi:10.3390/rs70100725

Calderón, R., Navas-Cortés, J.A., Lucena, C., Zarco-Tejada, P.J., 2013. High-resolution airborne hyperspectral and thermal imagery for early detection of Verticillium wilt of olive using

fluorescence, temperature and narrow-band spectral indices. Remote Sens. Environ. 139, 231–245. doi:10.1016/j.rse.2013.07.031

Colomina, I., Molina, P., 2014. Unmanned aerial systems for photogrammetry and remote sensing: A review. ISPRS J. Photogramm. Remote Sens. 92, 79–97. doi:10.1016/j.isprsjprs.2014.02.013

Damm, A., Guanter, L., Verhoef, W., Schläpfer, D., Garbari, S., Schaepman, M.E., 2015. Impact of varying irradiance on vegetation indices and chlorophyll fluorescence derived from spectroscopy data. Remote Sens. Environ. 156, 202–215. doi:10.1016/j.rse.2014.09.031

Dandois, J.P., Ellis, E.C., 2010. Remote Sensing of Vegetation Structure Using Computer Vision. Remote Sens. 2, 1157–1176. doi:10.3390/rs2041157

Elarab, M., Ticlavilca, A.M., Torres-Rua, A.F., Maslova, I., McKee, M., 2015. Estimating chlorophyll with thermal and broadband multispectral high resolution imagery from an unmanned aerial system using relevance vector machines for precision agriculture. Int. J. Appl. Earth Obs. Geoinformation 43, 32–42. doi:10.1016/j.jag.2015.03.017

Ellis, E.C., Klein Goldewijk, K., Siebert, S., Lightman, D., Ramankutty, N., 2010. Anthropogenic transformation of the biomes, 1700 to 2000: Anthropogenic transformation of the biomes. Glob. Ecol. Biogeogr. no–no. doi:10.1111/j.1466-8238.2010.00540.x

Foley, J.A., 2005. Global Consequences of Land Use. Science 309, 570–574. doi:10.1126/science.1111772

Foley, J.A., Ramankutty, N., Brauman, K.A., Cassidy, E.S., Gerber, J.S., Johnston, M., Mueller, N.D., O'Connell, C., Ray, D.K., West, P.C., Balzer, C., Bennett, E.M., Carpenter, S.R., Hill, J., Monfreda, C., Polasky, S., Rockström, J., Sheehan, J., Siebert, S., Tilman, D., Zaks, D.P.M., 2011. Solutions for a cultivated planet. Nature 478, 337–342. doi:10.1038/nature10452

Gamon, J.A., Peñuelas, J., Field, C.B., 1992. A narrow-waveband spectral index that tracks diurnal changes in photosynthetic efficiency. Remote Sens. Environ. 41, 35–44. doi:10.1016/0034-4257(92)90059-S

Geipel, J., Link, J., Claupein, W., 2014. Combined Spectral and Spatial Modeling of Corn Yield Based on Aerial Images and Crop Surface Models Acquired with an Unmanned Aircraft System. Remote Sens. 6, 10335–10355. doi:10.3390/rs61110335

Gitelson, A., Merzlyak, M.N., 1994. Quantitative estimation of chlorophyll-a using reflectance spectra: Experiments with autumn chestnut and maple leaves. J. Photochem. Photobiol. B 22, 247–252. doi:10.1016/1011-1344(93)06963-4

Gnyp, M.L., Yu, K., Aasen, H., Yao, Y., Huang, S., Miao, Y., Bareth, G., 2013. Analysis of Crop Reflectance for Estimating Biomass in Rice Canopies at Different Phenological Stages. Photogramm. - Fernerkund. - Geoinformation 2013, 351–365. doi:10.1127/1432-8364/2013/0182

Guyot, N., Baret, F., 1988. Utilisation de la haute resolution spectrale pour suivre l'etat des couverts vegetaux, in: Proceedings of the 4th International Colloquium on Spectral Signatures of Objects in Remote Sensing. Presented at the 4th International Colloquium on Spectral Signatures of Objects in Remote Sensing, NASA Astrophysics Data System, Aussois, France, pp. 279–286.

Haboudane, D., Miller, J.R., Pattey, E., Zarco-Tejada, P.J., Strachan, I.B., 2004. Hyperspectral vegetation indices and novel algorithms for predicting green LAI of crop canopies: Modeling and validation in the context of precision agriculture. Remote Sens. Environ. 90, 337–352. doi:10.1016/j.rse.2003.12.013

Haboudane, D., Miller, J.R., Tremblay, N., Zarco-Tejada, P.J., Dextraze, L., 2002. Integrated narrow-band vegetation indices for prediction of crop chlorophyll content for application to precision agriculture. Remote Sens. Environ. 81, 416–426.

Hakala, T., Suomalainen, J., Peltoniemi, J.I., 2010. Acquisition of Bidirectional Reflectance Factor Dataset Using a Micro Unmanned Aerial Vehicle and a Consumer Camera. Remote Sens. 2, 819–832. doi:10.3390/rs2030819

Hansen, P.M., Schjoerring, J.K., 2003. Reflectance measurement of canopy biomass and nitrogen status in wheat crops using normalized difference vegetation indices and partial least squares regression. Remote Sens. Environ. 86, 542–553. doi:10.1016/S0034-4257(03)00131-7

Harwin, S., Lucieer, A., 2012. Assessing the Accuracy of Georeferenced Point Clouds Produced via Multi-View Stereopsis from Unmanned Aerial Vehicle (UAV) Imagery. Remote Sens. 4, 1573–1599. doi:10.3390/rs4061573

Honkavaara, E., Markelin, L., Hakala, T., Peltoniemi, J.I., 2014. The Metrology of Directional, Spectral Reflectance Factor Measurements Based on Area Format Imaging by UAVs. Photogramm. - Fernerkund. - Geoinformation 2014, 175– 188. doi:10.1127/1432-8364/2014/0218

Honkavaara, E., Saari, H., Kaivosoja, J., Pölönen, I., Hakala, T., Litkey, P., Mäkynen, J., Pesonen, L., 2013. Processing and Assessment of Spectrometric, Stereoscopic Imagery Collected Using a Lightweight UAV Spectral Camera for Precision Agriculture. Remote Sens. 5, 5006–5039. doi:10.3390/rs5105006

Jaakkola, A., Hyyppä, J., Kukko, A., Yu, X., Kaartinen, H., Lehtomäki, M., Lin, Y., 2010. A low-cost multi-sensoral mobile mapping system and its feasibility for tree measurements. ISPRS J. Photogramm. Remote Sens. 65, 514–522. doi:10.1016/j.isprsjprs.2010.08.002

Kimes, D.S., Kirchner, J.A., Newcomb, W.W., 1983. Spectral radiance errors in remote sensing ground studies due to nearby objects. Appl. Opt. 22, 8. doi:10.1364/AO.22.000008

Koukal, T., Atzberger, C., Schneider, W., 2014. Evaluation of semi-empirical BRDF models inverted against multi-angle data from a digital airborne frame camera for enhancing forest type classification. Remote Sens. Environ. 151, 27–43. doi:10.1016/j.rse.2013.12.014

Küster, T., Spengler, D., Barczi, J.-F., Segl, K., Hostert, P., Kaufmann, H., 2014. Simulation of Multitemporal and Hyperspectral Vegetation Canopy Bidirectional Reflectance Using Detailed Virtual 3-D Canopy Models. IEEE Trans. Geosci. Remote Sens. 52, 2096–2108. doi:10.1109/TGRS.2013.2258162

Lucieer, A., Malenovský, Z., Veness, T., Wallace, L., 2014a. HyperUAS-Imaging Spectroscopy from a Multirotor Unmanned Aircraft System: HyperUAS-Imaging Spectroscopy from a Multirotor Unmanned. J. Field Robot. 31, 571–590. doi:10.1002/rob.21508

Lucieer, A., Turner, D., King, D.H., Robinson, S.A., 2014b. Using an Unmanned Aerial Vehicle (UAV) to capture micro-topography of Antarctic moss beds. Int. J. Appl. Earth Obs. Geoinformation 27, 53–62. doi:10.1016/j.jag.2013.05.011

Mac Arthur, A., MacLellan, C.J., Malthus, T., 2012. The Fields of View and Directional Response Functions of Two Field-spectroradiometers. IEEE Trans. Geosci. Remote Sens. 50, 3892–3907. doi:10.1109/TGRS.2012.2185055

Malenovský, Z., Turnbull, J.D., Lucieer, A., Robinson, S.A., 2015. Antarctic moss stress assessment based on chlorophyll content and leaf density retrieved from imaging spectroscopy data. New Phytol. 208, 608–624. doi:10.1111/nph.13524

Marshall, M., Thenkabail, P., 2015. Developing in situ Non-Destructive Estimates of Crop Biomass to Address Issues of Scale in Remote Sensing. Remote Sens. 7, 808–835. doi:10.3390/rs70100808

Mesas-Carrascosa, F.-J., Torres-Sánchez, J., Clavero-Rumbao, I., García-Ferrer, A., Peña, J.-M., Borra-Serrano, I., López-Granados, F., 2015. Assessing Optimal Flight Parameters for Generating Accurate Multispectral Orthomosaicks by UAV to Support Site-Specific Crop Management. Remote Sens. 7, 12793–12814. doi:10.3390/rs71012793

Milton, E.J., Schaepman, M.E., Anderson, K., Kneubühler, M., Fox, N., 2009. Progress in field-spectroscopy. Remote Sens. Environ. 113, S92–S109. doi:10.1016/j.rse.2007.08.001

Mulla, D.J., 2013. Twenty five years of remote sensing in precision agriculture: Key advances and remaining knowledge gaps. Biosyst. Eng. 114, 358–371. doi:10.1016/j.biosystemseng.2012.08.009

Näsi, R., Honkavaara, E., Lyytikäinen-Saarenmaa, P., Blomqvist, M., Litkey, P., Hakala, T., Viljanen, N., Kantola, T., Tanhuanpää, T., Holopainen, M., 2015. Using UAV-Based Photogrammetry and Hyperspectral Imaging for Mapping Bark Beetle Damage at Tree-Level. Remote Sens. 7, 15467–15493. doi:10.3390/rs71115467

Nicodemus, F.E., Richmond, J.C., Hsia, J.J., Ginsberg, I.W., Limperis, T., 1977. Geometrical considerations and nomenclature for reflectance. National Bureau of Standards, Washington DC, p. 67.

Ouédraogo, M.M., Degré, A., Debouche, C., Lisein, J., 2014. The evaluation of unmanned aerial system-based photogrammetry and terrestrial laser scanning to generate DEMs of agricultural watersheds. Geomorphology 214, 339–355. doi:10.1016/j.geomorph.2014.02.016

Pajares, G., 2015. Overview and Current Status of Remote Sensing Applications Based on Unmanned Aerial Vehicles (UAVs). Photogramm. Eng. Remote Sens. 81, 281–330. doi:10.14358/PERS.81.4.281

Puliti, S., Olerka, H., Gobakken, T., Næsset, E., 2015. Inventory of Small Forest Areas Using an Unmanned Aerial System. Remote Sens. 7, 9632–9654. doi:10.3390/rs70809632

Qi, J., Moran, M.S., Cabot, F., Dedieu, G., 1995. Normalization of sun/view angle effects using spectral albedo-based vegetation indices. Remote Sens. Environ. 52, 207–217. doi:10.1016/0034-4257(95)00034-X

Quemada, M., Gabriel, J., Zarco-Tejada, P., 2014. Airborne Hyperspectral Images and Ground-Level Optical Sensors As Assessment Tools for Maize Nitrogen Fertilization. Remote Sens. 6, 2940–2962. doi:10.3390/rs6042940

Rascher, U., Blossfeld, S., Fiorani, F., Jahnke, S., Jansen, M., Kuhn, A.J., Matsubara, S., Märtin, L.L.A., Merchant, A., Metzner, R., Müller-Linow, M., Nagel, K.A., Pieruschka, R., Pinto, F., Schreiber, C.M., Temperton, V.M., Thorpe, M.R., Dusschoten, D.V., Van Volkenburgh, E., Windt, C.W., Schurr, U., 2011. Non-invasive approaches for phenotyping of enhanced performance traits in bean. Funct. Plant Biol. 38, 968. doi:10.1071/FP11164

Ray, D.K., Mueller, N.D., West, P.C., Foley, J.A., 2013. Yield Trends Are Insufficient to Double Global Crop Production by 2050. PLoS ONE 8, e66428. doi:10.1371/journal.pone.0066428

Remondino, F., El-Hakim, S., 2006. Image-based 3D Modelling: A Review: Image-based 3D modelling: a review. Photogramm. Rec. 21, 269–291. doi:10.1111/j.1477-9730.2006.00383.x

Schaepman, M.E., 2007. Spectrodirectional remote sensing: From pixels to processes. Int. J. Appl. Earth Obs. Geoinformation 9, 204–223. doi:10.1016/j.jag.2006.09.003

Schaepman-Strub, G., Schaepman, M.E., Painter, T.H., Dangel, S., Martonchik, J.V., 2006. Reflectance quantities in optical remote sensing—definitions and case studies. Remote Sens. Environ. 103, 27–42. doi:10.1016/j.rse.2006.03.002

Schläpfer, D., Richter, R., Feingersh, T., 2015. Operational BRDF Effects Correction for Wide-Field-of-View Optical Scanners (BREFCOR). IEEE Trans. Geosci. Remote Sens. 53, 1855–1864. doi:10.1109/TGRS.2014.2349946

Szeliski, R., 2011. Computer Vision, Texts in Computer Science. Springer London, London.

Thenkabail, P.S., Lyon, J.G., Huete, A., 2012. Advances in Hyperspectral Remote Sensing of Vegetation and Agricultural Croplands, in: Hyperspectral Remote Sensing of Vegetation. CRC Press, Boca Raton, FL, pp. 3 – 38.

Tilly, N., Aasen, H., Bareth, G., 2015. Fusion of Plant Height and Vegetation Indices for the Estimation of Barley Biomass. Remote Sens. 7, 11449–11480. doi:10.3390/rs70911449

Tilly, N., Hoffmeister, D., Cao, Q., Huang, S., Lenz-Wiedemann, V., Miao, Y., Bareth, G., 2014. Multitemporal crop surface models: accurate plant height measurement and biomass estimation with terrestrial laser scanning in paddy rice. J. Appl. Remote Sens. 8, 083671. doi:10.1117/1.JRS.8.083671

Verrelst, J., Schaepman, M.E., Koetz, B., Kneubühler, M., 2008. Angular sensitivity analysis of vegetation indices derived from CHRIS/PROBA data. Remote Sens. Environ. 112, 2341–2353. doi:10.1016/j.rse.2007.11.001

von Bueren, S.K., Burkart, A., Hueni, A., Rascher, U., Tuohy, M.P., Yule, I.J., 2015. Deploying four optical UAV-based sensors over grassland: challenges and limitations. Biogeosciences 12, 163–175. doi:10.5194/bg-12-163-2015

Wallace, L., Watson, C., Lucieer, A., 2014. Detecting pruning of individual stems using Airborne Laser Scanning data captured from an Unmanned Aerial Vehicle. Int. J. Appl. Earth Obs. Geoinformation 30, 76–85. doi:10.1016/j.jag.2014.01.010

Yu, K., Lenz-Wiedemann, V., Chen, X., Bareth, G., 2014. Estimating leaf chlorophyll of barley at different growth stages using spectral indices to reduce soil background and canopy structure effects. ISPRS J. Photogramm. Remote Sens. 97, 58–77. doi:10.1016/j.isprsjprs.2014.08.005

Zarco-Tejada, P.J., Diaz-Varela, R., Angileri, V., Loudjani, P., 2014. Tree height quantification using very high resolution imagery acquired from an unmanned aerial vehicle (UAV) and automatic 3D photo-reconstruction methods. Eur. J. Agron. 55, 89–99. doi:10.1016/j.eja.2014.01.004

Zarco-Tejada, P.J., González-Dugo, V., Berni, J.A.J., 2012. Fluorescence, temperature and narrow-band indices acquired from a UAV platform for water stress detection using a micro-hyperspectral imager and a thermal camera. Remote Sens. Environ. 117, 322–337. doi:10.1016/j.rse.2011.10.007

Zhao, F., Li, Y., Dai, X., Verhoef, W., Guo, Y., Shang, H., Gu, X., Huang, Y., Yu, T., Huang, J., 2015. Simulated impact of sensor field of view and distance on field measurements of bidirectional reflectance factors for row crops. Remote Sens. Environ. 156, 129–142. doi:10.1016/j.rse.2014.09.01

5. ANGULAR DEPENDENCY OF HYPERSPECTRAL MEASUREMENTS OVER WHEAT CHARACTERIZED BY A NOVEL UAV BASED GONIOMETER

ANDREAS BURKART [1,†,], HELGE AASEN [2,†], LUIS ALONSO [3], GUNTER MENZ [4,5], GEORG BARETH [2], UWE RASCHER [1]*

Published in: Remote Sensing 2015, 7 (1), 725-746

DOI: 10.3390/rs70100725

Formatting and orthography of the manuscript is adapted to the dissertation style.

[1] Institute of Geography (GIS & Remote Sensing Group), University of Cologne, 50923 Cologne, Germany

[1] Research Center Jülich, Institute of Bio- and Geosciences, IBG-2: Plant Sciences, 52428 Jülich, Germany; E-Mail: u.rascher@fz-juelich.de

[2] Department of Geoscience, Working Group GIS and Remote Sensing, University of Cologne, 50923 Cologne, Germany; E-Mails: helge.aasen@uni-koeln.de (H.A.); g.bareth@uni-koeln.de (G.B.)

[3] Laboratory of image processing, University of Valencia, 46980 Paterna, Spain; E-Mail: luis.alonso@uv.es

[4] Department of Geography, Remote Sensing Research Group, University of Bonn, 53001 Bonn, Germany; E-Mail: g.menz@uni-bonn.de,

[5] Center for Remote Sensing for Land Surfaces, University of Bonn, 53113 Bonn, Germany

[†] These authors contributed equally to this work.

* Corresponding author: Tel.: +49-2461-61-8084; Email: an.burkart@fz-juelich.de

Abstract: In this study we present a hyperspectral flying goniometer system, based on a rotary-wing unmanned aerial vehicle (UAV) equipped with a spectrometer mounted on an active gimbal. We show that this approach may be used to collect multiangular hyperspectral data over vegetated environments. The pointing and positioning accuracy are assessed using structure from motion and vary from σ = 1° to 8° in pointing and σ = 0.7 to 0.8 m in positioning. We use a wheat dataset to investigate the influence of angular effects on the NDVI, TCARI and REIP vegetation indices. Angular effects caused significant variations on the indices: NDVI = 0.83–0.95; TCARI = 0.04–0.116; REIP = 729–735 nm. Our analysis highlights the necessity to consider angular effects in optical sensors when observing vegetation. We compare the measurements of the UAV goniometer to the angular modules of the SCOPE radiative transfer model. Model and measurements are in high accordance (r2 = 0.88) in the infrared region at angles close to nadir; in contrast the comparison show discrepancies at low tilt

angles (r2 = 0.25). This study demonstrates that the UAV goniometer is a promising approach for the fast and flexible assessment of angular effects.

Keywords: hyperspectral; UAV; vegetation; BRDF; goniometer; vegetation indices

5.1 Introduction

Spectral radiometers (spectrometers) reach beyond the capabilities of human vision and enable scientists to retrieve diverse information from reflected light. Field-spectroscopic measurements have a long history (Milton, 1987) and are nowadays a common investigative tool in various research areas. Moreover, spectral vegetation analysis from air- or spaceborne platforms is a mature technology, and is commonly used for the accurate derivation of land cover classes (Tian, 2004). Hyperspectral measurements, which consist of continuous narrow spectral bands, help to retrieve information about the biophysical and biochemical components of vegetation (Aasen et al., 2014; Gnyp et al., 2013; Yu et al., 2013) and may be used to discriminate healthy or stressed plants (Mahlein et al., 2013; Penuelas et al., 1997).

With their synoptic view, airborne and spaceborne imaging sensors typically capture a large swath. Discrete image elements (pixels) located in the geometric center of an image are commonly acquired from a nadir view angle, whereas pixels at image edges are recorded from oblique angles. Off-nadir view geometry depends on the field of view (FOV) specifications and measurement methodology and varies among sensor systems; MODIS, for example is imaging ±55° off nadir (Barnes et al., 1998).

The bidirectional reflectance distribution function (BRDF) is the conceptual framework that explains changes in reflectance that result from view angle changes dependent on surface property and illumination (Nicodemus, 1965; Schaepman-Strub et al., 2006). BRDF influence is not desirable in a nadir image, as it impacts reflectance values recorded by the sensor and complicates the compositing of multiple images or flight lines. However, angular or off-nadir imaging can complement nadir image data by integrating additional spectral information. In forest environments, for example, an oblique view will–depending on the stand density–detect less reflectance from tree crowns and more from tree trunks (Fassnacht and Koch, 2012; Schlerf and Atzberger, 2012). Lack of knowledge in effects created from different sun-sensor geometries throughout the vegetation season have for instance led to incorrect greening estimates from satellite data in the Amazon rainforest, as recently shown by Morton et al., (2014).

The need for BRDF correction, along with an interest in angular characteristics, has led to the development of various goniometric measurement approaches. These are able to exploit a center

point from multiple view angles. The most common approach utilizes a semi-automated goniometer equipped with a point spectrometer with a radius of one meter or larger (Bourgeois et al., 2006; Buchhorn et al., 2013; Peltoniemi et al., 2005). On larger scales the POLDER and MISR instruments and the orbiting sensor Chris/Proba are capable of retrieving spectral data of the same area from different angles during one or multiple overpasses (Barnsley et al., 2004; Deschamps et al., 1994). On a smaller scale Comar et al (2012) used a conoscope to assess the BRDF of wheat at leaf surface level. This technique allows characterizing the reflectance of small leaf structures, such as veins. Such multiangular measurements are necessary to accumulate knowledge regarding vegetation cover BRDF characteristics. The fundamental goal of these research efforts is to develop a model capable of predicting the BRDF of a known vegetation cover type as well as the other way round, to derive knowledge about unidentified vegetation cover from multiangular measurements. Various models have been introduced in the past to estimate BRDF on a mathematical or empirical basis (Andrieu et al., 1997; Qin and Goel, 1995), or to compute the aggregate energy balance of a vegetation canopy including radiative transfer, as done in the SCOPE (Soil-Canopy-Observation of Photosynthesis and the Energy balance) model (Tol et al., 2009).

Using these methods, an effective theoretical understanding of the BDRF was developed for flat and accessible land cover like snow or soil (Nolin and Liang, 2000). The small size of common goniometers along with their small FOV made the BRDF characterization of other important land cover types (including forest or agriculture) difficult (Deering et al., 1999) or impossible. Forest and agriculture land covers are of particular significant scientific and economic interest, and alternative analytic approaches are necessary to allow BRDF measurements on larger scales and within inaccessible areas.

Some recent studies have investigated UAVs as a novel platform for goniometric measurements. Burkhart et al. (2010) performed a survey over ice fields using a fixed-wing UAV equipped with an on-board spectrometer. Principally due to maneuvering and incident wind, the flight patterns of this platform introduced banking levels of up to ±30°, causing the spectrometer to collect multiangular hyperspectral measurements of numerous points that were overflown. A more defined method was presented by Hakala et al. (2010) and Honkavaara et al. (2014), who deployed a rotary-wing UAV equipped with a stabilized gimbal mounting RGB and multispectral camera, respectively. Utilizing specific flight patterns, multiangular information could be derived in the bands of the given camera.

To fully understand the BRDF effects of vegetation, we suggest that an optimized dataset providing a comprehensive understanding of multiple agricultural sites would consist of frequent multiangular hyperspectral measurements acquired at a number of different locations throughout a complete vegetation phenological cycle. Only airborne platforms can fulfill these requirements without

disturbing crop growth by physically stepping through the field or casting shadows within the sensor FOV. With their recent development and improving utility and stability, UAVs can be employed as platforms for multi-angular remote data collection.

The main focus of this study is to introduce a way of collecting multiangular hyperspectral data over almost every kind of terrain and scale with a flying spectrometer. The approach combines the benefits of goniometers equipped with a high-resolution spectrometer and the flexibility of UAV platforms. We then demonstrate the acquisition and analysis of a datasets to explore BRDF effects over wheat. The angular dependency of reflectance as measured with the UAV goniometer was also compared to the reflectance modeled by SCOPE.

5.2 Material and Methods

The Falcon-8 octocopter UAV (Ascending Technology, Krailing, Germany) was used in this study. This platform was chosen due to its accurate flight controls and inherent stability. A hyperspectral measurement system was integrated on the UAV (Burkart et al., 2014). This instrument was recently developed at the interdisciplinary Research Center Jülich (Forschungszentrum Jülich GmbH) and is based on the STS-VIS spectrometer (Ocean Optics Inc. Dunedin, USA). The FOV of this spectrometer is approximately 12°; spectral resolution was at a full width at half maximum (FWHM) of 3 nm, with 256 spectral bands (4 pixel spectrally binned) within the range of 338 to 823 nm.

The Falcon-8 was originally designed as a camera platform for photographers and video production. It is equipped with a camera mount whose angle can be set during flight within 1° increments. The vertical angle (tilt) is defined by the camera mount, while the horizontal angle (heading) is determined by UAV orientation. The position and navigation is done by combining the GPS information from a navigation grade GPS (Ublox LEA 6T) and the information of the orientation information of the sensors onboard the UAV. Wind gusts during the flight are counteracted by an active system, which stabilizes the camera by pitch and roll. The spectrometer is also equipped with a RGB camera, which feeds a live video stream to the operator to facilitate operation and allow proper aiming of the system.

Airborne hyperspectral target reflectance measurements were performed with the UAV spectrometer wirelessly synchronized with a second spectrometer on the ground. Latter measured a white reference (Spectralon®) to adapt to changing illumination. A thorough calibration of the hyperspectral system was performed following the procedure described by Burkart et al. (2014). This process included dark current correction (Kuusk, 2011), spectral shift, dual spectrometer cross-calibration and additional quality checks using the SpecCal tool (Busetto et al., 2011). Our approach allows to compute the ratio of light reflected by the target surface to the hemispherical illumination (diffuse-, ambient-, and direct-

sunlight) as reflected by the white reference and is termed a hemispherical/conical reflectance factor. The actual BRDF is thus only approximated by this approach. Schaepman-Strub et al. (2006) provide a comprehensive BRDF description and nomenclature.

5.2.1 Flight Pattern

Grenzdörffer and Niemeyer (2011) demonstrated that a distinct hemispherical flight pattern is necessary to enable goniometric measurements using an UAV-based airborne RGB camera. The flight pattern accurately defines the position of the UAV as well as the aiming of the camera. The flight path of the UAV is selected to follow waypoints (WP) in a hemisphere and the angle and heading of the spectrometer is set to continuously point towards the center of the hemisphere. In this manner the center of the hemisphere is measured from different viewing angles.

To quickly compute such flight patterns for UAVs, we developed the software mAngle. It was written in the platform independent open source language "Processing" and is freely available as source code and compiled versions (mAngle, 2015). mAngle calculates the desired WP around a given center GPS coordinate. Placement of the WP are optimized for speed, as the UAV can quickly change horizontal position but requires more time to climb vertically to a different altitude. Flight pattern parameters including number of WP, initial angle, and hemisphere diameter can be set as desired (Figure 5.1). A designated flight pattern can be exported as a *.kml file to Google Earth (Google Inc., Mountain View, CA, USA) for visualization. The flight pattern can also be exported as a *.csv file, the format used by the Falcon-8 flight planning software (AscTec Autopilot Control V1.68). Such a hemispheric flight pattern is also useful to acquire pictures around a center object of interest for 3D reconstruction.

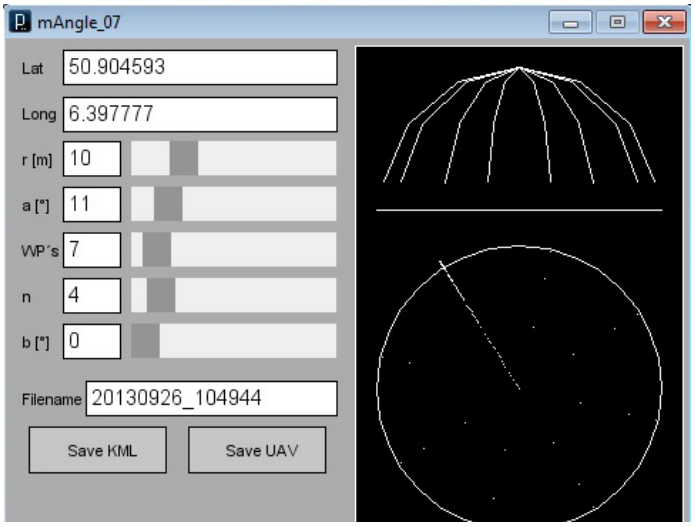

Figure 5.1 Graphical user interface of the mAngle software with input fields for the desired waypoint pattern. By setting radius, number of desired waypoints as well as starting angle and other parameters, a distinct goniometric flight pattern can be generated. A draft of the waypoint pattern is visualized in the right box of the program window.

5.2.2 Accuracy of the unmanned aerial vehicle Goniometer

To assess the positioning and pointing accuracy of the UAV goniometer the spectrometer was replaced by a high resolution RGB camera (NEX 5n, Sony, 16 mm lens) mounted on a similar active stabilized gimbal. In this configuration the UAV was flown following the same waypoint pattern as was used for a multi-angular spectrometer flight. In operation, the airborne spectrometer is triggered three times at each WP. The RGB camera also acquired three digital images at each WP (84 in total). Eleven ground control points (GCPs) were distributed within the covered area and registered using a differential GPS (Topcon HiPer Pro, Topcon). 3D reconstruction software (Agisoft Photoscan, version 1.0.4) was used to structure the spatial arrangement of the scene and georeference it with the GCPs. This rendering was calculated with a resolution of 3.53 mm/pixel and an average error of 1.46 pixels. The camera position and view angles for each individual image were exported and served as an estimator for the spatial accuracy of the UAV under operational conditions.

5.2.3 Field Campaign

Two multiangular flights (referred to as MERZ1, MERZ2) were conducted over farmland (Lat 50.93039, Lon 6.2968965) on 18 June 2013 during the ESA-HyFlex campaign in Merzenhausen, Germany. The two flights were performed under cloud-free moderate wind (1.6–5.5 m/s) conditions with an interval of two hours–one hour before and one hour after solar noon (Table 5.1). At the time of the study, the field contained mature wheat, with fully developed but still green (Figure 5.2). The centroid of the hemispherical waypoint pattern was located within the field in an area of uniform cover, avoiding farm equipment tracks and trails. The center point was defined using aerial imagery, in order to avoid disturbing measurements by walking into the area of interest. The two datasets produced in this campaign are freely available via SPECCHIO (Hueni et al., 2009) at the Server of the University of Zuerich

Figure 5.2 Wheat (Triticum aestivum) at the study site Merzenhausen, Germany, at the time of the multiangular flights, 18 June 2013. Ears were fully developed but still green.

under the campaign name “Merzen”. For these flights a hemisphere with a radius of 16 m was specified. The spectrometer has a FOV of 12°. The areal coverage of each measurement is a function of sensor tilt angle, encompassing here 9 m^2 at nadir up to 30 m^2 with 20° tilt. WPs around the hemisphere were set to cover vertical tilt angles of 90° (nadir), 66°, 43° and 20°, at 8 equally distributed heading angles, potentially producing a total of 28 WPs. However, nadir measurements were only acquired at four different headings, which were then merged into a single WP, leading to a total of 25 WPs included in the analysis.

Table 5.1 Local time and duration with the corresponding sun angle parameters for the two hyperspectral flights performed over wheat field in Merzenhausen, Germany.

Flight	Start Time	Duration	Sun Azimuth	Sun Elevation
MERZ1	12:43	09 min	155°	61°
MERZ2	14:47	11 min	213°	59°

In the following individual WPs will be identified as WP (tilt degree, heading degree). The spectrometer was activated three times at each WP to allow averaging and assessment of response variance. MERZ1 required a flight time of nine minutes, and MERZ2 required eleven minutes to consecutively measure the WP pattern. An additional UAV flight was conducted over the target using an RGB camera (NEX 5n, Sony Corporation, Minato, Japan, 16 mm lens) to image each WPs (Figure 5.3).

Figure 5.3 Example Red-Green-Blue (RGB) images with tilt angles of 20°, 66° and 90°. These images were acquired at the Merzenhausen site at approximately 13:30 following a multiangular flight path identical to the spectrometer flights. The Field-Of-View (FOV) of the RGB camera is 73.7° × 53.1° (compared to the 12° FOV of the airborne spectrometer) and allows observing multiangular effects within a single image–the bright hotspot with the shadow of the unmanned aerial vehicle in the center, located in the lower left corner of the 90° image is an example.

5.2.4 Data Preprocessing

Each spectrum captured from the UAV was transformed to reflectance using the reference spectra simultaneously measured by the ground spectrometer. Then, for each WP, the mean, standard deviation and coefficient of variation were calculated from the three measured spectra. All further analyses were based on the mean spectra. To analyze the data with regard to the tilt and heading angle, averaged values were calculated depending on the parameter of interest. Additionally, to

analyze relative changes in reflectance, spectra from all measurement positions were normalized using the nadir spectra response values (Sandmeier et al., 1999). The resulting normalized nadir anisotropy factor ($ANIF_{band}$) produces a coefficient for each band, which individually adjusts (increases or decreases) reflectance factor values for each spectral band in relation to those recorded at nadir (Eq. 5.1). Thus, an ANIF factor of one describes an identical reflectance as recorded for a given band at nadir, while values above or below one describe higher or lower reflectance than the nadir value.

$$ANIF_{band} = \frac{Reflectance(tilt, heading)_{band}}{Reflectance(NADIR)_{band}} \quad \text{(Eq. 5.1)}$$

5.2.5 Vegetation Indices

Broadband vegetation indices (VIs) have an extensive history in remote sensing. Together with their hyperspectral counterparts they are still widely used in vegetation studies (Lucieer et al., 2014; Quemada et al., 2014). VIs commonly ratio near-infrared (NIR) and red band reflectance values in order to compensate for influences of different illumination conditions or background materials. To investigate the effect of the BRDF we examined three common VIs (Table 5.2) and calculated their values for all WPs. The Normalized Difference Vegetation Index (NDVI) uses two wavelengths in the red and NIR domain and has been widely used in a diverse range of applications. In our study we used the NDVI as proposed by Blackburn (1998). As a second index we used the Transformed Chlorophyll Absorption in Reflectance Index (TCARI) developed by Haboudane et al. (2002). TCARI was developed to predict chlorophyll absorption and uses wavelengths in the green, red and NIR spectral regions. The last index used in this study is the Red Edge Inflection Point (REIP). Originally introduced by Guyot and Baret (1988) it characterizes the inflection in the spectral red edge by calculatingthe wavelength with maximum slope. It has been used to quantify leaf chlorophyll content (Lichtenthaler et al., 1996).

Table 5.2 Vegetation indices used in this study and their underlying formulas.

Index	Formula	Reference
NDVI	(R800 − R680)/(R800 + R680)	Blackburn (1998)
TCARI	3 ((R700–R760)–0.2(R700–R550) × (R700/R670))	Haboudane et al. (2002)
REIP	700 + 40 × (((R667 + R782)/2)–R702)/(R738–R702))	Guyot and Baret (1988)

5.2.6 Data Visualization

Several different visualizations or graphics were used in this study to focus on specific features under investigation. An effective method for assessing multiangular measurements includes the use of a

segmented circular display known as a "polar plot". The polar plot shown here in Figure 5.4 represents the UAV headings and sensor tilt angles within a circular matrix and illustrates the intensity of the measurement values by applying a color to each segment. To provide a useful overview of the dataset of this study and to include as well a comparison of the reflectance in the spectral domain, multiple plots are necessary.

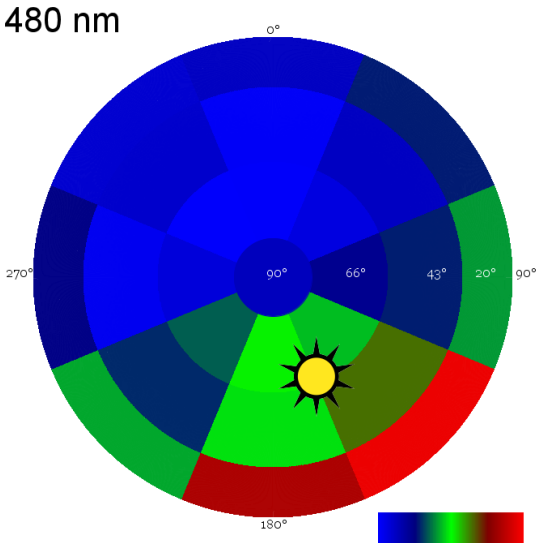

Figure 5.4 Reflectance of wheat at 480 nm measured at all 25 waypoints shown as a circular graph, or polar plot. Each "slice" represents a heading while each ring represents a sensor tilt angle. Spectral reflectance magnitude is color coded from low values of light blue, to high values in bright red. The angular position of the sun is depicted by the sun-symbol. In this figure no interpolation between waypoints is performed.

5.2.7 Radiative transfer model comparison

To compare the multiangular UAV measurements to modeled data, the SCOPE radiative transfer model was tested. The model generates the spectrum of outgoing radiation in the viewing direction as a function of vegetation structure (Tol et al., 2009). SCOPE input parameters were derived through comparison of the MERZ1 nadir spectrum with a lookup table of SCOPE spectra generated using a permutation of input parameters that were expected from wheat at the present phenological state. The resulting best-fit parameters are shown in Table 5.3.

Table 5.3 Soil-Canopy-Observation of Photosynthesis and the Energy balance model (SCOPE) input parameters: Leaf Area Index (LAI), Leaf Inclination (LIDFa), Chorophyll A/B (Cab) content in µg/cm^2, Leaf Thickness Parameter (N), Leaf water equivalent layer (Cw) in cm, Dry matter content (Cdm) in g/cm^2, Senescent material fraction (Cs), Variation in leaf inclination (LIDFb). Default values were used for all other SCOPE input parameters.

Fitted Parameters				**Constant Parameters**			
LAI	LIDFa	Cab	N	Cw	Cdm	Cs	LIDFb
3.5	−0.35	95	1.5	0.004	0.005	0.15	−0.15

Using the input parameters above, the angular module of SCOPE was run to estimate the reflectance spectra at identical angles as those measured with the UAV goniometer. Sun azimuth and zenith angles were set to match the values present at the time of the MERZ1 measurements.

5.3 Results

In this section we first present the results of the accuracy assessment of the UAV goniometer. We then summarize the results of the analysis of the MERZ1 dataset and the influence of the BRDF on the full hyperspectral data as well as on the vegetation indices. Then the BRDF effects of MERZ1 are compared to the MERZ2 dataset. Finally, we compare the data derived from the UAV goniometer with results of the SCOPE radiative transfer model.

5.3.1 Accuracy Assessment of the UAV Goniometer

Table 5.4 shows the deviation of the UAVs actual position from the planned position. Definitions of altitude and position in X and Y dimensions are commonly accepted. However, to describe the functions of vehicle and sensor heading and tilt angle, several different definitions exist. Figure 5.5 shows how heading and tilt angles were used in this study with the UAV and its spectrometer system. The average deviation in heading and tilt may differ slightly from the actual UAV spectrometer pointing error, as a small error may have been introduced during the process of replacing the spectrometer with the RGB camera in the gimbal mount using a tripod screw.

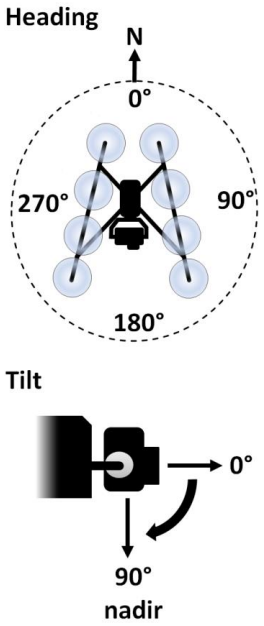

Figure 5.5 Camera orientation: Heading (azimuth) of the spectral measurements expressed in angular degrees from north. To assume a view angle of 0°, the UAV will hover north of the centeroid and aim the spectrometer at 180°. Tilt: 0° = horizontal and 90° = nadir view.

Table 5.4 Accuracy of the unmanned aerial vehicle (UAV) heading and spatial positioning calculated by structure from motion using 75 high-resolution images. Nine images were unusable due to motion induced "blur" and excluded from processing. Heading and tilt columns represent the deviation of the cameras actual pointing direction to the programmed angle. Altitude, X- and Y-position describe the deviation of the UAVs position as calculated from the differential-GPS ground-referenced structure from motion approach compared to the programmed waypoints.

Deviation of:	Heading (°)	Camera Tilt (°)	Altitude (m)	Position X (m)	Position Y (m)
Average	0.11	6.07	0.03	−1.15	−2.22
SD	8.67	1.22	0.70	0.68	0.82
Max	26.20	9.74	1.44	0.67	−0.39
Min	−17.99	3.68	−1.09	−2.79	−4.60

Movements of the airborne platform cause slight variations in the footprint of the spectrometer and introduce minor differences in the individual measurements at each waypoint. Figure 5.6 shows the average coefficient of variation (CV) of the spectral measurements acquired at all WP during the MERZ1 flight. CV values within the blue and red regions of the spectrum are between 5% and 6%; in the green portion the value is approximately 4%. The CV in the NIR is less than 1.5%.

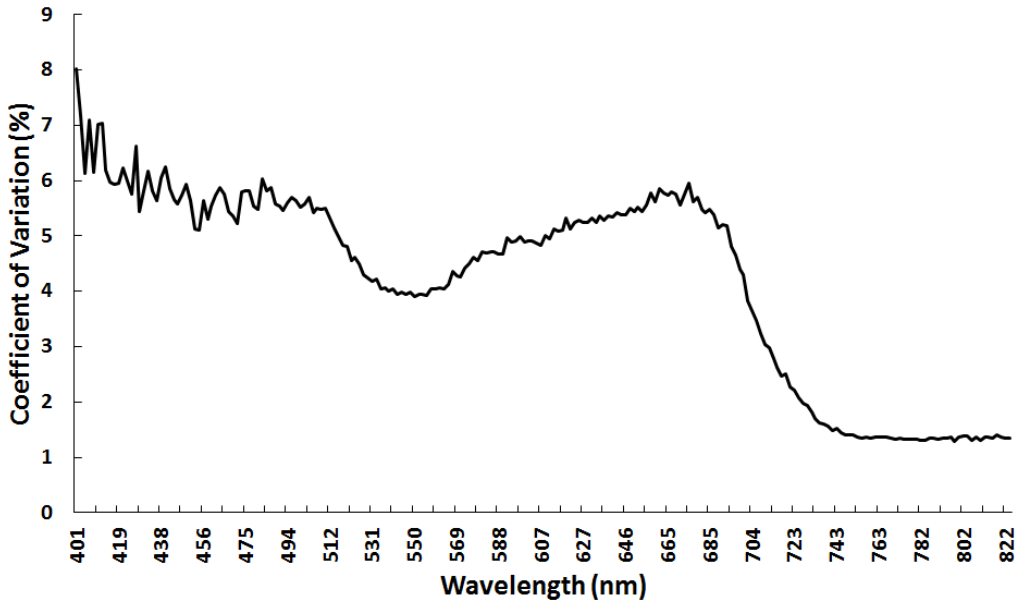

Figure 5.6 The spectrometer of the unmanned aerial vehicle goniometer was triggered three times at each waypoint. This figure shows the overall variation of the three spectra measured at each waypoint as average for the MERZ1 dataset.

5.3.2 Full Spectrum Analysis

In Figure 5.7 the ANIF for the MERZ1 dataset is shown for a tilt of 66°. All spectral measurements acquired at headings between 90° and 225° exceed nadir values, with the largest increases seen in measurements taken within the blue spectral region. When heading parameters are examined, the 180° heading shows an increase of approximately 95% (the highest). The 90° measurement shows the lowest increase at approximately 25%. Deviation for these headings show a gradual decrease until the

Table 5.5 Normalized nadir anisotropy factor (ANIF) values for five characteristic wavelengths in the blue (480 nm), green (550 nm), red (680 nm) spectral bands; red-edge-inflection-point (REIP) (733 nm) and near-infrared (NIR) (780 nm) for 20°, 43° and 66° tilt, as well as all headings together with their average values. Values greater than 1 (blue bar) represent spectral reflectance measurements greater than nadir; values below 1 (red bar) represent measurements less than nadir. The suns azimuth was 155° and elevation 66°.

		heading								
tilt	nm	0°	45°	90°	135°	180°	225°	270°	315°	average
20°	481	0.98	1.36	1.66	3.02	2.71	1.69	1.26	0.91	1.70
43°	481	0.72	0.98	1.36	2.24	1.83	1.39	0.76	0.93	1.28
66°	481	0.71	0.83	1.22	1.74	1.93	1.52	0.86	0.70	1.19
20°	550	1.12	1.35	1.58	2.71	2.49	1.63	1.32	1.09	1.66
43°	550	0.86	1.04	1.35	2.09	1.76	1.39	0.85	0.99	1.29
66°	550	0.76	0.89	1.19	1.62	1.74	1.42	0.90	0.78	1.16
20°	681	0.74	1.08	1.32	2.51	2.31	1.33	0.98	0.70	1.37
43°	681	0.59	0.81	1.15	1.96	1.56	1.21	0.60	0.77	1.08
66°	681	0.63	0.79	1.12	1.63	1.74	1.38	0.81	0.69	1.10
20°	733	1.27	1.34	1.43	1.89	1.81	1.44	1.34	1.26	1.47
43°	733	1.17	1.22	1.35	1.64	1.52	1.35	1.13	1.18	1.32
66°	733	0.99	1.05	1.18	1.33	1.41	1.27	1.05	0.98	1.16
20°	780	1.27	1.30	1.36	1.61	1.56	1.37	1.29	1.26	1.38
43°	780	1.25	1.27	1.33	1.49	1.42	1.32	1.25	1.25	1.32
66°	780	1.10	1.11	1.19	1.25	1.34	1.25	1.12	1.06	1.18
	average	0.94	1.09	1.32	1.91	1.81	1.40	1.03	0.97	

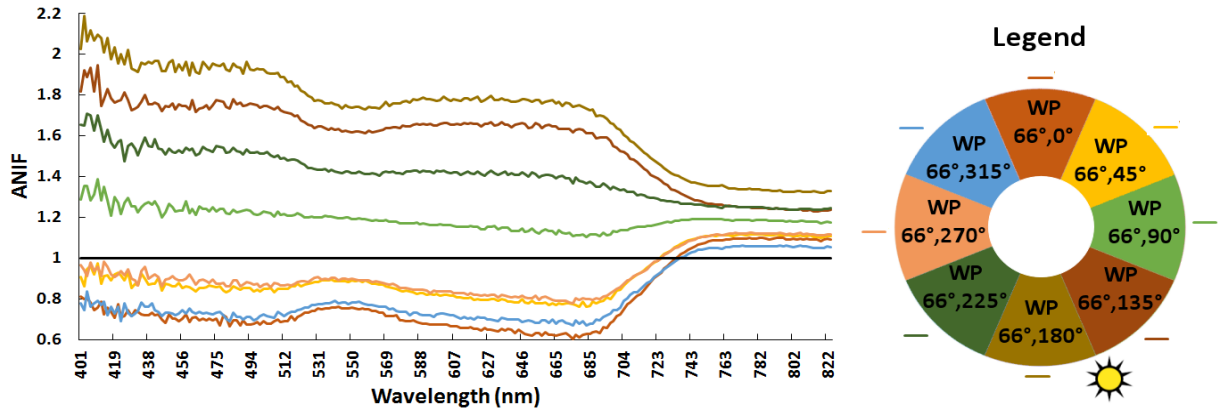

Figure 5.7 To present the angular influence at different waypoints on the full spectrum the normalized nadir anisotropy factor (ANIF) of 66° tilt for all headings at MERZ1 from 400 to 823 nm is plotted as example. By using the ANIF notation spectral deviation of single waypoints is referred to the nadir waypoint and thus can be relatively compared. A waypoint with the same spectrum as nadir would remain at an ANIF of 1 throughout all wavelengths. The legend on the right represents the color of each ANIF curve and depicts their respective heading angle. The azimuth position of the sun (155°) is visualized by the sun symbol.

red edge position where values for 135°, 180° and 225° headings drop to range between 25% and 30%.

For all these WP, the deviation decreases in the green spectral region. At headings of 0°, 45°, 270° and

315° reflectance measurements are 10% to 30% lower than nadir within the blue spectra. Until the red edge spectral region is reached, reflectance values decrease from 20% to 40% below the nadir measurement. In the red edge region the reflectance increases to approximately 10% above that of the nadir measurement.

This shape of the ANIF which was observed for the 66° sensor tilt angle can also be found for the other tilt angles used in the overflights. Table 5.5 shows the ANIF for five regions of the spectrum for all investigated tilt and heading angles. For all wavelengths the ANIF decreases with increase of the tilt angle. Only for most of the VIS region with heading from 180° to 270° the ANIF is smaller in the 43° tilt than in the 66°. On average the reflectance of the 135° and 180° show the highest increase from nadir with 191% and 181%, respectively. Lower reflectance values than in nadir are seen in the VIS spectral region with headings of 0°, 45°, 270° and 315°. At 0° and 315° even the average of all tilt reflection values is lower than in nadir.

5.3.3 Vegetation Indices

NDVI values range from 0.83 (WP 20°, 135°) to 0.95 (WP 43°, 0°), compared to the nadir value of 0.89. Values decrease for each tilt angle as the 135° heading is approached and generally increase toward the 0° heading, with an increase seen only at the WP (43°, 270°). On average, the 43° tilt yields the highest NDVI value with 0.92 (within a range of 0.86–0.95) while the 20° and 66° tilt parameters show an average NDVI of 0.9 (0.83–0.94, and 0.86–0.94, respectively). Relative differences from nadir NDVI range between −6.5% and 6.2%. The relative mean absolute difference is 3.3 percent. The 90° and the 225° headings show the smallest differences from the nadir NDVI. Aside from the 135° and 180° headings, all WPs return higher NDVI values when compared with the nadir position. The tilt angle has only a minor influence on the relative difference (Figure 5.8). TCARI values vary with UAV heading, ranging from 0.04 (WP 66°, 315°) to 0.116 (WP 20°, 135°), against a nadir value of 0.046. This pattern is opposite as observed for NDVI. Vehicle heading values vary systematically, increasing (for all tilt angles) towards 135° and decreasing as the 0° heading is approached. As seen for the NDVI, WP (43°, 270°) poses an exception with a lower TCARI value.

Sensor tilt parameter variability can be briefly summarized. The 20° tilt setting shows the highest mean TCARI value of 0.078 (within a range of 0.06–0.116); the 43° setting yields a mean TCARI value of 0.062 (with a range of 0.046–0.090) and the 66° tilt shows mean TCARI of 0.053 (range 0.038–0.074). In relative terms, the differences from the nadir TCARI range from −16.8% to 153.2%. The relative mean absolute difference is 40%. Most WPs greatly surpass the nadir TCARI value; at a sensor tilt of 20° no TCARI value is smaller than the nadir value at 43° only a single value is smaller and at tilt = 66° four values are smaller than the nadir value. The tilt parameter is shown to have a significant influence on

the relative difference. From 20° to 60° the relative mean absolute difference decreases from 69% to 25% (Figure 5.8 bottom).

The Red Edge Inflection Point (REIP) was also analyzed in this study (Figure 5.8). For nadir spectral measurements the REIP is approximately 733 nm. WP (20°, 135°) shows the lowest REIP (approximately 729 nm) while WP (66°, 0°) shows the highest REIP (735 nm). The average REIP value was slightly lower than the nadir value with 732.5 nm. At all WPs, measurements acquired at a heading of 135° show the lowest values; these increase towards the 0° heading. All the WPs measured with a sensor tilt angle of 20° surpass the nadir REIP. Measurements acquired at tilts of 43° and 66° produced two, respectively, 4 values that are smaller than the nadir value. The overall mean absolute difference was less than 0.2%, decreasing from approximately 0.3% at 20° tilt to 0.15% at 66° tilt.

5.3.4 Diurnal Variations of angular effects

Ideal clear weather conditions were present over the Merzenhausen study area throughout 18 June 2013. Sequencing a pair of overflights enabled us to compare these two datasets and analyze how the

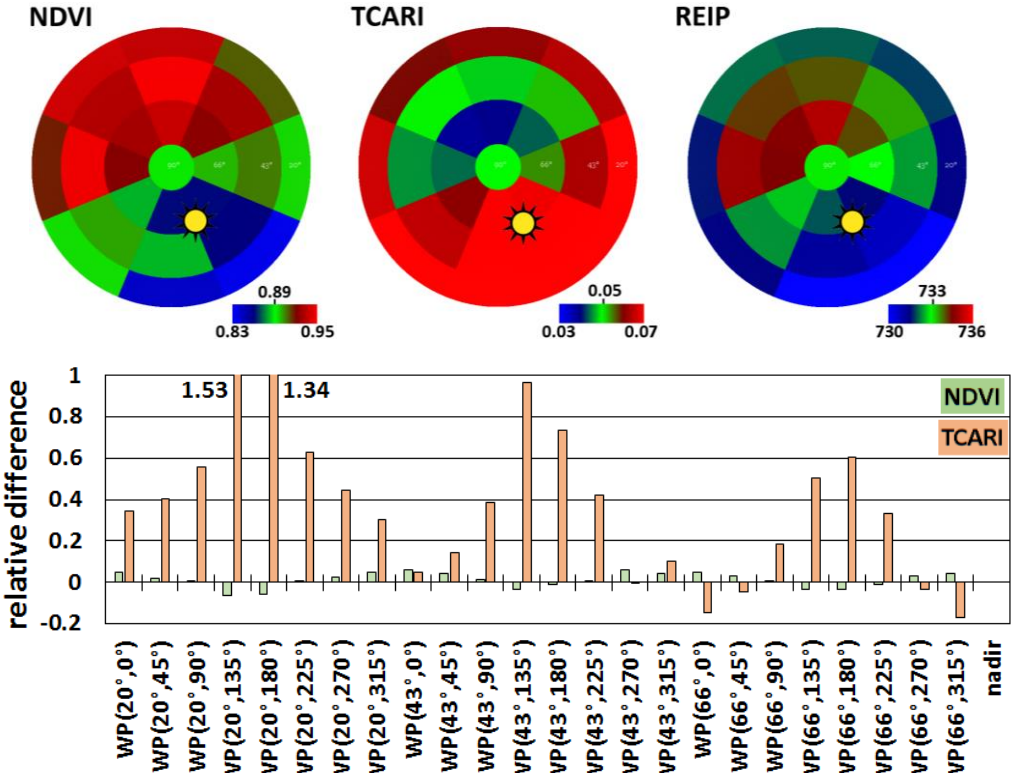

Figure 5.8 Top: Absolute values for the NDVI, TCARI and REIP compared to the nadir value (center of the polar plot) for all waypoints of MERZ1. The range of values is chosen with nadir as center value, respectively, for each plot. Figure 5.5 details the angular arrangement depicted here. Bottom: Relative differences for NDVI and TCARI compared to the nadir value.

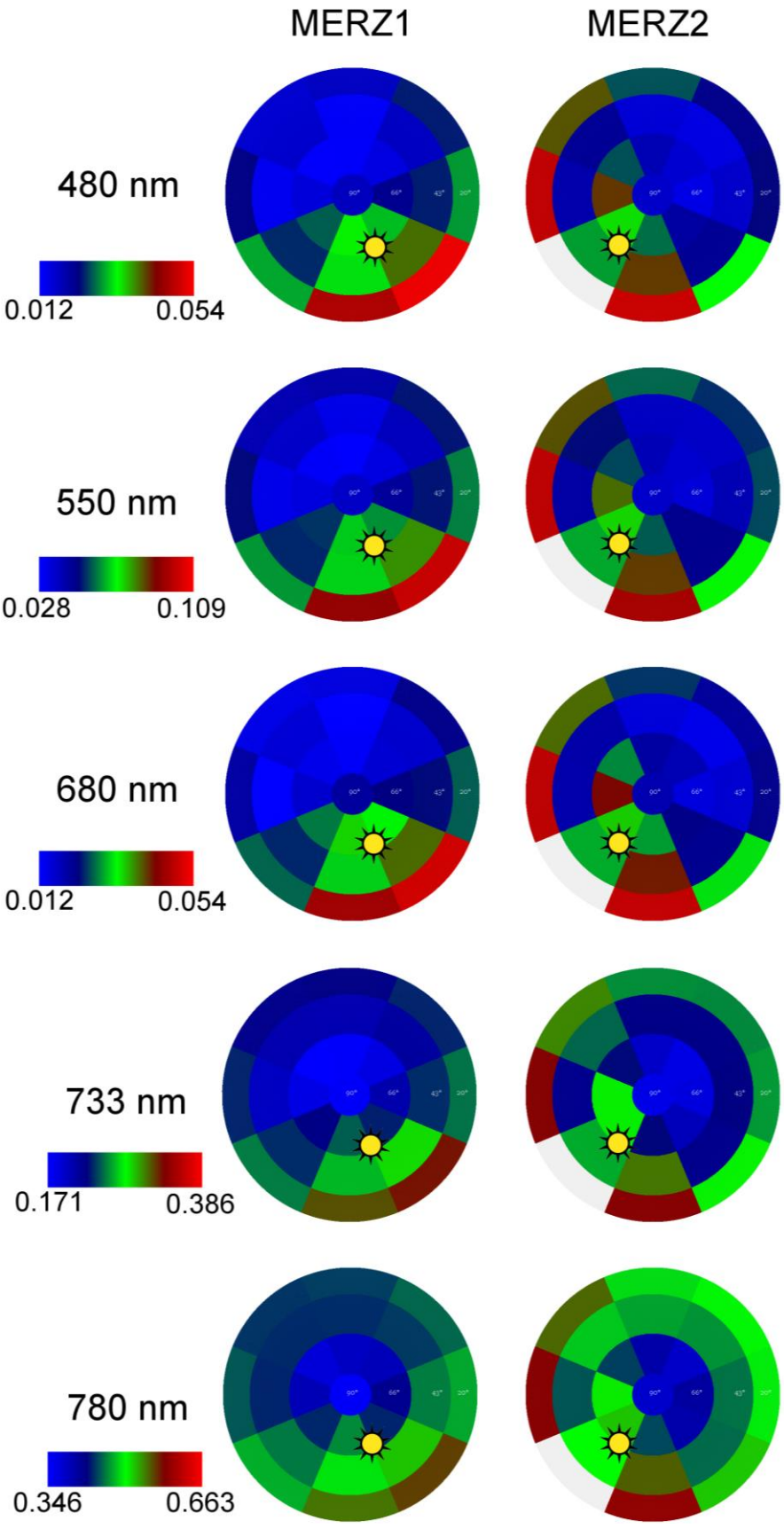

Figure 5.9 Reflection of MERZ1 and MERZ2 for 5 wavelengths of interest. The color legend of reflection for each horizontal pair was scaled to the occurring reflectance wavelength range. Figure 5.5 details the angular arrangement depicted here. Waypoint (20°, 225°) is missing in MERZ2 and coded in this graphic in grey.

change in sun illumination affects multiangular sensor response (Figure 5.9). Nadir measurements remained consistent during the day. However, significant changes in target response (including hotspot and backscattering features) were observed at lower sensor tilt angles, dependent on sun position (Table 5.1). These features show distinct spectral differences within the five different wavelengths (Figure 5.7 and Table 5.5). The hotspot feature is clearly visible and is characterized by higher spectral reflectance values within the shorter blue and green wavelengths. These spectral differences are less apparent in the infrared wavelengths.

Figure 5.9 shows the angular distribution of reflectance in five selected wavelengths of interest: 480 nm (blue), 550 nm (green), 680 nm (red), 733 nm (Red-REIP) and 780 nm (NIR). All bands show the directional effect of increased reflectance values as heading angles approach 180°, and decreased reflectance with the opposite orientation. This effect is most pronounced in the shorter spectral wavelengths (up to 680 nm) and is less characteristic in the NIR region. Angular distribution differs in MERZ1 and MERZ2. Elevated reflectance values cluster between 135° and 180° headings in the MERZ1 dataset, while in MERZ2 this phenomena is oriented to heading angles between 180° and 225°.

5.3.5 Flying goniometer vs. radiative transfer model

Results of the comparison between the scope model and the flying spectrometer measurements are shown in Figure 5.10 for exemplary wavelengths of 550 nm and 780 nm. Correlation of angular measurements with modeled data show clear differences in wavelengths and tilt angles. To test this

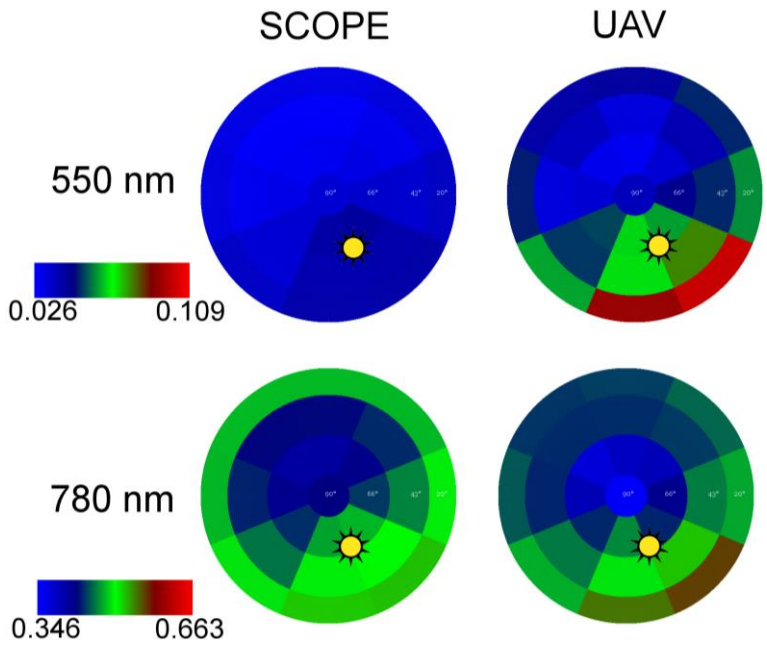

Figure 5.10 Comparison of modeled angular reflectance Soil-Canopy-Observation of Photosynthesis and the Energy balance (SCOPE) with the unmanned aerial vehicle (UAV) measured values for MERZ1. Shown are two exemplary wavelengths, which are scaled to the present range of values.

Table 5.6 Correlation of modeled data with measured data for different tilt angles.

Tilt	**20°**	**43°**	**66°**
Correlation (R^2)	0.2504	0.7484	0.8819

hypothesis, ANIF values were calculated for both datasets. Our comparison included sensor tilt angles of 66°, 43° and 20° and wavelengths at 480 nm, 570 nm, 680 nm and 750 nm. Correlation statistics (r^2) were calculated for the linear regression of UAV-ANIF against SCOPE-ANIF. While SCOPE produces results similar to UAV measurements at high tilt angles, r^2 is low at the 20° angle (Table 5.6). In the spectral domain the maximum UAV reflectance/SCOPE model r^2 was found in the NIR (750 nm); the lowest correlation value was derived for the 680 nm spectral wavelength (Table 5.7).

Table 5.7 Correlation of modeled data with measured data for all tilt angles at specific wavelengths.

Wavelength	**480 nm**	**570 nm**	**680 nm**	**750 nm**
Correlation (r^2)	0.4298	0.5685	0.3605	0.815

5.4 Discussion

In this study, a new goniometer approach for large-scale measurement of BRDF is presented and an initial hyperspectral dataset is analyzed. By deploying the spectrometer on a rotary-wing UAV there is no longer a need to mount the instrument on large ground-based positioning structures. The large FOV has the advantage of averaging out small variations, which are part of the canopies variability. As the device is flying, surfaces can be investigated with desired measurement patterns even over areas inaccessible by land and without disturbing the eventual surface cover like vegetation. Until now these areas had to be approached using satellites or by modeling (Gastellu-Etchegorry et al., 1999). In remote sensing applications, where goniometers cannot be deployed, angular effects are currently minimized or correction approaches are applied: field-spectrometer measurements are carried out around the same time (noon) and from nadir view (Aasen et al., 2014). Thus the sun-object-sensor geometry is almost stable. For UAV-, air- and spaceborne systems a number of correction methods have been developed. These include the use of image statistic based methods for flat terrain (Kennedy et al., 1997) and physical or semi-empirical models such as for the processing of MODIS data (Wanner et al., 1997). Lately, a more generic BRDF correction method was introduced, which builds on a surface cover characterization (Schläpfer et al., 2015). Since physical and empirical models are based on the current knowledge and BRDF effects depend on many factors, the flying goniometer could help to evaluate and eventually improve the correction methods.

We assessed the pointing accuracy of the UAV system and found it to be of acceptable accuracy for a GPS-aided flying system, although it is still not as precise as ground-based instrumentation (Peltoniemi et al., 2014; Sandmeier et al., 1999). Parameters of altitude, X/Y position and sensor tilt angle are highly

accurate within the navigation grade GPS specifications. Additionally, the remounting of the RGB camera described in Section 5.2.2 might have introduced an artificial error. The relative position as described by the low standard deviation demonstrates the precision of the system (Table 5.4). However, the vehicle heading parameters are less accurate. Relative heading inaccuracies may be ascribed to the Falcon-8 flight control system, which does not make use of a magnetic compass. If operated in an environment with a strong magnetic field, a compass system could produce serious errors in vehicle position and heading readings and cause catastrophic UAV failures. However, in the case of the UAV goniometer, the accuracy would improve through the use of a compass system for heading correction.

Additional sources of error in the platform/sensor system are found in gimbal calibration in the tilt axis and during the process of physically mounting the spectrometer on the gimbal. Inconsistencies in either or both of these procedures will lead to pointing offsets. The system could also be improved by deploying the spectrometer and a RGB camera in tandem, triggering both simultaneously. Camera and spectrometer could be aligned and calibrated in the laboratory to determine the spectrometer field of view in the camera image. The camera imagery could then be utilized to accurately calculate the position and pointing of the UAV using the structure from motion approach used in this study to evaluate the pointing accuracy (Section 5.2.2).

The UAV system in combination with the “mAngle” software enables users to plan, setup and perform a multiangular flight around a center point of interest efficiently and quickly (in less than 30 min, 10 min for the measurement flight itself). In addition, the UAV and spectrometer system is deployed in a single, easily portable package, making it highly mobile. Since the completion of this study, the system has been deployed at a number of other sites in Europe and New Zealand. The large radius and thus big footprint of the UAV ensures a good averaging over the fine structure of the vegetation (e.g., leaves, shaded areas, stems). This was assessed by calculating standard deviation of multiple spectra at the same waypoint (Figure 5.6) and shows good agreement of consecutive spectra taken at the same WP. If smaller footprints are desired the flying radius can be reduced or the spectrometer can be equipped with a fore optic with a narrower FOV.

The results of the multiangular reflectance measurements acquired in this study are consistent with previous measurements characterizing common angular reflectance distribution over vegetation (Strub et al., 2002). The common hotspot feature is clearly visible in the data and changes over time with sun angle. High levels of reflectance were found at the rather low tilt angle of 20° in the heading of the hotspot. As the tilt angle is lower than the hotspot feature, these high levels might be introduced by a viewing angle, whereas only the very top of the canopy is seen by the sensor (Figure 5.9). Along

with the results of our accuracy assessment of UAV imagery pointing and of the spectral domain response, we are confident that we have utilized a novel platform-sensor combination to acquire a valid and valuable hyperspectral dataset.

The complete spectrum analysis emphasizes that BRDF effects are both wavelength and angle dependent. Around the hot spot the measured reflection is higher than in nadir, in both in the VIS and NIR part of the spectrum. For WPs towards the dark spot the reflectance is lower in most parts of the VIS and higher in the NIR. Overall, lower sensor tilt angles increase reflectance compared with the nadir position. While the NDVI reduces angular effects quite efficiently, these effects were a significant factor in TCARI. This distinction can be ascribed primarily to the differing formula structures of the two VIs. For the NDVI, the reflectance in the NIR dominates the nominator of the formula. Thus the differences due to the observation angle influence the index nominator and denominator in similar ways and the entire ratio only slightly changes. The TCARI formula does not provide such normalization. The reflection factors at the wavelength of the first part of the term (R700–R760) are differently influenced by the angle (Figure 5.8) and introduce strong fluctuations to the VI. Minor influences are introduced by the second term. The first part (R700–R550) of the second term is not strongly influenced, since both reflection factors of the wavelengths are affected similarly by the angle. However, the second component of TCARI again uses the R700 and R760 band ratio. This increases the variations in the second term of the formula caused by the differing observation angles. In combination, these factors produce the significant differences (up to 150 percent), which are seen in the TCARI values. Differing observation angles cause only minor fluctuations in REIP values. As seen with NDVI, formula deviation normalizes most of the variation in REIP values. However, it must be emphasized that, as for most VIs, the practical dynamic range of the REIP is narrower than what is theoretically possible. Thus even the small observation angle variances suggested by the REIPs results could lead to errors in interpreting this index if BRDF effects are disregarded. Other studies have been carried out for other VIs or vegetation cover (Epiphanio and Huete, 1995; Kuusk, 1991; Leblanc et al., 1997; Verrelst et al., 2008) support the angular dependency found in this study.

Radiative transfer models show significant potential as tools for correcting angular influences introduced by solar effects or imaging sensors. They are based on existing theory of radiative transfer and plant physiology (Tol et al., 2009). So far, real world multiangular data for various vegetation covers are rare and thus, a rigorous validation of the model is challenging. With the approach described in this study datasets for the validation and improvement of those methods may be generated. However, it has to be taken into account that SCOPE does not account for certain sensor variables such as FOV and FWHM. Due to the footprint of the spectrometer, light reflected at different angles by the canopy is

collected by the sensor. Thus, this might be one source for the increasing discrepancies towards low tilt angles observed in this study. Following studies could minimize this effect by using spectrometer fore optics with narrower FOV. A careful investigation on the difference between modeled and measured spectra go beyond the scope of this study but should be investigated in the future.

Based on this study, we strongly encourage the extensive compilation of multiangular datasets for various vegetation cover types and environments. A more sophisticated knowledge base regarding vegetation angular effects could also enable researchers to derive accurate complementary information through the use of angular measurements that capture vegetation features not typically visible from a nadir perspective (Schlerf and Atzberger, 2012). Additionally, these results could help to understand influences of BRDF effects in imaging spectroscopy. Typically, current hyperspectral (image-frame and push broom) imaging systems as well as RGB systems have a FOV of up to 50° (Lucieer et al., 2014). Thus, pixels captured towards the edges of the image have tilt angles of about 66°. As shown here, angular effects have a significant contribution to these observation angles and need to be taken into account during analysis. To improve the correction of these effects consecutive studies should examine tilt angles found in the FOV of common UAV and airborne sensors. This is foreseen within a number of parallel research activities that are ongoing and focused on improving models and collecting spectral databases. These include COST Action ES0903 EUROSPEC, COST Action ES1309 OPTIMISE, and the SPECCHIO online spectral database (Hueni et al., 2009). These projects could also serve as a basis for enhanced training of models leading to highly accurate correction methods.

5.5 Conclusions

This study presents a novel hyperspectral (338 to 823 nm) goniometer system based on an unmanned aerial vehicle (UAV) and specifically developed software. The approach allows measurements over inaccessible areas and without disturbing the surface cover. Using the system in an exemplary field experiment, we test the positioning and spectral accuracy (VIS < 6% CV, NIR < 1.5% CV) While a larger footprint can be analyzed, this UAV system does not provide the same absolute pointing accuracy as common ground based goniometers. With the presented field data we highlight the influence of angular effects on the spectrum (0.6 to 3 fold relative difference) and vegetation indices (up to more than 1.5 fold relative difference) and thus the necessity for correction of angular effects in remote sensing data. Radiative transfer models like SCOPE represent an opportunity for angular corrections, but differ especially for low tilt angles from the UAV goniometer data. The fast and flexible UAV goniometer contributes a technique to assess angular effects over any given land cover with low efforts. Based on this assessment of relevant reflection parameters a new way of UAV-driven plant

parameter retrieval by the inclusion of oblique angels could be developed. Finally, we hope to contribute additional understanding to the broad and complex topic of BRDF in vegetation.

Acknowledgments

The authors thank Christian van der Tol for the preparation of the SCOPE exercise used in this study. Also, the authors acknowledge the funding of the CROP.SENSe.net and PhenoCrops project in the context of the Ziel 2-Programms NRW 2007–2013 “Regionale Wettbewerbsfähigkeit und Beschäftigung” by the Ministry for Innovation, Science and Research (MIWF) of the state North Rhine Westphalia (NRW) and European Union Funds for regional development (EFRE) (005-1103-0018). We also acknowledge the contribution of Mr. Joseph Scepan of Medford, Oregon, USA, in producing this document.

Author Contributions

Andreas Burkart developed the measurement system and participated in data analysis that was designed and led by Helge Aasen. Luis Alonso created multiangular flight patterns and contributed practical expertise in bidirectional effects characterization and spectrometer calibration. Gunter Menz gave essential scientific advice and contributed a major part of lecturing of the manuscript. Georg Bareth participated in spectral data analysis and interpretation and discussion of the results. Uwe Rascher did supervise the methodologies and provided the fundamental question that led to the research.

Conflicts of Interest

The authors declare no conflict of interest.

5.6 References

Aasen, H., Gnyp, M.L., Miao, Y., Bareth, G., 2014. Automated Hyperspectral Vegetation Index Retrieval from Multiple Correlation Matrices with HyperCor. Photogramm. Eng. Remote Sens. 80, 785–795. doi:10.14358/PERS.80.8.785

Andrieu, B., Baret, F., Jacquemoud, S., Malthus, T., Steven, M., 1997. Evaluation of an improved version of SAIL model for simulating bidirectional reflectance of sugar beet canopies. Remote Sens. Environ. 60, 247–257. doi:10.1016/S0034-4257(96)00126-5

Barnes, W.L., Pagano, T.S., Salomonson, V.V., 1998. Prelaunch characteristics of the Moderate Resolution Imaging Spectroradiometer (MODIS) on EOS-AM1. IEEE Trans. Geosci. Remote Sens. 36, 1088–1100. doi:10.1109/36.700993

Barnsley, M.J., Settle, J.J., Cutter, M.A., Lobb, D.R., Teston, F., 2004. The PROBA/CHRIS mission: a low-cost smallsat for hyperspectral multiangle observations of the Earth surface and atmosphere. IEEE Trans. Geosci. Remote Sens. 42, 1512–1520. doi:10.1109/TGRS.2004.827260

Blackburn, G.A., 1998. Spectral indices for estimating photosynthetic pigment concentrations: A test using senescent tree leaves. Int. J. Remote Sens. 19, 657–675. doi:10.1080/014311698215919

Bourgeois, C.S., Ohmura, A., Schroff, K., Frei, H.-J., Calanca, P., 2006. IAC ETH Goniospectrometer: A Tool for Hyperspectral HDRF Measurements. J. Atmospheric Ocean. Technol. 23, 573–584. doi:10.1175/JTECH1870.1

Buchhorn, M., Petereit, R., Heim, B., 2013. A Manual Transportable Instrument Platform for Ground-Based Spectro-Directional Observations (ManTIS) and the Resultant Hyperspectral Field Goniometer System. Sensors 13, 16105–16128. doi:10.3390/s131216105

Burkart, A., Cogliati, S., Schickling, A., Rascher, U., 2014. A Novel UAV-Based Ultra-Light Weight Spectrometer for Field-spectroscopy. IEEE Sens. J. 14, 62–67. doi:10.1109/JSEN.2013.2279720

Burkhart, J.F., Bogren, W.S., Storvold, R., Pedersen, C.A., Gerland, S., Vauuav Science Team, 2010. A new measure of BRDF, banking on UAS measurements, in: Proceedings of the AGU Fall Meeting Abstracts.

Busetto, L., Meroni, M., Crosta, G.F., Guanter, L., Colombo, R., 2011. SpecCal: Novel software for in-field-spectral characterization of high-resolution spectrometers. Comput. Geosci. 37, 1685–1691. doi:10.1016/j.cageo.2010.12.005

Comar, A., Baret, F., Viénot, F., Yan, L., de Solan, B., 2012. Wheat leaf bidirectional reflectance measurements: Description and quantification of the volume, specular and hot-spot scattering features. Remote Sens. Environ. 121, 26–35. doi:10.1016/j.rse.2011.01.028

Deering, D.W., Eck, T.F., Banerjee, B., 1999. Characterization of the Reflectance Anisotropy of Three Boreal Forest Canopies in Spring–Summer. Remote Sens. Environ. 67, 205–229. doi:10.1016/S0034-4257(98)00087-X

Deschamps, P.-Y., Breon, F.-M., Leroy, M., Podaire, A., Bricaud, A., Buriez, J.-C., Seze, G., 1994. The POLDER mission: instrument characteristics and scientific objectives. IEEE Trans. Geosci. Remote Sens. 32, 598–615. doi:10.1109/36.297978

Epiphanio, J.N., Huete, A.R., 1995. Dependence of NDVI and SAVI on sun/sensor geometry and its effect on fAPAR relationships in Alfalfa. Remote Sens. Environ. 51, 351–360. doi:10.1016/0034-4257(94)00110-9

Fassnacht, F., Koch, B., 2012. Review of forestry oriented multi-angular remote sensing techniques. Int. For. Rev. 14, 285–298. doi:10.1505/146554812802646602

Gastellu-Etchegorry, J.P., Guillevic, P., Zagolski, F., Demarez, V., Trichon, V., Deering, D., Leroy, M., 1999. Modeling BRF and Radiation Regime of Boreal and Tropical Forests. Remote Sens. Environ. 68, 281–316. doi:10.1016/S0034-4257(98)00119-9

Gnyp, M.L., Yu, K., Aasen, H., Yao, Y., Huang, S., Miao, Y., Bareth, G., 2013. Analysis of Crop Reflectance for Estimating Biomass in Rice Canopies at Different Phenological Stages. Photogramm. - Fernerkund. - Geoinformation 2013, 351–365. doi:10.1127/1432-8364/2013/0182

Grenzdörffer, G.J., Niemeyer, F., 2011. UAV based BRDF-measurements of agricultural surfaces with PFIFFikus. Int. Arch. Photogramm. Remote Sens. Spat. Inf. Sci. 38, 229–234.

Guyot, N., Baret, F., 1988. Utilisation de la haute resolution spectrale pour suivre l'etat des couverts vegetaux, in: Proceedings of the 4th International Colloquium on Spectral Signatures of Objects in Remote Sensing. Presented at the 4th International Colloquium on Spectral Signatures of Objects in Remote Sensing, NASA Astrophysics Data System, Aussois, France, pp. 279–286.

Haboudane, D., Miller, J.R., Tremblay, N., Zarco-Tejada, P.J., Dextraze, L., 2002. Integrated narrow-band vegetation indices for prediction of crop chlorophyll content for application to precision agriculture. Remote Sens. Environ. 81, 416–426.

Hakala, T., Suomalainen, J., Peltoniemi, J.I., 2010. Acquisition of Bidirectional Reflectance Factor Dataset Using a Micro Unmanned Aerial Vehicle and a Consumer Camera. Remote Sens. 2, 819–832. doi:10.3390/rs2030819

Honkavaara, E., Markelin, L., Hakala, T., Peltoniemi, J.I., 2014. The Metrology of Directional, Spectral Reflectance Factor Measurements Based on Area Format Imaging by UAVs. Photogramm. - Fernerkund. - Geoinformation 2014, 175– 188. doi:10.1127/1432-8364/2014/0218

Hueni, A., Nieke, J., Schopfer, J., Kneubühler, M., Itten, K.I., 2009. The spectral database SPECCHIO for improved long-term usability and data sharing. Comput. Geosci. 35, 557–565. doi:10.1016/j.cageo.2008.03.015

Kennedy, R.E., Cohen, W.B., Takao, G., 1997. Empirical methods to compensate for a view-angle-dependent brightness gradient in AVIRIS imagery. Remote Sens. Environ. 62, 277–291. doi:10.1016/S0034-4257(97)00111-9

Kuusk, A., 1991. The angular distribution of reflectance and vegetation indices in barley and clover canopies. Remote Sens. Environ. 37, 143–151. doi:10.1016/0034-4257(91)90025-2

Kuusk, J., 2011. Dark Signal Temperature Dependence Correction Method for Miniature Spectrometer Modules. J. Sens. 2011, 1–9. doi:10.1155/2011/608157

Leblanc, S.G., Chen, J.M., Cihlar, J., 1997. NDVI Directionality in Boreal Forests: A Model Interpretation of Measurements. Can. J. Remote Sens. 23, 369–380. doi:10.1080/07038992.1997.10855222

Lichtenthaler, H.K., Gitelson, A., Lang, M., 1996. Non-Destructive Determination of Chlorophyll Content of Leaves of a Green and an Aurea Mutant of Tobacco by Reflectance Measurements. J. Plant Physiol. 148, 483–493. doi:10.1016/S0176-1617(96)80283-5

Lucieer, A., Malenovský, Z., Veness, T., Wallace, L., 2014. HyperUAS-Imaging Spectroscopy from a Multirotor Unmanned Aircraft System: HyperUAS-Imaging Spectroscopy from a Multirotor Unmanned. J. Field Robot. 31, 571–590. doi:10.1002/rob.21508

Mahlein, A.-K., Rumpf, T., Welke, P., Dehne, H.-W., Plümer, L., Steiner, U., Oerke, E.-C., 2013. Development of spectral indices for detecting and identifying plant diseases. Remote Sens. Environ. 128, 21–30. doi:10.1016/j.rse.2012.09.019

mAngle, 2015. URL https://github.com/wemperor/mAngle/releases (accessed 1.8.15).

Milton, E.J., 1987. Principles of field-spectroscopy. Int. J. Remote Sens. 8, 1807–1827. doi:10.1080/01431168708954818

Morton, D.C., Nagol, J., Carabajal, C.C., Rosette, J., Palace, M., Cook, B.D., Vermote, E.F., Harding, D.J., North, P.R.J., 2014. Amazon forests maintain consistent canopy structure and greenness during the dry season. Nature 506, 221–224. doi:10.1038/nature13006

Nicodemus, F.E., 1965. Directional Reflectance and Emissivity of an Opaque Surface. Appl. Opt. 4, 767. doi:10.1364/AO.4.000767

Nolin, A.W., Liang, S., 2000. Progress in bidirectional reflectance modeling and applications for surface particulate media: Snow and soils. Remote Sens. Rev. 18, 307–342. doi:10.1080/02757250009532394

Peltoniemi, J.I., Hakala, T., Suomalainen, J., Honkavaara, E., Markelin, L., Gritsevich, M., Eskelinen, J., Jaanson, P., Ikonen, E., 2014. Technical notes: A detailed study for the provision of measurement uncertainty and traceability for goniospectrometers. J. Quant. Spectrosc. Radiat. Transf. 146, 376–390. doi:10.1016/j.jqsrt.2014.04.011

Peltoniemi, J.I., Kaasalainen, S., Naranen, J., Matikainen, L., Piironen, J., 2005. Measurement of directional and spectral signatures of light reflectance by snow. IEEE Trans. Geosci. Remote Sens. 43, 2294–2304. doi:10.1109/TGRS.2005.855131

Penuelas, J., Pinol, J., Ogaya, R., Filella, I., 1997. Estimation of plant water concentration by the reflectance Water Index WI (R900/R970). Int. J. Remote Sens. 18, 2869–2875. doi:10.1080/014311697217396

Qin, W., Goel, N.S., 1995. An evaluation of hotspot models for vegetation canopies. Remote Sens. Rev. 13, 121–159. doi:10.1080/02757259509532299

Quemada, M., Gabriel, J., Zarco-Tejada, P., 2014. Airborne Hyperspectral Images and Ground-Level Optical Sensors As Assessment Tools for Maize Nitrogen Fertilization. Remote Sens. 6, 2940–2962. doi:10.3390/rs6042940

Sandmeier, S.R., Itten, K., others, 1999. A field goniometer system (FIGOS) for acquisition of hyperspectral BRDF data. Geosci. Remote Sens. IEEE Trans. On 37, 978–986. doi:10.1109/36.752216

Schaepman-Strub, G., Schaepman, M.E., Painter, T.H., Dangel, S., Martonchik, J.V., 2006. Reflectance quantities in optical remote sensing—definitions and case studies. Remote Sens. Environ. 103, 27–42. doi:10.1016/j.rse.2006.03.002

Schläpfer, D., Richter, R., Feingersh, T., 2015. Operational BRDF Effects Correction for Wide-Field-of-View Optical Scanners (BREFCOR). IEEE Trans. Geosci. Remote Sens. 53, 1855–1864. doi:10.1109/TGRS.2014.2349946

Schlerf, M., Atzberger, C., 2012. Vegetation Structure Retrieval in Beech and Spruce Forests Using Spectrodirectional Satellite Data. IEEE J. Sel. Top. Appl. Earth Obs. Remote Sens. 5, 8–17. doi:10.1109/JSTARS.2012.2184268

Strub, G., Beisl, U., Schaepman, M., Schlaepfer, D., Dickerhof, C., Itten, K., 2002. Evaluation of diurnal hyperspectral HDRF data acquired with the RSL field goniometer during the DAISEX'99 campaign. ISPRS J. Photogramm. Remote Sens. 57, 184–193. doi:10.1016/S0924-2716(02)00122-3

Tian, Y., 2004. Comparison of seasonal and spatial variations of leaf area index and fraction of absorbed photosynthetically active radiation from Moderate Resolution Imaging Spectroradiometer (MODIS) and Common Land Model. J. Geophys. Res. 109. doi:10.1029/2003JD003777

Tol, van der C., Verhoef, W., Timmermans, J., Verhoef, A., Su, Z., 2009. An integrated model of soil-canopy spectral radiances, photosynthesis, fluorescence, temperature and energy balance. Biogeosciences 6, 3109–3129.

Verrelst, J., Schaepman, M.E., Koetz, B., Kneubühler, M., 2008. Angular sensitivity analysis of vegetation indices derived from CHRIS/PROBA data. Remote Sens. Environ. 112, 2341–2353. doi:10.1016/j.rse.2007.11.001

Wanner, W., Strahler, A.H., Hu, B., Lewis, P., Muller, J.-P., Li, X., Schaaf, C.L.B., Barnsley, M.J., 1997. Global retrieval of bidirectional reflectance and albedo over land from EOS MODIS and MISR data: Theory and algorithm. J. Geophys. Res. Atmospheres 102, 17143–17161. doi:10.1029/96JD03295

Yu, K., Leufen, G., Hunsche, M., Noga, G., Chen, X., Bareth, G., 2013. Investigation of Leaf Diseases and Estimation of Chlorophyll Concentration in Seven Barley Varieties Using Fluorescence and Hyperspectral Indices. Remote Sens. 6, 64–86. doi:10.3390/rs6010064

6. FUSION OF PLANT HEIGHT AND VEGETATION INDICES FOR THE ESTIMATION OF BARLEY BIOMASS

NORA TILLY [1,], HELGE AASEN [1], GEORG BARETH [1]*

Published in: Remote Sensing 2015, 7 (9), 11449-11480

DOI: 10.3390/rs70911449

Formatting and orthography of the manuscript is adapted to the dissertation style.

[1] Institute of Geography (GIS & Remote Sensing Group), University of Cologne, 50923 Cologne, Germany

* Corresponding author: Tel.: +49 221 470 6265; Email: nora.tilly@uni-koeln.de

Abstract: Plant biomass is an important parameter for crop management and yield estimation. However, since biomass cannot be determined non-destructively, other plant parameters are used for estimations. In this study, plant height and hyperspectral data were used for barley biomass estimations with bivariate and multivariate models. During three consecutive growing seasons a terrestrial laser scanner was used to establish crop surface models for a pixel-wise calculation of plant height and manual measurements of plant height confirmed the results (R^2 up to 0.98). Hyperspectral reflectance measurements were conducted with a field-spectrometer and used for calculating six vegetation indices (VIs), which have been found to be related to biomass and LAI: GnyLi, NDVI, NRI, RDVI, REIP, and RGBVI. Furthermore, biomass samples were destructively taken on almost the same dates. Linear and exponential biomass regression models (BRMs) were established for evaluating plant height and VIs as estimators of fresh and dry biomass. Each BRM was established for the whole observed period and pre-anthesis, which is important for management decisions. Bivariate BRMs supported plant height as a strong estimator (R^2 up to 0.85), whereas BRMs based on individual VIs showed varying performances (R^2: 0.07 - 0.87). Fused approaches, where plant height and one VI were used for establishing multivariate BRMs, yielded improvements in some cases (R^2 up to 0.89). Overall, this study reveals the potential of remotely sensed plant parameters for estimations of barley biomass. Moreover, it is a first step towards the fusion of 3D spatial and spectral measurements for improving non-destructive biomass estimations.

Keywords: terrestrial laser scanning; spectrometer; plant height; hyperspectral vegetation indices; biomass; precision agriculture; plot level; multi-temporal

6.1 Introduction

Over the past several decades remote sensing has increased in importance for precision agriculture (Atzberger, 2013; Liaghat and Balasundram, 2010; Mulla, 2012). Since the world population is expected to increase by more than one third until 2050 a main goal is shrinking the gap between potential and current yield (UNFPA, 2010; van Wart et al., 2013). Field management strategies in precision agriculture that aim to maximize yield must involve a reasonable use of natural resources and have to take spatial and temporal variabilities into account (Oliver, 2013), as agricultural production is influenced by the physical landscape, climatic variables, and agricultural management practices (Atzberger, 2013). Studies reveal that grain yield is correlated with total biomass (Boukerrou and Rasmusson, 1990; Fischer, 1993). A quantitative measure is the harvest index, which expresses yield vs. total biomass (Price and Munns, 2010). Moreover, adequate crop condition in early growing stages could buffer the yield against environmental stresses, such as droughts, during later stages (Bidinger et al., 1977). In-season, the nitrogen nutrition index, the ratio between actual and critical nitrogen (N) content, is widely used as a measure of the plant status (Greenwood et al., 1991). The critical value is defined by a crop-specific N dilution curve, showing the relation between N concentration and biomass. Hence, an exact in-season acquisition of biomass is important in precision agriculture.

Since plant biomass cannot be determined non-destructively, other plant parameters are used as estimators. Therefore, remote sensing measurements enable an objective and accurate acquisition in a high temporal frequency (Atzberger, 2013). A review of remote sensing methods for assessing biomass is given by Ahamed et al. (2011). At the field level, ground-based methods are commonly used to achieve sufficiently high resolutions and over the last several decades, several studies investigated the relationship between spectral reflectance measurements and crop characteristics. For extracting information, various vegetation indices (VIs) were developed from the reflectance in determined wavelengths. Two band VIs like the normalized difference vegetation index (NDVI) were traditionally used with multispectral broad band systems to estimate biomass or biomass-related parameters, like LAI. Such VIs have been adapted to narrow band hyperspectral data and other band combinations (Aasen et al., 2014; Marshall and Thenkabail, 2015; Thenkabail et al., 2013, 2000). Additionally, other VIs with more than two bands, such as the GnyLi, have been developed for the same purpose (Gnyp et al., 2014b).

Moreover, active sensors based on light detection and ranging (LiDAR) have been increasingly used in vegetation studies since the 1980s (Lee et al., 2010). Indeed, a main benefit of LiDAR is the very high resolution, which enables the acquisition of complex canopies (Danson et al., 2009). In agricultural applications, for example, ground-based LiDAR methods, also known as terrestrial laser scanning (TLS),

reveal potential for assessing plant height (Zhang and Grift, 2012), leaf area index (Gebbers et al., 2011), crop density (Hosoi and Omasa, 2012, 2009; Saeys et al., 2009), or post-harvest growth (Koenig et al., 2015). Furthermore, the potential for estimating biomass with TLS is supported through studies on small grain cereals (Ehlert et al., 2009, 2008; Lumme et al., 2008), sagebrush (Olsoy et al., 2014), and paddy rice (Tilly et al., 2015, 2014b). The 3D architecture of single plants was modeled under laboratory conditions (Paulus et al., 2014a, 2014b), however the transferability of those laboratory results to field conditions has not yet been shown.

Generally, the accuracy of estimations is a major issue, with the accuracy being limited when calculations are based on one estimator. Whilst biomass estimations based on VIs are affected by saturation effects (Blackburn, 1998; Reddersen et al., 2014; Thenkabail et al., 2000), plant height may reach limitations when differences in plant height are low. Consequently, the fusion of multiple parameters should be examined to enhance estimations. So far, studies on the fusion of spectral and non-spectral information have been applied for characterization of forest ecosystems (Torabzadeh et al., 2014) and modeling of corn yield (Geipel et al., 2014). As both studies applied airborne methods, the spatial resolution was low. A ground-based multi-sensor approach for predicting biomass of grassland based on measurements of plant height, leaf area index (LAI), and spectral reflectance showed that combining multiple sensors can improve the estimation (Reddersen et al., 2014). However, in that study, spectral data were not well suited. Recently, the potential of the combined use of spectral and non-spectral ground-based measurements for estimating biomass was demonstrated for rice, maize, cotton, and alfalfa (Marshall and Thenkabail, 2015).

The overall aim of this study was to compare the potential of plant height (PH), VIs, and a fusion of PH and VIs for estimations of above ground fresh and dry barley biomass. More specifically, this study compares the potential of 3D spatial and spectral information for different time frames during the growing season and investigates if a fusion of both can improve the estimation. Therefore, a spring barley experiment was monitored during three growing seasons in various campaigns with a TLS system and a field-spectrometer. PH was derived from the TLS data and VIs from the hyperspectral data. Four major working tasks were carried out: (I) conduct extensive multi-annual field measurements during the growing seasons, (II) derive bivariate biomass regression models (BRMs) from 3D spatial and spectral measurements for biomass estimations, (III) fuse the 3D spatial and spectral data in multivariate BRMs to estimate biomass based on this extensive data set, and (IV) evaluate the robustness of the BRMs with a cross-validation.

6.2 Methods

6.2.1 Field measurements

In three growing seasons (2012, 2013, and 2014), field experiments were carried out at the Campus Klein-Altendorf (50°37'51"N, E 6°59'32") belonging to the Faculty of Agriculture at the University of Bonn, Germany. Due to crop rotation, the locations of the fields were slightly different between the years. However, soil and climatic conditions were similar with the surface of the soil being flat with a clayey silt luvisol and well suited for crop cultivation (Uni Bonn, 2010a). According to the campus' own weather records, the long-term average yearly precipitation was about 600 mm with a daily average temperature of 9.3 °C (Uni Bonn, 2010b).

Each year, the field consisted of 36 small-scale plots (3 × 7 m) where different cultivars of barley were cultivated with two levels of N fertilization. For half of the plots, a farmer's common rate of 80 kg/ha N fertilizer was applied, for the other half a reduced rate of 40 kg/ha. In 2012 and 2013 each fertilization scheme was carried out once for 18 cultivars of spring barley (Barke, Wiebke, Beatrix, Eunova, Djamila, Streif, Ursa, Victoriana, Sissy, Perun, Apex, Isaria, Trumpf, Pflugs Intensiv, Heils Franken, Ackermanns Bavaria, Mauritia and Sebastian). In 2014, the set-up for the experiment was changed in that each fertilization scheme was repeated three times for six selected cultivars (Barke, Beatrix, Eunova, Trumpf, Mauritia and Sebastian). The experiments were carried out within the interdisciplinary research network CROP.SENSe.net (www.cropsense.uni-bonn.de). The research focus of this project was non-destructive sensor-based methods for detecting crop status such as nutrients, stress, and quality.

In this study, 3D spatial measurements from a TLS system, spectral measurements from a field-spectrometer, and manual reference measurements were used. Due to the weather conditions the time of seeding changed and therefore so did the start of the growing season. The seeding dates were 21 March 2012, 9 April 2013, and 13 March 2014. In Table 6.1, all dates of TLS and spectrometer campaigns are listed as day after seeding (DAS) and a universal scale, known as the BBCH scale, was used to describe phenological stages and steps in the plant development, encoded in a decimal code (Lancashire et al., 1991; Meier, 2001).

Table 6.1. Dates of the terrestrial laser scanning (TLS) and spectrometer (S) campaigns listed as day after seeding (DAS). Averaged codes for the developmental steps are given for the dates of manual plant parameter measurements (BBCH). For some dates BBCH codes were not determined (N/A).

	2012		2013		2014			2012		2013		2014			2012		2013		2014	
DAS	Sensor	BBCH	Sensor	BBCH	Sensor	BBCH	DAS	Sensor	BBCH	Sensor	BBCH	Sensor	BBCH	DAS	Sensor	BBCH	Sensor	BBCH	Sensor	BBCH
15					TLS		45							75	TLS					
16							46							76						
17							47							77						
18							48							78			TLS/S	57		
19							49			TLS/S	30			79						
20			TLS/S	N/A			50	TLS/S						80						
21							51							81						
22							52							82					S	
23							53							83		N/A				
24							54		30			S		84	S				TLS	56
25							55							85						
26							56					TLS	31	86	TLS					
27							57							87						
28							58	TLS						88						
29							59							89						
30							60							90						
31							61							91			S	68		
32							62							92			TLS			
33							63							93						
34			TLS				64			TLS/S	41			94						
35			S	18			65							95						
36							66							96						74
37							67							97					TLS/S	
38							68							98						
39							69							99						
40							70	S	49			TLS/S	49	100						
41					TLS/S	29	71							101						
42							72							102						
43		N/A					73							103						
44							74							104			TLS/S	81		

The acronym BBCH is derived from the funding organizations: Biologische Bundesanstalt (German Federal Biological Research Centre for Agriculture and Forestry), Bundessortenamt (German Federal Office of Plant Varieties), and Chemical industry. The first number of the two-digit code represents the principal growth stage (Table 6.2) and the second subdivides further in short developmental steps. Through determining the BBCH codes during the growing seasons, the annual comparability was ensured. For each plot, the BBCH developmental step was determined as a mean of three plants. In Table 6.1, BBCH codes are given for the dates where plant parameters were manually measured. The codes are averaged per campaign, as the values were almost similar for all cultivars. Although the plant development varied among the years it can be seen that the BBCH codes indicate a comparable development.

Table 6.2. Principal growth stages of the BBCH scale.

Principal Growth Stage[a]	Stage Description	Time Frames Regarded for Biomass Estimation	
0	Germination		
1	Leaf development		
2	Tillering		
3	Stem elongation	Pre-anthesis	Whole observed period
4	Booting		
5	Inflorescence emergence, heading		
6	Flowering, anthesis		
7	Development of fruit		
8	Ripening		
9	Senescence		

[a] first number of the two-digit code.

As reference measurements, the heights of ten plants were measured for each plot and averaged in the post-processing. Moreover, in a defined sampling area of each plot, the above ground biomass of a 0.2 × 0.2 m area was destructively taken each time. The sampling area was neglected for the remote sensing measurements. In the laboratory, plants were cleaned and fresh weights were measured. After drying the samples for 120 h at 70 °C, dry biomass was weighted and extrapolated across the plot (g/m^2).

Furthermore, a digital terrain model (DTM) is required as a common reference surface for calculating plant height from the TLS data. In 2014, the bare ground of the field was scanned after seeding but before any vegetation was visible (Table 6.1: DAS 15). For technical reasons, it was not possible to acquire such data in 2012 and 2013, however, the ground was identifiable in the point cloud of the first campaigns due to the low and less dense vegetation.

6.2.1.1 Terrestrial laser scanning

The TLS configuration and setup was almost equal in all years. Thus for each campaign, the time-of-flight scanner Riegl LMS-Z420i was used (Figure 6.1 A) (Riegl LMS GmbH, 2010). The sensor operates with a near-infrared laser beam, has a beam divergence of 0.25 mrad, and a measurement rate of up to 11,000 points/sec. In addition its field of view is up to 80° in the vertical and 360° in the horizontal direction and this study used resolutions between 0.034° and 0.046°. The digital camera Nikon D200 was mounted on the laser scanner and the TLS point clouds were colorized from the images captured. Furthermore the sensor should be as high as possible above ground, resulting in a steep angle between scanner and investigated area enabling the best possible coverage of the crop surface and a homogenous penetration of the vegetation. Accordingly the scanner was mounted on the hydraulic platform of a tractor, raising the sensor to approximately 4 m above ground (Figure 6.1 B). In order to

lower shadowing effects and to attain an almost uniform spatial coverage, the field was scanned from its four corners. The coordinates of all scan positions and an additional target were required for the georeferencing and co-registration of the positions in the post-processing. Highly reflective cylinders arranged on ranging poles were used as targets (Figure 6.1 C). These reflective cylinders can be easily detected by the scanner meaning their exact position in relation to the scan position can be measured (Hoffmeister et al., 2010). The coordinates of the scan positions and ranging poles were measured with the highly accurate RTK-DGPS system Topcon HiPer Pro (Topcon Positioning Systems, 2006). By establishing an own reference station each year, the precise merging of all data sets per year was ensured with the relative accuracy of this system being approximately 1 cm.

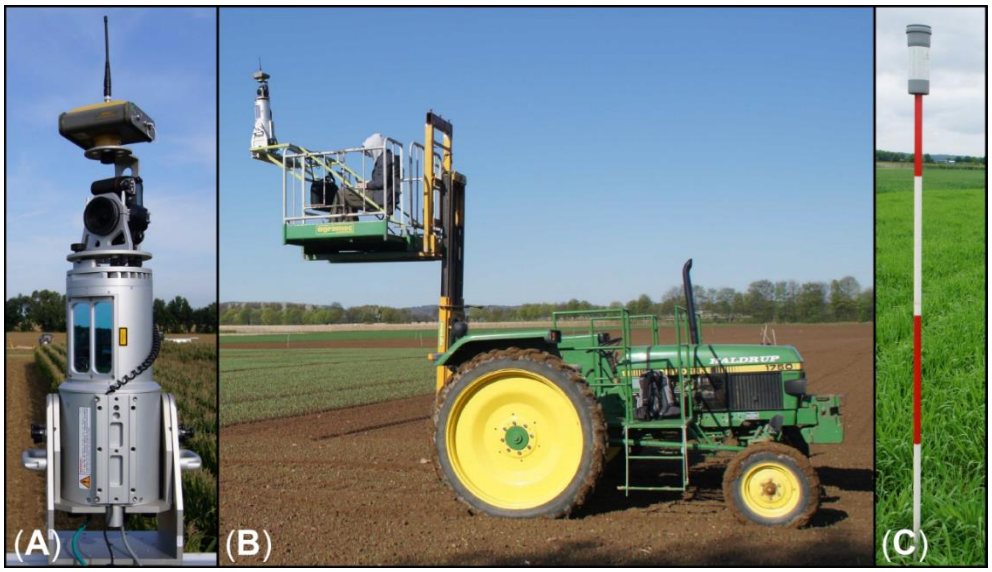

Figure 6.1 Instrumental set-up: (A) terrestrial laser scanner Riegl LMS-Z420i; (B) tractor with hydraulic platform; (C) ranging pole with reflective cylinder.

6.2.1.2 Field-spectrometer measurements

The ASD® FieldSpec3 was used for measuring the reflectance several times during the growing seasons (all dates are listed in Table 6.1 above). This spectrometer measures the incoming light from 350 to 2500 nm with a sampling interval of 1.4 nm in the VNIR (350 - 1000 nm) and 2 nm in the SWIR (1001 - 2500 nm). These measurements are resampled to spectra with 1 nm resolution by the manufacturer's software. At each position, ten measurements were taken and instantly averaged by the software, from 1 m above the canopy with a pistol grip, which was mounted on a cantilever to avoid shadows obscuring the sampling area. Additionally, a water level was used to ensure nadir view and no fore optic was used, resulting in a field of view of 25° and thus, a footprint area on the canopy with a radius of approximately 22 cm was achieved. Before the measurements, the spectrometer warmed up for at least 30 min and every 10 min or after illumination change, the spectrometer was optimized and calibrated with a spectralon calibration panel (polytetrafluoroethylene reference

panel). Six positions were measured within each plot and for each position, the detector offset was corrected (Aasen et al., 2014). Then the six spectra were averaged, resulting in one spectrum per field plot, which was used in the further analysis.

6.2.2 Post-processing

6.2.2.1 TLS data

In the scanner software RiSCAN Pro, the DGPS data and the scans of all campaigns were imported into one project file per year. Based on the coordinates of the scan positions and reflectors, a direct georeferencing method was applied for the registration of all scan positions. However, a further adjustment was required due to small alignment errors between the point clouds. Based on the iterative closest point (ICP) algorithm (Besl and McKay, 1992), the Multi Station Adjustment in RiSCAN Pro allows the position and orientation of each scan position to be modified in multiple iterations and thus the best fitting result for all of them to be acquired. After optimizing the alignment with the ICP algorithm, the error, measured as standard deviation between used point-pairs, was 0.04 m on average for each campaign.

The point clouds were then merged to one dataset per campaign, and the area of interest was extracted. As reflections on insects or small particles in the air produced noise those points were manually removed. In addition a filtering scheme for selecting maximum points was used for determining the crop surface and in the same way, a filtering scheme for selecting minimum points was applied to extract ground points from the data sets of each first campaign. Finally, the data sets with XYZ coordinates of each point were exported.

The spatial analyses and visualization of the data were carried out in Esri ArcGIS Desktop 10.2.1. All point clouds were interpolated using the inverse distance weighting (IDW) algorithm, resulting in a raster with a consistent spatial resolution of 1 cm. IDW is an exact, deterministic algorithm that retains measured values at their sample location. The accuracy of measurements with a high density is maintained as all values are kept at their discrete location and not moved to fit the interpolation better (Johnston et al., 2001). As introduced by Hoffmeister et al. (2010), the created raster data sets are referred to as crop surface models (CSMs). Similarly, a digital terrain model (DTM) was generated from the ground points and by subtracting the DTM from a CSM, plant heights were calculated pixel-wise. Moreover, by calculating the difference between two CSMs, plant growth was spatially measured. Hereinafter, growth is defined as temporal difference in height (for a detailed description of the CSMs creation and the calculation of plant heights see Tilly et al. (2014b)). The raster data sets with pixel-wise stored plant heights and growth were visualized as maps of plant height and growth, respectively.

Then the plant heights were averaged plot-wise, allowing a common spatial base with the other measurements to be attained. It should be noted that previously, each plot was clipped with an inner buffer of 0.5 m to prevent border effects.

6.2.2.2 Spectral data

For this study, established VIs were used to extract information from the hyperspectral data, measured with the field-spectrometer. From the widespread of known hyper- and multispectral VIs for deriving different vegetation properties, six VIs were selected from the literature which have been found to be related to biomass and LAI. The selection was based on two criteria: Firstly, to make this study comparable to other studies VIs were selected which have been widely used in literature. Secondly, VIs with different spectral domains were used to examine if this would influence the prediction power of the fused models.

The NDVI was originally created for broad band satellite remote sensing (Rouse et al., 1974) and has been widely used in the literature. It has been adapted to hyperspectral narrow bands and was specified for sensors such as GreenSeeker™ and Crop Circle™ (Gnyp et al., 2014b). Several articles reported relationships between the NDVI and biomass or LAI. However, NDVI has been shown to saturate in cases of dense and multi-layered canopy (Thenkabail et al., 2000) and to have a non-linear relationship with biophysical parameters such as green LAI (Haboudane et al., 2004).

On this basis, Roujean and Breon (1995) developed the renormalized difference vegetation index (RDVI) for estimating the fraction of photosynthetically active radiation absorbed by vegetation, independent of a priori knowledge of the vegetation cover (Roujean and Breon, 1995). The RDVI showed strong relationships to LAI for different crops below an LAI of 5 (Broge and Leblanc, 2001; Haboudane et al., 2004). In dense crop canopies with an LAI above five, RDVI tended to overestimate the LAI (Haboudane et al., 2004). Simulations with the radiative transfer models PROSPECT and SAIL indicated that the RDVI is less affected by canopy structure, biochemistry, and soil background when estimating the LAI (Broge and Leblanc, 2001).

The red edge inflection point (REIP) was introduced by Guyot and Baret (1988). The REIP characterizes the inflection in the spectral red edge by calculating the wavelength with maximum slope. A variation of the inflection is mainly related to leaf chlorophyll content, leaf area index, and leaf inclination angle. Furthermore, soil reflectance and sun position have a limited effect (Guyot et al., 1992).

GnyLi is a four-band VI for estimating biomass in the NIR and SWIR domain (Gnyp et al., 2014b). This VI was developed for winter wheat and showed good performance on different scales from plot to regional level and across several growth stages (Gnyp et al., 2014b). The GnyLi considers the two

reflectance maxima and minima between 800 and 1300 nm. While the high reflectance is caused by the plants intercellular structure, the absorption at the minima is caused by cellulose, starch lignin, and water. These components contribute substantially to dry and fresh biomass and combining the two products helps to avoid saturation problems—this is a major advantage of this VI.

Similar to the GnyLi, the normalized reflectance index (NRI) was also developed for estimating biomass in winter wheat. The NRI was empirically developed by combining the shape of the NDVI and the best two band combination for biomass estimation with EO-1 Hyperion satellite data (Koppe et al., 2010).

The red green blue vegetation index (RGBVI) was developed for estimating biomass based on bands available in a standard digital camera (Bendig et al., 2015). In this study, the RGB data was simulated from hyperspectral data where green, red, and blue values were calculated as the mean of the reflectance from 530 to 560 nm, 645 to 765 nm, and 465 to 495 nm, respectively. Thus, in contrast to other studies (Bareth et al., 2015; Bendig et al., 2015; Geipel et al., 2014), the RGBVI was derived from radiometrically and spectrally calibrated data.

The six VIs used in this study can be categorized by the wavelength domains that are used in their formula. The NDVI, RDVI, and REIP use wavelengths in the visible and near-infrared domain (VISNIR VIs), the GnyLi and NRI use wavelengths in the near-infrared domain (NIR VIs), while the RGBVI uses wavelengths in the visible domain (VIS VI). The formulas of the VIs used in this study are given in Table 6.3 (Bendig et al., 2015; Gnyp et al., 2014a; Guyot and Baret, 1988; Koppe et al., 2010; Roujean and Breon, 1995; Rouse et al., 1974).

Table 6.3. Vegetation indices (VIs) used in this study.

Wave-length Domains	**VIs**	**Formula**	**References**
NIR	GnyLi	$\frac{(R900 \times R1050 - R955 \times R1220)}{(R900 \times R1050 + R955 \times R1220)}$	(Gnyp et al., 2014a)
	NRI	$(R874 - R1225)/(R874 + R1225)$	(Koppe et al., 2010)
VISNIR	NDVI	$(R798 - R670)/(R798 + R670)$	(Rouse et al., 1974)
	RDVI	$(R798 - R670)/\left(\sqrt{R798 + R670}\right)$	(Roujean and Breon, 1995)
	REIP	$700 + 40 * \frac{\left(\frac{R670 + R780}{2}\right) - R700}{R740 - R700}$	(Guyot and Baret, 1988)
VIS	RGBVI	$\frac{({R_{green}}^2 - R_{blue} \times R_{red})}{({R_{green}}^2 + R_{blue} \times R_{red})}$	(Bendig et al., 2015)

6.2.3 Biomass regression models

The main aim of this study was to establish biomass regression models (BRMs) and compare the potential of PH, VIs, and a fusion of PH and VIs for estimating barley biomass. The workflow for the BRM calibration and validation and the distinction of considered cases are shown in Figure 6.2. All calculations were performed in the R software environment (R Development Core Team, 2015). The measurements from 2012 were excluded because the spectral data set was inconsistent, since due to unsuitable weather, no spectral data or only data for less than half of the plots could be acquired corresponding to the second and fourth TLS campaign, respectively (Table 6.1). Furthermore, as mentioned above, the number of cultivars was reduced in 2014 so as a result only these six cultivars were used from the 2013 data set to ensure comparability.

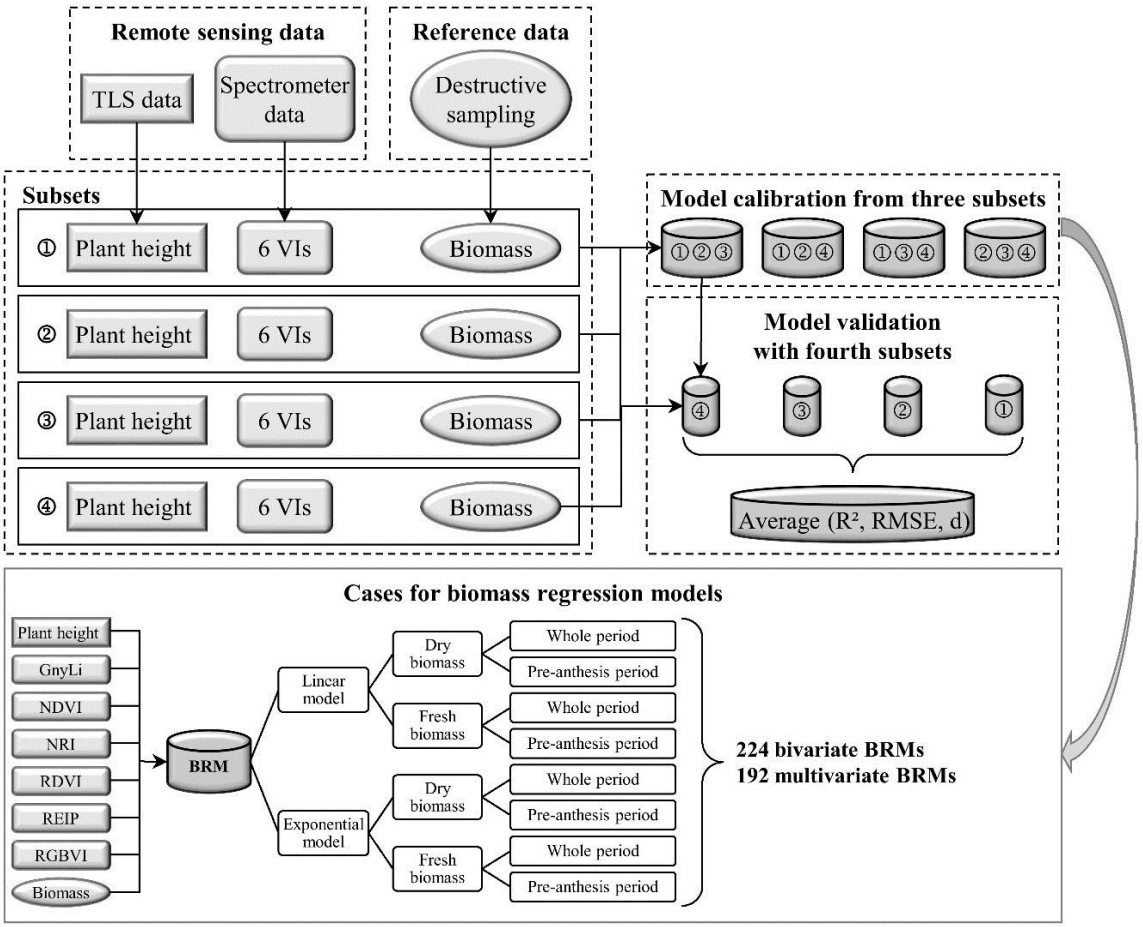

Figure 6.2 Workflow for the calibration and validation of the biomass regression models and distinction of cases for each model.

The reduced data set was split into four subsets to obtain independent values for calibration and validation. The first subset contained the plot-wise averaged measurements of plant height, calculated VIs and destructively taken biomass from 2013 (n = 48). Each other subset contained the same measurements of one repetition from 2014 (each n = 60). Thus, each subset contained the

measurements of each cultivar from one plot with low and one with high N fertilizer level for the given campaign dates. A cross-validation was performed using these data sets: For each run, one subset was excluded from the BRM calibration and used for validating the resulting BRM.

First, bivariate BRMs for fresh and dry biomass were developed based on the CSM-derived PH or one of the six VIs. Linear and exponential BRMs were established since no trend regarding their usability for biomass estimations based on PH was clearly identifiable in earlier studies (Tilly et al., 2015). However, the biomass accumulation during the vegetative phase is exponential and other studies have shown that it is best estimated with exponential models (Aasen et al., 2014; Thenkabail et al., 2000). For the exponential BRMs, the fresh and dry biomass values were natural log-transformed. Each BRM was calculated for two time frames, the whole observed period from tillering (BBCH stage 2) till the end of fruit development (BBCH stage 7) and the pre-anthesis period (till BBCH stage 6) (Table 6.2).

The latter period is important as, for example, adequate crop conditions could buffer the grain yield against later environmental stress (Bidinger et al., 1977). Thus, campaign numbers 3 to 6 and 2 to 6 were considered for 2013 and 2014, respectively, whereas each final campaign was excluded for the pre-anthesis BRMs. Considering the four possible subset combinations, overall 224 bivariate BRMs were established. Second, multivariate BRMs were established based on PH fused with each VI. Since they were also established as linear and exponential BRMs for fresh and dry biomass for both time frames, the four possible subset combinations led to 192 multivariate BRMs in total.

The calibration was evaluated by calculating the coefficient of determination (R^2) for PH or VI vs. measured biomass and the standard error of the estimate (SE_E) (Hair et al., 2010). For the validation, besides the R^2 (estimated vs. measured biomass), the root mean square error (RMSE), and Willmott's index of agreement (d) (Willmott and Wicks, 1980; Willmott, 1981) were determined. For each case, the results from the four runs were averaged. Finally, the robustness of the BRMs was evaluated by calculating the ratio between the R^2 values of BRM calibration and validation.

6.3 Results

6.3.1 Acquired plant parameters

The TLS-derived point clouds were used to establish CSMs and spatially calculate plant height. Results of the pixel-wise calculation were visualized in maps of plant height for each plot. As an example for this, maps of four plots and corresponding mean heights are shown in Figure 6.3 for the barley cultivar Trumpf. In the first campaign of 2013, plants were too small to obtain reasonable results. Thus, maps are presented for the last six and five campaigns of 2013 and 2014, respectively. One plot of each N fertilizer level is shown for both years. For the temporal development, an increase in plant height is

observable until anthesis (BBCH stage 6) and afterwards, the development of ears begins and plant heights decrease due to the associated sinking of heads. Within all plots, the detailed representation of plant height is visible, which enables spatial differences in plant height to be detected. As a result, the exact calculation of mean heights can be assumed. A comparison of the plot-wise averaged values does not show that the fertilization rate directly influenced plant height.

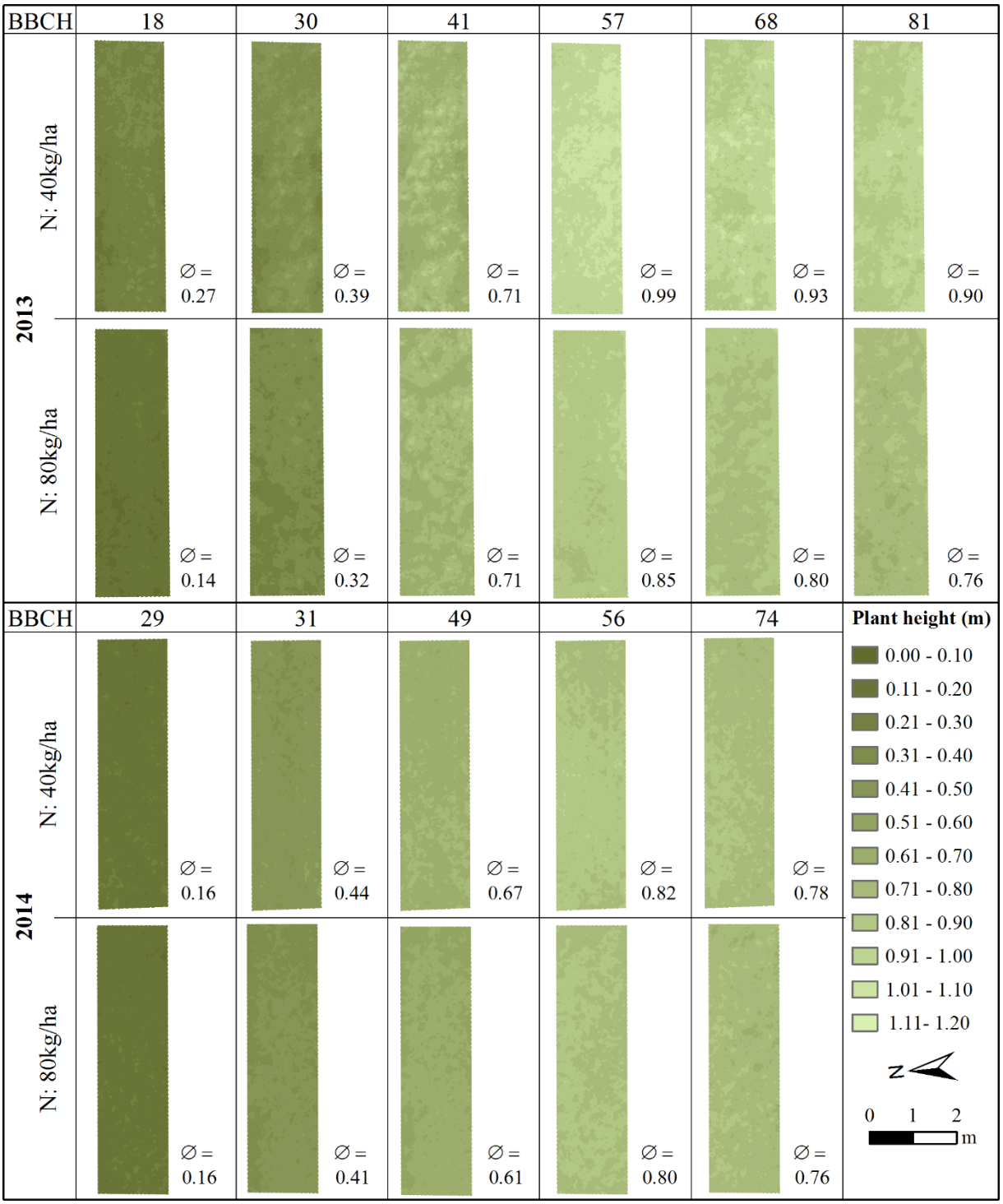

Figure 6.3 Maps of four plots from the last six and five campaigns of 2013 and 2014, respectively. One plot of each N fertilizer level of the barley cultivar Trumpf is shown for each year (∅: Plot mean height).

The plot-wise averaged plant heights were used for statistical analysis and a comparison with the manual measurements. The linear regressions between all mean CSM-derived and manual measured plant heights for each of the three years is illustrated below in Figure 6.4. High coefficients of determination (R^2) confirm the TLS-derived results. The R^2 across all years is 0.92, yearly separated values are also given in Figure 6.4. Moreover, a varying scattering between the years is indicated. The scattering is the lowest in the 2014 data set, which is presumably caused by the reduced number of cultivars in 2014 and associated with more similar plant heights. Table A 6.1 in the Appendix gives the mean, minimum, and maximum values of all plot-wise averaged values as well as the standard deviation per campaign of the CSM-derived and manual measured plant heights. Clearly observable lodging occurred in some plots between the second and third or fourth and fifth campaign in 2012 and 2013, respectively (for more details see Tilly et al. (2014a). Those plots were neglected for the analysis and thus reduced the number of samples for the affected campaigns. As already stated for the visualized plots (Figure 6.3), an increase in plant height is detectable during pre-anthesis and a slight decrease is detectable afterwards. In addition, the difference between the mean values of both measurement methods is lower than 10% for almost all campaigns.

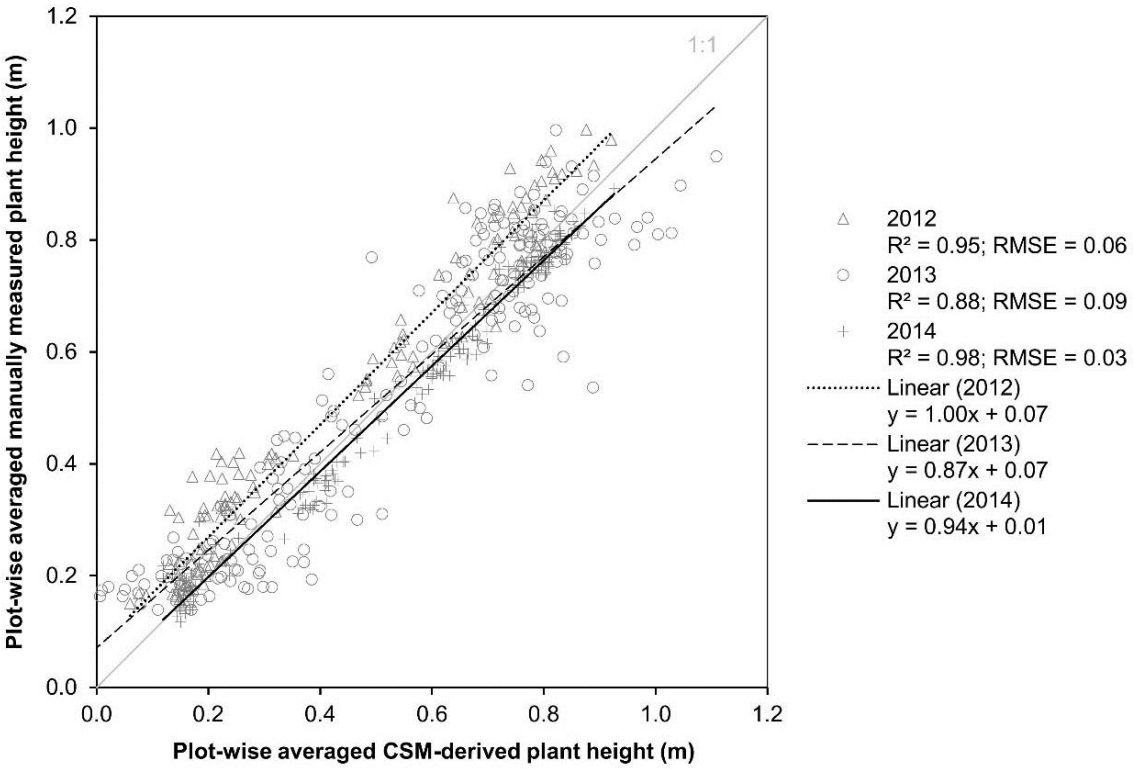

Figure 6.4 Regression of the mean CSM-derived and manual measured plant heights (2012: n = 131; 2013: n = 196; 2014: n = 180).

The field-spectrometer measurements were used for calculating the six VIs (GnyLi, NDVI, NRI, RDVI, REIP, and RGBVI). As the spectral measurements from 2012 were not usable for a linkage with the TLS data, only the data sets from 2013 to 2014 were used. Moreover, from the data set of 2013 only measurements of the cultivars selected in 2014 were considered and the data sets of plant height and

biomass were accordingly adapted to ensure comparability. For each campaign, the values for both N fertilizer levels were averaged. Table 6.4 shows the statistics for the reduced data sets of the nine regarded campaigns. Additionally, the yearly mean biomass values were calculated for the pre-anthesis and whole observed period, as reference for the later evaluation of the biomass estimation.

Table 6.4. Statistics for the plot-wise averaged CSM-derived plant heights and destructively taken biomass for the reduced data sets of 2013 and 2014 (n: number of samples; $\bar{x}$: mean value; min: minimum; max: maximum; SD: standard deviation).

		CSM-derived plant height (m)				Fresh biomass (g/m²)				Dry biomass (g/m²)			
	n	$\bar{x}$	min	max	SD	$\bar{x}$	min	max	SD	$\bar{x}$	min	max	SD
2013													
3	12	0.22	0.01	0.39	0.13	1282.92	491.00	2172.50	473.20	168.31	52.00	272.00	56.59
4	12	0.47	0.24	0.71	0.17	2891.54	1560.25	4465.50	806.12	415.31	205.00	725.00	146.02
5	12	0.78	0.58	0.99	0.13	5070.42	2668.75	7730.00	1561.62	883.38	434.50	1429.25	328.93
6	12	0.78	0.65	0.93	0.07	4631.73	2986.25	7655.75	1193.95	1258.88	886.75	1687.50	219.92
	Mean pre-anthesis period					3081.63	1573.33	4789.33	946.98	489.00	230.50	808.75	177.18
	Mean whole observed period					3469.15	1926.56	5505.94	1008.72	681.47	394.56	1028.44	187.86
2014													
2	36	0.17	0.12	0.25	0.03	656.28	266.25	1116.50	202.07	89.01	33.00	155.25	27.66
3	36	0.41	0.34	0.52	0.04	2227.08	1226.75	3236.50	531.72	289.83	165.75	417.75	66.03
4	36	0.63	0.53	0.70	0.04	2825.48	1643.75	4162.00	603.19	465.49	276.62	706.65	97.89
5	36	0.81	0.69	0.99	0.05	3185.13	2106.50	5433.25	687.74	777.23	486.35	1271.35	156.02
6	36	0.78	0.66	0.99	0.05	3569.34	1994.75	6044.00	898.59	1166.38	652.60	1876.35	276.46
	Mean pre-anthesis period					2223.49	1310.81	3487.06	506.18	405.39	240.43	637.75	86.90
	Mean whole observed period					2492.66	1447.60	3998.45	584.66	557.59	322.86	885.47	124.81

6.3.2 Biomass estimation

The barley biomass was estimated by establishing 224 bivariate and 192 multivariate biomass regression models (BRMs) based on plant height (PH) and vegetation indices (VIs). Table 6.5 shows the statistical parameters for the BRM calibration. The table is vertically divided into bivariate or multivariate BRMs and the regarded time frames. Horizontally it distinguishes between dry or fresh biomass and linear or exponential BRMs. However, the results of the linear and exponential BRMs cannot be directly compared due to the log-transformation of biomass for the latter ones. Since the biomass accumulation during the vegetative phase is exponential and other studies have shown that it is best estimated with exponential BRMs (Aasen et al., 2014; Thenkabail et al., 2000) only the exponential BRMs are regarded in the following. For each model the coefficient of determination (R^2) and the standard error of the estimate (SE_E) are given as mean values of the four possible subset combinations.

Each established BRM was validated with the remaining fourth subsets. Table 6.6 shows the R^2, root mean square error (RMSE), and Willmott's index of agreement (d) for the model validation as mean

values of the four subset combinations. The subdivision of the table is equivalent to that of Table 6.5. The results of the bivariate BRMs are regarded in the following subsection; the fusion of both plant parameters to multivariate BRMs is examined in the last subsection of this chapter. As the results of the calibration and validation show a similar tendency, only the values of the validation are stated. However, to evaluate the robustness of the BRMs, an overall comparison of differences between calibration and validation is given at the end of this chapter.

Table 6.5. Statistics for the model calibration as mean values of the four subset combinations (R^2: coefficient of determination; SE_E: standard error of the estimate).

			Bivariate BRMs					Multivariate BRMs			
			Whole period		Pre-anthesis			Whole period		Pre-anthesis	
		Estimator	R^2	SE_E [a]	R^2	SE_E [a]	Estimator[b]	R^2	SE_E [a]	R^2	SE_E [a]
Dry biomass	Linear	PH	0.65	10.03	0.76	5.73					
		GnyLi	0.52	11.75	0.68	6.67	GnyLi	0.65	34.63	0.77	25.41
		NDVI	0.07	16.38	0.34	9.56	NDVI	0.69	21.49	0.76	20.73
		NRI	0.54	11.58	0.70	6.40	NRI	0.65	35.04	0.77	24.86
		RDVI	0.13	15.87	0.39	9.21	RDVI	0.69	19.18	0.76	21.40
		REIP	0.12	15.92	0.58	7.60	REIP	0.73	1933.86	0.76	258.29
		RGBVI	0.05	16.55	0.26	10.10	RGBVI	0.68	22.28	0.76	23.23
	Exponential	PH	0.84	0.37	0.84	0.34					
		GnyLi	0.80	0.42	0.85	0.32	GnyLi	0.86	2.43	0.88	2.14
		NDVI	0.30	0.77	0.61	0.53	NDVI	0.85	2.84	0.88	3.99
		NRI	0.81	0.40	0.87	0.30	NRI	0.87	2.29	0.89	1.96
		RDVI	0.41	0.71	0.68	0.48	RDVI	0.85	2.52	0.88	2.84
		REIP	0.37	0.73	0.77	0.40	REIP	0.84	30.37	0.86	48.49
		RGBVI	0.23	0.81	0.48	0.60	RGBVI	0.85	2.51	0.87	2.73
		Estimator	**R^2**	**SE_E [a]**	**R^2**	**SE_E [a]**	**Estimator[b]**	**R^2**	**SE_E [a]**	**R^2**	**SE_E [a]**
Fresh biomass	Linear	PH	0.59	901.99	0.60	843.32					
		GnyLi	0.58	913.81	0.62	829.48	GnyLi	0.62	3295.30	0.64	2968.91
		NDVI	0.25	1222.39	0.42	1022.79	NDVI	0.60	4561.69	0.63	5008.60
		NRI	0.59	909.94	0.62	821.35	NRI	0.62	3056.34	0.64	2718.09
		RDVI	0.35	1143.49	0.50	945.26	RDVI	0.61	3813.94	0.64	3955.80
		REIP	0.30	1180.82	0.55	894.62	REIP	0.60	14599.87	0.63	59169.39
		RGBVI	0.22	1243.84	0.37	1066.53	RGBVI	0.61	4007.93	0.64	3881.46
	Exponential	PH	0.70	0.37	0.68	0.39	PH				
		GnyLi	0.76	0.33	0.76	0.34	GnyLi	0.77	1.87	0.77	1.77
		NDVI	0.46	0.50	0.65	0.41	NDVI	0.77	3.74	0.79	4.30
		NRI	0.77	0.33	0.77	0.33	NRI	0.77	1.67	0.77	1.56
		RDVI	0.59	0.43	0.74	0.35	RDVI	0.79	2.69	0.82	2.89
		REIP	0.47	0.49	0.71	0.37	REIP	0.72	22.27	0.74	73.05
		RGBVI	0.38	0.53	0.55	0.47	RGBVI	0.77	2.58	0.78	2.68

[a] The SE_E for exponential models is calculated from natural log-transformed biomass values; [b] each fused with PH.

Table 6.6. Statistics for the model validation as mean values of the four subset combinations (R^2: coefficient of determination; RMSE: root mean square error (g/m²); d: Willmott's index of agreement).

		Bivariate BRMs						Multivariate BRMs						
			Whole period			Pre-anthesis			Whole period			Pre-anthesis		
		Estimator	R^2	RMSE[a]	d	R^2	RMSE[a]	d	Estimator[b]	R^2	RMSE[a]	d	R^2	RMSE[a]	d
Dry biomass	Linear	PH	0.66	257.57	0.88	0.80	147.75	0.92							
		GnyLi	0.54	299.67	0.81	0.72	173.31	0.88	GnyLi	0.65	262.19	0.88	0.79	148.20	0.92
		NDVI	0.07	412.70	0.33	0.38	244.47	0.64	NDVI	0.71	250.35	0.89	0.80	148.32	0.92
		NRI	0.55	295.41	0.82	0.74	166.41	0.89	NRI	0.66	261.77	0.88	0.80	147.67	0.92
		RDVI	0.13	400.36	0.44	0.41	233.53	0.71	RDVI	0.72	247.16	0.89	0.80	148.27	0.92
		REIP	0.15	404.95	0.46	0.68	197.50	0.83	REIP	0.73	228.46	0.91	0.80	147.88	0.92
		RGBVI	0.04	416.42	0.26	0.28	254.41	0.58	RGBVI	0.70	261.30	0.88	0.80	149.33	0.92
	Exponential	PH	0.85	0.39	0.95	0.85	0.36	0.95							
		GnyLi	0.80	0.42	0.94	0.86	0.33	0.95	GnyLi	0.87	0.36	0.96	0.89	0.31	0.96
		NDVI	0.29	0.77	0.63	0.59	0.54	0.81	NDVI	0.85	0.38	0.95	0.87	0.30	0.96
		NRI	0.81	0.40	0.94	0.87	0.31	0.96	NRI	0.87	0.36	0.96	0.89	0.29	0.96
		RDVI	0.40	0.71	0.73	0.66	0.48	0.87	RDVI	0.85	0.38	0.95	0.88	0.30	0.96
		REIP	0.40	0.75	0.72	0.82	0.43	0.90	REIP	0.85	0.39	0.95	0.89	0.34	0.95
		RGBVI	0.22	0.82	0.55	0.48	0.62	0.75	RGBVI	0.85	0.38	0.95	0.86	0.31	0.96
		Estimator	R^2	RMSE[a]	d	R^2	RMSE[a]	d	Estimator[b]	R^2	RMSE[a]	d	R^2	RMSE[a]	d
Fresh biomass	Linear	PH	0.67	963.45	0.84	0.70	892.55	0.85							
		GnyLi	0.65	970.70	0.83	0.72	886.24	0.84	GnyLi	0.69	939.84	0.85	0.74	861.73	0.86
		NDVI	0.27	1254.02	0.58	0.51	1053.83	0.70	NDVI	0.67	952.58	0.84	0.73	862.84	0.85
		NRI	0.65	962.49	0.83	0.72	873.75	0.85	NRI	0.69	938.46	0.85	0.74	857.99	0.86
		RDVI	0.38	1175.32	0.67	0.59	964.42	0.77	RDVI	0.68	943.96	0.85	0.74	841.36	0.86
		REIP	0.41	1244.11	0.66	0.77	951.74	0.81	REIP	0.67	966.67	0.84	0.77	908.74	0.84
		RGBVI	0.21	1260.32	0.53	0.41	1066.26	0.67	RGBVI	0.66	948.90	0.85	0.71	852.97	0.86
	Exponential	PH	0.73	0.40	0.89	0.71	0.42	0.88							
		GnyLi	0.78	0.35	0.92	0.79	0.36	0.91	GnyLi	0.79	0.34	0.92	0.80	0.36	0.92
		NDVI	0.44	0.51	0.73	0.64	0.42	0.83	NDVI	0.78	0.34	0.92	0.79	0.34	0.92
		NRI	0.77	0.34	0.92	0.79	0.35	0.92	NRI	0.79	0.34	0.92	0.79	0.35	0.92
		RDVI	0.57	0.44	0.82	0.73	0.36	0.89	RDVI	0.80	0.33	0.93	0.83	0.31	0.93
		REIP	0.54	0.53	0.77	0.82	0.42	0.87	REIP	0.77	0.39	0.90	0.82	0.40	0.88
		RGBVI	0.36	0.54	0.68	0.53	0.47	0.78	RGBVI	0.76	0.34	0.92	0.76	0.34	0.92

[a] The RMSE for exponential models is calculated from natural log-transformed biomass values; [b] each fused with PH.

6.3.2.1 Bivariate models

All cases show moderate to good results for bivariate BRMs based on PH. For each time frame, PH shows the same and similar relationship with dry and fresh biomass, respectively (Table 6.6). Scatterplots of measured vs. estimated biomass for selected examples are shown in the last subsection in comparison with multivariate BRMs.

Most VIs lead to better results for pre-anthesis than for the whole observed period. For dry biomass, the RGBVI performs worst for both time frames (Table 6.6, top left quarter). The largest difference between the whole observed period and the pre-anthesis can be found for the NDVI (R^2 = 0.29 vs. 0.59), while the NIR VIs as the GnyLi perform more consistently (R^2 = 0.80 vs. 0.86). Both, the NRI and the GnyLi also reveal best results for pre-anthesis (R^2 = 0.87, 0.86) and for the whole observed period

(R^2 = 0.81, 0.80). In pre-anthesis, the relative difference between the NIR VIs and VISNIR VIs is smaller. Figure 6.5 shows scatterplots of measured vs. estimated dry biomass of one validation dataset for selected VIs and as expected from the high R^2 values, the estimated biomass from the GnyLi BRM corresponds well with the measured biomass (close to the 1:1 line). In pre-anthesis, the same applies the REIP whereas the NDVI and RGBVI saturate at about 185 g/m². For the whole observed period, biomass estimated by the BRM of REIP, NDVI and RGBVI does not align well with what was measured. The scatterplots reveal that the dynamic range of the models does not cover the range of the measured biomass values.

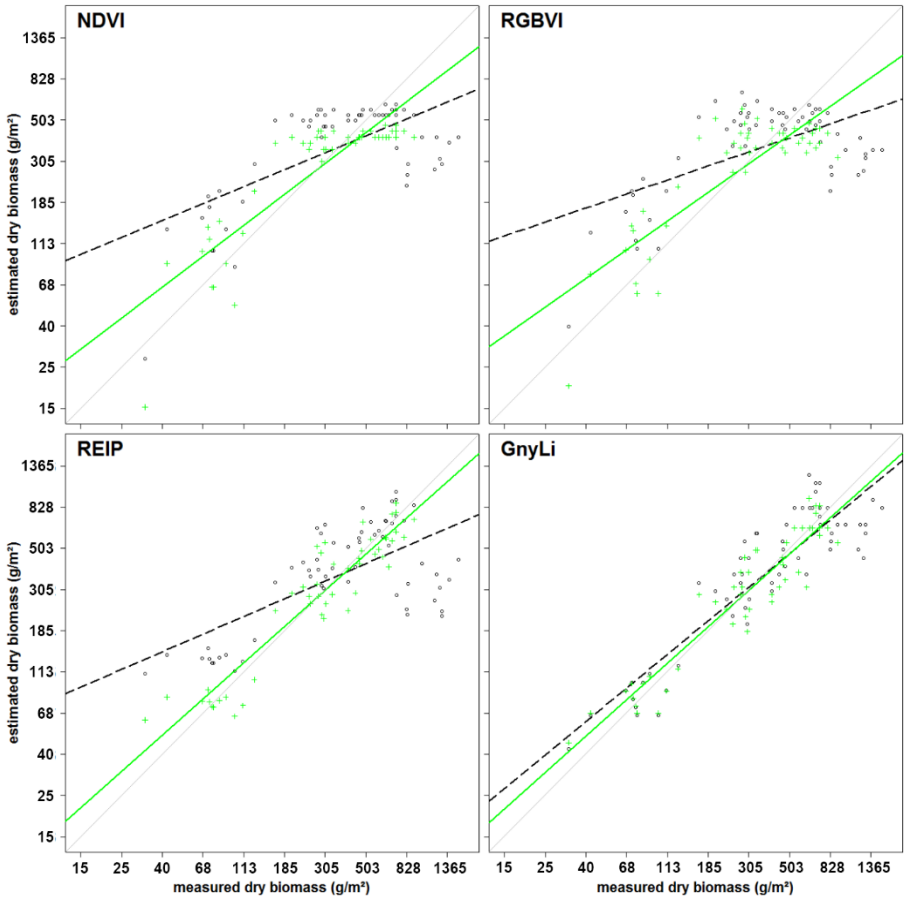

Figure 6.5 Scatterplots of measured vs. estimated dry biomass for one validation data set for NDVI, RGBVI, REIP, and GnyLi (exponential model). Pre-anthesis: crosses and solid green line; whole observed period: circles and dashed black line; 1:1 line: light grey.

Better results are also obtained for pre-anthesis of fresh biomass than for the whole observed period, although the differences are smaller than for dry biomass. The NIR VIs perform most consistently for both periods and have the highest R^2 values for the whole observed period. However, particularly for the whole observed period, the relative difference between the NIR VIs and the VIS and VISNIR VIs is smaller than for dry biomass and in pre-anthesis, the relative difference between the NIR VIs and other VIs is further reduced. Additionally, the REIP (R^2 = 0.82) yields better results than the NIR VIs (each R^2 = 0.79). Again, the RGBVI performs worst.Figure 6.6 shows scatterplots of measured vs. estimated fresh biomass of one validation dataset for selected VIs. As expected from the high R^2 values, biomass

estimated from the GnyLi BRM corresponds well with the measured values (close to the 1:1 line). In pre-anthesis, the same applies for the REIP, whereas the NDVI and RGBVI saturate at about 1,375 g/m². As for dry biomass, the BRMs based on the REIP and particularly the NDVI and RGBVI show a poor relationship between estimated and measured fresh biomass. Overall, most VISNIR VIs and the RGBVI yield better results for fresh biomass than for dry biomass. The NIR VIs perform best and most consistently (Table 6.6, bottom left quarter).

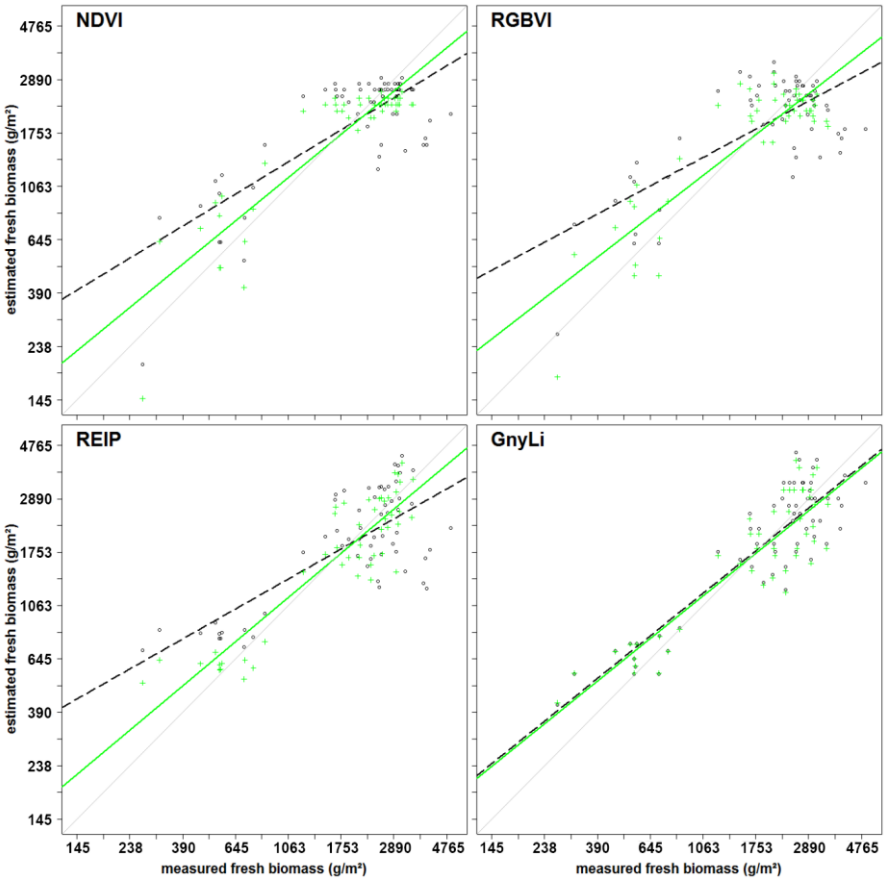

Figure 6.6 Scatterplots of measured vs. estimated fresh biomass for one validation data set for NDVI, RGBVI, REIP, and GnyLi (exponential model). Pre-anthesis: crosses and solid green line; whole observed period: circles and dashed black line; 1:1 line: light grey.

6.3.2.2 Multivariate models

For dry biomass, PH is the best individual estimator across the whole observed period (R^2 = 0.85) and a slight improvement is only achieved when fused with one of the NIR VIs in a multivariate BRM (both R^2 = 0.87). In pre-anthesis, PH and the NIR VIs perform similarly to the bivariate BRMs (R^2 = 0.85, 0.86, 0.87) and when PH is fused with the NIR VIs or the REIP, the predictability slightly increases (R^2 = 0.89).

For fresh biomass across the whole observed period, PH (R^2 = 0.73) yields comparable results to the NIR VIs (both R^2 = 0.77) although the fusion of PH with NIR VIs slightly improves the estimation (both R^2 = 0.79). Only the multivariate BRM from PH and RDVI is very slightly better (R^2 = 0.80). In

pre-anthesis, REIP, GnyLi, NRI, and RDVI explain up to 11% more variation (R^2 = 0.82, 0.79, 0.79, 0.73) then PH (R^2 = 0.71). When PH is fused with any VI, the predictability is improved compared to most individual estimators and even the RGBVI in combination with PH improves the estimation of dry and fresh biomass for pre-anthesis yielding an R^2 of 0.71 and 0.76, respectively. In the fused analysis, the RGBVI performs only slightly weaker than the other VIs. Nevertheless, only the RDVI fused with PH slightly increases the predictability (R^2 = 0.83) compared to the bivariate BRM based on the RDVI. Figure 6.7 shows the scatterplots of measured vs. estimated values of one validation dataset from the bivariate BRM of PH and the multivariate BRM of PH and GnyLi for dry biomass in pre-anthesis and fresh biomass across the whole observed period. The model fit is only slightly improved by fusing PH with the VI.

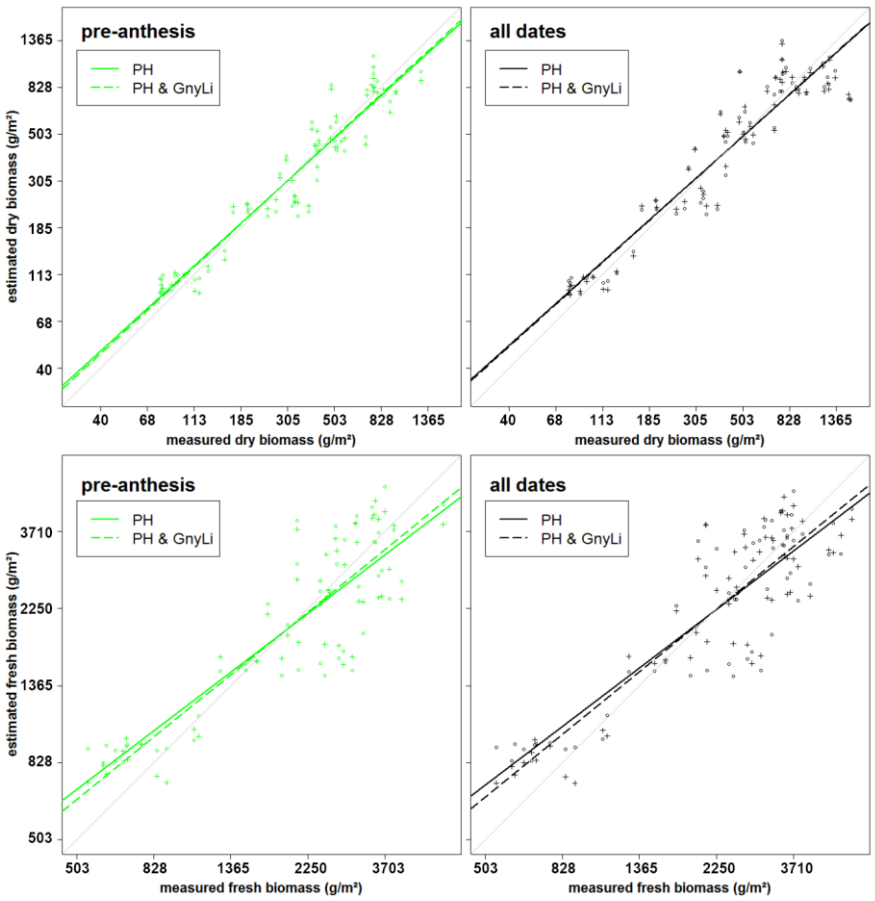

Figure 6.7 Scatterplot for one validation data set for the pre-anthesis (green) and for the whole observed period (black) of the bivariate BRM of PH (circles and solid regression line) and multivariate BRM of PH and GnyLi (crosses and dashed regression line) for dry biomass (top) and fresh biomass (bottom) (all exponential models); 1:1 line: light grey.

The robustness of the models was evaluated by calculating the ratio between the R^2 values of model calibration and validation for each BRM (Appendix Table A 6.2). Since the R^2 of calibration was divided through the R^2 of validation, values above 1 indicate better results from the calibration and below 1 indicate better results from the validation. Consequently, values close to 1 show a robust performance.

For the bivariate BRMs, PH and almost all VIs are supported as robust estimators by ratios close to 1 for all cases. The weakest ratios are attained for the REIP, in particular for fresh biomass with linear BRMs (0.73, 0.71). For the multivariate BRMs, good ratios are found for all cases. Only the linear BRMs for fresh biomass show slightly weaker values for the pre-anthesis period.

6.4 Discussion

The overall aim of this study was to evaluate whether the fusion of PH and VIs can improve the predictability of dry and fresh barley biomass compared to each parameter as individual estimator. For this work, the use of TLS to derive PH was verified and bivariate BRMs based on PH or one of six VIs as well as multivariate BRMs based on the fusion of PH with each VI were established. Extensive fieldwork over three years supported the practical application of the presented methods for monitoring crop development on plot level. The same instruments were used for all measurements whereby variations through different sensors could be excluded. However, the design of the field experiment and the measurement program was slightly modified and optimized over the years. Hence, only a part of the acquired data was used for the final model generation in order to ensure the comparability between the data sets. In the following, first the retrieval of PH from TLS data is discussed before the different BRMs are examined.

6.4.1 TLS-derived plant height

The presented study verified the reliability of the laser scanner Riegl LMS-Z420i for capturing crop surfaces. In comparison with past studies (Hoffmeister et al., 2010; Tilly et al., 2015), the scanning angle to the field was optimized through the elevated position on the hydraulic platform. However, uncertainties still remain about the influence of the scanning angle and the fixed position of the scanner during the measurements. As maintained by Ehlert and Heisig (2013)—the scanning angle can cause overestimations in the height of reflection points and should be considered in the calculation of heights. In this study, the crop surface was determined from the merged and cleaned point clouds of four scan positions, filtered with a scheme for selecting maximum points. Overestimations should therefore be precluded.

For the practical implementation of CSM-derived plant height measurements, further aspects have to be considered. Usually, the factors time and cost have a major influence on choosing a system. As shown by Hämmerle and Höfle (2014) the appropriate point density for generating a CSM varies depending on the application. In further studies, cost-efficient systems, such as the Velodyne HDL-64E (Velodyne, 2014), should be considered to investigate their potential for capturing crop surfaces in an adequate resolution. In the distant future, low-cost stationary systems might get permanently

established for monitoring plant growth on field level. Moreover, recent developments have brought up new laser scanning platforms that might accelerate the field measurement process and optimize the scanning angle. First, ground-based mobile laser scanning (MLS) systems (Kukko et al., 2012) should be taken into account for increasing the homogeneous distribution in the point cloud and thus enhancing a uniform field coverage. Second, unmanned aerial vehicles (UAVs), such as the recently introduced Riegl RiCOPTER (Riegl LMS GmbH, 2015), should be examined as a potential platform of a lightweight airborne laser scanning (ALS) systems. Promising results have already been achieved for measuring tree heights (Jaakkola et al., 2010) or detecting pruning of individual stems (Wallace et al., 2014) with UAV-based laser scanning. However, as examined in a comparative study for TLS and common plane-based ALS, the scanning angle and possible resolution influence the results (Luscombe et al., 2014) and thus have also to be taken into account for studies on UAV-based scanning systems.

In this study, TLS measurements were used to derive 3D information of points. As shown in other studies, captured intensity values could be used for qualitative analyses of the points, such as detecting single plants (Hoffmeister et al., 2012; Höfle, 2014). Whilst such analyses were not an object of this study they should be considered for further investigations. Moreover, full-waveform analysis, commonly known from ALS, can simplify the distinction between laser returns on canopy and ground returns in TLS data (Elseberg et al., 2011; Pirotti et al., 2013). The scanner used in this study however is not capable of capturing the full waveform.

The maps of plant height demonstrate the potential of the present approach for deriving plant height information on plot level in a very high resolution. The methodology of spatial plant height mapping can be scaled to field level, as long as the maximum range of the scanner is regarded and the point density is above the required minimum. As shown by Hämmerle and Höfle (2014), the coverage of the field and attained mean heights are influenced by the point density. The approach of pixel-wise calculating plant height from TLS-derived CSMs has already shown good results at the field level for monitoring a maize field, about 80 m by 160 m in size (Tilly et al., 2014c) and a sugar beet field, about 300 m by 500 m in size (Hoffmeister et al., 2010) captured from four and eight scan positions, respectively. Further studies are necessary for determining crop- or case-specific minimum values for the point density. In this context, the used sensor and its maximum range influence the required number of scan positions.

Nevertheless, for this study, high coefficients of determination between averaged CSM-derived and manual measured plant heights validate the TLS measurements. For the absolute values, differences between the measurement methods have to be considered. Whereas for the manual measurement the heights of ten plants were averaged per plot, the CSM captured the entire crop surface. Consequently, differences in the mean heights occurred, which make precision analysis between TLS

data and manual measurements infeasible. The precision of TLS measurements for agricultural applications is presumed from other studies (Höfle, 2014; Lumme et al., 2008). It is important to note that a key advantage of the TLS data is that while plants for the manual measurements are subjectively selected, CSMs enable an objective assessment of spatially continuous plant height.

6.4.2 Biomass estimation from plant height

Generally, PH performed well for the estimation of biomass in the pre-anthesis and the whole observed period. For dry biomass, PH was the best predictor for the whole observed period and similar good predictor as the best performing VIs for the pre-anthesis. However, PH performed far better for dry biomass than for fresh biomass, although these values are only distinguished by the water content of the sample. Thus, a possible explanation is the fact that the water content is not only influenced by the changing plant phenology across the growing season, but also by varying weather conditions. Moreover, during each day the available soil water and transpiration conditions vary. Hence, the amount of fresh biomass might vary more between the campaigns while the dry biomass is less influenced. Since PH is hardly affected by the water content of the plants, the varying water content in the fresh biomass adds noise to the BRM based on PH which results in lower R^2 values.

6.4.3 Biomass estimation from vegetation indices

All VIs in this study have previously shown a relationship with biomass and LAI. Since the VIs use different bands within the spectral range, they were subdivided into three categories VIS VIs (RGBVI), VISNIR VIs (NDVI, RDVI, REIP), and NIR VIs (NRI, GnyLi). The VIs showed varying performances for the estimation of dry and fresh biomass, also depending on the regarded time frame of the growing season. Generally, the VIs within a category showed a similar behavior.

The saturation problem of the NDVI type VISNIR VIs was confirmed: Typically, crops reach 100% canopy cover around mid-vegetative phase. However, most crops continue to accumulate biomass and LAI afterwards. At a LAI of about 2.5 - 3, the absorbed amount of red light reaches a peak while the NIR scattering by leaves continues to increase. Thus, the ratio of NDVI type VISNIR VIs will only show slight changes (Thenkabail et al., 2000). In this study, the sensitivity thresholds were about 185 g/m² and 1,375 g/m² for dry and fresh biomass, respectively. Additionally, after heading the canopy de-greens due to flowering and fruit development (after BBCH 5, Table 6.2) This leads to an increased reflectance in the red part of the spectrum and thus, decreases values of the VISNIR VIs, while the biomass does not decrease. Herein, this discrepancy resulted in an inadequate model parameterization for the BRMs of the VISNIR VIs and poorer results for the whole observed period than for pre-anthesis.

A similar behavior was observable for the RGBVI. The inferior results might be explained by the fact that this VI does not take the reflectance in the NIR region into account, where most of the absorption features for biomass-related plant compounds are situated (Kumar et al., 2001). These results align well with the ones presented by Bendig et al. (2015), where low correlations were found for the RGBVI with biomass after booting stage (BBCH 4, Table 6.2).

In pre-anthesis, relationships of the RGBVI with dry and fresh biomass were similar. These results suggest that the RGBVI is mostly related with vegetation cover and not directly with biomass.

In contrast, NIRVIs, such as GnyLi and NRI, use bands only in the NIR and are thus not affected by the absorption in the red part of the spectrum, which could explain the overall more consistent and better performance of the NIR VIs, particularly after anthesis. A later saturation of these VIs aligns well with other studies (Gnyp et al., 2014a; Koppe et al., 2010). Similarly, the REIP did not show any saturation effects in the pre-anthesis and yielded very good results for dry and fresh biomass. These findings can be explained by the major influence of the NIR bands that are not normalized as they are in the NDVI type VIs. Thus, the REIP saturated later than the VISNIR and VIS VIs. Nevertheless, across the whole observed period, the performance of the REIP also decreased due to saturation. The importance of the NIR domain for biomass estimation aligns with other studies (Aasen et al., 2014; Gnyp et al., 2014a; Koppe et al., 2010; Marshall and Thenkabail, 2015) and should be further investigated. Similar to PH, the NIR VIs performed better for dry than for fresh biomass while the VISNIR VIs generally performed better with fresh biomass. This suggests that the VISNIR VIs respond more to the canopy water content and the related reflectance change in the NIR shoulder rather than directly to the biomass.

Overall, the results show that the NIR VIs perform best in the prediction of fresh and dry biomass. Moreover, the results indicate that the VIS and VISNIR VIs might not be directly related to biomass. However, no rigorous sensitivity analysis was carried out in this study but, as indicated by the results, such analyses should be carried out in the future.

In general, hyperspectral field measurements have been shown to be useful in earlier studies to estimate biomass (Aasen et al., 2014; Gnyp et al., 2014b; Marshall and Thenkabail, 2015; Thenkabail et al., 2013). However, VIs are prone to errors by illumination changes (Damm et al., 2015) and multiangular reflection effects (Burkart et al., 2015). So far, the influence of these effects on the estimation of plant parameters have not been comprehensively investigated and should be examined for evaluating the potential of VIs for plant parameter estimations. Moreover, ground-based spectrometer measurements are laborious and time-consuming. Automated platforms are under development in different fields of remote sensing to overcome this difficulty but they have not yet become standard. Kicherer et al. (2015) developed a robotic platform for phenotyping grapevine based

on automatic image acquisition. Results of a mobile multi-sensor phenotyping platform for phenotyping of winter wheat are presented by Kipp et al. (2014). Moreover, hyperspectral UAV-based systems showed promise (Aasen et al., 2015; Bareth et al., 2015; Honkavaara et al., 2013; Quemada et al., 2014; Suomalainen et al., 2014). Unfortunately, the promising NIR domain is currently not well covered by UAV sensing systems.

6.4.4 Biomass estimation with fused models

Leaves make up a major part of the biomass, and VIs related to biomass are often also responsive to LAI (Thenkabail et al., 2002, 2000). Thus, it was assumed that the spectral information would complement the PH information by adding information about the canopy density and cover.

As described above, PH and VIs showed varying performances in the estimation of fresh and dry biomass and for pre-anthesis or the whole observed period. For dry biomass in pre-anthesis, the NIR VIs performed slightly better than PH. Here, the fusion with all VIs improved the predictability, whereby the NIR and VISNIR VIs yielded the best results. This can be explained by the sensitivity of the VIs to the vegetation cover in early growth stages. For the whole observed period, PH clearly outperformed the VIs in the multivariate BRMs and only the fusion with the NIR VIs increased the predictability slightly compared to PH alone. For the VIS and VISNIR VIs, the above described saturation effects might have counteracted the positive effect of the vegetation cover estimation in the early growth stages. Additionally, for pre-anthesis and across the whole observed period, the multivariate BRMs performed similarly regardless which VI was used. This indicates that most of the prediction power can be accounted to PH.

For fresh biomass across the whole observed period, the NIR VIs performed best, followed by PH. Although the VISNIR VIs did not perform well in the bivariate BRMs, they could improve the results when fused with PH. As described above, VISNIR VIs respond to the water content. Thus, they might have complement the PH information for the estimation of fresh biomass. Still, only a slight improvement was achieved with the fused models compared to the NIR VIs alone and overall, the results of multivariate BRMs with different VIs differed only slightly.

In pre-anthesis, only the NDVI and RGBVI performed poorer than PH while the REIP performed best for the fresh biomass. In combination with PH, the results of the NDVI and RDVI were improved the most, while the latter one also achieved the best results of all fused models. For the NIR VIs and REIP none or only very minor improvements were achieved and as for the whole observed period, the water was important because it influences the reflectance in the NIR. Additionally, the VIs correspond to vegetation cover in the early growth stages. Thus, in pre-anthesis already the VIs performed well and

PH only rarely contributed to the prediction power. Only the RGBVI, NDVI, and RDVI might have carried complementary information to the PH.

In this study, the NIR VIs showed the overall best performance of the VIs and seemed to carry similar information as PH. Overall, PH and NIR VIs showed the best potential for biomass estimation as individual and fused estimators. This aligns with a recent study by Marshall and Thenkabail (2015), in which they have shown the importance of PH and the NIR domain for fresh biomass estimations. The VISNIR VIs seemed to be influenced by the water content and their performance strongly depended on the regarded time frame of the growing season. Although, no comprehensive sensitivity analysis was carried out, these findings align well with other studies (Gnyp et al., 2014a, 2013). Further studies are needed to investigate the influence of the growing stage on the estimation, and whether estimators, which have been found as suitable in across growth stage estimations, are suitable for estimation at individual growth stages. Such in-season estimations are particularly important for applications in precision agriculture. Additionally, in this study VIs known for estimating biomass from hyperspectral data were used. Thus, the full potential of the fusion of 3D spatial and spectral data may not have been explored. Future studies should investigate whether other parts of the spectral range complement PH information better.

Overall, this study demonstrated the strength of bivariate BRMs based on PH and NIR VIs for estimating biomass, with only slight improvements achievable through multivariate models. In contrast, the weak performances of the VIS and VISNIR VIs as individual estimators were compensated through the fusion with PH. However, statements have to be limited, since the models indicated that PH contributed the most to the prediction power. In this context, it has to be noted that neither linear nor exponential models reflected the relation between estimators and biomass perfectly and thus more complex functions have to be considered, which might take the benefits of VIs, like sensitivity to water content, better in to account.

For practical applications the benefit of the fused models might be outweighed by the expenses to deploy two different systems. Referring to this, limitations through the attainable spatial and temporal resolution of each system have to be regarded. As already mentioned, TLS measurements can be scaled up to larger fields, as long as a sufficiently point density can be achieved, which has to be determined crop- and case-specific in further studies. Apart from that, laser scanning appeared as powerful tool for the non-destructive and objective assessment of spatially resolved plant height data. Statements about the accuracy of the measured plant heights are hardly possible due to the already mentioned different spatial resolution of the plant height measurements, however the averaged difference of 0.05 m between TLS-derived and manual measured plant heights corroborate the results (Table A 6.1). A main benefit of the field-spectrometer measurements is the high credibility of the acquired spectral

data, based on a large number of former studies, however the dependence on solar radiation and the small numbers of measurements per regarded spatial area, herein per plot, are the main disadvantages. Consequently, systems are required which are capable to assess larger areas in less time with the same accuracy of the results. Ideally, spatial and spectral information should be acquired directly through one sensor. For example, recently developed sensing systems and techniques allow to create hyperspectral point clouds (Vauhkonen et al., 2013) and hyperspectral digital surface models (Aasen et al., 2015) with only one sensor and thus, derive 3D spatial and hyperspectral information at the same time. Thus, it can be expected that 3D hyperspectral information will become increasingly available and combined analysis approaches should be further developed.

6.5 Conclusion and outlook

Continuously conducting a field experiment with different barley cultivars and the related TLS, field-spectrometer, and manual measurements enabled the acquisition of an extensive data set. High R^2 values up to 0.89, between TLS-derived and manual measured plant heights verified the applicability of the presented approach for a pixel-wise calculation of plant height (PH) from high resolution crop surface models (CSMs). Six established vegetation indices (VIs) were used to extract information from the hyperspectral data. Based on PH and VIs, bivariate and multivariate biomass regression models (BRMs) were established, with varying performances. Whereas PH was supported as strong estimator in the bivariate models (R^2 up to 0.85), VIs showed highly different results (R^2: 0.07 - 0.87). The multivariate models yielded improvements in some cases (R^2 up to 0.89), however in most cases PH had the greatest contribution to the prediction power.

Different models appeared best suitable for dry or fresh biomass estimations, also depending on the regarded time frame of the growing season, but in all cases exponential models performed better than the linear ones: For dry biomass, the bivariate BRM with PH showed the best results for the whole observed period (R^2 = 0.85), whereas for the pre-anthesis the REIP and the near-infrared (NIR) VIs GnyLi and NRI showed slightly better results than PH (R^2 = 0.86, 0.87). Multivariate BRMs from PH and one VI slightly improved the R^2 values compared to the bivariate BRMs in some cases. For fresh biomass, the bivariate BRMs of the NIR VIs showed the best results for the whole observed period (both R^2 = 0.77). For pre-anthesis, the REIP (R^2 = 0.82) showed slightly better results that the NIR VIs (both R^2 = 0.79). The multivariate BRM could slightly improve the results in some cases. Additionally, it can be noted that also weakly performing VIs, such as the NDVI or RGBVI, improved the estimations slightly when fused with PH in the multivariate BRMs, both for fresh and dry biomass. These results suggest that specific models should be chosen for specific applications, and a fusion of PH and VIs does not

always substantially improve the results. Additionally, when PH and VIs are fused, the choice of the VI does not seem critical in all cases.

Altogether, it should be noted that the presented results are a first step towards the fusion of remotely sensed 3D spatial and spectral data for a precise and non-destructive estimation of crop biomass. Other ways of data fusion may further increase the prediction power. Further studies are also necessary to investigate differences between the years, cultivars, and fertilizer treatments. Moreover, as already mentioned, in-season biomass estimations are important for precision agriculture. Therefore models should be established based on data sets from only one campaign to investigate the potential for timely monitoring and in-season estimations. Accurate and rapidly ascertainable estimations in a high spatial resolution during the growing season could support spatially resolved nitrogen nutrition index calculations. Thereby in-field variations can be considered for optimizing fertilizer application and shrinking the gap between potential and current yield. The fusion of 3D spatial and spectral data might improve such calculations as weaknesses and limitations of one estimator might be compensated through the other one.

With regard to the application in the field, the usability of new platforms should be further investigated. UAV-based lightweight ALS systems reveal potential for vegetation mapping. Futhermore, new technologies like hyperspectral snapshot camera systems which enable the derivation of 3D spatial and hyperspectral information at the same time carry great potential for agricultural applications. Combined with estimation models based on structural and spectral and information, such approaches can become a powerful tool for applications in precision agriculture and biomass monitoring.

Acknowledgments

We would like to thank Dirk Hoffmeister for his knowledgeable support of the TLS measurements and Martin Gnyp for his expertise and effort in collecting the spectral data. Further we extend our thanks to the student assistants for their great work in the field and during the post-processing (Simon Bennertz, Jonas Brands, Janis Broscheit, Markus Drahs, Silas Eichfuss, Sven Ortloff, Maximilian Willkomm), the staff of the Campus Klein-Altendorf for carrying out the experiment (Bernd Bünten, Winfried Bungert, Georg Völkering, Helmut Rehkopf), and the collaborators at the Forschungszentrum Jülich for supporting the laboratory work (Uwe Rascher, Edelgard Schölgens, Mark Müller-Linow, Francisco Pinto). Agim Ballvola is acknowledged for the coordination of the CROP.SENSe.net research group barley. We thank the anonymous reviewers for their valuable comments and Anne Wegner and Lesley-Anne Weiling for the English editing of the manuscript. Helge Aasen was supported by the Grant No. GSGS-2015B-F01 of the Graduate School of Geosciences, University of Cologne during the

preparation of this manuscript. This work was carried out within the CROP.SENSe.net project in context of the Ziel 2-Programms NRW 2007–2013 “Regionale Wettbewerbsfähigkeit und Beschäftigung”, financially supported by the Ministry for Innovation, Science and Research (MIWF) of the state North Rhine Westphalia (NRW) and European Union Funds for regional development (EFRE) (005-1103-0018).

Author Contributions

Nora Tilly and Helge Aasen were responsible for the TLS and spectrometer measurements, respectively. The post-processing of the TLS data was carried out by Nora Tilly. Helge Aasen and Georg Bareth selected the used vegetation indices. Nora Tilly substantially designed and established the analysis and mainly wrote this article. Helge Aasen carried out large parts of the analysis and added extensive sections to the manuscript. The research was directed by Georg Bareth, who supervised the whole acquiring, analyzing, and writing process.

6.6 Appendix

Table A 6.1. Statistics for the plot-wise averaged CSM-derived and manual measured plant heights (n: number of samples; $\bar{x}$: mean value; min: minimum; max: maximum; SD: standard deviation).

				CSM-derived plant height (m)				Manual measured plant height (m)			
	BBCH	N level	n	$\bar{x}$	min	max	SD	$\bar{x}$	min	max	SD
2012											
1	N/A	40	18	0.15	0.06	0.22	0.04	0.20	0.15	0.25	0.03
		80	18	0.18	0.14	0.24	0.03	0.20	0.15	0.26	0.03
2	30	40	18	0.21	0.13	0.28	0.04	0.35	0.28	0.42	0.05
		80	18	0.27	0.20	0.35	0.04	0.35	0.30	0.42	0.04
3	49	40	16	0.58	0.47	0.72	0.08	0.63	0.52	0.80	0.09
		80	15	0.64	0.48	0.80	0.11	0.66	0.54	0.79	0.08
4	N/A	40	14	0.73	0.61	0.81	0.06	0.86	0.74	0.96	0.06
		80	14	0.81	0.71	0.92	0.06	0.89	0.80	1.00	0.06
2013											
2	18	40	18	0.21	0.05	0.37	0.09	0.19	0.14	0.25	0.03
		80	18	0.11	-0.07	0.25	0.08	0.20	0.16	0.27	0.03
3	30	40	18	0.33	0.15	0.51	0.11	0.29	0.19	0.56	0.09
		80	18	0.25	0.01	0.40	0.11	0.28	0.17	0.45	0.08
4	41	40	18	0.57	0.33	0.83	0.17	0.52	0.39	0.70	0.09
		80	18	0.56	0.24	0.79	0.18	0.57	0.31	0.81	0.13
5	57	40	16	0.84	0.64	1.11	0.13	0.77	0.66	0.95	0.07
		80	16	0.79	0.58	1.04	0.12	0.81	0.54	0.94	0.11
6	68	40	14	0.78	0.65	0.97	0.09	0.77	0.66	0.84	0.05
		80	14	0.77	0.66	0.90	0.08	0.83	0.76	1.00	0.06
7	81	40	14	0.75	0.62	0.96	0.10	0.72	0.65	0.82	0.06
		80	14	0.72	0.62	0.83	0.07	0.79	0.67	0.89	0.07
2014											
2	29	40	18	0.16	0.12	0.24	0.03	0.19	0.12	0.30	0.04
		80	18	0.18	0.15	0.25	0.03	0.18	0.13	0.27	0.04
3	31	40	18	0.41	0.36	0.51	0.04	0.38	0.31	0.52	0.05
		80	18	0.42	0.34	0.52	0.05	0.36	0.27	0.45	0.05
4	49	40	18	0.63	0.53	0.70	0.04	0.59	0.53	0.65	0.03
		80	18	0.63	0.57	0.70	0.04	0.57	0.51	0.64	0.04
5	56	40	18	0.80	0.69	0.87	0.04	0.78	0.68	0.85	0.04
		80	18	0.81	0.75	0.93	0.04	0.78	0.72	0.89	0.04
6	74	40	18	0.76	0.66	0.84	0.04	0.77	0.68	0.83	0.03
		80	18	0.79	0.73	0.85	0.03	0.75	0.71	0.82	0.03

Table A 6.2. Ratio between model calibration and validation (R^2_{cal}: coefficient of determination from calibration; R^2_{val}: coefficient of determination from validation).

		Bivariate BRMs			Multivariate BRMs	
		Whole period	Pre-anthesis		Whole period	Pre-anthesis
	Estimator	**R^2_{cal} / R^2_{val}**	**R^2_{cal} / R^2_{val}**	**Estimator[a]**	**R^2_{cal} / R^2_{val}**	**R^2_{cal} / R^2_{val}**
Dry biomass – Linear	PH	0.98	0.95			
	GnyLi	0.96	0.94	GnyLi	1.00	0.97
	NDVI	1.00	0.89	NDVI	0.97	0.95
	NRI	0.98	0.95	NRI	0.98	0.96
	RDVI	1.00	0.95	RDVI	0.96	0.95
	REIP	0.80	0.85	REIP	1.00	0.95
	RGBVI	1.25	0.93	RGBVI	0.97	0.95
Dry biomass – Exponential	PH	0.99	0.99			
	GnyLi	1.00	0.99	GnyLi	0.99	0.99
	NDVI	1.03	1.03	NDVI	1.00	1.01
	NRI	1.00	1.00	NRI	1.00	1.00
	RDVI	1.03	1.03	RDVI	1.00	1.00
	REIP	0.93	0.94	REIP	0.99	0.97
	RGBVI	1.05	1.00	RGBVI	1.00	1.01
	Estimator	**R^2_{cal} / R^2_{val}**	**R^2_{cal} / R^2_{val}**	**Estimator[a]**	**R^2_{cal} / R^2_{val}**	**R^2_{cal} / R^2_{val}**
Fresh biomass – Linear	PH	0.88	0.86			
	GnyLi	0.89	0.86	GnyLi	0.90	0.86
	NDVI	0.93	0.82	NDVI	0.90	0.86
	NRI	0.91	0.86	NRI	0.90	0.86
	RDVI	0.92	0.85	RDVI	0.90	0.86
	REIP	0.73	0.71	REIP	0.90	0.82
	RGBVI	1.05	0.90	RGBVI	0.92	0.90
Fresh biomass – Exponential	PH	0.96	0.96			
	GnyLi	0.99	0.96	GnyLi	0.97	0.96
	NDVI	1.05	1.02	NDVI	0.99	1.00
	NRI	1.00	0.97	NRI	0.97	0.97
	RDVI	1.04	1.01	RDVI	0.99	0.99
	REIP	0.87	0.87	REIP	0.94	0.90
	RGBVI	1.06	1.04	RGBVI	1.01	1.03

Conflicts of Interest

The authors declare no conflict of interest.

6.7 References

Aasen, H., Burkart, A., Bolten, A., Bareth, G., 2015. Generating 3D Hyperspectral Information with Lightweight UAV Snapshot Cameras for Vegetation Monitoring: From Camera Calibration to Quality Assurance. ISPRS J. Photogramm. Remote Sens. 108, 245–259. doi:10.1016/j.isprsjprs.2015.08.002

Aasen, H., Gnyp, M.L., Miao, Y., Bareth, G., 2014. Automated hyperspectral vegetation index retrieval from multiple correlation matrices with HyperCor. Photogramm. Eng. Remote Sens. 80, 785–796. doi:10.14358/PERS.80.8.785

Ahamed, T., Tian, L., Zhang, Y., Ting, K.C., 2011. A review of remote sensing methods for biomass feedstock production. Biomass and Bioenergy 35, 2455–2469. doi:10.1016/j.biombioe.2011.02.028

Atzberger, C., 2013. Advances in Remote Sensing of Agriculture: Context Description, Existing Operational Monitoring Systems and Major Information Needs. Remote Sens. 5, 949–981. doi:10.3390/rs5020949

Bareth, G., Aasen, H., Bendig, J., Gnyp, M.L., Bolten, A., Jung, A., Michels, R., Soukkamäki, J., 2015. Low-weight and UAV-based Hyperspectral Full-frame Cameras for Monitoring Crops: Spectral Comparison with Portable Spectroradiometer Measurements. Photogramm. - Fernerkundung - Geoinf. 1, 69–79. doi:10.1127/pfg/2015/0256

Bendig, J., Yu, K., Aasen, H., Bolten, A., Bennertz, S., Broscheit, J., Gnyp, M.L., Bareth, G., 2015. Combining UAV-based plant height from crop surface models, visible, and near infrared vegetation indices for biomass monitoring in barley. Int. J. Appl. Earth Obs. Geoinf. 39, 79–87. doi:10.1016/j.jag.2015.02.012

Besl, P.J., McKay, N.D., 1992. A Method for Registration of 3D Shapes. IEEE Trans. Pattern Anal. Mach. Intell. 14, 239–256. doi:10.1117/12.57955

Bidinger, F., Musgrave, R.B., Fischer, R.A., 1977. Contribution of stored pre-anthesis assimilate to grain yield in wheat and barley. Nature 270, 431–433. doi:10.1038/270431a0

Blackburn, G.A., 1998. Quantifying Chlorophylls and Caroteniods at Leaf and Canopy Scales. Remote Sens. Environ. 66, 273–285. doi:10.1016/S0034-4257(98)00059-5

Boukerrou, L., Rasmusson, D.D., 1990. Breeding for High Biomass Yield in Spring Barley. Crop Sci. 30, 31–35. doi:10.2135/cropsci1990.0011183X003000010007x

Broge, N.H., Leblanc, E., 2001. Comparing prediction power and stability of broadband and hyperspectral vegetation indices for estimation of green leaf area index and canopy chlorophyll density. Remote Sens. Environ. 76, 156–172. doi:10.1016/S0034-4257(00)00197-8

Burkart, A., Aasen, H., Alonso, L., Menz, G., Bareth, G., Rascher, U., 2015. Angular Dependency of Hyperspectral Measurements over Wheat Characterized by a Novel UAV Based Goniometer. Remote Sens. 7, 725–746. doi:10.3390/rs70100725

Damm, A., Guanter, L., Verhoef, W., Schläpfer, D., Garbari, S., Schaepman, M.E., 2015. Impact of varying irradiance on vegetation indices and chlorophyll fluorescence derived from spectroscopy data. Remote Sens. Environ. 156, 202–215. doi:10.1016/j.rse.2014.09.031

Danson, F.M., Morsdorf, F., Koetz, B., 2009. Airborne and Terrestrial Laser Scanning for Measuring Vegetation Canopy Structure, in: Heritage, G.L., Large, A.R.G. (Eds.), Laser Scanning for the Environmental Sciences. Wiley-Blackwell, West Sussex, UK, pp. 201–219. doi:10.1002/9781444311952.ch13

Ehlert, D., Adamek, R., Horn, H.-J., 2009. Laser rangefinder-based measuring of crop biomass under field conditions. Precis. Agric. 10, 395–408. doi:10.1007/s11119-009-9114-4

Ehlert, D., Heisig, M., 2013. Sources of angle-dependent errors in terrestrial laser scanner-based crop stand measurement. Comput. Electron. Agric. 93, 10–16. doi:10.1016/j.compag.2013.01.002

Ehlert, D., Horn, H.-J., Adamek, R., 2008. Measuring crop biomass density by laser triangulation. Comput. Electron. Agric. 61, 117–125. doi:10.1016/j.compag.2007.09.013

Elseberg, J., Borrmann, D., Nüchter, A., 2011. Full Wave Analysis in 3D laser scans for vegetation detection in urban environments, in: 2011 XXIII International Symposium on Information, Communication and Automation Technologies. IEEE, pp. 1–7. doi:10.1109/ICAT.2011.6102101

Fischer, R.A., 1993. Irrigated spring wheat and timing and amount of nitrogen fertilizer. II. Physiology of grain yield response. F. Crop. Res. 33, 57–80. doi:10.1016/0378-4290(93)90094-4

Gebbers, R., Ehlert, D., Adamek, R., 2011. Rapid Mapping of the Leaf Area Index in Agricultural Crops. Agron. J. 103, 1532–1541. doi:10.2134/agronj2011.0201

Geipel, J., Link, J., Claupein, W., 2014. Combined Spectral and Spatial Modeling of Corn Yield Based on Aerial Images and Crop Surface Models Acquired with an Unmanned Aircraft System. Remote Sens. 6, 10335–10355. doi:10.3390/rs61110335

Gnyp, M.L., Bareth, G., Li, F., Lenz-Wiedemann, V.I.S., Koppe, W., Miao, Y., Hennig, S.D., Jia, L., Laudien, R., Chen, X., Zhang, F., 2014a. Development and implementation of a multiscale biomass model using hyperspectral vegetation indices for winter wheat in the North China Plain. Int. J. Appl. Earth Obs. Geoinf. 33, 232–242. doi:10.1016/j.jag.2014.05.006

Gnyp, M.L., Miao, Y., Yuan, F., Ustin, S.L., Yu, K., Yao, Y., Huang, S., Bareth, G., 2014b. Hyperspectral canopy sensing of paddy rice aboveground biomass at different growth stages. F. Crop. Res. 155, 42–55. doi:10.1016/j.fcr.2013.09.023

Gnyp, M.L., Yu, K., Aasen, H., Yao, Y., Huang, S., Miao, Y., Bareth, G., 2013. Analysis of crop reflectance for estimating biomass in rice canopies at different phenological stages. Photogramm. - Fernerkundung - Geoinf. 4, 351–365. doi:http://dx.doi.org/10.1127/1432-8364/2013/0182

Greenwood, D.J., Gastal, F., Lemaire, G., Draycott, A., Millard, P., Neeteson, J.J., 1991. Growth rate and %N of field grown crops: Theory and experiments. Ann. Bot. 67, 181–190.

Guyot, G., Baret, F., 1988. Utilisation de la haute resolution spectrale pour suivre l'etat des couverts vegetaux, in: NASA Astrophysics Data System (Ed.), Proceedings of the 4th International Colloquium on Spectral Signatures of Objects in Remote Sensing. Aussois, France, pp. 279–286.

Guyot, G., Baret, F., Jacquemoud, S., 1992. Imaging spectroscopy for vegetation studies, in: Toselli, F., Bodechtel, J. (Eds.), Imaging Spectroscopy for Vegetation Studies. Kluwer, Dordrecht, Netherlands, pp. 145–165.

Haboudane, D., Miller, J.R., Pattey, E., Zarco-Tejada, P.J., Strachan, I.B., 2004. Hyperspectral vegetation indices and novel algorithms for predicting green LAI of crop canopies: Modeling and validation in the context of precision agriculture. Remote Sens. Environ. 90, 337–352. doi:10.1016/j.rse.2003.12.013

Hair, J.F., Black, W.C., Babin, B.J., Anderson, R.E., 2010. Multivariate Data Analysis, 7th ed. Pearson, Upper Saddle River, N.J.

Hämmerle, M., Höfle, B., 2014. Effects of Reduced Terrestrial LiDAR Point Density on High-Resolution Grain Crop Surface Models in Precision Agriculture. Sensors 14, 24212–24230. doi:10.3390/s141224212

Hoffmeister, D., Bolten, A., Curdt, C., Waldhoff, G., Bareth, G., 2010. High resolution Crop Surface Models (CSM) and Crop Volume Models (CVM) on field level by terrestrial laser scanning, in: Guo, H., Wang, C. (Eds.), Proc. of SPIE, 6th International Symposium on Digital Earth. Beijing, China. doi:10.1117/12.872315

Hoffmeister, D., Tilly, N., Bendig, J., Curdt, C., Bareth, G., 2012. Detektion von Wachstumsvariabilität in vier Zuckerrübensorten, in: Clasen, M., Fröhlich, G., Bernhardt, H., Hildebrand, K., Theuvsen, B. (Eds.), Informationstechnologie Für Eine Nachhaltige Landbewirtschaftung, Proc. 32. GIL-Jahrestagung. Köllen Verlag, Bonn, Germany, Freising, pp. 135–138.

Höfle, B., 2014. Radiometric Correction of Terrestrial LiDAR Point Cloud Data for Individual Maize Plant Detection. Geosci. Remote Sens. Lett. IEEE 11, 94–98. doi:10.1109/LGRS.2013.2247022

Honkavaara, E., Saari, H., Kaivosoja, J., Pölönen, I., Hakala, T., Litkey, P., Mäkynen, J., Pesonen, L., 2013. Processing and assessment of spectrometric, stereoscopic imagery collected using a lightweight UAV spectral camera for precision agriculture. Remote Sens. 5, 5006–5039. doi:10.3390/rs5105006

Hosoi, F., Omasa, K., 2012. Estimation of vertical plant area density profiles in a rice canopy at different growth stages by high-resolution portable scanning LiDAR with a lightweight mirror. ISPRS J. Photogramm. Remote Sens. 74, 11–19. doi:10.1016/j.isprsjprs.2012.08.001

Hosoi, F., Omasa, K., 2009. Estimating vertical plant area density profile and growth parameters of a wheat canopy at different growth stages using three-dimensional portable LiDAR imaging. ISPRS J. Photogramm. Remote Sens. 64, 151–158. doi:10.1016/j.isprsjprs.2008.09.003

Jaakkola, A., Hyyppä, J., Kukko, A., Yu, X., Kaartinen, H., Lehtomäki, M., Lin, Y., 2010. A low-cost multi-sensoral mobile mapping system and its feasibility for tree measurements. ISPRS J. Photogramm. Remote Sens. 65, 514–522. doi:10.1016/j.isprsjprs.2010.08.002

Johnston, K., Ver Hoef, J.M., Krivoruchko, K., Lucas, N., 2001. Using ArcGIS Geostatistical Analyst. ESRI, USA.

Kicherer, A., Herzog, K., Pflanz, M., Wieland, M., Rüger, P., Kecke, S., Kuhlmann, H., Töpfer, R., 2015. An Automated Field Phenotyping Pipeline for Application in Grapevine Research. Sensors 15, 4823–4836. doi:10.3390/s150304823

Kipp, S., Mistele, B., Baresel, P., Schmidhalter, U., 2014. High-throughput phenotyping early plant vigour of winter wheat. Eur. J. Agron. 52, 271–278. doi:10.1016/j.eja.2013.08.009

Koenig, K., Höfle, B., Hämmerle, M., Jarmer, T., Siegmann, B., 2015. Comparative classification analysis of post-harvest growth detection from terrestrial LiDAR point clouds in precision agriculture. ISPRS J. Photogramm. Remote Sens. 104, 112–125. doi:10.1016/j.isprsjprs.2015.03.003

Koppe, W., Li, F., Gnyp, M.L., Miao, Y., Jia, L., Chen, X., Zhang, F., Bareth, G., 2010. Evaluating Multispectral and Hyperspectral Satellite Remote Sensing Data for Estimating Winter Wheat Growth Parameters at Regional Scale in the North China Plain. Photogramm. - Fernerkundung - Geoinf. 3, 167–178. doi:10.1127/1432-8364/2010/0047

Kukko, A., Kaartinen, H., Hyyppä, J., Chen, Y., 2012. Multiplatform Mobile Laser Scanning: Usability and Performance. Sensors 12, 11712–11733. doi:10.3390/s120911712

Kumar, L., Schmidt, K., Dury, S., Skidmore, A., 2001. Imaging Spectrometry and Vegetation Science, in: Meer, F. va. der, Jong, S.D. (Eds.), Imaging Spectrometry: Basic Principles and Prospective Applications, Remote Sensing and Digital Image Processing. Springer Netherlands, Dordrecht, pp. 111–155. doi:10.1007/978-0-306-47578-8_5

Lancashire, P.D., Bleiholder, H., van den Boom, T., Langelüddeke, P., Strauss, R., Weber, E., Witzenberger, A., 1991. A uniform decimal code for growth stages of crops and weeds. Ann. Appl. Biol. 119, 561–601. doi:10.1111/j.1744-7348.1991.tb04895.x

Lee, W.S., Alchanatis, V., Yang, C., Hirafuji, M., Moshou, D., Li, C., 2010. Sensing technologies for precision specialty crop production. Comput. Electron. Agric. 74, 2–33. doi:10.1016/j.compag.2010.08.005

Liaghat, S., Balasundram, S.K., 2010. A Review : The role of remote sensing in precision agriculture. Am. Soc. Agric. Biol. Eng. 5, 50–55. doi:10.3844/ajabssp.2010.50.55

Lumme, J., Karjalainen, M., Kaartinen, H., Kukko, A., Hyyppä, J., Hyyppä, H., Jaakkola, A., Kleemola, J., 2008. Terrestrial laser scanning of agricultural crops. Int. Arch. Photogramm. Remote Sens. Spat. Inf. Sci. 37 (Part B5) 563–566.

Luscombe, D.J., Anderson, K., Gatis, N., Wetherelt, A., Grand-Clement, E., Brazier, R.E., 2014. What does airborne LiDAR really measure in upland ecosystems? Ecohydrology 8, 584–594. doi:10.1002/eco.1527

Marshall, M., Thenkabail, P., 2015. Developing in situ Non-Destructive Estimates of Crop Biomass to Address Issues of Scale in Remote Sensing. Remote Sens. 7, 808–835. doi:10.3390/rs70100808

Meier, U., 2001. Growth stages of mono- and dicotyledonous plants, 2nd ed. Blackwell, Berlin.

Mulla, D.J., 2012. Twenty five years of remote sensing in precision agriculture: Key advances and remaining knowledge gaps. Biosyst. Eng. 114, 358–371. doi:10.1016/j.biosystemseng.2012.08.009

Oliver, M., 2013. An overview of precision agriculture, in: Oliver, M., Bishop, T., Marchant, B. (Eds.), Precision Agriculture for Sustainability and Environmental Protection. Springer, USA, pp. 3–19.

Olsoy, P.J., Glenn, N.F., Clark, P.E., 2014. Estimating sagebrush biomass using terrestrial laser scanning. Rangel. Ecol. Manag. 67, 224–228. doi:10.2111/REM-D-12-00186.1

Paulus, S., Dupuis, J., Riedel, S., Kuhlmann, H., 2014a. Automated analysis of barley organs using 3D laser scanning: an approach for high throughput phenotyping. Sensors 14, 12670–12686. doi:10.3390/s140712670

Paulus, S., Schumann, H., Kuhlmann, H., Léon, J., 2014b. High-precision laser scanning system for capturing 3D plant architecture and analysing growth of cereal plants. Biosyst. Eng. 121, 1–11. doi:10.1016/j.biosystemseng.2014.01.010

Pirotti, F., Guarnieri, A., Vettore, A., 2013. Vegetation filtering of waveform terrestrial laser scanner data for DTM production. Appl. Geomatics 5, 311–322. doi:10.1007/s12518-013-0119-3

Price, C., Munns, R., 2010. Growth analysis: a quantitative approach, in: Munns, R., Schmidt, S., Beveridge, C. (Eds.), Plants in Action. Australia.

Quemada, M., Gabriel, J., Zarco-Tejada, P., 2014. Airborne Hyperspectral Images and Ground-Level Optical Sensors As Assessment Tools for Maize Nitrogen Fertilization. Remote Sens. 6, 2940–2962. doi:10.3390/rs6042940

R Development Core Team, 2015. The R Project for Statistical Computing. http://www.r-project.org/

Reddersen, B., Fricke, T., Wachendorf, M., 2014. A multi-sensor approach for predicting biomass of extensively managed grassland. Comput. Electron. Agric. 109, 247–260. doi:10.1016/j.compag.2014.10.011

Riegl LMS GmbH, 2015. Infosheet RiCOPTER. http://www.riegl.com/uploads/tx_pxpriegldownloads/RiCOPTER_at_a_glance_2015-03-31.pdf

Riegl LMS GmbH, 2010. Datasheet Riegl LMS-Z420i. http://www.riegl.com/uploads/tx_pxpriegldownloads/10_DataSheet_Z420i_03-05-2010.pdf

Roujean, J.L., Breon, F.M., 1995. Estimating PAR absorbed by vegetation from bidirectional reflectance measurements. Remote Sens. Environ. 51, 375–384. doi:10.1016/0034-4257(94)00114-3

Rouse, J.W., Haas, R.H., Schell, J.A., Deering, D.W., 1974. Monitoring Vegetation Systems in the Great Plains with Erts, in: NASA (Ed.), Third Earth Resources Technology Satellite-1 Symposium. Washington, D.C., pp. 309–317.

Saeys, W., Lenaerts, B., Craessaerts, G., De Baerdemaeker, J., 2009. Estimation of the crop density of small grains using LiDAR sensors. Biosyst. Eng. 102, 22–30. doi:10.1016/j.biosystemseng.2008.10.003

Suomalainen, J., Anders, N., Iqbal, S., Roerink, G., Franke, J., Wenting, P., Hünniger, D., Bartholomeus, H., Becker, R., Kooistra, L., 2014. A Lightweight Hyperspectral Mapping System and Photogrammetric Processing Chain for Unmanned Aerial Vehicles. Remote Sens. 6, 11013–11030. doi:10.3390/rs60x000x

Thenkabail, P.S., Mariotto, I., Gumma, M.K., Middleton, E.M., Landis, D.R., Huemmrich, K.F., 2013. Selection of hyperspectral narrowbands (HNBs) and composition of hyperspectral twoband vegetation indices (HVIs) for biophysical characterization and discrimination of crop types using field reflectance and Hyperion/EO-1 data. IEEE J. Sel. Top. Appl. Earth Obs. Remote Sens. 6, 427–439. doi:10.1109/JSTARS.2013.2252601

Thenkabail, P.S., Smith, R.B., De Pauw, E., 2000. Hyperspectral Vegetation Indices and Their Relationships with Agricultural Crop Characteristics. Remote Sens. Environ. 71, 158–182. doi:10.1016/S0034-4257(99)00067-X

Thenkabail, P.S., Smith, R.B., Pauw, E. De, De Pauw, E., 2002. Evaluation of Narrowband and Broadband Vegetation Indices for Determining Optimal Hyperspectral Wavebands for Agricultural Crop Characterization. Photogramm. Eng. Remote Sensing 68, 607–621. doi:0099-111210216806-60

Tilly, N., Hoffmeister, D., Aasen, H., Brands, J., Bareth, G., 2014a. Multi-temporal Crop Surface Models derived from terrestrial laser scanning for accurate plant height measurement and biomass estimation of barley. Kölner Geogr. Arb. 94, 83–91. doi:10.5880/TR32DB.KGA94.12

Tilly, N., Hoffmeister, D., Cao, Q., Huang, S., Lenz-Wiedemann, V., Miao, Y., Bareth, G., 2014b. Multitemporal crop surface models: accurate plant height measurement and biomass estimation with terrestrial laser scanning in paddy rice. J. Appl. Remote Sens. 8, 083671–1 –22. doi:10.1117/1.JRS.8.083671

Tilly, N., Hoffmeister, D., Cao, Q., Lenz-Wiedemann, V., Miao, Y., Bareth, G., 2015. Transferability of Models for Estimating Paddy Rice Biomass from Spatial Plant Height Data. Agriculture 5, 538–560. doi:10.3390/agriculture5030538

Tilly, N., Hoffmeister, D., Schiedung, H., Brands, J., Bareth, G., 2014c. Terrestrial laser scanning for plant height measurement and biomass estimation of maize. Int. Arch. Photogramm. Remote Sens. Spat. Inf. Sci. XL-7. doi:10.5194/isprsarchives-XL-7-181-2014

Topcon Positioning Systems, I., 2006. HiPer Pro Operator's Manual. http://www.top-survey.com/top-survey/downloads/HiPerPro_om.pdf

Torabzadeh, H., Morsdorf, F., Schaepman, M.E., 2014. Fusion of imaging spectroscopy and airborne laser scanning data for characterization of forest ecosystems – A review. ISPRS J. Photogramm. Remote Sens. 97, 25–35. doi:10.1016/j.isprsjprs.2014.08.001

UNFPA, 2010. State of world population 2010-from conflict and crisis to renewal: generations of change. http://www.unfpa.org/sites/default/files/pub-pdf/EN_SOWP10.pdf

Uni Bonn, 2010a. Soil Campus Klein-Altendorf. http://www.cka.uni-bonn.de/standort/copy_of_boden

Uni Bonn, 2010b. Climate Campus Klein-Altendorf. http://www.cka.uni-bonn.de/standort/copy_of_klima

van Wart, J., Kersebaum, K.C., Peng, S., Milner, M., Cassman, K.G., 2013. Estimating crop yield potential at regional to national scales. F. Crop. Res. 143, 34–43. doi:10.1016/j.fcr.2012.11.018

Vauhkonen, J., Hakala, T., Suomalainen, J., Kaasalainen, S., Nevalainen, O., Vastaranta, M., Holopainen, M., Hyyppä, J., 2013. Classification of Spruce and Pine Trees Using Active Hyperspectral LiDAR. Geosci. Remote Sens. Lett. IEEE 10, 1138–1141. doi:10.1109/LGRS.2012.2232278

Velodyne, 2014. Velodyne HDL-64E User's Manual. http://www.velodyneLiDAR.com/LiDAR/products/manual/63-HDL64E S2 Manual_Rev D_2011_web.pdf

Wallace, L., Watson, C., Lucieer, A., 2014. Detecting pruning of individual stems using airborne laser scanning data captured from an Unmanned Aerial Vehicle. Int. J. Appl. Earth Obs. Geoinf. 30, 76–85. doi:10.1016/j.jag.2014.01.010

Willmott, C.J., 1981. On the validation of models. Phys. Geogr. 2, 184–194. doi:10.1080/02723646.1981.10642213

Willmott, C.J., Wicks, D.E., 1980. An Empirical Method for the Spatial Interpolation of Monthly Precipitation within California. Phys. Geogr. 1, 59–73. doi:10.1080/02723646.1980.10642189

Zhang, L., Grift, T.E., 2012. A LIDAR-based crop height measurement system for Miscanthus giganteus. Comput. Electron. Agric. 85, 70–76. doi:10.1016/j.compag.2012.04.001

7. COMBINING UAV-BASED PLANT HEIGHT FROM CROP SURFACE MODELS, VISIBLE, AND NEAR INFRARED VEGETATION INDICES FOR BIOMASS MONITORING IN BARLEY

JULIANE BENDIG [1,], KANG YU [1], HELGE AASEN [1], ANDREAS BOLTEN [1], SIMON BENNERTZ [1], JANIS BROSCHEIT [1], MARTIN L. GNYP [1,2,3], GEORG BARETH [1,3]*

Published in: *International Journal of Applied Earth Observation* and *Geoinformation*, 39, 79–87

DOI: 10.1016/j.jag.2015.02.012

Formatting and orthography of the manuscript is adapted to the dissertation style.

[1] Institute of Geography, GIS & RS Group, University of Cologne, Albertus-Magnus-Platz, 50923 Cologne, Germany; E-Mails: kyu@uni-koeln.de (K.Y.); helge.aasen@uni-koeln.de (H.A.); andreas.bolten@uni-koeln.de (A.B.); s.bennertz@gmail.com (S.B.); janis.b@arcor.de (J.B.); g.bareth@uni-koeln.de (G.B.)

[2] Research Centre Hanninghof, Yara International ASA, Hanninghof 35, 48249 Dülmen, Germany; E-Mail: martin.gnyp@yara.com (M.L.G.)

[3] ICASD-International Center for Agro-Informatics and Sustainable Development, College of Resources and Environmental Sciences, China Agricultural University, Beijing 100193, China

* Corresponding author: Tel.: +49-221-470-6551; E-Mail: juliane.bendig@uni-koeln.de

Abstract: In this study we combined selected vegetation indices (VIs) and plant height information to estimate biomass in a spring barley experiment. The VIs were calculated from ground-based hyperspectral data and unmanned aerial vehicle (UAV)-based red green blue (RGB) imaging. In addition, the plant height information was obtained from UAV-based multi-temporal crop surface models (CSMs). The test site is a spring barley experiment comprising 18 cultivars and two nitrogen treatments located in Western Germany. We calculated five VIs from hyperspectral data. The normalised ratio index (NRI)-based index GnyLi (Gnyp et al., 2014) showed the highest correlation (R^2=0.83) with dry biomass. In addition, we calculated three visible band VIs: the green red vegetation index (GRVI), the modified GRVI (MGRVI) and the red green blue VI (RGBVI), where the MGRVI and the RGBVI are newly developed VI. We found that the visible band VIs have potential for biomass prediction prior to heading stage. A robust estimate for biomass was obtained from the plant height models (R^2=0.80-0.82). In a cross validation test, we compared plant height, selected VIs and their combination with plant height information. Combining VIs and plant height information by using multiple linear regression or multiple non-linear regression models performed better than the VIs alone. The visible band GRVI and the newly developed RGBVI are promising but need further investigation. However, the relationship between plant height and biomass produced the most robust results. In summary, the

results indicate that plant height is competitive with VIs for biomass estimation in spring barley. Moreover, visible band VIs might be a useful addition to biomass estimation. The main limitation is that the visible band VIs work for early growing stages only.

Keywords: point cloud; structure from motion; green red vegetation index; GnyLi; SAVI; NDVI

7.1 Introduction

It is a well-known fact that biomass estimation is crucial for yield prediction of crops (Oerke et al., 2010). Crop parameters, like biomass, are frequently used to assess crop health status, nutrient supply and effects of agricultural management practices (Adamchuk et al., 2010). For management optimization, the nitrogen nutrition index (NNI) plays a key role (Chen et al., 2010; Tremblay et al., 2011). Biomass is needed for calculating the NNI (Lemaire and Gastal, 1997). A well-established method for biomass estimation is the calculation of vegetation indices (VIs) in the near infrared region (NIR) (Qi et al., 1994; Rouse et al., 1974), here defined as the range between 700 and 1300 nm (Kumar et al., 2001). Field-spectroradiometers are commonly used for the collection of hyperspectral reflectance data that are used for such calculations (Clevers and Jongschaap, 2001; Kumar et al., 2001; Royo and Villegas, 2011).

An alternative possibility is to model biomass using plant height information. Lumme et al. (2008) and Tilly et al. (2014) demonstrated the suitability of the method in wheat, oat, barley and paddy rice. Plant height information is most useful when it is available at high spatial and temporal resolution. The method of multi-temporal crop surface models (CSMs) derived from 3D point clouds delivers the desired centimeter resolution (Bendig et al., 2013; Tilly et al., 2014). The method was studied for different crops by Hoffmeister et al. (2013, 2010) for sugar beet, Tilly et al. (2014) for paddy rice and Bendig et al. (2014, 2013) for spring barley. For small fields of a few hectares, suitable data collection platforms can be ground-based like terrestrial laser scanners (Hoffmeister et al., 2013; Kraus, 2004; Tilly et al., 2014) or airborne like unmanned aerial vehicles (UAVs) (Bendig et al., 2014, 2013). Through the availability of high resolution consumer digital cameras, red green blue (RGB) aerial imaging with cm-resolution can easily be obtained using UAVs (d'Oleire-Oltmanns et al., 2012; Lucieer et al., 2014; Neitzel and Klonowski, 2012). At the same time, the emergence of structure from motion (SfM)-based software (Dandois and Ellis, 2010; Verhoeven, 2011) has enabled efficient creation of 3D point clouds and super high detail orthophotos.

Visible band VIs (VI_{RGB}) may be calculated from the orthophotos as demonstrated by Hunt et al. (2014; 2005). Motohka et al. (2010) used RGB-imagery obtained from a tower. These are some of the rare examples for small-scale field trials. Near infrared VIs (VI_{NIR}) are more widely used because of the

characteristic difference between red and NIR reflection in green vegetation (Bannari et al., 1995). In addition, smaller, but significant spectral differences in the visible bands exist, which are caused by biochemical plant constituents such as chlorophyll (Hatfield et al., 2008; Roberts et al., 2011).

Collecting RGB-imagery by UAV is simple, cost-effective and VI_{RGB} can easily be calculated from the imagery. Consequently, the goal of this study is to investigate if UAV-based VI_{RGB} can compete with VI_{NIR} for biomass estimation. Crop monitoring by UAV-based RGB imagery enables obtaining the VI_{RGB} and the plant height information from the same dataset suggesting to combine both parameters to improve biomass estimation. According to Koppe et al. (2013), a combination of hyperspectral satellite imagery and radar can improve the model quality of biomass prediction. The objective of this study is to build up on this approach of combining the two parameters plant height and vegetation indices for biomass estimation by developing suitable regression models for UAV-based non-calibrated RGB imagery and ground-based hyperspectral reflectance data. We investigate the combination of VI_{NIR} and VI_{RGB} with CSM-based plant height information.

7.2 Materials and Methods

7.2.1 Test Site

The study site is based at the Campus Klein-Altendorf agricultural research station (50°37'N, 6°59'E, altitude 186 m), located 40 km south of Cologne, Germany. In 2013, 18 spring barley (*hordeum vulgare*) cultivars were planted, of which 10 were new cultivars and eight were old cultivars (Figure 7.1, Bendig et al., 2014). They were treated with two levels of nitrogen fertilizer (40 and 80 kg N/ha). The experiment was organized in 36 small 3×7 m plots with a randomised order of the cultivars. Seedlings were planted with 300 plants/m² and a row spacing of 0.104 m. In addition, the plots are divided into a 3×5 m measuring area for plant height (PH) and reflectance measurements, and a 3×2 m sampling area for destructive biomass sampling. Biomass samples were taken frequently from April to July in 36 of the plots. For the UAV image collection, ground control points (GCPs) were evenly distributed across the field (Figure 7.1). The positions were taken using a HiPer® Pro Topcon DGPS (Topcon Corporation, Tokyo, Japan) with 0.01 m horizontal and vertical precision. Later, the GCPs were identified in the images and used for georeferencing.

7.2.2 Biomass Sampling and BBCH Measurements

A destructive sample of 0.2×0.2 m above ground biomass was taken in the sampling area for each date (Figure 7.1). The sampling dates were within one day before or after the UAV campaigns and the field-spectroradiometer measurements. For the fresh biomass, the samples were cleaned, the roots were clipped and stem, leaves and ears were weighed. In a next step, the samples were dried at 70°C for

120 h and dry biomass was weighed again for each plant. The weights were extrapolated to kg/m² for analysis. Plant growth stages were determined according to the 10 principal growth stages and 10 secondary growth stages of the "Biologische Bundesanstalt, Bundessortenamt und CHemische Industrie" (BBCH) scale (Lancashire et al., 1991) along with PH measurements. Three plant representatives for the crop stand were chosen for each plot.

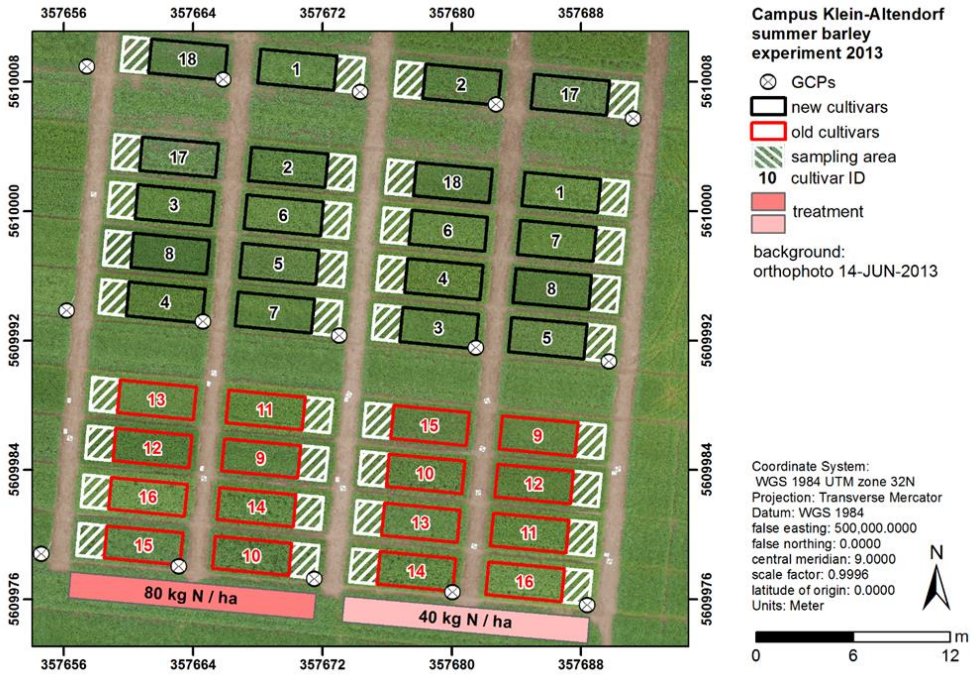

Figure 7.1 Test site: spring barley experiment at Campus Klein-Altendorf agricultural research station in 2013 (Bendig et al., 2014) with ground control points (GCPs) used for crop surface model (CSM) generation.

7.2.3 UAV-based Data Collection

The UAV used in this study was a multi-rotor MK-Oktokopter by HiSystems GmBH (Bendig et al., 2013). It is equipped with an RGB-sensor, a 16 Megapixel Panasonic Lumix GX1 (F1.7 aspheric (ASPH) fixed 20 mm lens) digital camera that is attached to the UAV on a gimbal. The gimbal compensates for the UAV movement (pitch and roll) during the flight and guarantees close to nadir image collection (Bendig et al., 2014). To trigger the sensor, we used the UAV's remote control. An autopilot was used for waypoint navigation to achieve the desired coverage of the AOI. On 30 April 2013, a bare ground ground model was recorded in a flight. Data from six flights (15 May, 28 May, 14 June, 25 June, 08 July and 23 July) were used for the plant height derived from the CSM (PH_{CSM}). Images were captured at 2 frames per second (fps) at 50 m above ground level (AGL). Camera settings were adjusted to lighting conditions and set to a fixed exposure for each flight, thus the settings changed between acquisition dates. The shutter speed varied from 1/400 s to 1/3200 s and the aperture was set to f/2.0 or f/2.8. Identical camera settings were used on three dates with shutter speed 1/1000 s and aperture f/2.0. The images were recorded during homogeneous and stable radiation conditions.

7.2.4 Field-spectroradiometer Measurements

Barley canopy reflectance was sensed with an ASD FieldSpec3 spectroradiometer (Analytical Spectral Devices, Inc., Boulder, CO, USA). The FieldSpec3 is a passive field device that is dependent on solar or artificial illumination. The spectroradiometer acquired the reflectance in the wavelength domain of 350-2500 nm with three detectors, one for the visible near infrared (VNIR: 350-1000 nm) and two for shortwave-infrared (SWIR1: 1001-1830 nm, SWIR2: 1831-2500 nm). The FieldSpec3 has a 1.4 nm sampling interval in the VNIR and 2 nm sampling interval in the SWIR. Within the manufacturer's software the bands were resampled to a resolution of 1 nm. For continuous measurements of the same footprint, the spectroradiometer's fibre probe was fixed on an orthogonal frame with a 1 m sensor-canopy distance (Laudien and Bareth, 2006), and the same field of view of 25° was used. Hence, the acquisition geometry is described by sensor-canopy distance and field of view, resulting in a 0.155 m² sample area with a 44 cm diameter at the barley canopy surface.

Reflectance measurements were taken between 11 a.m. and 2 p.m. local mean time under solar illumination at the study site. Calibration measurements were carried out with a Spectralon (polytetrafluoroethylene (PTFE)) reference panel (white colour) and a dark current at least every 10-15 minutes, depending on illumination changes. In the ASD RS3 software, twenty sample counts were set for a calibration and ten sample counts for the reflectance measurements at each scanning position of the barley canopy. Within one experimental plot, six scanning positions with representative plant growth were selected randomly and the six reflectance measurements were averaged to one value.

7.2.5 Plant Height Generation from CSM

In a first step, the collected images were mosaiced in the structure from motion (SfM)-based software Agisoft PhotoScan Professional (Verhoeven, 2011). For georeferencing the mosaic, the GCP positions were imported, manually placed on one image and automatically projected to the remaining images (Lucieer et al., 2014). Additionally, the positions were checked and adjusted manually. The software uses matching features in the images to perform a bundle adjustment and generates a point cloud (Sona et al., 2014). Finally, a digital surface model in *TIF image format is exported, which contains the crop surface model (CSM) information at a 0.01 m resolution. In addition, orthophotos are generated using the software's 'mosaicing blending mode'. In this mode, the software uses the pixel value of the most appropriate photo, in the case of overlapping photos, to calculate the orthophoto (Agisoft LLC, 2014). The orthophoto is then exported in *TIF image format at 0.01 m resolution for the VI_{RGB} calculations. For the derivation of the PH_{CSM}, we used the workflow in Esri ArcGIS® 10.2.1 described in Bendig et al. (2013). An area of interest (AOI) is defined by the outline of the measuring area of the plots, which is buffered by a 0.3 m inside buffer to exclude the plot boundaries and the sampling area.

To get information of the PH, each CSM (for each date) was subtracted from a bare ground model (Bendig et al., 2014). In a last step, the mean PH_{CSM} for each plot was averaged for each date.

7.2.6 Vegetation Indices

7.2.6.1 Near Infrared Vegetation Indices

In this study we examined the correlation of different near infrared vegetation indices (VI_{NIR}), which are reported to be well correlated with biomass or leaf area index (LAI) (Thenkabail et al., 2000). These are the normalized difference vegetation index (NDVI), the soil adjusted vegetation index (SAVI), modified SAVI (MSAVI) and optimized SAVI (OSAVI) (Table 7.1). The NDVI (Rouse et al., 1974) is the most popular VI (Pettorelli, 2013), but its applicability is limited by atmospheric influences, soil reflectance in the spectra and saturation with the occurrence of high biomass values in later growth stages (Carlson and Ripley, 1997; Haboudane, 2004). The SAVI (Huete, 1988), MSAVI (Qi et al., 1994) and OSAVI (Rondeaux et al., 1996) are based on the NDVI but include correction factors for the soil reflectance in the spectra. In addition, we calculated the GnyLi (Gnyp et al., 2014) that is based on the normalised ratio index (NRI) equation (Thenkabail et al., 2000). The GnyLi exploits the difference of two reflectance and absorption features around 900 and 1200 nm. The reflectance peak at 900 nm is caused by the intercellular plant structure, while the reflection minimum between 970 and 1200 nm is affected by plant moisture, cellulose, starch and lignin (Curran, 1989; Pu et al., 2003). In contrast to NDVI, SAVI, MSAVI and OSAVI, the GnyLi is calculated from narrow bands in the NIR domain only.

Table 7.1 Near infrared vegetation indices (VI_{NIR}) used in this study where R = reflectance (%), R_R = red (630-690 nm), R_i = reflectance in a narrow band e.g. R_{1220} = 1220 nm, L = constant *(Huete, 1988).*

VI	Name	Formula	References
NDVI	Normalized Difference Vegetation Index	$\frac{R_{900} - R_{680}}{R_{900} + R_{680}}$	(Peñuelas et al., 1993; Rouse et al., 1974)
SAVI	Soil Adjusted Vegetation Index	$(1 + L)x\frac{R_{800} - R_{670}}{R_{800} + R_{670} + L}$	(Huete, 1988)
MSAVI	Modified SAVI	$0.5\left(2R_{800}+1-\sqrt{(2xR_{800}+1)^2-8(R_{800}-R_{670})}\right)$	(Qi et al., 1994)
OSAVI	Optimized Soil-Adjusted Vegetation Index	$(1 + 0.16)x\frac{R_{800} - R_{670}}{R_{800} + R_{670} + 0.16}$	(Rondeaux et al., 1996)
GnyLi	Named by the developers Gnyp and Li	$\frac{R_{900}xR_{1050} - R_{955}xR_{1220}}{R_{900}xR_{1050} + R_{955}xR_{1220}}$	(Gnyp et al., 2014)

7.2.6.2 Visible Band Vegetation Indices

Three VI_{RGB} were calculated from the orthophotos (Table 7.2) based on the NDVI equation (Motohka et al., 2010; Tucker, 1979). The green red vegetation index (GRVI) (Tucker, 1979) is used as a phenology indicator and has potential for biomass estimation (Hunt Jr. et al., 2005). It exploits the high reflectance of plants in the green (around 540 nm) and the absorption in the red and blue part of the visible spectrum (400-700 nm) through plant chlorophylls (Gao, 2006; Gitelson et al., 2002; Motohka et al., 2010). Squaring the band reflectance values helps to amplify the differences between red, green and blue reflectance. Based on these assumptions, we developed two new VIs. The modified GRVI (MGRVI) is defined as the normalized difference of the squared green reflectance and the squared red reflectance. To capture reflectance differences due to chlorophyll a-absorption (420, 490 and 660 nm) and chlorophyll b-absorption (435, 643 nm) (Kumar et al., 2001), we further introduced the new red green blue vegetation index (RGBVI). The RGBVI is defined as the normalized difference of the squared green reflectance and the product of blue×red reflectance (Table 7.2).

Table 7.2 Visible band vegetation indices (VIRGB) used in this study where R = reflectance (%), RR = red, RG = green, RB = blue. Red, Green and Blue are the DN values in the respective channels extracted from the orthophotos.

VI	Name	Formula	References
GRVI	Green Red Vegetation Index	$\frac{R_G - R_R}{R_G + R_R}$	(Tucker, 1979)
MGRVI	Modified Green Red Vegetation Index	$\frac{(R_G)^2 - (R_R)^2}{(R_G)^2 + (R_R)^2}$	introduced here
RGBVI	Red Green Blue Vegetation Index	$\frac{(R_G)^2 - (R_B * R_R)}{(R_G)^2 + (R_B * R_R)}$	introduced here

To calculate the VI_{RGB} we processed the above mentioned orthophotos in Esri ArcGIS® 10.2.1 by using the program's ModelBuilder. We extracted the digital numbers (DN) for each band (red, green and blue) by converting the *.TIF files to float files (*.FLT; Figure 7.2). The equations in Table 7.2 served as input to the raster calculator that was used to calculate the VI_{RGB}. To obtain the mean for each plot, we used the command 'zonal statistics as table'. We repeated the process for each VI_{RGB} and each orthophoto by employing an iterator.

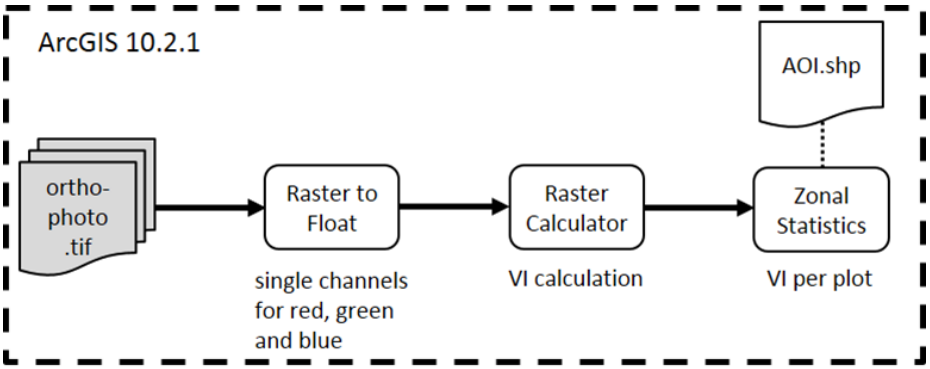

Figure 7.2 Workflow for VIRGB calculation. (AOI = old and new cultivars in Figure 7.1)

7.2.7 Statistical Analyses

The statistical analyses were executed in Microsoft® Excel® 2013 and IBM® SPSS® Statistics 22.0.0.0. Depending on the growth stages, we calculated a simple linear regression or exponential regression (Hansen and Schjoerring, 2003) for dry biomass and the VIs and PH_{CSM} (Table 7.3). To investigate the influence of combing VIs and PH_{CSM} we computed a multiple linear regression (MLR). Previous studies have shown that the relationships between the biomass and VIs or PH are often non-linear (Thenkabail et al., 2000). Therefore, a multiple non-linear regression (MNLR) model was employed to estimate the biomass. The non-linear model is a quadratic regression model (Berthold and Hand, 2006) using two variables and it takes the form of the Eq. 7.1, where y is the biomass, and x_{PH} and x_{VI} are the PH_{CSM} and VI values, respectively. The model coefficients (β_0,…, β_5) were determined for the non-linear regression model based on the calibration dataset. All processes of the non-linear model were implemented in the SPSS software package.

$$y = \beta_0 + \beta_1 x_{PH} + \beta_2 x_{VI} + \beta_3 x_{PH} x_{VI} + \beta_4 {x_{PH}}^2 + \beta_5 {x_{VI}}^2 \quad \text{(Eq. 7.1)}$$

7.3 Results

7.3.1 Plant Height and Biomass Samples

On each flight date between 200 and 800 photos of the field were taken, resulting in a point density between 2653 and 3452 (pts./m²) and a mean of >9 images covering the same part of the AOI. To cover the AOI, we undertook two consecutive flights with an average 5 min flight time per flight on each date around 9 am local mean time (2 pm on 14 July). Lighting conditions were homogeneous for all flights except 25 June. On 25 June, the lighting conditions changed between flight one and flight two. We excluded images from the second flight to maintain radiation homogeneity. From 25 June onwards, lodging occurred in the plots with cultivars 10, 11, 12 and 14 (Figure 7.1, details in Bendig et al. (2014)), resulting in lower PH and reflection changes in the affected plots. The average measured PH_{CSM} varies between 0.14 to 1.00 m with a standard error (SE) of 0.25 m. The biomass samples of plots 7 and 46

on 08 July were identified as erroneous and therefore excluded from further analysis. The averaged dry biomass ranges from 0.03 to 2.70 kg/m² with a SE of 0.68 kg/m².

7.3.2 Biomass Modelling

7.3.2.1 Model Development

Biomass modelling was carried out from 15 May until 08 July 2013 ('all data'). On 23 July, the ripening crop substantially yellowed (BBCH Stages 77-89) and was thus unsuitable for biomass estimation from VIs. The results presented below are divided into 'all data' (n = 178) and 'pre heading' (n = 108), with 'pre heading' covering 15 May until 16 June 2013, due to significantly changing performance of the VI_{RGB} with the beginning of the heading stage. The general relationship between dry biomass and the VIs or the PH_{CSM} has an exponential trend in the 'all data' class and a linear trend in the 'pre heading' class.

The coefficients of determination (R^2) for the exponential regression (ER) and linear regression (LR) between the PH_{CSM} and dry biomass and VIs and dry biomass are presented in Table 7.3. We classified R^2 in high (> 0.7), medium (0.5 <R^2< 0.7) and low (<0.5) correlation. In the ER 'all data' class, high correlations were found between PH_{CSM} (R^2 = 0.85) and the GnyLi (R^2 = 0.83). All other combinations yielded medium correlations (SAVI, MSAVI and OSAVI, R^2 = 0.54-0.6) or low correlations (NDVI, GRVI, MGRVI, RGBVI, R^2 = 0.12-0.41). In the LR of 'pre heading' growth stages we found a high correlation between dry biomass and PH_{CSM} (R^2 = 0.85) and GnyLi (R^2 = 0.71). All other relationships were medium (SAVI, MSAVI, GRVI, MGRVI, R^2 = 0.51-0.62) or low (NDVI, RGBVI, R^2 = 0.39-0.47).

Table 7.3 Coefficient of determination (R^2) and root mean square error (RMSE) for regression between dry biomass and either CSM derived plant height (PH_{CSM}) or near infrared (VI_{NIR}) or visible band (VI_{RGB}) vegetation indices where n = number of samples; ER = exponential regression and LR = linear regression.

VI/PH_{CSM} *versus* dry biomass		**exponential regression (ER)**				**linear regression (LR)**			
		all data n = 178		**pre heading n = 108**		**all data n = 178**		**pre heading n = 108**	
		R^2	**RMSE (kg/m²)**	**R^2**	**RMSE (kg/m²)**	**R^2**	**RMSE (kg/m²)**	**R^2**	**RMSE (kg/m²)**
PH_{CSM}		0.85	0.324	0.81	0.112	0.65	0.311	0.85	0.083
VI_{NIR}	GnyLi	0.83	0.350	0.76	0.119	0.62	0.326	0.71	0.113
	NDVI	0.40	0.515	0.61	0.162	0.16	0.484	0.39	0.164
	SAVI	0.59	0.468	0.70	0.144	0.30	0.441	0.51	0.147
	MSAVI	0.60	0.466	0.70	0.144	0.32	0.437	0.52	0.146
	OSAVI	0.54	0.481	0.68	0.148	0.25	0.457	0.47	0.153
VI_{RGB}	GRVI	0.13	0.596	0.79	0.117	0.00	0.528	0.62	0.130
	MGRVI	0.13	0.596	0.79	0.117	0.00	0.528	0.61	0.131
	RGBVI	0.41	0.439	0.67	0.156	0.33	0.434	0.47	0.153

7.3.2.2 Model Application

Based on the results from Table 7.3, PH_{CSM}, GnyLi, MSAVI, GRVI and RGBVI were selected for model application. The dataset was divided into a calibration and validation dataset. The validation dataset consisted of the randomly selected cultivars 1, 6, 13 and 18 (two old and two new cultivars), while the remaining cultivars served for the calibration. We developed exponential regression and multiple non-linear regression (MNLR) models for the 'all data' class and linear regression and multiple linear regression (MLR) models for the 'pre-heading' class. The calibration models (Table 7.4) were then applied to the validation datasets and evaluated by the relation between observed and predicted biomass (Figure 7.3 and 7.4).

Table 7.4 Cross-validation relationships between observed and predicted biomass (kg/m²) for selected vegetation indices, PH_{CSM} respectively and combinations of both; ER = exponential regression; MLR = multiple linear regression, LR = linear regression; MNLR = multiple non-linear regression; n = number of samples; SE = standard error; R^2 = coefficient of determination; RMSE = root mean square error; RE = relative error.

observed *versus* predicted biomass			regression model	n	SE (kg/m²)	R^2	RMSE (kg/m²)	RE (%)
All data	ER	PH_{CSM}	BIOM = 0.070×exp(PH_{CSM}×4.155)	40	0.56	0.80	0.24	44.61
		GnyLi	BIOM = 0.025×exp(GnyLi×11.757)	40	0.52	0.65	0.30	56.45
		MSAVI	BIOM = 0.001×exp(MSAVI×6.436)	40	0.40	0.22	0.46	86.84
		GRVI	BIOM = 0.187×exp(GRVI×5.594)	40	0.39	0.00	0.53	99.87
		RGBVI	BIOM = 0.062×exp(RGBVI×3.553)	40	0.47	0.59	0.32	61.18
	MNLR	GnyLi+PH_{CSM}	BIOM = 0.073+(1.206×PH_{CSM})+(-2.678×GnyLi) +(-11.109×(PH_{CSM}×GnyLi)) +(2.743×PH_{CSM}^2)+(21.811×$GnyLi^2$)	40	0.59	0.74	0.26	48.86
		MSAVI+PH_{CSM}	BIOM = 1.321+(4.243×PH_{CSM})+(-3.910×MSAVI) +(-4.403×(PH_{CSM}× MSAVI)) +(2.050×PH_{CSM}^2)+(2.865×$MSAVI^2$)	40	0.60	0.77	0.25	47.87
		GRVI+PH_{CSM}	BIOM = 0.052+(3.146×PH_{CSM})+(-2.229×GRVI) +(-3.172×(PH_{CSM}×GRVI)) +(-1.200× PH_{CSM}^2)+(1.439×$GRVI^2$)	40	0.58	0.74	0.26	49.10
		RGBVI+PH_{CSM}	BIOM = 0.404+(1.664×PH_{CSM})+(-2.332×RGBVI) +(0.275×(PH_{CSM}×RGBVI)) +(-0.285× PH_{CSM}^2)+(2.508×$RGBVI^2$)	40	0.61	0.84	0.21	40.69
Pre heading	LR	PH_{CSM}	BIOM=1.009×PH+0.018	24	0.22	0.81	0.09	45.01
		GnyLi	BIOM=2.651×GnyLi-0.196	24	0.24	0.74	0.10	51.30
		MSAVI	BIOM=1.074×MSAVI-0.651	24	0.23	0.72	0.11	55.34
		GRVI	BIOM=2.240×GRVI-0.032	24	0.24	0.76	0.10	54.22
		RGBVI	BIOM=0.878×RGBVI-0.140	24	0.23	0.64	0.10	53.21
	MLR	GnyLi+PH_{CSM}	BIOM =0.909×PH_{CSM}+0.324×GnyLi-0.014	24	0.22	0.82	0.09	44.43
		MSAVI+PH_{CSM}	BIOM =1.139×PH_{CSM}-0.220×MSAVI+0.174	24	0.22	0.78	0.09	44.24
		GRVI+PH_{CSM}	BIOM =1.077×PH_{CSM}-0.206×GRVI+0.029	24	0.22	0.79	0.09	45.01
		RGBVI+PH_{CSM}	BIOM =1.111×PH_{CSM}-0.158×RGBVI+0.067	24	0.22	0.78	0.09	45.79

In the 'all data' class (Figure 7.3), the PH_{CSM} model had a high fit with R^2 = 0.80 and a low relative error (RE) of 44.61%. Comparably high fits were found for the MNLR model combinations of GnyLi+PH_{CSM} (R^2 = 0.74, RE = 48.86%) and MSAVI+PH_{CSM} (R^2 = 0.77, RE = 47.86%) and RGBVI+PH_{CSM} (R^2 = 0.84, RE = 40.69%). The R^2 in the 'pre heading' dataset (Figure 7.4) were all above 0.64 with RE under 55.34%. The highest fit occurred for the GnyLi+PH_{CSM} MLR model (R^2 = 0.82, RE = 44.43%).

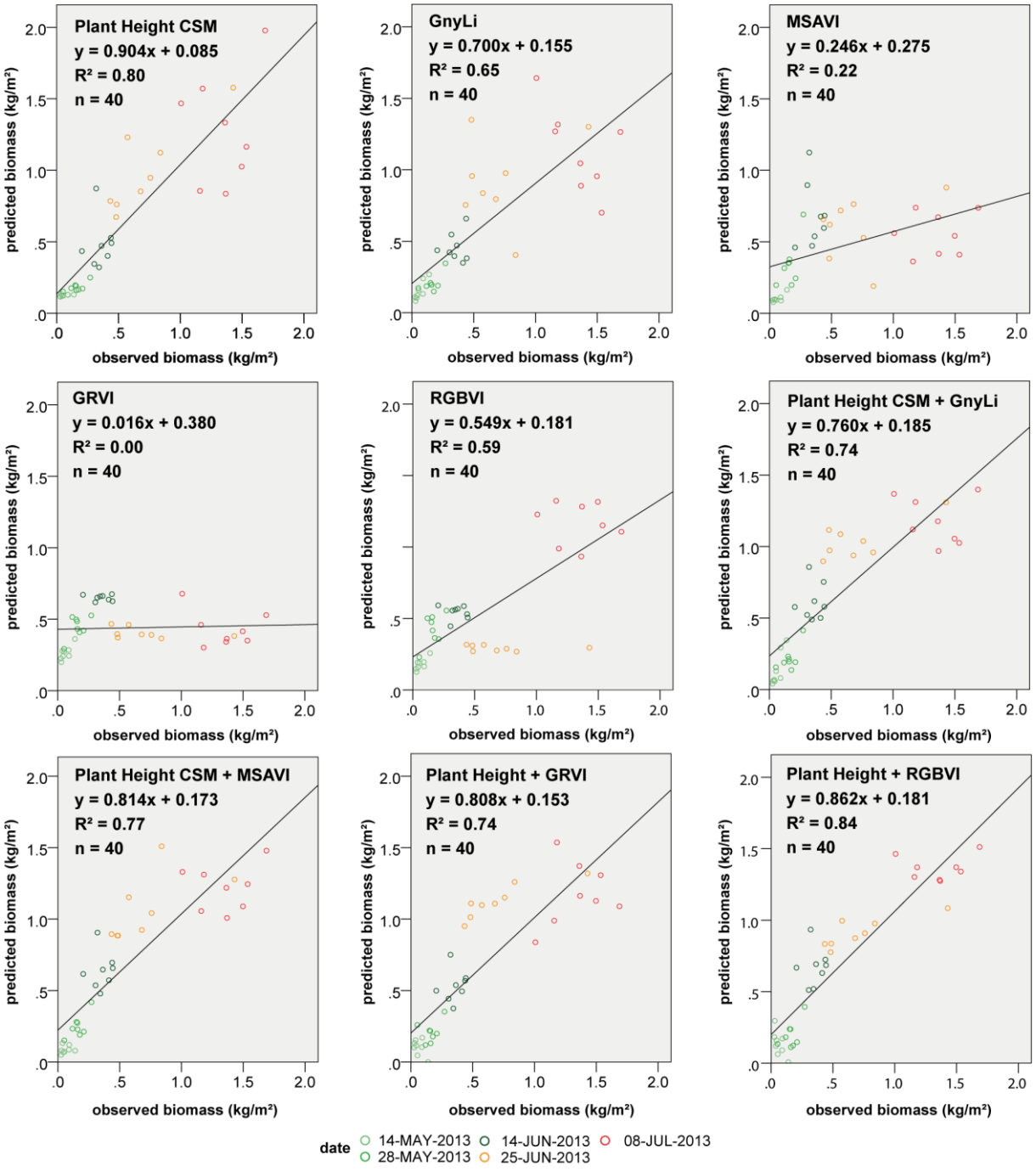

Figure 7.3 'All data' class cross-validation scatter plots for observed dry biomass versus predicted biomass derived from validation datasets listed in Table 7.4; $p < 0.0001$ for all R^2.

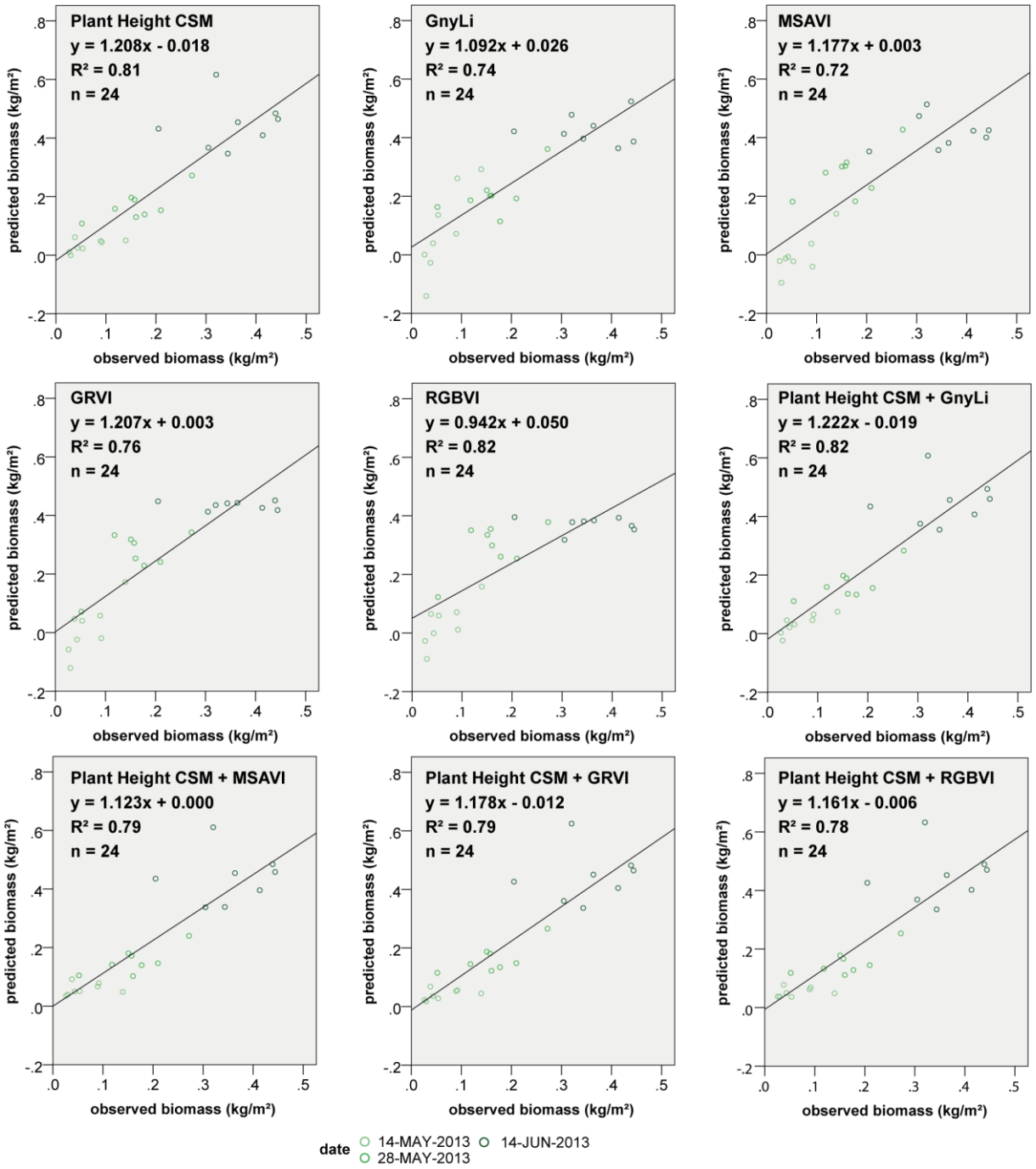

Figure 7.4 'Pre-heading' class cross-validation scatter plots for observed dry biomass versus predicted biomass derived from validation datasets listed in Table 7.4; $p < 0.0001$ for all R^2.

7.4 Discussion

The primary aim of this study is to evaluate UAV-based RGB imaging and two of its products: the plant height (PH) and VI_{RGB}. Both are available at cm-resolution derived from imagery acquired by a low flying multi-rotor UAV. We compared the performance in biomass estimation of PH, VI_{RGB}, high spectral resolution VI_{NIR} from point measurements, and the combination of the VIs with PH. It appears from the

results in Table 7.3 and Table 7.4 that CSM-derived plant height (PH_{CSM}) and GnyLi are the most robust parameters for biomass estimation in spring barley, while PH_{CSM} performs slightly better than GnyLi. In addition, combinations of PH_{CSM} with VI_{RGB} or VI_{NIR} performed better than the VIs alone. In early growth stages, only the combination of GnyLi+PH_{CSM} (R^2 = 0.82) yielded a slightly higher R^2 than the PH_{CSM} (R^2 = 0.81). Although, the RGBVI+PH_{CSM} produces a higher R^2 than the PH_{CSM} across all growth stages, this result should be regarded with caution. The performances of the VI_{RGB} vary significantly between model development and model application due to a small calibration and validation set. Thus, strong relationships in model applications might be produced randomly. Generally, the statistically more complex MLR and MNLR produce robust results, but a more significant improvement was expected. Positive examples for combining remotely sensed information from different sources are found in the literature (Koppe et al., 2013; Liu et al., 2006). Most studies comparable to this one either investigate the relationship between PH and biomass (Ehlert et al., 2008; Lumme et al., 2008) or the relationship between VIs and biomass (Hunt Jr. et al., 2005; Motohka et al., 2010; Tucker, 1979). Geipel et al. (2014) investigated yield prediction from UAV-based CSMs and VI_{RGB} for early growth stages in maize. They found a slightly higher correlation (up to R^2 = 0.74) between yield and PH_{CSM} in combination with one of three tested VI_{RGB}.

Of the VI_{NIR} investigated here, the GnyLi clearly outperformed the NDVI-based indices. This result is consistent with a multi-scale study for winter wheat, where the GnyLi outperformed 14 other indices (Gnyp et al., 2014). The NDVI-based indices perform lower, due to the well-known saturation effect. Similar results are reported by (Baret and Guyot, 1991; Gnyp et al., 2014; Haboudane, 2004; Mutanga and Skidmore, 2004). According to the statistics, the GRVI and MGRVI showed no correlation and the RGBVI produced a low correlation to the biomass after the booting stage (14 June 2013). Nevertheless, high positive correlations were found until booting stage, which is important for fertilizer management to improve crop yield. Management recommendations show that spring barley is commonly fertilized after seeding and at the tillering stage (Munzert and Frahm, 2006). Additionally, Chang et al. (2005) state that the booting stage is best suited for yield prediction using canopy reflectance. Similarly, studies in different crops and grasses by Motohka et al. (2010), Hunt et al. (2005) and Tucker (1979) demonstrate that the applicability of VI_{RGB} is limited to certain growth stages.

Generally, there are noteworthy constraints in the VI_{RGB} generation method. We collected images with fixed exposure under homogeneous radiation conditions. We then calculated the VI_{RGB} from an image mosaic. Minor changes in radiation can cause varying RGBVI values. As a result, there is no radiometric correction for changes in lighting conditions between single photos. Changing light incidence introduces bidirectional reflectance distribution function (BRDF) effects, even in close to nadir imaging

(Grenzdörffer and Niemeyer, 2011). Capturing the whole AOI in one image can partly eliminate the problem. Furthermore, no calibration between the images was possible because no object of known reflectance was present, like e.g. calibration panels or colored tarpaulins. Moreover, no investigation was made of the exact wavelengths covered by the red, green and blue bands of the digital camera. On the one hand, a calibration of digital numbers (DN) in the images with a monochromatic light source is highly recommended (Hunt Jr. et al., 2005). On the other hand, a comparison of RGBVI values calculated from the field-spectroradiometer and the UAV-based data yielded an R^2 of 0.9 for the early growth stages. Ultimately, multi-year studies are required to evaluate and improve the method for obtaining VI_{RGB} from UAV-based RGB imagery.

Practically speaking, the data collection for hyperspectral reflectance data with a field-spectroradiometer is more complex and time-consuming than the data collection with an UAV-system. A field-spectroradiometer produces point data, while UAV-based imaging has the advantage of capturing infield variability faster and with a dense spatial coverage. Moreover, a field-spectroradiometer is a sensitive and expensive instrument that requires significant expertise. A spectroradiometer's main advantage is the high spectral resolution of calibrated spectra. On the other hand an out-of-the-box UAV-system can be operated by a larger user group at a low cost. Moreover, with an 800€ sensor plant height can be measured and biomass can be estimated almost as good as with VI_{NIR} from the spectroradiometer.

7.5 Conclusions and Outlook

In this study, we examined the suitability of plant height and vegetation indices in the visible and near infrared region in their suitability for biomass prediction in a spring barley experiment. The statistical analysis showed that the GnyLi near infrared index is a suitable indicator for biomass as well as unmanned aerial vehicle-derived plant height from crop surface models. Secondly, there is potential for biomass estimation by combining plant height and visible band vegetation indices like Green Red Vegetation Index (GRVI), newly developed Modified Green Red Vegetation Index (MGRVI), and Red Green Blue Vegetation Index (RGBVI). We found that the visible band indices showed a better ability to model biomass in early growth stages in comparison to late growth stages. Contrary to expectation, the combination of vegetation indices and plant height did not significantly improve the model performance.

Using an unmanned aerial vehicle with a non-calibrated optical camera to calculate visible band vegetation indices and plant height is a unique way to estimate biomass on small agricultural research

fields. It is a simple and timely alternative to cost-intensive and complex ground-based reflectance measurements.

Future studies should examine these simple and cost effective method for multiple year datasets to improve robustness and applicability. In addition, new hyperspectral full frame cameras for unmanned aerial vehicles are a promising development for research in near infrared vegetation indices by combining high spectral and spatial resolution, opening up new possibilities in crop monitoring.

Acknowledgments

The authors acknowledge the funding of the CROP.SENSe.net project in the context of the Ziel 2-Programm North Rhine-Westphalia (NRW) 2007–2013 “Regionale Wettbewerbsfähigkeit und Beschäftigung (Europäischer Fonds für regionale Entwicklung (EFRE))” by the Ministry for Innovation, Science and Research (Ministerium für Innovation, Wissenschaft und Forschung (MIWF)) of the state North Rhine-Westphalia (NRW) and European Union Funds for regional development (EFRE) (005-1103-0018).

7.6 References

Adamchuk, V.I., Ferguson, R.B., Hergert, G.W., 2010. Soil Heterogeneity and Crop Growth, in: Oerke, E.-C., Gerhards, R., Menz, G., Sikora, R.A. (Eds.), Precision Crop Protection - the Challenge and Use of Heterogeneity. Springer, Dordrecht, Netherlands, pp. 3–16.

Agisoft LLC, 2014. Agisoft PhotoScan [WWW Document]. Agisoft PhotoScan. URL http://www.agisoft.com (accessed 10.9.14).

Bannari, A., Morin, D., Bonn, F., Huete, A.R., 1995. A review of vegetation indices. Remote Sensing Reviews 13, 95–120. doi:10.1080/02757259509532298

Baret, F., Guyot, G., 1991. Potentials and limits of vegetation indices for LAI and APAR assessment. Remote Sensing of Environment 35, 161–173. doi:10.1016/0034-4257(91)90009-U

Bendig, J., Bolten, A., Bareth, G., 2013. UAV-based Imaging for Multi-Temporal, very high Resolution Crop Surface Models to monitor Crop Growth Variability. Photogrammetrie - Fernerkundung - Geoinformation 6, 551–562. doi:10.1127/1432-8364/2013/0200

Bendig, J., Bolten, A., Bennertz, S., Broscheit, J., Eichfuss, S., Bareth, G., 2014. Estimating Biomass of Barley Using Crop Surface Models (CSMs) Derived from UAV-Based RGB Imaging. Remote Sensing 6, 10395–10412. doi:10.3390/rs61110395

Berthold, M.R., Hand, D., 2006. Intelligent Data Analysis, 2nd ed. Springer, Berlin, Germany.

Carlson, T.N., Ripley, D.A., 1997. On the relation between NDVI, fractional vegetation cover, and leaf area index. Remote Sensing of Environment 62, 241–252. doi:10.1016/S0034-4257(97)00104-1

Chang, K.-W., Shen, Y., Lo, J.-C., 2005. Predicting Rice Yield Using Canopy Reflectance Measured at Booting Stage. Agronomy Journal 97, 872. doi:10.2134/agronj2004.0162

Chen, P., Haboudane, D., Tremblay, N., Wang, J., Vigneault, P., Li, B., 2010. New spectral indicator assessing the efficiency of crop nitrogen treatment in corn and wheat. Remote Sensing of Environment 114, 1987–1997. doi:10.1016/j.rse.2010.04.006

Clevers, J.P.G.W., Jongschaap, R., 2001. Imaging Spectrometry For Agricultural Applications, in: Meer, F.D. van der, Jong, S.M.D. (Eds.), Imaging Spectrometry, Remote Sensing and Digital Image Processing. Kluwer Academic Publishers, Dordrecht, Netherlands, pp. 157–199.

Curran, P.J., 1989. Remote sensing of foliar chemistry. Remote Sensing of Environment 30, 271–278. doi:10.1016/0034-4257(89)90069-2

Dandois, J.P., Ellis, E.C., 2010. Remote Sensing of Vegetation Structure Using Computer Vision. Remote Sensing 2, 1157–1176. doi:10.3390/rs2041157

d'Oleire-Oltmanns, S., Marzolff, I., Peter, K., Ries, J., 2012. Unmanned Aerial Vehicle (UAV) for Monitoring Soil Erosion in Morocco. Remote Sensing 4, 3390–3416. doi:10.3390/rs4113390

Ehlert, D., Horn, H.-J., Adamek, R., 2008. Measuring crop biomass density by laser triangulation. Computers and Electronics in Agriculture 61, 117–125. doi:10.1016/j.compag.2007.09.013

Gao, J., 2006. Canopy chlorophyll estimation with hyperspectral remote sensing (dissertation). Kansas State University, Manhattan, Kansas, US.

Geipel, J., Link, J., Claupein, W., 2014. Combined Spectral and Spatial Modeling of Corn Yield Based on Aerial Images and Crop Surface Models Acquired with an Unmanned Aircraft System. Remote Sensing 6, 10335–10355. doi:10.3390/rs61110335

Gitelson, A.A., Kaufman, Y.J., Stark, R., Rundquist, D., 2002. Novel algorithms for remote estimation of vegetation fraction. Remote Sensing of Environment 80, 76–87. doi:10.1016/s0034-4257(01)00289-9

Gnyp, M.L., Bareth, G., Li, F., Lenz-Wiedemann, V.I.S., Koppe, W., Miao, Y., Hennig, S.D., Jia, L., Laudien, R., Chen, X., Zhang, F., 2014. Development and implementation of a multiscale biomass model using hyperspectral vegetation indices for winter wheat in the North China Plain. International Journal of Applied Earth Observation and Geoinformation 33, 232–242. doi:10.1016/j.jag.2014.05.006

Grenzdörffer, G.J., Niemeyer, F., 2011. UAV based BRDF-measurements of agricultural surfaces with PFIFFIKUS. International Archives of the Photogrammetry, Remote Sensing and Spatial Information Sciences XXXVIII-1/C22, 229–234.

Haboudane, D., 2004. Hyperspectral vegetation indices and novel algorithms for predicting green LAI of crop canopies: Modeling and validation in the context of precision agriculture. Remote Sensing of Environment 90, 337–352. doi:10.1016/j.rse.2003.12.013

Hansen, P.M., Schjoerring, J.K., 2003. Reflectance measurement of canopy biomass and nitrogen status in wheat crops using normalized difference vegetation indices and partial least squares regression. Remote Sensing of Environment 86, 542–553. doi:10.1016/S0034-4257(03)00131-7

Hatfield, J.L., Gitelson, A.A., Schepers, J.S., Walthall, C.L., 2008. Application of Spectral Remote Sensing for Agronomic Decisions. Agronomy Journal 100, S117–S131. doi:10.2134/agronj2006.0370c

Hoffmeister, D., Bolten, A., Curdt, C., Waldhoff, G., Bareth, G., 2010. High-resolution Crop Surface Models (CSM) and Crop Volume Models (CVM) on field level by terrestrial laser scanning, in: Guo, H., Wang, C. (Eds.), SPIE Proceedings of the Sixth International Symposium on Digital Earth: Models, Algorithms, and Virtual Reality. Presented at the Sixth International Symposium on Digital Earth: Models, Algorithms, and Virtual Reality, Beijing, China, p. 78400E–78400E–6. doi:10.1117/12.872315

Hoffmeister, D., Waldhoff, G., Curdt, C., Tilly, N., Bendig, J., Bareth, G., 2013. Spatial variability detection of crop height in a single field by terrestrial laser scanning, in: Stafford, J.V. (Ed.), Precision Agriculture ’13. Presented at the 9th European Conference on Precision Agriculture, Wageningen Academic Publishers, Lleida, Spain, pp. 267–274.

Huete, A.R., 1988. A soil-adjusted vegetation index (SAVI). Remote Sensing of Environment 25, 295–309. doi:10.1016/0034-4257(88)90106-X

Hunt, E., Daughtry, C., Mirsky, S., Hively, W., 2014. Remote Sensing With Simulated Unmanned Aircraft Imagery for Precision Agriculture Applications. IEEE Journal of Selected Topics in Applied Earth Observations and Remote Sensing. doi:10.1109/JSTARS.2014.2317876

Hunt Jr., E.R., Cavigelli, M., Daughtry, C.S.T., McMurtrey III, J.E., Walthall, C.L., 2005. Evaluation of Digital Photography from Model Aircraft for Remote Sensing of Crop Biomass and Nitrogen Status. Precision Agriculture 6, 359–378. doi:10.1007/s11119-005-2324-5

Koppe, W., Gnyp, M.L., Hütt, C., Yao, Y., Miao, Y., Chen, X., Bareth, G., 2013. Rice monitoring with multi-temporal and dual-polarimetric TerraSAR-X data. International Journal of Applied Earth Observation and Geoinformation 21, 568–576. doi:10.1016/j.jag.2012.07.016

Kraus, K., 2004. Photogrammetrie: Geometrische Informationen aus Photographien und Laserscanneraufnahmen, 7th ed. Walter de Gruyter, Berlin, Germany.

Kumar, L., Schmidt, K., Dury, S., Skidmore, A., 2001. Imaging Spectrometry and Vegetation Science, in: Meer, F.D. van der, Jong, S.M.D. (Eds.), Imaging Spectrometry, Remote Sensing and Digital Image Processing. Kluwer Academic Publishers, Dordrecht, Netherlands, pp. 111–155.

Lancashire, P.D., Bleiholder, H., Boom, T.V.D., Langelüddeke, P., Stauss, R., Weber, E., Witzenberger, A., 1991. A uniform decimal code for growth stages of crops and weeds. Annals of Applied Biology 119, 561–601. doi:10.1111/j.1744-7348.1991.tb04895.x

Laudien, R., Bareth, G., 2006. Multitemporal Hyperspectral Data Analysis for Regional Detection of Plant Diseases by using a Tractor- and an Airborne-based Spectrometer. Photogrammetrie - Fernerkundung - Geoinformation 3, 217–227.

Lemaire, G., Gastal, F., 1997. N Uptake and Distribution in Plant Canopies, in: Lemaire, D.G. (Ed.), Diagnosis of the Nitrogen Status in Crops. Springer, Berlin, Germany, pp. 3–43.

Liu, L., Wang, J., Bao, Y., Huang, W., Ma, Z., Zhao, C., 2006. Predicting winter wheat condition, grain yield and protein content using multi-temporal EnviSat-ASAR and Landsat TM satellite images. International Journal of Remote Sensing 27, 737–753. doi:10.1080/01431160500296867

Lucieer, A., Turner, D., King, D.H., Robinson, S.A., 2014. Using an Unmanned Aerial Vehicle (UAV) to capture micro-topography of Antarctic moss beds. International Journal of Applied Earth Observation and Geoinformation 27, 53–62. doi:10.1016/j.jag.2013.05.011

Lumme, J., Karjalainen, M., Kaartinen, H., Kukko, A., Hyyppä, J., Hyyppä, H., Jaakkola, A., Kleemola, J., 2008. Terrestrial laser scanning of agricultural crops. The International Archives of the Photogrammetry, Remote Sensing and Spatial Information Sciences 37, 563–566.

Motohka, T., Nasahara, K.N., Oguma, H., Tsuchida, S., 2010. Applicability of Green-Red Vegetation Index for Remote Sensing of Vegetation Phenology. Remote Sensing 2, 2369–2387. doi:10.3390/rs2102369

Munzert, M., Frahm, J., 2006. Pflanzliche Erzeugung: Grundlagen des Acker- und Pflanzenbaus und der Guten fachlichen Praxis, Grundlagen der Verfahrenstechnik, Produktions- und Verfahrenstechnik für Kulturpflanzen, Dauergrünland, Sonderkulturen, Nachwachsende Rohstoffe, Ökologischer Landbau, Naturschutz und Landschaftspflege, 12th ed. BLV, Munich, Germany.

Mutanga, O., Skidmore, A.K., 2004. Narrow band vegetation indices overcome the saturation problem in biomass estimation. International Journal of Remote Sensing 25, 3999–4014. doi:10.1080/01431160310001654923

Neitzel, F., Klonowski, J., 2012. Use of point cloud with a low-cost UAV system for 3D mapping, in: International Archives of the Photogrammetry, Remote Sensing and Spatial Information Science. Presented at the 2011 ISPRS Zurich 2011 Workshop, 14-16 September 2011, Zurich, Switzerland, Zurich, pp. 39–44.

Oerke, E.-C., Gerhards, R., Menz, G., Sikora, R.A. (Eds.), 2010. Precision Crop Protection - the Challenge and Use of Heterogeneity. Springer, Dordrecht, Netherlands.

Peñuelas, J., Gamon, J.A., Griffin, K.L., Field, C.B., 1993. Assessing community type, plant biomass, pigment composition, and photosynthetic efficiency of aquatic vegetation from spectral reflectance. Remote Sensing of Environment 46, 110–118. doi:10.1016/0034-4257(93)90088-F

Pettorelli, N., 2013. The Normalized Difference Vegetation Index. Oxford University Press, Oxford, UK.

Pu, R., Ge, S., Kelly, N.M., Gong, P., 2003. Spectral absorption features as indicators of water status in coast live oak (Quercus agrifolia) leaves. International Journal of Remote Sensing 24, 1799–1810. doi:10.1080/01431160210155965

Qi, J., Chehbouni, A., Huete, A.R., Kerr, Y.H., Sorooshian, S., 1994. A modified soil adjusted vegetation index. Remote Sensing of Environment 48, 119–126. doi:10.1016/0034-4257(94)90134-1

Roberts, D., Roth, K., Perroy, R., 2011. Hyperspectral Vegetation Indices, in: Thenkabail, P.S., Huete, A. (Eds.), Hyperspectral Remote Sensing of Vegetation. CRC Press, Boca Raton, FL, US, pp. 309–328.

Rondeaux, G., Steven, M., Baret, F., 1996. Optimization of soil-adjusted vegetation indices. Remote Sensing of Environment 55, 95–107. doi:10.1016/0034-4257(95)00186-7

Rouse, J.W., Haas, R.H., Schell, J.A., Deering, D.W., 1974. Monitoring Vegetation Systems in the Great Plains with Erts. NASA Special Publication 351, 309.

Royo, C., Villegas, D., 2011. Field Measurements of Canopy Spectra for Biomass Assessment of Small-Grain Cereals, in: Matovic, M.D. (Ed.), Biomass - Detection, Production and Usage. InTech, Rijeka, Croatia, pp. 27–52.

Sona, G., Pinto, L., Pagliari, D., Passoni, D., Gini, R., 2014. Experimental analysis of different software packages for orientation and digital surface modelling from UAV images. Earth Sci Inform 7, 97–107. doi:10.1007/s12145-013-0142-2

Thenkabail, P.S., Smith, R.B., De Pauw, E., 2000. Hyperspectral vegetation indices and their relationships with agricultural crop characteristics. Remote sensing of Environment 71, 158–182. doi:10.1016/S0034-4257(99)00067-X

Tilly, N., Hoffmeister, D., Cao, Q., Huang, S., Lenz-Wiedemann, V.I.S., Miao, Y., Bareth, G., 2014. Multitemporal crop surface models: accurate plant height measurement and biomass estimation with terrestrial laser scanning in paddy rice. Journal of Applied Remote Sensing 8, 083671–083671. doi:10.1117/1.JRS.8.083671

Tremblay, N., Fallon, E., Ziadi, N., 2011. Sensing of crop nitrogen status: Opportunities, tools, limitations, and supporting information requirements. HortTechnology 21, 274–281.

Tucker, C.J., 1979. Red and photographic infrared linear combinations for monitoring vegetation. Remote Sensing of Environment 8, 127–150. doi:10.1016/0034-4257(79)90013-0

Verhoeven, G., 2011. Taking computer vision aloft - archaeological three-dimensional reconstructions from aerial photographs with photoscan. Archaeological Prospection 18, 67–73. doi:10.1002/arp.399

8. AUTOMATED HYPERSPECTRAL VEGETATION INDEX RETRIEVAL FROM MULTIPLE CORRELATION MATRICES WITH HYPERCOR

*HELGE AASEN [1, *], MARTIN LEON GNYP[1], YUXIN MIAO, Y. [2], GEORG BARETH [1]*

Published in: Photogrammetric Engineering & Remote Sensing, 80 (8), 785–796.

DOI: 10.14358/PERS.80.8.785

Formatting and orthography of the manuscript is adapted to the dissertation style.

[1] Institute of Geography (GIS & Remote Sensing Group), University of Cologne, 50923 Cologne, Germany

[2] College of Resources and Environmental Science, China Agricultural University, 100193 Beijing, China

* Corresponding author: Tel.: +49 221 470 6265; Email: helge.aasen@uni-koeln.de

Abstract: Hyperspectral vegetation indices and optimized hyperspectral narrow bands have shown high potential for characterizing, classifying, monitoring, and modeling of vegetation and agricultural crops. Correlation matrices from hyperspectral vegetation indices and plant growth parameters help select important wavelength domains and identify redundant bands to overcome the Hughes phenomenon. We introduce HyperCor as a tool for automated pre-processing of narrowband hyperspectral data and computation of correlation matrices. Furthermore, we propose a multi-correlation matrix strategy which combines multiple correlation matrices and uses more information not only from each matrix but also from different datasets. We applied this method to a large multi-temporal spectral library to derive vegetation indices for rice biomass detection in the tillering, stem elongation, and heading stages. The models were calibrated with data from three consecutive years and validated using independent data from two different years. The validation results revealed that the multi-correlation matrix strategy could improve the model performance.

Keywords: multi-correlation matrix strategy, data mining, data processing, model development, spectral library, biomass, rice, software development

8.1 Introduction

Plants have a decisive role in the ecosystems of the earth as they cover more than two-thirds of the land surface and are able to produce organic compounds through photosynthesis (Jensen, 2007). Due to the increasing demand for energy and food with limited or even diminishing agricultural areas, the productivity of existing arable land must be enhanced (Thenkabail et al., 2012). This may be accomplished by implementing more efficient management methods supported by remote sensing (Moran et al., 1997; Mariotto et al., 2013).

Hyperspectral sensors monitor agricultural crops by collecting continuous narrow band spectral reflectance. With the resulting hyperspectral narrow bands (HNBs), dynamic changes in the biophysiology and biochemical compounds of plants can be detected (Gitelson, 2011; Thenkabail et al., 2011; Zhu et al., 2011). Additionally, hyperspectral close range sensors such as field-spectrometers, which provide high spectral resolution, represent a valuable data source for calibration and simulation of potential upcoming sensors (Milton et al., 2009; Roberts et al., 2011).

However, from the huge amount of data collected by hyperspectral sensors optimized HNBs have to be selected to characterize, differentiate, and model vegetation (Thenkabail et al., 2000; Galvao et al., 2011; Thenkabail et al., 2011). In the past, researchers have investigated the best suited hyperspectral vegetation indices (HVIs) for various agricultural plants monitoring. Biophysical parameters such as biomass (Hansen and Schjoerring, 2003; Koppe et al., 2010; Gnyp et al., 2013), and LAI (Shibayma and Akiyama, 1989; Haboudane et al., 2004), as well as biochemical parameters such as nitrogen (Hansen and Schjoerring, 2003; Stroppiana et al., 2009; Li et al., 2010; Yu et al., 2013), and chlorophyll (Gitelson et al., 1996; Miao et al., 2009), and plant stress (Mahlein et al., 2013) were examined. Nevertheless, there is still a demand for systematic analysis of the HVIs. Huete et al. (1994) and Running et al. (1994) defined the requirements of vegetation indices which also count for HVIs. Thus, further research has to address the robustness of already proposed and future HVIs with respect to influences of different climatic conditions (annual and regional), soils, management practices, or plant varieties as well as how specific vegetation indices perform on different plant parameters. The first step to address these research questions is the establishment of comprehensive spectral libraries, which cover a wide variety of different experiments (Laudien et al., 2006; Rao et al., 2007; Chauhan and Mohan, 2013). On the other hand, standardized analysis procedures have to be applied to extract the information from those databases and identify redundant data to overcome the Hughes phenomenon (or the curse of high dimensionality, see Bajwa and Kulkarni, 2011) resulted from advances in technology and its application.

In this study, we introduce HyperCor as a software tool to carry out standard procedures of hyperspectral data analysis, namely the computation of correlation and redundancy matrices introduced by Thenkabail et al. (2000; 2004a; 2004b), to identify optimal HNBs and HVIs. HyperCor automates the data pre-processing, redundant bands detection, and correlation matrices (CMs) computation between hyperspectral data and desired plant parameters based on different vegetation index types. In addition, the tool also calculates descriptive statistics of the input data and generates supplements for the interpretation of the output CMs. The whole process is controlled by a Graphical User Interface (GUI). Thus, it may support researchers in the development and evaluation of optimized HNBs and HVIs for crop sensing, and in the identification of redundant data in hyperspectral datasets to overcome the curse of dimensionality.

As a new and innovative approach, we propose the multi-correlation matrix strategy (MCMS) which is based on the correlation matrices computed by HyperCor for hyperspectral data mining. The MCMS combines the information contained in multiple CMs from different datasets to identify important HNBs or spectral domains. In this study we applied the MCMS to a large multi-temporal dataset from a spectral library of rice in order to develop HVIs for the non-destructive monitoring and modeling of rice biomass in different growth stages.

8.2 Study site and data

8.2.1 Study site and experiment design

The study site, Jiansanjiang (47.2°N, 132.8°N E), is located in the Sanjiang Plain, which is an alluvial plain of the three rivers, Heilong, Songhua, and Wusuli River and covers approximately 108,900 km². During the past decades, the Plain has been converted from a marsh ecosystem to a rice crop system and became a granary in the Heilongjiang Province of Northeast China. The area is characterized by the warm-temperature sub-humid continental East Asian monsoon climate controlled by the thermal low-pressure area at the Tibetan Plateau, which defines clear seasonal changes between a cold, sunny, and dry winter and a temperate, cloudy, and wet summer.

Field experiments were conducted from 2007 to 2009 and from 2011 to 2012. The experiments had seven nitrogen rates in 2007 and five rates in 2008-2009 and 2011-2012 (0-160 kg N ha-1) using a randomized block design with three or four replications and the two cultivars Kongyu131 and Longjing21. More detailed information about the experiment design can be found in Cao et al. (2013), Gnyp et al. (2013) and Yu et al. (2013). Spatio-temporal changes in the weather conditions affected rice plant growth and its growing season, which started approximately in mid-May and ended late September of each year. The rice growing period received more precipitation and insolation in 2007 and 2008 than in 2009, 2011, and 2012. The warmest growing season was in 2007 and the coldest in 2009, coincided with higher precipitation during the monsoon time in 2009.

8.2.2 Hyperspectral data collection

Spectral reflectance was measured using three non-imaging passive devices in 2007-2009 and 2011-2012: QualitySpec® (350-1800 nm) and FieldSpec3® (350-2500 nm) by ASD (Analytical Spectral Devices, Inc., Boulder, CO, USA) and HandySpec® (305-1705 nm) (tec5, Oberursel, Germany). The devices differ in their spectral ranges and sensor configurations and were used in different years (Table 8.1). They were carried with a 25° field of view and a senor canopy distance of 0.3 m (2007-2009) and 1 m (2011, 2012) in the paddy fields. Spectral measurements were taken from 9 a.m. to 2 p.m. local mean time (solar noon at 11 a.m.) under cloudless conditions. Calibration measurements were taken with a white

barium sulfate (BaSO4) reference panel for the ASD devices and with a grey reference panel shipped with the tec5 device. Twenty sample counts were collected and averaged for the optimization standard and ten for each scanning position at the rice canopy. For each plot, six scans were performed randomly and averaged to represent each individual experimental plot.

8.2.3 Destructive plant parameter samples

Destructive above ground biomass samples were collected after taking the spectral reflectance measurements. Three (heading stage) to five (tillering and stem elongation stage) hills with the representative number of tillers per plot were harvested in the field. The samples were rinsed with water and the roots were cut. They were oven-dried at 105 °C for 30 minutes and then dried at 70 °C to constant weight.

Table 8.1 Overview of the three spectrometers and their configurations.

	QualitySpec	**FieldSpec3***	**HandySpec Field**
Producer	ASD	ASD	tec5
Spectral domain	350-1800 nm	350-2500 nm *	305-1705 nm
Sensor VNIR	VNIR	VNIR	MMS1 NIR
Domain	350-1000 nm	350-1000 nm	305-950 nm
Spectral resolution	3 nm (at 700 nm)	3 nm (at 700 nm)	10 nm
Sampling interval	1.4 nm	1.4 nm	3.3 nm
Sensor SWIR	SWIR1	SWIR1	PGS NIR 1.7
Domain	1000-1800 nm	350-1800 nm	950-1705 nm
Spectral resolution	10 nm (at 1400 nm)	10 nm (at 1400 nm)	5 nm
Sampling interval	2 nm	2 nm	1.5 nm
Sensor offset	1000 nm	1000 nm, 1800 nm	950-1000 nm
Field campaign	2007, 2009, 2011,	2008, 2009	2011

* SWIR2 was not used in this study; used domain at 350-1705 nm

8.3 Methods

8.3.1 Spectral library

In at total five years (2007 to 2009, 2011, 2012) nearly 16,500 raw rice spectra were collected from two experimental sites and on farmers' fields. The data was incorporated into a multi-temporal spectral library. In addition, the metadata containing information about the year, growth stage, site, cultivar, fertilizer input, and measured plant biomass was linked to the spectral information. For this study we selected the data which was consistently available for all five years. From the around 1,900 available mean spectra from the experimental sites, totally 319 mean spectra were used. In particular, we used the data from one site were data was available for all five years and selected those with the four main

fertilizer rates, namely N1=0 kg N ha-1, N2=65-75 kg N ha-1, N3=95-105 kg N ha-1, and N4=120-150 kg N ha-1 (n=1,360). We then focused our analysis on the tillering (t), stem elongation (se) and heading (h) phenological growth stages for the cultivar Kongyu131 (n=319). To take the annual variability into account, data collected from the first three years (2007 to 2009) were utilized as the calibration dataset (n=238) and measurements from the last two years (2011 and 2012) were used as validation dataset (n=81). Detailed information of the sample sizes by growth stages and years for the calibration and validation datasets along with the corresponding biomass statistics are given in Table 8.2.

For all years and both the calibration and validation dataset the mean biomass increased with the growth stages, where in 2008 the highest gain was observed. Also, the standard deviation (std) increased with the growth stages whereas the coefficient of variation (cv) decreased. However, for the complete calibration dataset in the stem elongation a very high cv of 75% was observed.

Table 8.2 Descriptive statistics of the biomass with number of samples (#), mean, standard deviation (std) and coefficient of variation (cv) separated by year and stages tillering (t), stem elongation (se) and heading (h).

	Calibration data												Validation data		
Year	**2007**			**2008**			**2009**			**2007 - 2009**			**2011, 2012**		
Stage	t	se	h	t	se	h	t	se	h	t	se	h	t	se	h
#	28	23	31	16	16	16	36	36	36	80	75	83	24	24	33
mean (t/ha)	1.22	3.88	8.18	0.60	1.41	9.40	0.57	0.83	6.69	0.80	1.89	7.77	1.01	2.11	6.65
std (t/ha)	0.31	0.78	1.69	0.25	0.32	1.08	0.19	0.19	0.95	0.39	1.43	1.66	0.37	0.65	1.60
cv (%)	25.48	20.16	20.63	41.40	22.93	11.53	32.85	22.46	14.18	48.94	75.27	21.38	36.44	30.87	23.99

8.3.2 Vegetation indices

Different types of vegetation indices link two or more bands together through a mathematical formula. The types differ by the structure of the formula. In HyperCor we implemented three types of vegetation indices: The Difference Vegetation Index, the Ratio Vegetation Index, and the Normalized Difference Vegetation Index. These were introduced by Tucker (1979), Jordan (1969), and Rouse et al. (1974) four decades ago for satellite remote sensing. Lately, they also have been used with HNBs. In this publication, we use the abbreviations to refer to vegetation index types and thus use DI (Difference Index), RI (Ratio Index) and NDI (Normalized Difference Index) to emphasize their structural properties and prevent confusion with already published vegetation indices. Eq. 8.1 to Eq. 8.3 show the formulas used in HyperCor together with their domain and co-domain. Each vegetation index consists of the specific type (e.g. DI, RI, NDI) and two reflectance values from the bands i and j (Ri, Rj).

$$DI_{(i,j)}(R_i, R_j) = R_i - R_j;\ [0,1] \times [0,1] \mapsto [-1,1] \quad \text{(Eq. 8.1)}$$

$$RI_{i,j}(R_i, R_j) = \frac{R_i}{R_j}\ ;\ [0,1] \times [0,1] \mapsto [0, \propto] \quad \text{(Eq. 8.2)}$$

$$NDI_{(i,j)}(R_i, R_j) = \frac{R_i - R_j}{R_i + R_j}\ ;\ [0,1] \times [0,1] \mapsto [-1,1] \quad \text{(Eq. 8.3)}$$

8.3.3 HyperCor

To perform comprehensive hyperspectral data analysis, the Java program HyperCor was developed. It automates several pre-processing steps such as device detection and detector offset correction as well as the process of computing correlation matrices (CMs) from hyperspectral data and any given plant parameter. In addition, descriptive statistics for the input dataset are calculated and supplements of the output CMs are generated to support their analysis. Each functional feature can be controlled and adjusted through a GUI as shown in Figure 8.1. For the analysis the data has to be prepared in comma separated values (csv-files) containing header information for each spectrum, the target feature (e.g. the investigated plant parameters), and the hyperspectral data organized in columns, where the first column represents the spectral wavelength. One or more datasets can then be loaded from the file system via the GUI for (pre-) processing. In the following, the functional features of HyperCor are presented. However, due to the object-oriented implementation, the program further provides a framework to incorporate extra analysis methods. In addition, the HyperCor.Viewer was implemented to systematically review visualized correlation matrices (Figure 8.3).

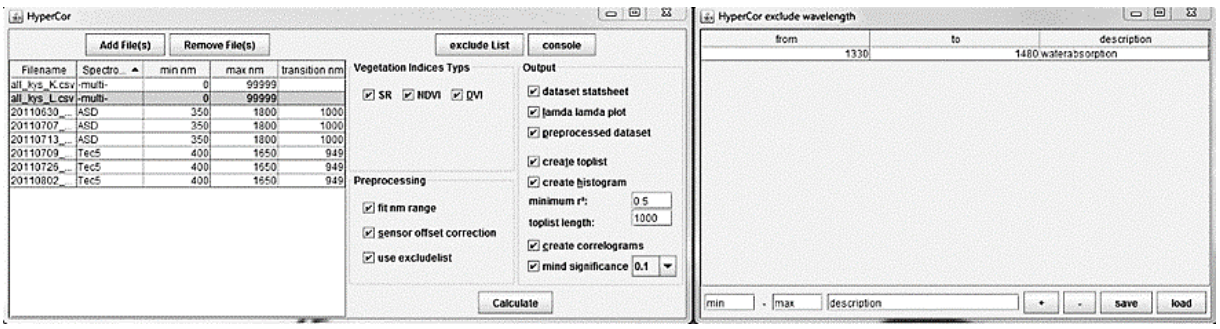

Figure 8.1 Graphical user interface of HyperCor (left) with band exclusion table (right).

8.3.3.1 Data pre-processing

HyperCor provides two pre-preprocessing steps for hyperspectral data. The first feature is to limit the wavelengths to the range of interest by identifying the device that was used to collect the spectra in a given dataset. This is done by matching the file name and the header information of each spectrum with an initialization file provided with the program. This file contains the name of several devices together with their minimum and maximum wavelengths as well as the particular wavelength, where the transition from one detector for a spectral range to another (e.g. VIS to SWIR1) takes place.

Information on other devices may be manually added to the initialization file. In case the device cannot be identified automatically, the user can manually assign a sensor to a loaded dataset through the GUI. After this has been done, the user may choose if the data analysis should be limited to the wavelength according to the device's specifications and to the combined range by all devices in the case of several sensors being used. In addition, the user can specify the wavelengths to be excluded (e.g. water absorption bands as in Figure 8.2) from the analysis through a menu in the GUI. This list can be saved and reloaded for later use.

The second pre-processing function is to eliminate the detector offset at the transition wavelengths from one detector to another. The offset occurs in measurements of hyperspectral data due to environmental interferences or insufficient sensor calibration (ASD Inc. 1999) and results in strong influences on the calculated HVIs (Figure 8.2). To correct the detector offset, for each input spectral reflectance curve, HyperCor computes the difference between the two reflectances next to the particular transition wavelength and then subtracts the difference from the reflectance values beyond the transition wavelength (linear correction). After pre-processing, the dataset may be exported as a csv-file.

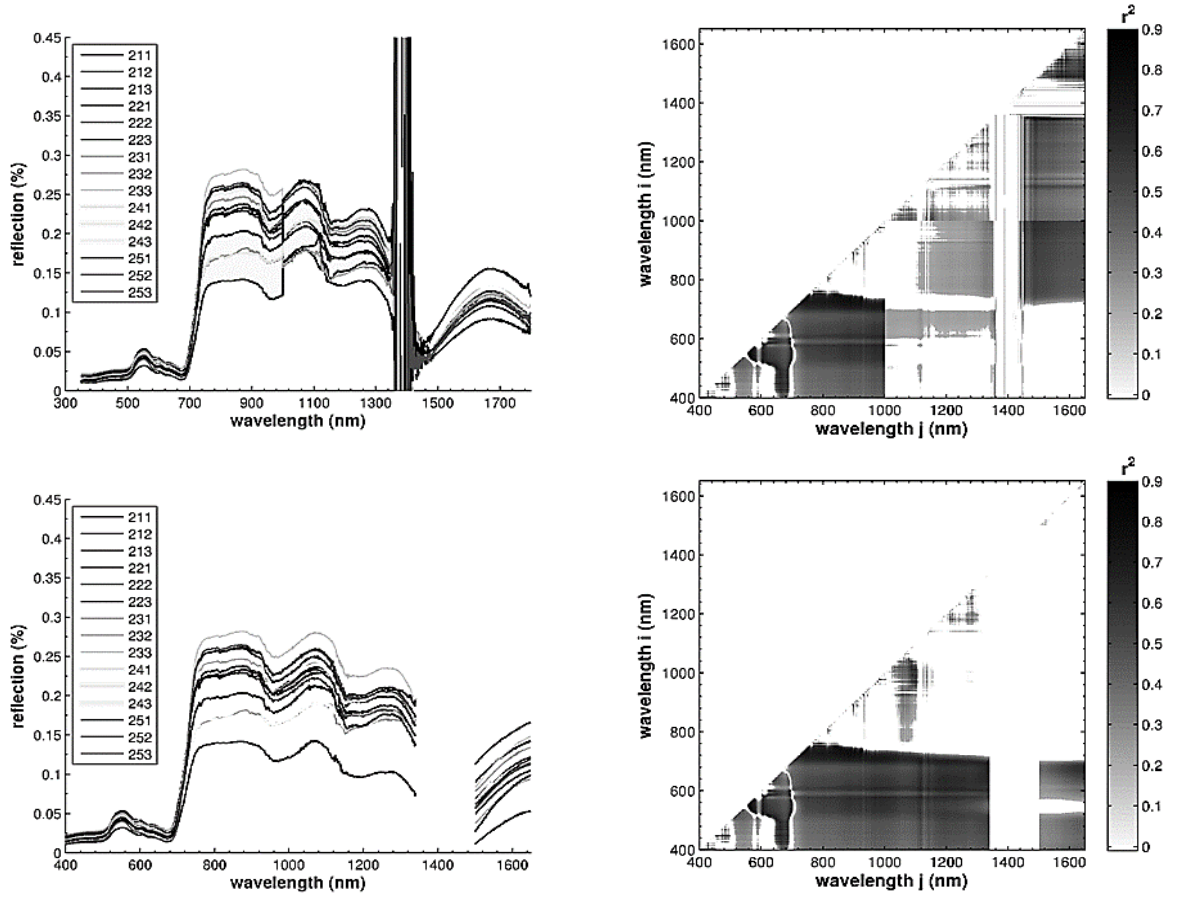

Figure 8.2 Spectral reflectance curves before (top) and after the pre-processing (bottom) with resulting correlogram for biomass.

8.3.3.2 Identifying substantial and redundant bands

Optionally, HyperCor provides two functions which may help analyze hyperspectral data and focus on relevant parts of the spectrum. First, descriptive statistics, including the mean, standard deviation, and coefficient of variation, of an (pre-processed) input dataset are calculated which help pointing out important parts of the spectrum (Bajwa and Kulkarni, 2011; Mahlein et al., 2013). The results are saved as a csv-file. Second, redundancy matrices (lambda – lambda plots) are calculated to identify redundant bands in the dataset. This methodology was introduced by Thenkabail et al. (2004a; 2004b) for hyperspectral data analysis and consists of calculating the correlations between all wavelength pairs of the dataset. The calculated value represents the degree of redundancy between the two wavelengths. With this method, bands over a certain threshold of redundancy can be excluded from further analysis. Thus, this method helps determine the most useful HNBs (Thenkabail et al. 2004a; 2004b; 2013).

8.3.3.3 Calculation of the correlation matrices and identification of potential hyperspectral vegetation indices

Correlation matrices (and correlograms as their visual representation) represent a standard procedure to derive optimal band combinations for HVIs (Thenkabail et al., 2011; 2013). Every cell(i,j) of a correlation matrix (CM) denotes the correlation of a given VI type based on two reflectance bands of the input hyperspectral reflectance data (Ri,Rj) and the target feature (e.g. plant parameter). Since each axis of a CM represents one wavelength, which is used to compute a HVI(i,j) for a given VI type, the entire matrix represents the correlations of all possible band combinations for a given VI type. The main functional feature of HyperCor is the automated calculation of the correlation matrices and supplementary summaries of these to support the analysis. The latter consists of best band combination lists and histograms of the used wavelength. So far, the vegetation index types RI, DI, and NDI are implemented for the computation in HyperCor. The implementation of the NDI and DI takes their symmetries into account, which reduces the processing time by 50%. To calculate the correlation between the HVI and a given plant parameter the Pearson correlation coefficient is used and squared to the coefficient of determination. Given the object-oriented implementation of HyperCor, other types of vegetation indices and correlation coefficients may easily be incorporated into the program. Via the GUI the user may choose which type of vegetation index to use for the calculation (Figure 8.1). Additionally, the user may define a minimum threshold and a level of significance (p-value) to be met by the correlations that will be considered for further analysis. After the calculation, the correlation matrices are saved as csv files. Meanwhile, a designated number of band combinations with the best

correlations may be exported into a separate file along with a histogram, which summarizes the bands used for the best correlations. This information may be used for further analysis.

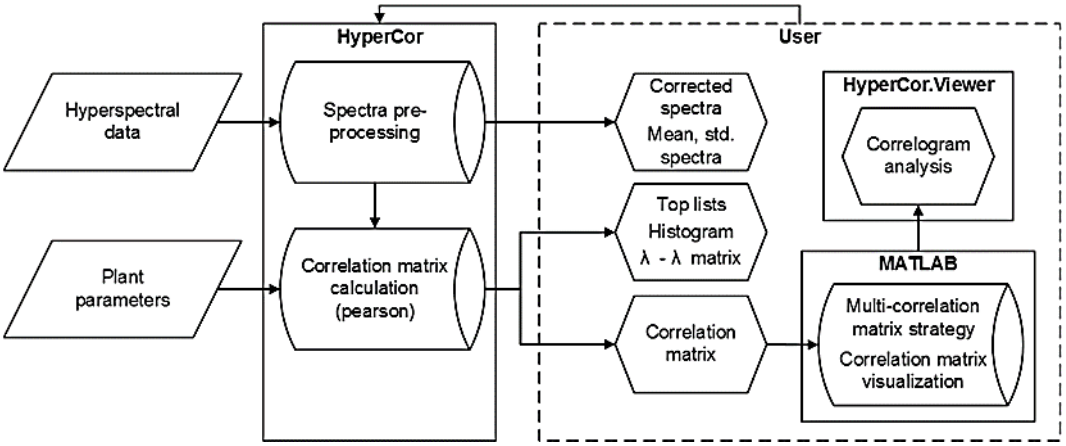

Figure 8.3 Data processing and analysis with HyperCor.

8.3.4 Multi-correlation matrix strategy

To identify potential bands to be used for a HVI, we developed the multi-correlation matrices strategy (MCMS). A band combination or domain, which may look insignificant in one single CM computed with one method (e.g. VI type) or from one dataset (categorized by growth stages, years, plant parameters, species, sites), may show its information content when combined with other CMs. Thus, the information content of several CMs is connected with the multi-correlation matrix strategy function (fMCMS). This function consists of calculating the average, difference, variance, and other mathematical functions and is carried out cell wise. Cells with desired features can be selected from the resulting matrix and the coordinates (respectively band combination) can be either used directly (e.g. as HVI) or for further processing (Figure 8.4).

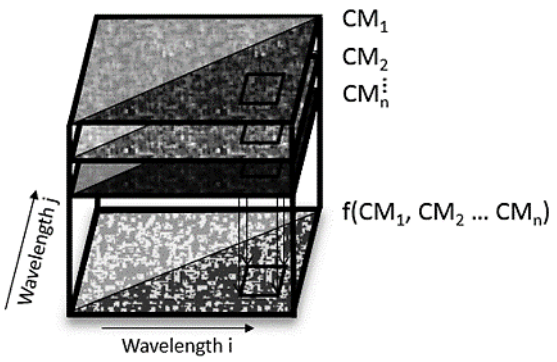

Figure 8.4 Scheme of the multi-correlation matrix strategy with input correlation matrix CM1, CM2 … CMn and the resulting matrix f(CM1,CM2 … CMn) after applying a function.

In the case of the rice study described above, the goal was to develop HVIs that serve as best predictors for rice biomass at different growth stages. The datasets from the spectral library from the years 2007

– 2009 were used as calibration data. The detector offset was corrected and the water absorption bands from 1330 – 1480 nm were excluded for each year and each growth stage. In addition, the spectral range was restricted to 350 – 1705 nm since this range was available for all datasets. Based on this data, HyperCor computed the CMs. Neither a minimum r^2 nor a significance level was taken into account and the NDI was specified as the VI type. In total, nine CMs (three years 2007 - 2009 by three growth stages) were computed for the MCMS approach. Since our goal was to obtain a HVI which performed consistently throughout the years, an average function was applied as fMCMS. The procedure was carried out in MATLAB (MathWorks R2011b). The CMs for each growth stage were imported and stacked to multi-dimensional arrays. These 1,355 (spectral range i) by 1,355 (spectral range j) by 3 (three years per growth stage) values were averaged using the mean function of MATLAB. The band combinations of the highest value in the mean correlation matrix were extracted and the mean correlograms were visualized to identify areas with high mean correlation values (Figure 8.5). The resulting band combinations for each of the three growth stages were used to develop a linear prediction model with the combined datasets from 2007 to 2009 for a given growth stage. This step was carried out in Microsoft Excel.

At the same time, we used HyperCor to apply a direct approach. Specifically, we computed CMs for combined datasets from 2007 to 2009 data for each of the three growth stages and identified the best band combinations. Again, the band combinations were used to develop a linear prediction model in Microsoft Excel. Thus, the direct approach used all the available measurements of one growth stage to derive the best band combination from the CM and to develop the model. The MCMS used the band combination with the highest mean r^2 from the data, separated by year from one grow stage, to develop the model together with all available data for the growth stage from the calibration dataset. For each growth stage, the linear models derived from the MCMS method and from the direct approach were then validated using the combined data from 2011 and 2012, separated by growth stage.

8.4 Results

The results from both approaches are summarized in Table 8.3. Comparing the best results of the MCMS approach to those of the direct approach, we found that the identified wavelengths differed for all stages with the biggest difference discovered in the tillering stage. However, all identified band combinations were located in the VIS or NIR region.

Table 8.3 Summary of the results of MCMS and direct approach with the correlation of calibration and validation.

Stage	VI	MCMS r^2	Calibration r^2	Validation r^2	Validation RMSE (t/ha)
Tillering	MCMS(757,746)	0.4	0.51	0.85	0.22
	NDI(436,488)		0.65	0.23	0.46
Stem elongation	MCMS(411,420)	0.25	0.2	0.67	1.51
	NDI(360,380)		0.88	0.16	0.88
Heading	MCMS(786,769)	0.31	0.47	0.60	1.21
	NDI(800,770)		0.5	0.37	1.40

The results in the averaged correlation matrices illustrate that for none of the growth stages the mean r^2 of the years 2007 to 2009 was greater than 0.4 (Figure 8.5). For the calibration dataset the MCMS approach achieved poor (r^2 = 0.2) to moderate (r^2 = 0.51) results. In all cases, better correlations occurred with the direct approach.

The biggest difference was achieved in the stem elongation (r^2 = 0.88) while it was smaller for the other two growth stages. The smallest difference was found in the heading. Figure 8.5 shows the models derived from the calibration dataset.

In the validation dataset the MCMS approach achieved good (stem elongation, heading r^2 = 0.67, 0.60) to very good results (tillering r^2 = 0.85). The direct approach showed poor performance for the validation dataset. The highest coefficient of determination was attained in heading (r^2 = 0.37). In all growth stages, higher correlations were reached by the MCMS approach than by the direct approach, with the biggest relative difference in the stem elongation (Table 8.3). However, in the latter both models were inversely related to the observed biomass (Figure 8.6), which will be discussed later. In the tillering and heading the MCMS showed a lower RMSE than the direct approach, for the stem elongation the opposite was the case.

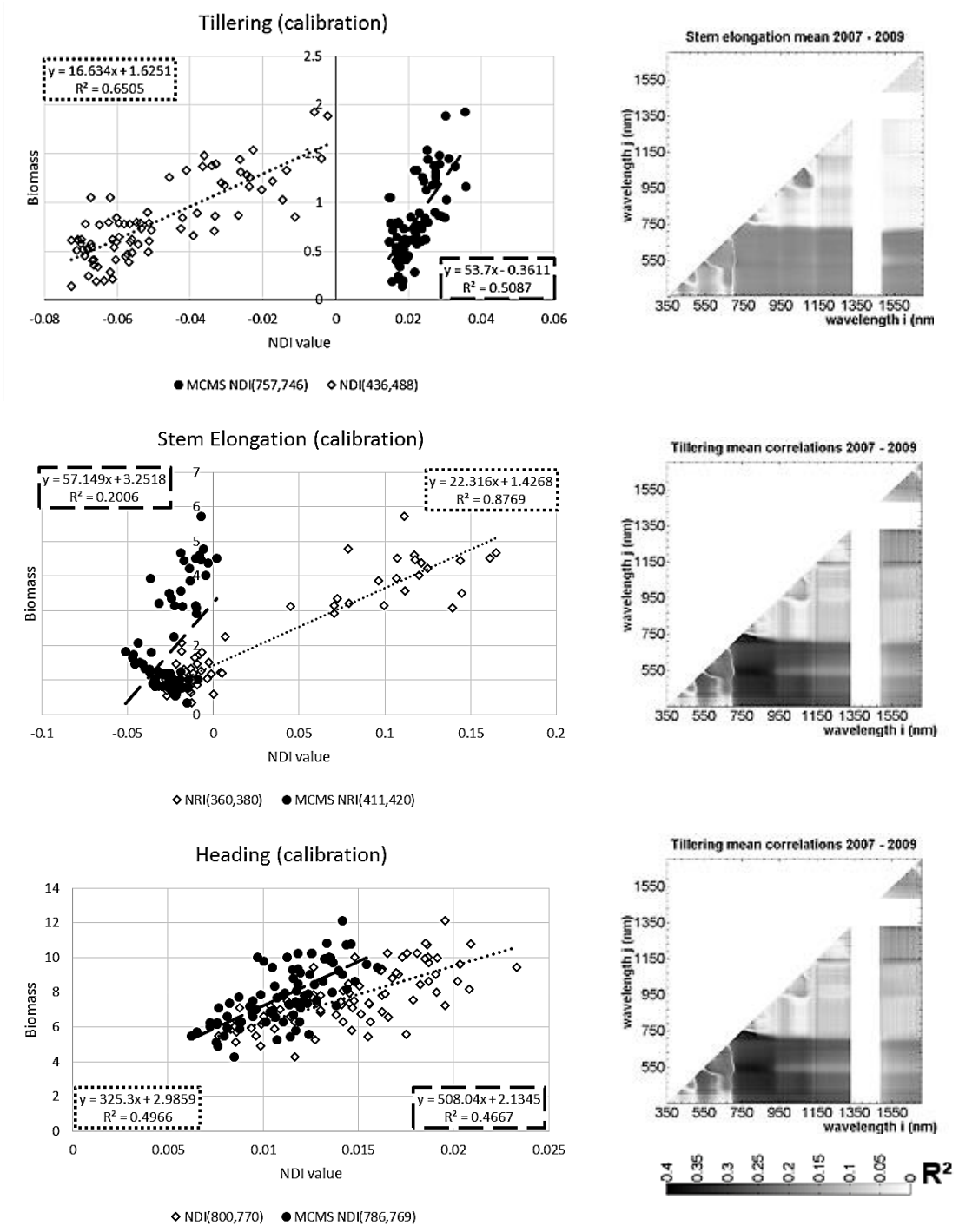

Figure 8.5 Plot of biomass against the NDI for the MCMS (dashed) and standard approach (dotted) and the derived prediction model for tillering, stem elongation and heading (left). The corresponding correlograms of the mean coefficient of determination (R²) for the years 2007 to 2009 for tillering, stem elongation and heading (right).

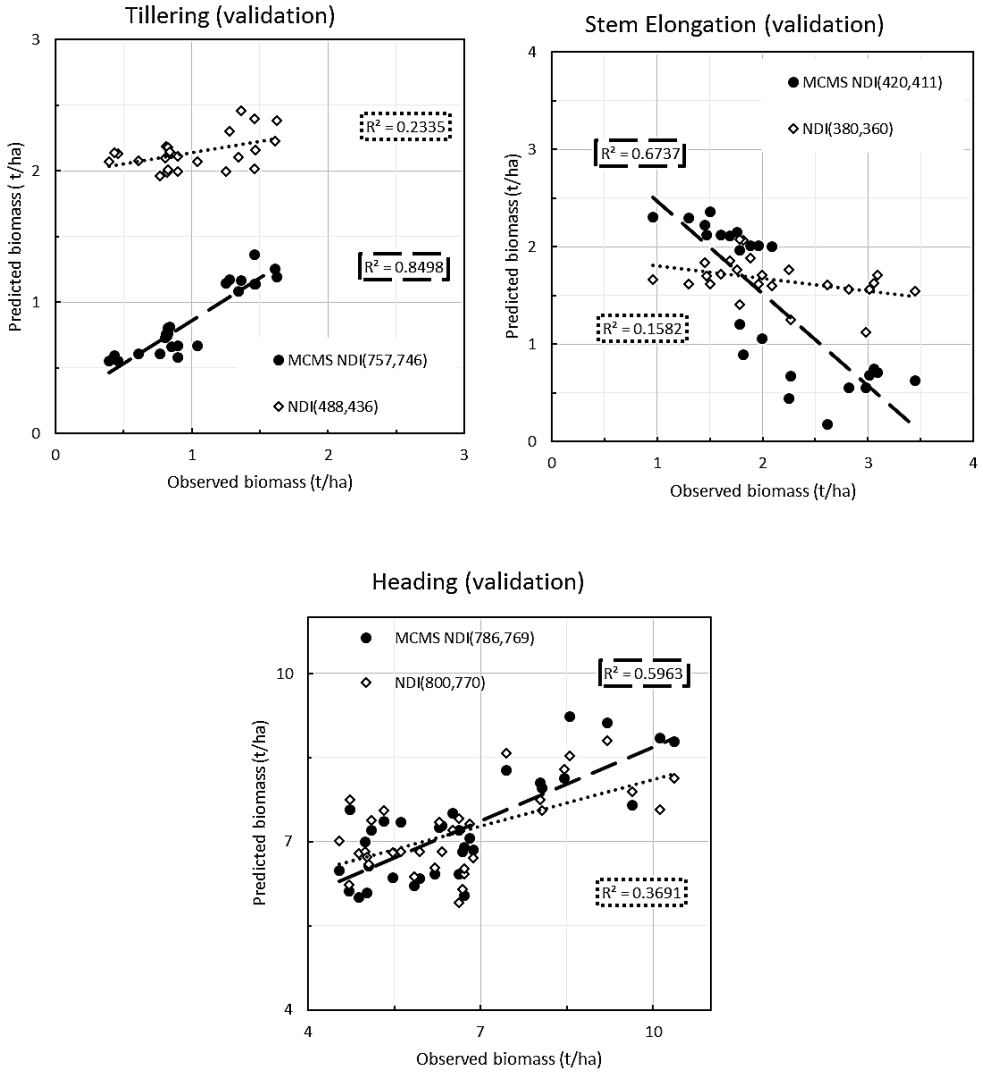

Figure 8.6 Plot of the predicted and observed biomass from the MCMS (dashed) and direct approach (dotted) for the validation dataset for tillering, stem elongation and heading.

8.5 Discussion

8.5.1 HyperCor

Correlation matrices are commonly used for the development of hyperspectral vegetation indices for different plants and plant parameters (Mutanga and Skidmore, 2004; Stroppiana et al., 2009; Koppe et al., 2010; Thenkabail et al., 2011;Yu et al., 2013). Additionally, redundant matrix have been proven useful to identify redundant bands (Thenkabail et al., 2004a; 2004b). Together, they help overcome the Hughes phenomenon through narrowing down the number of bands which has to be used for the analysis and plays a major role in identifying the most important bands for current and future hyperspectral sensors (Mariotto et al., 2013; Thenkabail et al., 2013). Supplements such as histograms support this process (e.g. Mutanga and Skidmore, 2004; Mariotto et al., 2013). So far, different commercial software packages such as Statistical Analysis System SAS (e.g. Thenkabail et al., 2000) or

MATLAB (e.g. Yu et al., 2013) have been used to compute CMs. These packages require licensing fees. Most of all, they are not designed for the derivation of HVIs and thus extra efforts are needed to implement an automated processing chain with a high level of customization of the outputs.

In contrast, HyperCor is implemented with Java and thus is free. Besides, it provides the entire processing chain for computing CMs out of hyperspectral data. With the GUI, researchers without a programming background can use it conveniently to solve research questions using correlation matrices. In addition, it provides a framework to implement further features. One of those might be the implementation of another detector offset correction. As shown in Figure 8.2, the offset significantly influences the results and thus is essential for a reliable analysis of the entire spectrum. Although linear correction has been recommended by a manufacturer of spectrometers (Kirchler, personal correspondence, 2012), it might not be the best option from a physical-technical perspective due to the effects of dark current increasing and detector sensitivity decreasing towards the edges of the specified spectral range of the detectors (ASD Inc., 1999). Further research is needed to address this uncertainty. With the introduced features, HyperCor provides a well suited tool to compute CMs, which gives the opportunity to apply standard procedures to and develop new ways of deriving optimized HNBs and HVIs such as the MCMS from hyperspectral data.

8.5.2 Multi-correlation matrix strategy

So far, CMs have been mostly used as direct sources for the retrieval of best band combinations for a given parameter (e.g. Thenkabail et al., 2000; Hansen and Schjoerring, 2004; Stroppiana et al., 2009; Gnyp et al., 2013; Mariotto et al., 2013). In this paper, we propose a strategy to use more information contained in each correlation matrix by linking multiple CMs (e.g. computed from different VI types and datasets). The results of more than one CM have been used before to establish vegetation indices (Stroppiana et al., 2009; Zhu et al., 2011). However, the MCMS applies a mathematical function (fMCMS) on every cell of the CMs and thus use the complete information contained in the CMs. For biomass prediction, we chose to develop different prediction models for each growth stage since background signals from soil and water may influence the rice reflectance at the early growth stages (Van Niel and McVicar, 2004).

Plant growth is greatly influenced by climate conditions and thus may differ annually. In the present dataset, the growth of biomass differed from one year to another. Especially at the stem elongation stage, the biomass differed by more than quadruple from 2007 to 2009. Also the growth patterns differed. The lowest biomass was observed in 2009 in all stages. Compared with 2008, the biomass of 2007 was more than doubled in the stem elongation, but a lower biomass amount was found in the heading stage. In all years, the coefficient of variation decreased from the tillering to heading (Table

8.2). These differences may have affected the spectra measured from the plants (Hatfield and Prueger, 2010; Gnyp et al., 2014). This assumption is supported by the low maximum mean correlations of CMs of the growth (r^2 = 0.4, 0.25, 0.31, respectively). Thus, results from one year may not be transferred to another year, which has also been reported from other researchers (e.g. Li et al., 2010).

The different results for the calibration datasets of the direct and the MCMS approach may be explained by a combination of the described heterogeneity in growth and biomass, and the asymmetric sample size of the calibration dataset. Since the direct approach used all the available measurements for one growth stage from the calibration dataset, each sample was weighted the same for the computation of the CM and respectively, for the identification of the best band combination. Thus, the developed prediction model is fitted specifically for the calibration dataset. With the MCMS, first the CMs are computed separately by year and growth stage, and then averaged across the years. Thus, in contrast to the direct approach, the resulting CMs (respectively the years) are weighted the same and the resulting best band combinations are not biased by (and thereby not fitted to) the different sample sizes. Hence, the direct method outperformed the MCMS models for the calibration dataset.

However, in the independent validation datasets for the growth stages in 2011 and 2012 the models derived from the MCMS perform better with higher r^2 and manly lower RMSE. This might indicate that the MCMS is more robust against asymmetric datasets and annual changes due to the reasons described above. In particular, the MCMS improved the r^2 by 62% and reduced the RMSE by more than 50% in the tillering. In the heading stage, it improved the r^2 by 23% and reduced the RMSE by over 10%. In the stem elongation, the r^2 was also improved. However, for both the direct approach and the MCMS, observed and predicted biomass were correlated inversely (Figure 8.6). This might be due to the very high coefficient of variation (75%) of the calibration dataset for this growth stage and the different annual growth patterns mentioned above which both methods did not seem to model well. These results underline the need of independent calibration and validation datasets as well as the careful assessment of good correlations. Comparing the results of our study to others, the identified red edge bands and NIR bands at the tillering stage conform to Hansen and Schjoerring (2003)'s findings. For the stem elongation stage, several researchers reported the need of the SWIR domain for rice biomass estimation. Especially, bands around 1200, 1480, and 1650 nm were suggested (Shibayama and Akiyama, 1989; Huang et al., 2004). In our case, both bands were situated in the blue domain. This may result from the limitation to only one study site. This assumption is supported by the results of Gnyp et al. (2013), in which the present calibration dataset was pooled with another site's dataset and optimal SWIR bands were identified. With this extended dataset, best bands from the NIR domain were also selected by Gnyp et al. (2013) for the heading, which aligns with our findings for this stage.

8.6 Conclusion and outlook

In this study, we presented HyperCor as a tool for automated pre-processing of hyperspectral data and computation of correlation matrices. In addition, we proposed the multi-correlation matrix strategy to use the full information contained in multiple correlation matrices and applied it to a multi-temporal dataset for rice biomass prediction. The results confirm the challenges of transferring findings between years. However, with the multi-correlation matrix approach the results in an independent validation datasets could be improved for the tillering and heading stage. Further research has to address the robustness of the new method by using different datasets collected at diverse sites and years, other plant parameters, and different multi-correlation matrix strategy functions. Besides, HyperCor could be incorporated into a website in the future and thus serves as a standardized and open resource for researchers to develop new and evaluate existing optimized hyperspectral narrow bands and hyperspectral vegetation indices.

8.7 References

ASD Inc., 1999. ASD Technical Guide. Third edition. Boulder, CO USA.

Bajwa, S.G. and S.S. Kulkarni, 2011. Hyperspectral data mining, Hyperspectral Remote Sensing of Vegetation (Thenkabail, P. S., Lyon, J. G., Huete, A., editors), CRC Press- Taylor und Francis group, Boca Raton, London, New York, pp. 94–120.

Cao, Q., Y. Miao, S. Huang, S. Cheng, R. Khosla, R. Jiang, 2013. Non-destructive estimation of rice plant nitrogen status with Crop Circle multispectral active canopy sensor. Field Crops Research. http://dx.doi.org/10.1016/j.fcr.2013.08.005.

Chauhan, H.J., B.K. Mohan, 2013. Development of agricultural crops spectral library and classification of crops using Hyperion hyperspectral data. Journal of Remote Sensing Technology, 1(1), 9-12.

Galvao, L. S., J. C. N. Epiphanio, F. M. Breunig and A. R. Formaggio, 2011. Crop type discrimination using hyperspectral data, Hyperspectral Remote Sensing of Vegetation (Thenkabail, P. S., Lyon, J. G., Huete, A., editors), CRC Press- Taylor und Francis group, Boca Raton, London, New York, pp. 397–442.

Gitelson, A.A., M. N. Merzlyak, 1996. Signature analysis of leaf reflectance spectra algorithm development for remote sensing of chlorophyll, Journal of Plant Physiology, 148(3-4), 494-500.

Gitelson, A. A., 2012. Remote sensing estimation of crop biophysical characteristics at various scales, Hyperspectral Remote Sensing of Vegetation (Thenkabail, P. S., Lyon, J. G., Huete, A., editors), CRC Press- Taylor und Francis group, Boca Raton, London, New York, pp. 329–393.

Gnyp, M.L., K. Yu, H. Aasen, Y. Yao, S. Huang, Y. Miao and G. Bareth, 2013. Analysis of Crop Reflectance for Estimating Biomass in Rice Canopies at different Phenological Stages, Photogrammetrie Fernerkundung Geoinformation, 2013(4): 351-365.

Gnyp, M.L., Y. Miao, F. Yuan, S.L. Ustin, K. Yu, Y. Yao, S. Huang and G. Bareth, 2014. Hyperspectral canopy sensing of paddy rice aboveground biomass at different growth stages, Field Crops Research (accepted).

Haboudane, D., Miller, J.R., Pattey, E., Zarco-Tejada, P.J., Strachan, I.B., 2004. Hyperspectral vegetation indices and novel algorithms for predicting green LAI of crop canopy: Modeling and validation in the context of precision agriculture, Remote Sensing of Environment, 90(3): 337-352.

Hansen, P.M. and J.K, Schjoerring, 2003. Reflectance measurements of canopy biomass and nitrogen status in wheat crops using normalized difference vegetation indices and partial least squares regression, Remote Sensing of Environment, 86(4): 542-553.

Hatfield, J. L. and J. H. Prueger, 2010. Value of using different vegetative indices to quantify agricultural crop characteristics at different growth stages under varying management practices, Remote Sensing 2(2): 562-578.

Huang J., F. Wang, X. Wang, Y. Tang and R. Wang, 2004. Relationship between Narrow Band Normalized Deference Vegetation Index and Rice Agronomic Variables, Communications in Soil Science and Plant Analysis, 35(19-20): 2689-2708.

Huete, A., C. Justice and H. Liu, 1994. Development of Vegetation and Soil Indices for MODIS-EOS, Remote Sensing of Environment, 49(3): 224-234.

Jensen, R.R., 2007. Remote Sensing of the environment. Pearson Prentice Hall, Upper Saddle River, USA, 592 p.

Jordan, C.F., 1969. Derivation of leaf area index from quality of light on the forest floor. Ecology, 50(4):663-666.

Koppe, W., Li, F., Gnyp, M.L., Miao, Y., Jia, L., Chen, X., Zhang, F., Bareth, G., 2010. Evaluating Multispectral and Hyperspectral Satellite Remote Sensing Data for Estimating Winter Wheat Growth Parameters at Regional Scale in the North China Plain. Photogrammetrie Fernerkundung Geoinformation, 2010(3): 171-182.

Laudien, R., K. Burcky, R. Doluschitz, G. Bareth, 2006. Establishment of a Web-based spectral database for the analysis of hyperspectral data from Rhizoctonia solani-inoculated sugarbeets, Zuckerindustrie, 131(3): 164-170.

Li., F., Miao, Y., Hennig, S.D., Gnyp, M.L., Chen, X., Jia, L., Bareth, G., 2010. Evaluating hyperspectral vegetation indices for estimating nitrogen concentration of winter wheat at different growth stages, Precision Agriculture, 11(4): 335-357.

Mahlein, A.-K., T. Rumpf, P. Welke, H.-W. Dehne, L. Plümer, U. Steiner, E.-C. Oerke 2013. Development of spectral indices for detecting and identifying plant diseases, Remote Sensing of Environment 128(1): 21-30.

Mariotto, I., P.S. Thenkabail, A. Huete, E.T. Slonecker and A. Platonov, 2013. Hyperspectral versus multispectral crop-productivity modeling and type discrimination for the HyspIRI mission, Remote Sensing of Environment 139(in progress): 291-305.

Miao, Y., D.J. Mulla, G.W. Randall, J.A. Vetsch, R. Vinlita, 2009. Combining chlorophyll meter reading and high spatial resolution remote sensing images for in-season site-specific nitrogen management of corn. Precision Agriculture 10: 45-62.

Milton E.J., M.E. Schaepman, K. Anderson, M. Kneubühler and N. Fox, 2009. Progress in field-spectroscopy, Remote Sensing of Environment, 113(S1): 92-109.

Moran, M. S., Y. Inoue and E.M. Barnes, 1997. Opportunities and limitations for image-based remote sensing in precision crop management, Remote Sensing of Environment, 61(3): 319-346.

Mutanga, O. and A.K. Skidmore, 2004. Narrow band vegetation indices overcome the saturation problem in biomass estimation, International Journal of Remote Sensing, 25(19): 3999-4014.

Oppelt, N., W. Mauer, 2004. Hyperspectral monitoring of physical parameters of wheat during a vegetation period using AVIRIS data. International Journal of Remote Sensing, 25(1), 145-159.

Rao, N.R., P.K., Garg, S.K. Ghosh, 2007. Development of an agricultural crops spectral library and classication of crops at cultivar level using hyperspectral data. Precision Agriculture, 8: 173-185.

Roberts, D.A., 2011. Hyperspectral vegetation indices, Hyperspectral Remote Sensing of Vegetation (P.S. Thenkabail, Lyon, J.G., and Huete, A., editors), CRS Press/Taylor, Boca Raton, London, New York, pp.309-328.

Rouse, J.W., Has, R.H., Schell, J.A., Deering, D.W., 1974. Monitoring vegetation systems in the Great Plains with ERTS. Third ERTS Symposium, NASA Sp-351, Vol. 1, NASA: pp.309-317.

Running, S.W., C.O. Justice, V. Salomonson, D. Hall, J. Barker, Y.J. Kaufmann, A.H. Strahler, A.R. Huete, J.-P. Muller, V. Vanderbilt, Z.M. Wan, P. Teillet and D. Carneggie, 1994. Terrestrial remote sensing science and algorithms planned for EOS/MODIS, International Journal of Remote Sensing, 15(17): 3587-3620.

Shibayma, M. and K. Akiyama, 1989. Seasonal visible, near-infrared and mid-infrared spectra of rice canopies in relation to LAI and aboveground dry phytomass, Remote Sensing of Environment, 27(2): 119-127.

Stroppiana, D., M. Boschetti, P.A. Brivio and S. Bocchi, 2009. Plant nitrogen concentration in paddy rice from field canopy hyperspectral radiometry, Field Crops Research 111(1-2): 119-129.

Thenkabail, P.S., R.B. Smith and E. De Pauw, 2000. Hyperspectral Vegetation Indices and Their Relationship with Agricultural Crop Characteristics, Remote Sensing of Environment, 71(2): 152-182.

Thenkabail, P.S., E.A. Enclona, M.S. Ashton, C. Legg and M.J. De Dieu, 2004a. Hyperion, IKONOS, ALI, and ETM+ sensors in the study of African rainforests, Remote Sensing of Environment, 90(1): 23–43.

Thenkabail, P.S., E.A. Encloda, M.S. Ashton and B. Van Der Meer, 2004b. Accuracy assessments of hyperspectral waveband performance for vegetation analysis application, Remote Sensing of Environment, 91(3-4): 354-376.

Thenkabail, P.S., G. J. Lyon and A. Huete, 2011. Advances in hyperspectral remote sensing of vegetation and agricultural crops, Hyperspectral Remote Sensing of Vegetation (P.S. Thenkabail, Lyon, J.G., and Huete, A., editors), CRS Press/Taylor, Boca Raton, London, New York, pp.3-29.

Thenkabail, P.S., J.W. Knox, M. Ozdogan, M.K. Gumma, R.G. Congalton, Z. Wu, C. Milesi, A. Finkral, M. Markshall, I. Mariotto, S. You, C. Giri and P. Nagler, 2012. Assesing future risks to agricultural productivity, water resources and food security: How can remote sensing help? Photogrammetric Engineering and Remote Sensing 78(SI 8): 773-782.

Thenkabail, P.S., I. Mariotto, M.K. Gumma, E.M. Middleton, D.R. Landis and K.F. Huemmrich, 2013. Selection of Hyperspectral Narrowbands (HNBS) and Composition of Hyperspectral Twoband Vegetation Indices (HVIs) for Biophysical Characterization and Discrimination of Crop Types Using Field Reflectance and Hyperion/EO-1 data, IEEE Journal of Selected Topics in Applied Earth Observation and Remote Sensing, 6(2): 427-439.

Tucker, C., 1979. Red and photographic infrared linear combinations for monitoring vegetation. Remote Sensing of Environment, 8(2), 127-150.

Van Niel, T. G. and T.R. McVicar, 2004. Current and potential uses of optical remote sensing in rice-based irrigation systems: a review, Australian Journal of Agricultural Research 55 (2), 155-185.

Yu, K., F. Li, M.L. Gnyp, Y. Miao, G. Bareth and X. Chen, 2013. Remotely detecting canopy nitrogen concentration and uptake of paddy rice in the Northeast China Plain, ISPRS Journal, 78: 102-115.

Zhu, Y., W. Wang and X. Yao, 2011: Estimating leaf nitrogen concentration (LNC) of Cereal crops with Hyperspectral Data, Hyperspectral Remote Sensing of Vegetation (P.S. Thenkabail, Lyon, J.G., and Huete, A., editors), CRS Press/Taylor, Boca Raton, London, New York, pp.187-206

9. OVERALL DISCUSSION

Chapter 1 set the stage for the three research objectives to evaluate whether HS DSMs of crops are suitable to support a site-specific crop management. These research objectives are to investigate the influences on the spectral information along the path from particle to pixel, the comparability of HS DSMs to data from other sensing systems and the potentials of HS DSMs acquired with UAV snapshot cameras. In the following sections, these research objectives are discussed in consideration of the insights gained in the research studies in Chapter 3 to 8. At the end of the discussion, an overall conclusion is drawn.

9.1 Influences on the spectral information along the path from particle to pixel

Along the path from particle to pixel, the information may be influenced and modified by interactions with the environment, by the sensing system and measurement protocol, and by the data processing (Figure 1.3). In the following subsections, sources of influences will be identified and their possible impact discussed.

9.1.1 Interactions with the environment

The environmental illumination conditions and their interaction with the canopy anisotropy affect the apparent reflectance. The results in Burkart et al. (2015, Chapter 5) demonstrated that differences in the measurement geometry had a strong wavelength-dependent influence on the apparent spectrum. Moreover, these differences could only be compensated by some VIs and only to a certain degree. However, it must be noted that the tilt angles (66°, 43°, 20°) investigated in Burkart et al. (2015, Chapter 5) correspond to very large zenith angles (25°, 47°, 70°). Common airborne imaging spectroscopy line-scanning systems have a FOV of about 30° (HyPlant: 32.2°, Rascher et al., 2015; APEX: 28.1°, Schaepman et al., 2015). Therefore the resulting zenith angle of the outermost pixel is about 15°. More relevant are the results for UAV sensing systems. Due to their lower flying altitude, these systems usually have a wider FOV to increase the area covered during an overpass (Aasen and Bolten, in review, Chapter 4). Common UAV hyperspectral linescanners have FOVs of about 50° (Lucieer et al., 2014; Zarco-Tejada et al., 2012). Similarly, RGB cameras such as the Panasonic Lumix GX1 used in Bendig et al. (2014, Chapter 7) have FOVs of 55.8° x 38.9°. Thus, the angular effects retrieved with a tilt angle of 66° (corresponds to a 24° zenith angle) can be regarded as approximations for these sensors. At this angle, the apparent reflection towards the solar position might almost be doubled in comparison to nadir (1.93 ANIF at 481 nm), while it might be reduced by approximately one third (ANIF 0.63 at 681 nm) on the sun-averted side, depending on the wavelength (Figure 5.7). Consequently, the VIs are also significantly influenced at this angle (Table 5.5 and Figure 5.8). As previously discussed in Aasen and Bolten (in review, Chapter 4) and Burkart et al. (2015, Chapter 5), these results align well

with other studies. Nevertheless, these measurements can only be seen as a rough approximation of directional effects, since the UAV goniometer measurements represent conical measurements (HCRF) relative to nadir (ANIF) in contrast to HDRFs measured by imaging instruments (c.f. Subsection 2.1.2).

Relevant in the context of HSCs is the question of how the results from Burkart et al. (2015, Chapter 5) can be interpreted with regards to the data of the UHD. The camera has a FOV of only 20°, which potentially reduces BRDF effects. Nevertheless, Aasen and Bolten (in review, Chapter 4) identified angular effects within HS DSMs generated from the HSC data. While this will be subject of discussion in the context of the influence of the data processing (Subsection 9.1.3), the influence of the different angular properties of the pixels within an image were not addressed in Aasen and Bolten (in review, Chapter 4). To get an impression of the effects within one image, Figure 9.1 shows the area of one plot (plot 35 at DAS 70 in 2014), extracted from several images and visualized corresponding to its position within the image (pixel position). The procedure is based on a novel way to generate a multi-angular pixel database from HSC data (Aasen, 2016). Each image corresponds to a different image-capturing positions (IC1 – IC6). From the corresponding image cubes the 670 and 798 nm band is shown in Figure 9.1 (A and B). As introduced in Aasen et al. (2015, Chapter 3), the pixel position denotes its position within the image. The flight was carried out such that the along-track pixel position was almost parallel to the solar principal plane. Therefore this axis corresponds to changes in the zenith angle, and pixels at lower pixel positions have a more acute angle to the sun (closer to the hotspot at a zenith angle of 30°). Besides of some within-plot heterogeneity, an overall trend can be seen in both wavelengths: with increasing along-track pixel position, the reflectance decreases in both wavelengths (Figure 9.1, A and B). Burkart et al. (2015, Chapter 5) found that the relative change in the RED and NIR is different. This can also be seen in the HSC data when the average reflectance per plot is normalized by the average of all ICs. Figure 9.1 (D) shows the averaged reflectance per plot for 670 nm (RED) and 798 nm (NIR) relative to the mean value of all images. For IC2 to 4, the reflectance in both wavelengths has the same relative change. In the other ICs, the apparent reflectance at 670 nm deviates more from the mean value than at 798 nm, which indicates the higher angular sensitivity at 670 nm. The maximum relative deviation from the mean value is about 25% at 670 nm and about 15% at 798 nm (Figure 9.1, D). Commonly, VIs as the NDVI are among other things used to normalize for angular effects resulting from the measurement geometry (Huete et al., 1994; Jensen, 2007). In Figure 9.1 (D) the NDVI for the six capturing positions is shown. Besides of IC2 to 4 the VI is not able to normalize for the different viewing geometries. These findings align with other studies, which found that VIs are sensitive to view-angle differences, while the sensitivity is VI (Verrelst et al., 2008) and surface cover dependent (Weyermann et al., 2014). Thus, future studies should investigate how other VIs are affected by different viewing geometries in HSC images.

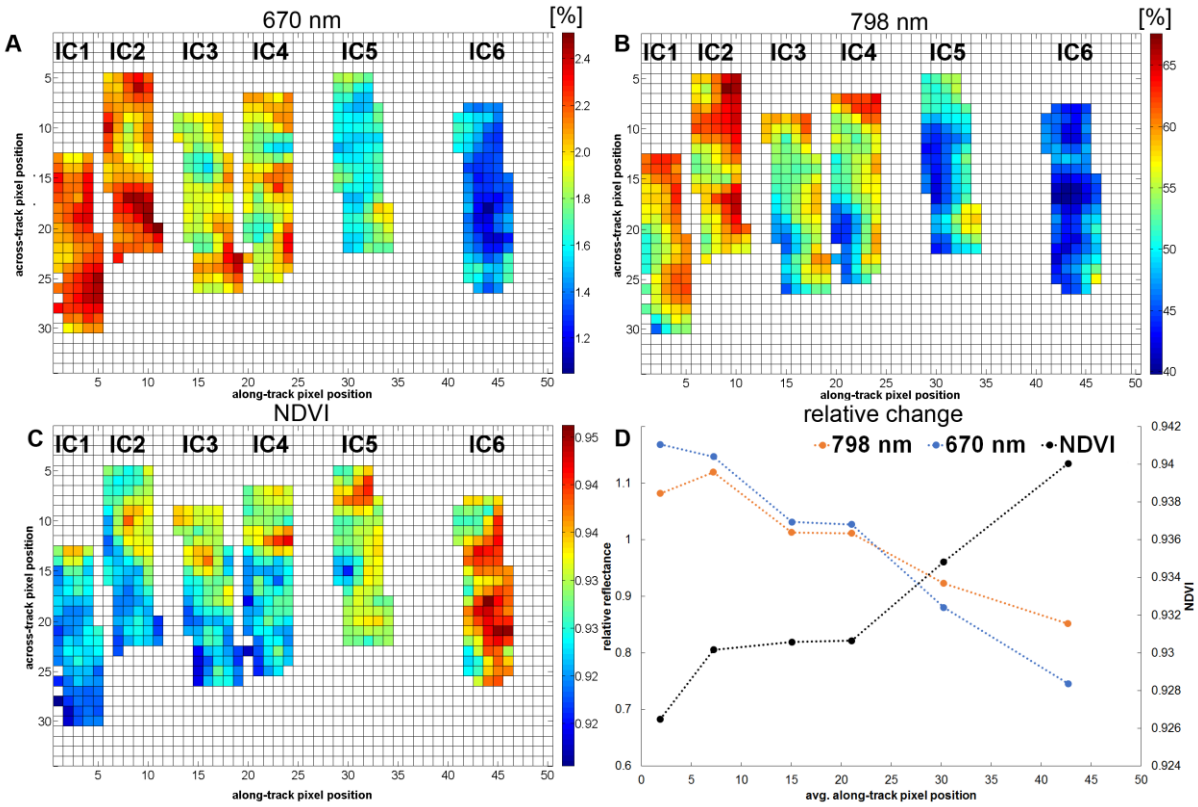

Figure 9.1 The same plot extracted from different positions within six images (IC1 - IC6) seen at 670 nm (A), 798 nm (B) and as NDVI (C). The across-track pixel position is cropped at pixel 35. Additionally, the average relative change in reflectance at the two wavelengths and the NDVI along the average along-track position of the images is shown (D). The along-track pixel positions are almost parallel to the solar principal plane and pixels at lower pixel positions have a more acute angle to the sun. Since the sun's elevation is about 60°, the hotspot is at a zenith angle of about 30°. The along-track pixel position corresponds to the zenith angle of 10° towards the sun (pixel position 0) and 10° towards the sun averted side (pixel position 50).

Two important conclusions can be drawn from these results: first, although Burkart et al. (2015, Chapter 5) used a non-imaging spectrometer, the results are also relevant for HSCs since they basically align with those shown in this chapter. Second, the position within the image of an HSC influences the retrieved reflectance values, and VIs such as the NDVI cannot generally compensate for this influence. Thus, it can be concluded that the measurement geometry influences the data and that the variety of different viewing geometries of the pixels within an image might be sufficient to have an impact on the parameter retrieval, despite the small FOV of the UHD. Furthermore the results from Figure 9.1 were derived on a plot scale. For individual pixels, these differences are likely to be more pronounced. These results align with Rasmussen et al. (2016), who found that the impact of angular variations on VIs derived by RGB and CIR imagery were even greater than the experimental treatments.

It should be noted, however, that while these effects are related to the viewing geometry of the sensing system, they result from the vegetation structure and the illumination conditions and thus, may vary with the growth stage (Rasmussen et al., 2016), management (e.g. row distance; c.f. Zhao et al. (2015))

and the sun's path. Thus the influence of these angular effects should not be interpreted as errors of the sensing system. Rather, they are meant to estimate the magnitude by which the data might be misinterpreted when the measurement geometry is neglected. Besides, it should be noted that angular effects are not specific for HSC and is common for all optical remote sensing systems (e.g. Nagol et al., 2015; Rasmussen et al., 2016; Schläpfer et al., 2015; Weyermann et al., 2014). In the future, the novel pixel-tracing method developed in Aasen et al. (2015, Chapter 3) could commonly be used to trace angular properties for every pixel and thus help to address BRDF effects appropriately. Moreover, multi-angular measurements with HSCs could be used to derive information about the surface anisotropy and thus provide an additional source of information.

Also other environmental conditions introduce uncertainty into HSC measurements. Although not regarded within this thesis and hardly appreciated in the literature in conjunction with spectral measurements, wind might interrupt the structure of a canopy. Lord et al. (1985) demonstrated that gusts of wind can cause differences of up to 60% in the BRF of barley in red wavelengths. Even if the wind was only strong enough to cause the leaves to flutter, variations of up to 12% in BRF were reported. Due to the high resolution of data captured by HSCs, it is likely that wind gusts as shown in Figure 9.2 would have an influence on the data. More research is needed on how this might affect the generated spectral data. Additionally, the signal is influenced by its path through the atmosphere. Therefore data from high altitude and spaceborne sensing systems are commonly corrected for atmospheric influences (Campbell and Wynne, 2011; Datt et al., 2003; Richter and Schläpfer, 2002). This is usually not the case for low-altitude UAV sensing systems under the assumption of negligible effects due to the small atmospheric layer between the surface and the sensor. Nevertheless, the atmosphere is thickest close to the surface and might also have an influence on data from low-altitude sensing systems. Thus, the influences of the atmosphere should be investigated in future studies.

Figure 9.2 Two images taken within seconds of each other at the experimental field at Campus Klein-Altendorf on 5 June 2014. The impact of wind gusts on the canopy is apparent.

9.1.2 Sensing system and measurement protocol

After its path through the atmosphere, the signal is digitized by the HSC system and then translated into physical traceable quantities during initial post-processing. During that process, the signal is influenced by the technical properties of the camera and the measurement protocol, which defines the data calibration procedure.

The relevant technical properties of the UHD were characterized by quantifying the radiometric response function and sensor noise. The radiometric response function was found to be linear until 3500 DN. But at the same time, a strong decrease of the maximum DN towards the edges of the image due to the vignetting effect was found. Moreover, also an undulated pattern influenced the signal (Aasen et al., 2015, Chapter 3). Although the spatial variability can be corrected for by a flat fielding procedure, it still affects the radiometric resolution and thus influences the data quality. During the application of the sensor, no pixel should be illuminated beyond its linear range to prevent additional uncertainty. Therefore the brightest pixel defines the maximum integration time and implicitly sets the maximum value for all other pixels—even if they might be illuminated well below the linear range limit. However, the maximum possible value of a pixel also sets the radiometric resolution (the range by which a signal can be resolved). The impact of this effect is barely investigated in the remote sensing literature. Rao et al. (2007, 2006) found that a reduced radiometric resolution did not strongly influence the retrieval of LAI of crops or land cover mapping of agricultural areas. Still, a low radiometric resolution decreases the signal to noise ratio and might hinder the analysis of parameters with small response signals such as chlorophyll. Aasen et al. (2015, Chapter 3) thus suggested to limit the used spectral of the UHD to range from 466 nm to 866 nm, since the minimum radiometric resolution in this range stayed above 1% reflectance for all pixels under in-field illumination conditions. As a result, the maximum error can be estimated by 0.5% to account for potential rounding errors. Nevertheless, for most pixels and bands the error is significantly smaller.

The sensor noise is generally a function of the CCD temperature. Since the UHD has no temperature sensor, it was impossible to model the noise of the camera and thus, it was measured multiple times under in-field conditions. The average noise of 30 measurements ranged from 0.03 to 2.9 DN (Aasen et al., 2015, Chapter 3), which is less than 0.1% of the linear dynamic range (3500 DN) of the camera. The highest noise value ever measured with the UHD was 19 DN (unpublished data), but can be regarded as a strong outlier. Since even this value is below 1% of the signal, 1% can be considered a generous approximation of the influence introduced by the sensor noise. However, it should be noted that for individual pixels with a very poor radiometric resolution, the error might increase due to the poor signal to noise ratio. Comparable characterization and calibration studies of frame-based cameras systems are sparse. Except for the undulated pattern, a study by Kelcey and Lucieer (2012) found

similar results for a multispectral camera system. Additionally, it can be assumed that similar results are also obtained for other systems since the vignetting effect result from the design of optical imaging systems. Due to the increasing appearance and variety of different spectral sensing systems—many of them manually manufactured—it is strongly argued that every camera system is characterized before use. Additionally, the results need to be provided as metadata to enable users to assess the quality of the data.

In this thesis, the measurement protocol for the HSC included an initial post-processing step to translate the DN values (after the noise removal) to reflectance by comparing the in-flight measurements to a measurement of a white reference panel before the flight (Aasen et al., 2015, Chapter 3). This method turned out to be suboptimal, since it was prone to external factors and introduced wavelength dependent influences of up to 14% under cloudy conditions and 8.5% under sunny conditions depending on the cloud cover and the distance and position of the UAV operator to the calibration panel. With the best practice scenario (no clouds, operator perpendicular to the solar principal plane), the influence was reduced to 3.4% under clear sky conditions (Figure 4.8). Nevertheless, Aasen et al. (2015, Chapter 3) demonstrated that good results can be acquired with the described radiometric calibration: in an overflight over several reference panels with 5% to 60% reflectance, the relative difference per panel was less than 1% in the range of 466 to 846 nm compared to FS3 measurements (Figure 3.8). Still, since these influences by the current way of radiometric calibration cannot be retraced after the calibration measurement is performed, an uncertainty is introduced that compromises the reliability of the measurements to a certain degree. Based on the results presented in Aasen et al. (2015, Chapter 3), the influence introduced by the radiometric calibration procedure is optimistically estimated at 1% of the magnitude of the signal. However it is strongly advised to respect the best practice case as described in Aasen and Bolten (in review, Chapter 4). Alternatively, to mitigate the described influence on the radiometric calibration to a certain degree, future studies could apply an empirical line calibration (c.f. Smith and Milton, 1999) and extract the calibration parameters from calibration targets of images captured during the flight similar to Lucieer et al. (2014). Moreover, the measurement protocol should be changed from a static radiometric calibration to an adaptive calibration procedure, which allows for adaptation to heterogeneous illumination conditions. Imaging spectroscopy is usually carried out during sunny clear sky conditions under the assumption that the atmospheric conditions during the acquisition are spatially homogeneous. However, constant clear sky conditions are rare—at least in central Europe. Additionally, slight variations during a measurement campaign may not be apparent but may influence the retrieval of biophysical parameters such as chlorophyll (Damm et al., 2015). One of the benefits of UAVs stated in the literature is the ability to fly below clouds to capture data (e.g. Honkavaara et al., 2013; Puliti et al., 2015; van der Wal et al., 2013). At the same time, a study by Hakala et al. (2013)

stated an influence on spectral UAV measurements of more than 100% due to “fluctuating levels of cloudiness”. Although approaches towards adaptive radiometric calibration procedures based on cross-calibration between image blocks (Honkavaara et al., 2012) or constant irradiance measurements (Burkart et al., 2014; Hakala et al., 2013) exist, they are based on custom-built software and hardware and are thus not generally applicable. Still, as long as such approaches are not commonly available the advantage provided by the ability of UAVs to fly below clouds is annulled. Thus, robust approaches capable of adapting to varying irradiance are strongly needed and should become a standard for spectral UAV sensing systems. Not only would this greatly increase the flexibility of their application by nullifying the need for stable illumination conditions, but also decrease the potential uncertainty with other calibration procedures. To highlight the importance of this topic for the further development of the field, the estimate of more than 100% by Hakala et al. (2013) is adapted as an estimate of the potential influence on the data quality by non-adaptive sensing systems applied under poor illumination conditions.

9.1.3 Data processing

After the initial post-processing, the individual images are composed to the HS DSM. The processing scheme defines how this composition is carried out. Since every pixel in the final scene is seen from multiple images, the spectral data is majorly influenced by the selected blending mode. It defines whether the spectral information assigned to a pixel is taken from one image or multiple images (Aasen and Bolten, in review, Chapter 4). If a standardized data product needs to be generated, the result might be influenced in an unwanted manner by the processing scheme. When only one image per pixel is taken into account, an HDRF data product is generated. However, each pixel within the final scene has its own angular properties defined by the measurement geometry of the individual pixel and the illumination geometry during the acquisition of the corresponding image (Aasen and Bolten, in review, Chapter 4). With the method developed in Aasen et al. (2015, Chapter 3) these properties can be traced. Additionally, some sophisticated techniques for BRDF correction exist for airborne data (Schläpfer et al., 2015; Weyermann et al., 2014). These were developed for imaging spectroscopy data with a resolution of less than 1 m and depend on a rather coarse statistical characterization of the surface. Therefore, it is questionable how well these perform for high-resolution data from HSC systems. Thus, if a data product in a specific HDRF geometry (e.g. nadir HDRF) is desired, so far the influence of the BRDF effects assessed in Subsection 9.1.1 cannot be corrected in HS DSMs. Nevertheless, since only the most nadir parts of the images are used (due to the mosaicking), it is likely that the influence is significantly smaller than the 25% which were accounted for at image scale. It has to be noted that these considerations assume that the gimbal sufficiently stabilizes the camera in a nadir viewing geometry. However, with the current setup this cannot be guaranteed. Although the

camera is mounted with the help of a level, an exemplary evaluation of the pitch and roll angles of the images showed that the gimbal was slightly off nadir (average offset 3.0° and 1.7° of pitch and roll, respectively). The stabilization by the gimbal itself was quite robust (standard deviation of the offset 1.1° and 1.6° for pitch and roll, respectively). For an estimation of the angular properties of each pixel, the real orientation of each individual image should be used.

When multiple images are taken into account for a pixel within a scene, pixel values with different angular properties are averaged and the resulting quantities can be regarded as an approximation of HCRF measurements. Thus, the resulting data could be described as an HCRF data product (Aasen and Bolten, in review, Chapter 4). The angular properties of a pixels in this data product are a composition of the angular properties of the pixels which were averaged from the individual images. Although it can be assumed that multiple images overlap, the exact composition depends on the flight trajectory and capturing position of the sensing system. Additionally, the angular properties of the averaged pixels cannot be traced with the method developed in Aasen et al. (2015, Chapter 3). In the worst-case scenario, a part of a scene is only covered by one image and the value of a pixel close to the edge of that image is assigned to a pixel in the scene. In this case the approximated offset due to the position within an image of about 25% (at 670 nm, c.f. Subsection 9.1.1) can be seen as a good approximation of the maximum offset within an HCRF data product. If more reliable HCRF approximations are needed, the spectra of an entire HSC image could be averaged: as seen in Aasen and Bolten (in review, Chapter 4), the angular properties of point measurements by a field-spectrometer and the entire FOV of an HSC are similar. Thus, such measurements would be similar to the point measurements of the flying goniometer introduced in Burkart et al. (2015, Chapter 5).

9.1.4 Conclusion on the spectral data quality

Motivated by the complexity of spectral remote sensing of vegetation, this chapter examined the path from particle to pixel for potential sources of influence and their potential impact was discussed. Table 9.1 summarizes the results. Two sources of influence stand out, namely those related angular effects (due to surface anisotropy and measurement geometry) and the varying irradiance, which cannot be compensated for with the current measurement protocol.

Overall, the radiometric calibration procedure within the field protocol has to be acknowledged as the current Achilles' heel for the reliability of the HSC data. Although good results can be acquired (Aasen et al., 2015, Chapter 3), they might be strongly biased (Aasen and Bolten, in review, Chapter 4). Moreover, this bias is hardly traceable, which violates the reliability of the data. Besides, this calibration procedure impedes the use of HSC in unstable illumination conditions and therefore strongly limits the flexibility of HSC sensing systems. In the future, HSC systems should commonly

measure the incident irradiance to avoid possibly biased in-field calibration procedures and exploit the full potential of cloud independent hyperspectral remote sensing.

However, drawing conclusions about influences related to angular effects is considerably more complex, and must take into account several different factors. In contrast to the influences from the measurement protocol or the sensing system, angular effects are not errors per se. They complicate the interpretation of hyperspectral data but are property of the surface. For standardized data products (e.g. in a homogeneous viewing geometry), angular effects need to be reliably normalized. A necessary prerequisite is the precise estimation of an irradiance field per pixel, which is currently hindered by the lack of high-resolution DSMs (Damm et al., 2015). Incorporating high-resolution information to characterize the structural properties of the surface is seen as the way forward (Weyermann et al., 2014). HSCs can provide 3D and spectral information at the same time. Thus, their data is potentially suited to address this issue. On the other hand, surface BRDF information holds great potential to not only retrieve structural information about crop canopies with spectral data (Casa and Jones, 2005), but also about biochemical parameters, as a very recent study has shown (He et al., 2016). In the future, this potential should be exploited. Since HSC sensing systems capture multiple overlapping images during an overflight, they are an optimal tool for multi-angular data retrieval. First attempts in this direction have already been undertaken with non-hyperspectral cameras (Hakala et al., 2010; Koukal and Atzberger, 2012).

Compared to the influences of the measurement protocol and surface anisotropy, the technical aspects of the sensor only have a minor impact on the data quality. The sensor noise and response function influence the data by less than 1.5%. Under optimal conditions, the overall calibration procedure influences the data less than 2.5%. Professional calibration facilities are able to radiometrically calibrate imaging spectrometers to levels of 3% relative to national standards (Gege et al., 2009). The procedures to evaluate the data quality within this thesis must be described as rather rough compared to for example the calibration facility of APEX at the Deutsches Zentrum für Luft und Raumfahrt e.V. (DLR) in Oberpfaffenhofen. Still, in comparison the magnitude of the influences introduced by the technical aspects of the camera seem satisfactory. However, this only applies as long as the uncertainties introduced by the measurement protocol are disregarded (c.f. above).

Overall, these results highlight the need for specific metadata for all data entity levels. Previously, Heuvelink et al. (1989) argued that methods are needed to trace errors on a pixel specific level in raster GIS data. Due to the complexity of data products such as HS DSMs, this has become even more important. To properly interpret the data under consideration of different influences along the path of particle to pixel, information about the data quality (e.g. noise or radiometric resolution) and the measurement geometry needs to be made available for each pixel. For each image, information about

the calibration procedure has to be recorded in addition to the information about the position and orientation during the image acquisition. On a scene level, precise information about the data processing procedure needs to be recorded. For a reliable data product, the information from all levels should be provided for each pixel within the final scene, to provide the user with metadata not only on a generic but also on a more detailed level, as requested by Hunter et al. (2009). While efforts have been undertaken to provide pixel-wise quality information for airborne (e.g. Itten et al., 2008) and spaceborne (e.g. Roy et al., 2002) missions, so far this has been missing for UAV data. The pixel-wise quality assurance approach introduced in Aasen et al. (2015, Chapter 3) provides the prerequisite to generate the necessary metadata to transform the data within the pixels into information about the particles.

Table 9.1 Sources of influence along the path from particle to pixel with an approximated potential impact on the information relative to the signal.

Source of influence	Data entity level	Relative potential impact	Comment	Reference
Environment				
Angular effects due to surface anisotropy	image	25%	Wavelength dependent	Burkart et al. (2015, Chapter 5), refined in Subsection 9.1.1
Sensing system and measurement protocol				
Noise	pixel	<< 1%	Increased for individual pixels with low radiometric resolution	Aasen et al. (2015, Chapter 3) and Subsection 9.1.2
Radiometric response	pixel	< 0.5%	Significantly smaller for most pixels and spectral bands	Aasen et al. (2015, Chapter 3) and Subsection 9.1.2
Radiometric calibration	image	1%	Additionally, a constant offset might be introduced by the calibration procedure in the magnitude of 14% under cloudy conditions and 3.4% under sunny conditions	Aasen et al. (2015, Chapter 3) and Aasen and Bolten (in review, Chapter 4)
Varying incident irradiance	scene	> 100%	During poor illumination conditions with fluctuating levels of cloudiness for calibration procedures without the possibility to adapt for illumination changes	Hakala et al. (2013)
Data processing				
Scene composition	scene	< 25% in HDRF data product (blending mode 'disabled')	For the hemispherical-directional reflectance factor (HDRF) data product, influences are introduced by not-corrected surface anisotropy	Aasen and Bolten (in review, Chapter 4), refined in Subsection 9.1.3
		< 25% for HCRF data product (blending mode 'average')	For hemispherical-conical reflectance factor (HCRF) data product, influences are introduced by insufficient view-angle coverage	

9.2 Comparability of hyperspectral digital surface models to data from other sensing systems

In the following section, the comparability of data contained in HS DSMs derived with HSCs will be discussed. The first subsection highlights the comparability of spectral data to data from other sensing systems. In the subsequent subsections, the comparability of the 3D data with regards to different SfM software tools and TLS data and their processing schemes will be discussed.

9.2.1 Spectral data

In this thesis, different imaging and non-imaging devices were used to record spectral and RGB data. Besides the obvious differences resulting from their properties (e.g. spectral and spatial resolution) listed in Table 2.1, the data produced by the different sensing systems also differs in other ways.

The first aspect is the type of spectral data, which is generated by the sensing systems. As described in Subsection 2.1.2, different reflectance quantities exist. From its definition, HDRF measurements can be carried out by instruments with an infinitesimal small measurement cone (Schaepman-Strub et al., 2006). However, measurements from devices with very small IFOVs can be described as HDRF due to their high degree of directionality (Schläpfer et al., 2015). Table 2.1 summarizes the properties of the different sensors used in this study. The imaging devices UHD and GX1 have IFOVs well below 1°. Thus, their measurements can be described as HDRF. The non-imaging devices FS3 (deployed as field-spectrometer in several studies within this thesis) and UAV-STS (deployed in Burkart et al., 2015, Chapter 5) have an FOV (= IFOV) of well above 10° and represent HCRF measurements. In Bareth et al. (2015a), significant differences were found between FS3 and UHD measurements, which were suspected to result from calibration issues. In Aasen and Bolten (in review, Chapter 4) these differences were further investigated. Although the radiometric calibration was found to potentially impact the data, the systematic differences between imaging and non-imaging devices were found to play a significant role. Specifically, the different angular properties of the data, in combination with different data processing schemes accounted for a relative increase of up to 55% in reflectance (DAS 84 at 466 nm) depending on the wavelength between the FS3 and UHD data (Figure 4.4). These results question whether results obtained by measurements with different geometries and from HDRF and HCRF measurements can generally be transferred and compared with each other. Literature that explicitly compares imaging and non-imaging (HDRF and HCRF, respectively) measurements is rare. Von Bueren et al. (2015) deployed the multispectral imaging camera Mini-MCA (TETRACAM Inc, 2015) and the non-imaging UAV-STS over grassland and compared it to ground-based ASD HandHeld2 (ASD Inc., 2014) measurements. In von Bueren et al. (2015), Figure 4 shows the results for a grazed pasture and a non-grazed pasture with dense vegetation and no soil visible. To compare the reflectance, a 0.3 by 0.3 m

area approximately matching the ASD measurement position was extracted and averaged in the Mini-MCA imagery. In the grazed case, the ASD had a lower reflection in the VIS and a higher reflection in the NIR. In the non-grazed case, the reflection in the VIS was comparable for both devices, while in the NIR the Mini-MCA derived lower reflection values. Although these results were not explicitly discussed in the article, this is similar to what was found in Aasen and Bolten (in review, Chapter 4): in denser vegetation, differences between imaging and non-imaging devices are less pronounced than in sparse vegetation (Figure 4.4 in conjunction with Figure 4.5). In general, it is more likely that beams from the soil surface reach the sensor in a viewing geometry close to nadir (Figure 9.3). However, in dense vegetation, (almost) no beams from the soil reach the sensor and the influence of the beam geometry decreases (Figure 9.3, B). In contrast, in sparse vegetation beams in a close-to-nadir geometry are likely to contain a soil signature (Figure 9.3, A). Since the imaging data within the HS DSMs is composed of pixels with a viewing geometry close to nadir (SFOV, c.f. Figure 4.6), their spectra contain more soil signature than the integrated measurement of the non-imaging device (Figure 9.3). Generally, it should be concluded that even if HDRF and HCRF measurements (e.g. derived from an HS DSM and the FS3) are used to characterize the same area, they do not necessarily capture the same objects. Consequently, both types of measurements are not directly comparable. These results are of particular interest, since they potentially have great impact on the comparability of near-ground, air- and spaceborne observations but have not yet been systematically discussed in a similar manner as in Aasen and Bolten (in review, Chapter 4).

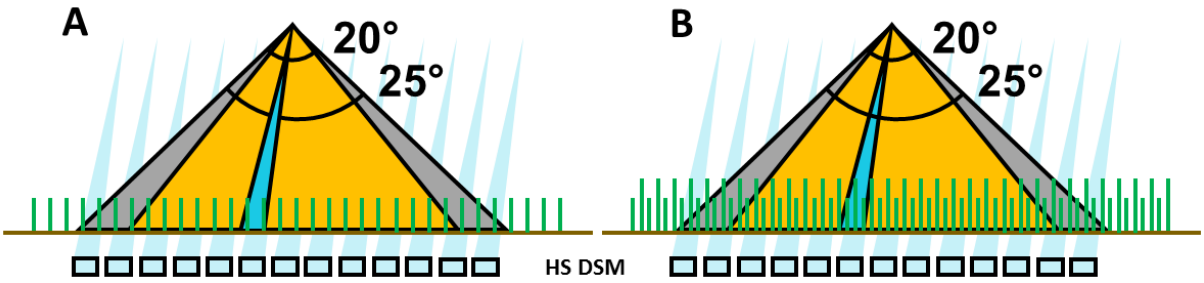

Figure 9.3 Field of view of the FS3 (gray), UHD (yellow) and of multiple pixels within an HS DSM used to characterize an area (SFOV (light blue), c.f. Figure 4.6) with sparse vegetation (A) and dense vegetation (B). Towards a nadir viewing geometry beams from the soil are more likely to reach the sensor. The spectral data within the HS DSM is composed by pixels with a close-to-nadir viewing geometry captured from multiple positions.

Common air- and spaceborne hyperspectral pushbroom imaging systems also record HDRF data. While APEX has an IFOV of about 0.028° (Schaepman et al., 2015), every Hyperion pixel has an IFOV of 0.0024° (Pearlman et al., 2000). Although the IFOVs of the UHD are more than one magnitude larger (0.4°), the measured reflectance quantity is more comparable to the satellite and airborne system than the HCRF of the FS3 with a FOV (=IFOV) of 25°. Still, also the sensing principles and data processing schemes of pushbroom and HSC systems result in different angular properties within the data product. Pushbroom

scanners record individual lines of hyperspectral data, which are aligned with the help of precise information on the position and orientation of the sensing system. Therefore, all pixels from the same position within an image line, and consequently at that position in the final scene (or flight strip), have the same angular properties (under the assumption that the sensor is geometrically stabilized and the surface geometry is constant). On the contrary, HSCs record hyperspectral data in two spatial dimensions (c.f. Subsection 2.1.4) where each pixel has its own angular properties. These are composed to a final scene based on a mosaicking process (c.f. Aasen et al., 2015, Chapter 3). As a result, the angular properties not only differ in the across-track direction (as for the pushbroom systems) but also in the along-track direction (Aasen and Bolten, in review, Chapter 4), even if only one flight line is regarded. Figure 9.4 visualizes these considerations. The maps show the pixel positions of scenes generated from a pushbroom camera (micro-Hyperspec NIR: Headwall Photonics Inc, 2015) and an HSC (UHD) together with the generated hyperspectral scenes. The shift of the across-track pixel position of both devices results from the roll movement and the non-linear flight of the sensing system. Additionally the different pixel positions in along-track direction are visible in the HSC data.

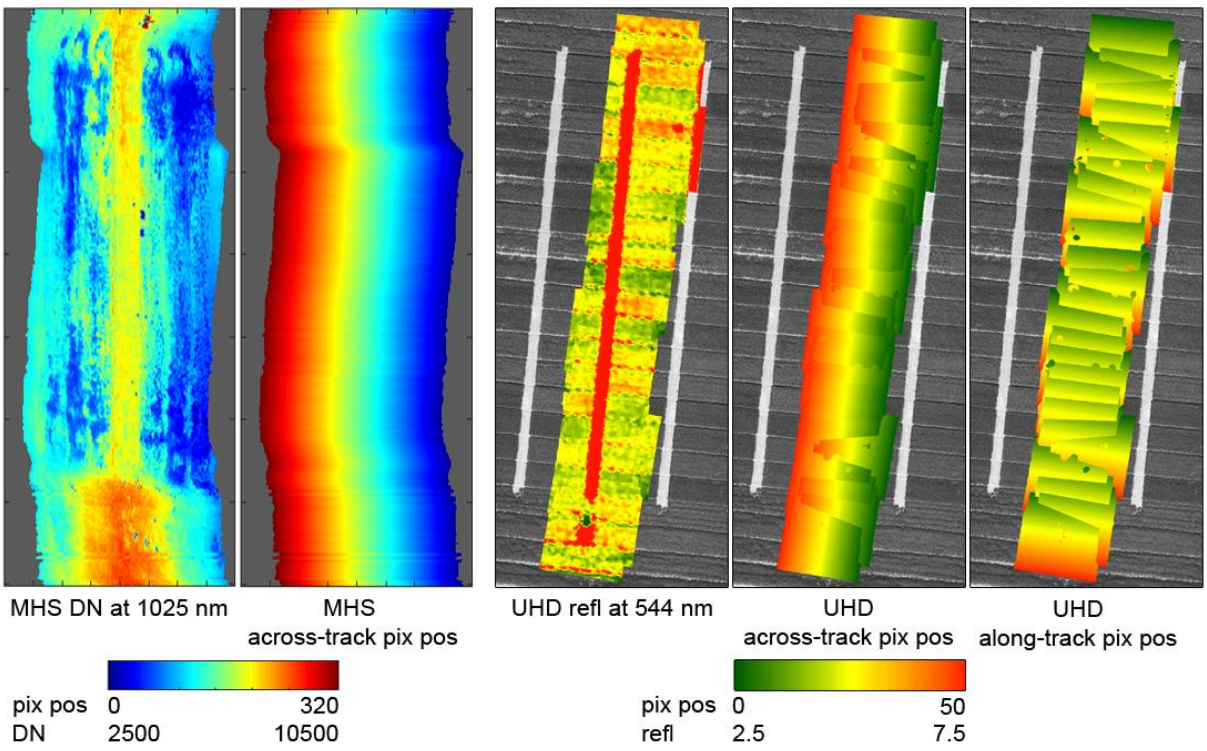

Figure 9.4 Properties of single flight lines of the pushbroom camera micro-Hyperspec NIR (MHS) flown at the University of Tasmania after preliminary orthorectification (03/20/2014 unpublished data, left) and the HSC UHD flown at the Campus Klein-Altendorf (2014 DAS 70, right). For the MHS, digital numbers (DN) at 1025 nm and the across-track pixel position (pix pos) are shown. For the UHD, the reflectance (refl) at 544 nm and the corresponding across-track and along-track pixel positions are shown. Within the UHD data, some processing artifacts due to the exclusion of the other flight lines are visible.

This is particularly important with regards to angular effects, since they are most pronounced in the solar principal plane (Küster et al., 2014). Thus, pushbroom systems are mostly flown in parallel to the solar principal plane to reduce complexity. For HSC systems, such an approach is not possible because of the two dimensionality of the images and the way the data is processed. Thus, the influence of the differing measurement geometries is visible in scenes composed by HSC data (Figure 4.7 and Figure 4.9, second row of plots to the left at DAS 84). In future, higher frame rates together with principle plane parallel flight patterns could help to minimize the influence of multiple view angles. Nevertheless, to fully compare data from different devices, algorithms are needed which can correct or transform reflectance factors derived from different devices, IFOVs and measurement geometries.

Besides the different data processing approaches of pushbroom and HSC systems, the sophistication of the processing scheme can also be compared. As an example, the APEX data processing scheme consists of four stages transforming the raw DN to radiance, to HCRF, and to a desired data product. During that process, customized modules can be applied to minimize the impact of atmospheric and topographic effects if the user wishes to obtain uniform geo-locatable bottom-of-atmosphere reflectance values (Richter and Schläpfer, 2002; Schaepman et al., 2015; Schläpfer and Richter, 2002). Additionally, APEX data can be normalized to nadir-viewing geometry by applying a Li-Ross BRDF correction based on land cover classification (Weyermann et al., 2014). This processing scheme demonstrates that after more than six years in operation, APEX is a mature sensing system that produces scientific-grade data. In comparison, the data processing scheme to generate HS DSMs from the UHD data is much simpler. As described earlier, the raw DNs are directly transformed to reflectance with a rather simplistic approach prone to errors (Subsection 9.1.2). Currently, no modules are ready to be applied to correct HSC data for radiometric correction of atmospheric, topographic or BRDF effects. A promising approach towards the correction of illumination conditions within image-frame camera data has been described by Honkavaara et al. (2013) and is based on irradiance measurements and radiometric block adjustment. Still, the approach has not yet been made available for other systems. An adaption of modules from airborne missions should be possible from a theoretical point of view, but will remain a task for forthcoming research. Thus, it has to be concluded that the data processing schemes of HSC sensing systems are not yet on a comparable level to the highly standardized data products as e.g. of the APEX. Still, the outcome of this thesis, in particular the pixel-tracing method developed in Aasen et al. (2015, Chapter 3), provides the necessary basis for further development and standardization of HSC data.

Besides HSCs, consumer-grade RGB and CIR cameras are also used for vegetation monitoring. Similar to HSCs, they allow for the generation of 3D information linked to the color information of the RGB bands. Recently, some studies have used the color data of uncalibrated RGB and CIR cameras

(sometimes incorrectly referred to as spectral data) to derive information about the vegetation (Bareth et al., 2015b; Bendig et al., 2015; Dandois and Ellis, 2013; Geipel et al., 2014; Rasmussen et al., 2016). However, this must be viewed critically as long as no spectral and radiometrical calibration and referencing is applied: most consumer-grade cameras do not come with a sufficient description of the radiometric response and spectral band properties. This prohibits the comparison or transfer of results achieved by these sensors to other sensors, particularly when images are not captured in RAW mode but compressed to JPEGs. Even worse, if onboard image correction algorithms such as automatic white balancing (color correction) are not disabled, images are tuned to 'look nice' and their color information is altered based on image statistics (c.f. Zapryanov et al., 2012). However, this makes the color information unusable for quantitative remote sensing approaches, since the same area might appear different depending on the image capturing conditions. Besides, if the signal is not transformed to physically traceable units (and if no reference object is placed within the images) scenes captured under different illumination conditions (e.g. during different campaigns) cannot be compared. Additionally, most RGB cameras have a wide FOV. Although widely disregarded in studies of RGB data, it should be mentioned that a wider FOV increases the BRDF effects within the images (c.f. Subsection 9.1.1). Thus, great caution needs to be taken when using the color information of consumer-grade cameras. Overall, it can be concluded that orthophotos from uncalibrated RGB and the spectral data within HS DSMs are not comparable from a theoretical point of view. However, when RGB cameras are radiometrically and spectrally calibrated, they might provide spectral information comparable to a multispectral camera with three bands in the VIS. This aspect will be considered in Subsection 9.3.1 from a practical point of view.

9.2.2 Digital surface model

In this thesis, different devices were used to reconstruct the 3D surface of a canopy as DSMs. The 3D data within the HS DSMs is derived by SfM implemented in the commercially available software Photoscan (Aasen et al., 2015, Chapter 3). The quality of the reconstruction depends on several aspects. Furthermore different implementations of SfM exist. In addition to SfM, LiDAR can also be used to derive 3D information (e.g. Tilly et al., 2015, Chapter 6). However, it is based on fundamentally different principles (c.f. Subsection 2.2.1 and 2.2.2). In this subsection, these aspects are discussed in the context of the comparability of the 3D data within HS DSM.

SfM can reconstruct the 3D geometry of a surface from 2D images, as long as the images meet the necessary requirements (c.f. Subsection 2.2.1). A variety of 3D reconstruction tools exist with different implementations of the feature detection, bundle block adjustment and the dense point cloud reconstruction (Eltner and Schneider, 2015; Remondino et al., 2014). In this thesis, Photoscan was used for the reconstruction process since it has been shown to be suitable for agricultural monitoring in

other studies (Bendig et al., 2014, 2013; Turner et al., 2014). Additionally, preliminary trials with the UHD data and another software package (Pix4D, 2016) were unsuccessful. Nevertheless, studies have shown that significant differences exist between different software packages (Eltner and Schneider, 2015; Gómez-Gutiérrez et al., 2014; Remondino et al., 2014). Grenzdörffer (2014) specifically compared different software packages for the reconstruction of the canopy height of winter wheat in an experimental plot layout similar to the experiments in this thesis. He found significant differences, which were attributed to the different algorithms used for the reconstruction and filtering of the 3D point cloud. Figure 9.5 demonstrates these differences. Additionally, Aasen and Bolten (in review, Chapter 4) found Photoscan to be prone to the 'bowl-effect', with suboptimal GCP coverage. In Ouédraogo et al. (2014) the same effect was found with Photoscan, however a different tool did not show the effect using the same data. Nevertheless, since software suites such as Photoscan use proprietary algorithms and limit the parameters which can be controlled by the user–sometimes rendering these software packages a 'black-box' (Remondino et al., 2014)–it is difficult to understand these differences. Additionally these are likely to change due to the ongoing rapid development in the field. In this thesis, Photoscan seems to reconstruct the plot edges significantly better than the (supposedly older) version of Photoscan used in Grenzdörffer (2014). Thus, with every new version of a software or after settings are changed the results should be scrutinized before a workflow is operationally used. As an example, Aasen et al. (2015, Chapter 3) found that Photoscan processed the spectral data differently than stated in the manual.

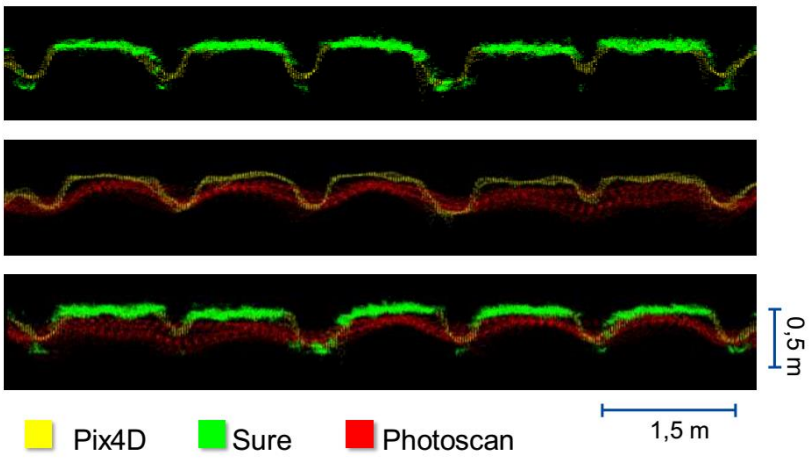

Figure 9.5 Transects through point clouds of winter wheat plots derived with the software packages Pix4D, Sure and Photoscan (Grenzdörffer, 2014).

In addition to the systematic differences introduced by the 3D reconstruction algorithm, factors like the flight pattern, image overlap, ground sampling distance, GCP placement and illumination conditions (and the resulting image contrast) also influence the 3D reconstruction (Dandois et al., 2015; Gerke and Przybilla, 2016; Grenzdörffer, 2014; Remondino and El-Hakim, 2006). In theory SfM can generate point clouds with a resolution similar to the ground sampling distance of the input images

(c.f. Subsection 2.2.1; Haala, 2013). With the common above ground altitude of the UHD and GX1 of 30 and 50 m, respectively, images with a ground sampling distance of 0.01 m were captured. However, in an applied setting, parameters such as the flight trajectory and the illumination conditions may vary for each measurement campaign. Figure 9.6 (top) shows the point density within a 0.1 m x 0.1 m area relative to x-y space of a point cloud derived from a flight with the UHD and the GX1 for the same date. In the UHD point cloud (Figure 9.6, top center), the dependence of the density on the image overlap is visible. Due to wind, the second and third flight lines to the west largely align, which produces a great overlap of images (c.f. Figure 4.10) and a high point density. The low image overlap to the east of the scene leads to a lower point density. In the point cloud of the GX1 such a pattern is not clearly apparent. Additionally, the point cloud is generally denser (Figure 9.6, bottom). Due to the larger FOV of the GX1, the image overlap is higher compared to the UHD, despite the flight pattern being less dense. Interestingly, the plots of the two fast-growing varieties Eunova and Isaria (c.f. Figure 2.10) can be distinguished from the other plots by their low point densities in the GX1 point cloud but not in the UHD data. At the date of the flights, these varieties were ahead in growth and thus had an increased roughness of the canopy compared to the other varieties.

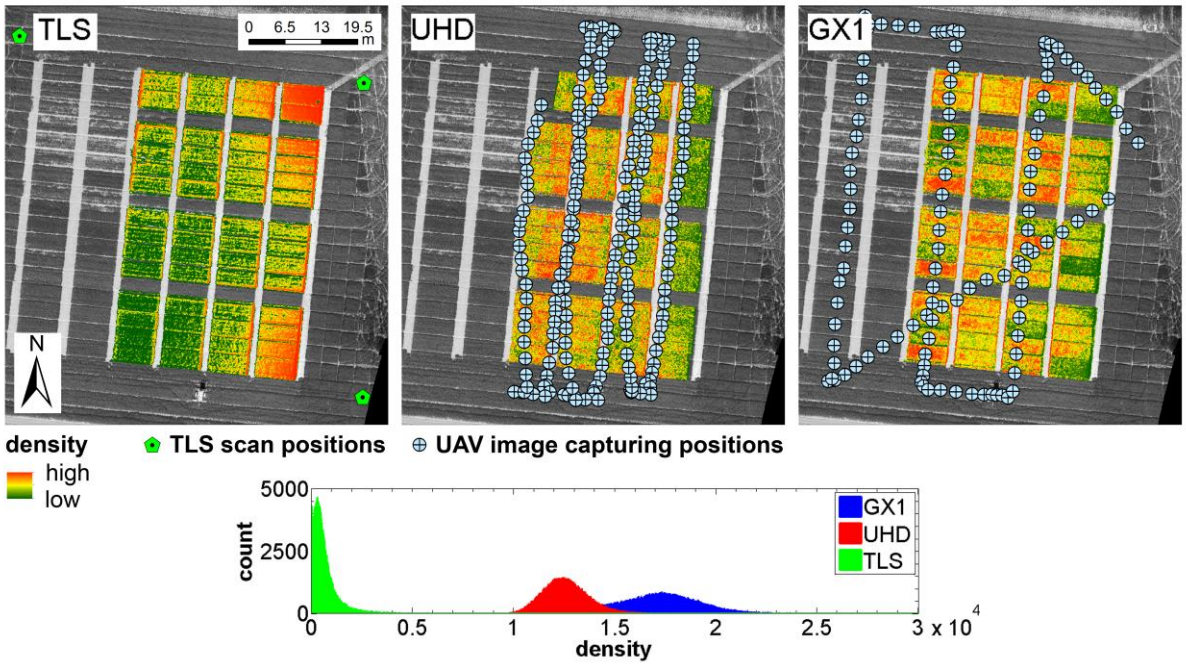

Figure 9.6 The maps at the top show the density within 0.1 m by 0.1 m cells of point clouds derived by a terrestrial laser scanning system (TLS), the UHD flown at 30 m and the GX1 camera flown at 50 m. The different flying altitudes in combination with the camera specifications result in ground resolution of approximately 0.01 m for both systems. All measurement were carried out around DAS 70 in 2014. The color represents the point density per square decimeter (a histogram equalizer is applied to the color scheme to emphasize the different patterns). Additionally, the scan and image capturing positions are shown in light green and light blue, respectively. The histogram at the bottom shows the distribution of densities for the three point clouds. It has to be noted that the TLS point cloud was filtered with a maximum point filter. Thus, the absolute point density values cannot be compared.

The differences of the point clouds derived from the two camera systems might result from the different approaches in how the image overlap is created. While the GX1 images overlap mainly because of the wide FOV, the UHD overlap is created by a high frame rate. However, with a shallower angle, beams are more unlikely to penetrate the vegetation (similar to oblique TLS, c.f. Figure 9.7). Additionally, during the reconstruction, point matching starts to rapidly decrease when view-angles exceed 20° (Lowe, 2004). These results suggest that it is not just the overlap, but also the area and its viewing geometry that is influencing the 3D reconstruction. These results highlight the complexity and need for further investigations on the robustness and comparability of 3D data derived from SfM. In the future, such effects and their impact on plant parameter retrieval need to be evaluated.

LiDAR and SfM are fundamentally different techniques for deriving 3D information of a scene. While the former is an active sensing technique, the latter is a passive technique and relies on the illumination of the scene from other sources. Thus, features need to be visible to produce stable keypoints for the SfM approach (visible in the sense of contrast, c.f. Lowe, 2004), while fully un-illuminated features can be detected by LiDAR, as long as they are not obscured by other features. In the case of complex structures such as vegetation, these differences play a major role. Several studies have investigated the differences of airborne LiDAR- and SfM-based approaches in the reconstruction of forest canopies (Dandois et al., 2015; Dandois and Ellis, 2013, 2010; Lisein et al., 2013). Generally, SfM performed nearly as well as LiDAR in relatively homogeneous canopies (Dandois and Ellis, 2010). At the same time, overstory occlusion limited the observation of the lower canopy (Dandois and Ellis, 2013), which led to differences in the reconstruction depending on the density of stands (Lisein et al., 2013). Generally, point density and canopy penetration relates to image overlap (Dandois et al., 2015). Still, SfM was described as being not suited to deriving a DTM below forest canopies, due to its inability to deeply penetrate the canopy in comparison to LiDAR. While it is likely that these results are also of significance for crop canopies, the latter have a different structure than forests. However, studies comparing LiDAR to SfM approaches for dense cereal crops are still missing.

For TLS systems as used in (Tilly et al., 2015, Chapter 6) the situation is different. Figure 9.6 (left) shows a map of the point density for a TLS scene for the CROP.SENSe.net experiment together with three out of the four scan positions used to generate the 3D model of the canopy (the fourth scan position is to the south-west outside of the map excerpt). Towards the scan position, the point density strongly increases. This results from the scanning principle of the laser scanner, which sends and receives angular evenly spaced beams. Thus, the sampling distance on a surface decreases (the distance between points increase) with distance to the scanner. Additionally, the entry angle into the canopy decreases with the distance from the scanner, which decreases the ability of the laser to penetrate the canopy and increases the chance of the beams of being obscured before hitting deeper canopy layers

or lower plants. This obscuration effect is visible in Figure 9.6 (left), where the density within the plot is increased in higher areas compared to lower parts within the same plot. This effect can also be seen at the plot edges. Since they represent a vertical plane behind a patch of bare soil, they are hit by more beams than the other canopy and have a high point density per ground area. But the point density of these planes also decreases with an increasing distance to the scan position. This is mostly caused by the increased obscuration from the plot in front due to the shallower beam angle – similar to what happens at the vegetation layers within the plot. Although the plot edges also show a higher point density within the SfM-derived point clouds, the point density is similar for all edges. Most likely this results from the steeper view angle of the cameras. Figure 9.7 schematically visualizes these considerations. These differences may also influence the derivation of DSMs and canopy heights, which will be discussed in the next chapter. Finally, it should be mentioned that, besides of the already mentioned systematic differences, also unpredictable environmental effects such as wind (e.g. Figure 9.2) may influence the generation of the point cloud. Future studies should investigate the impact of such influences.

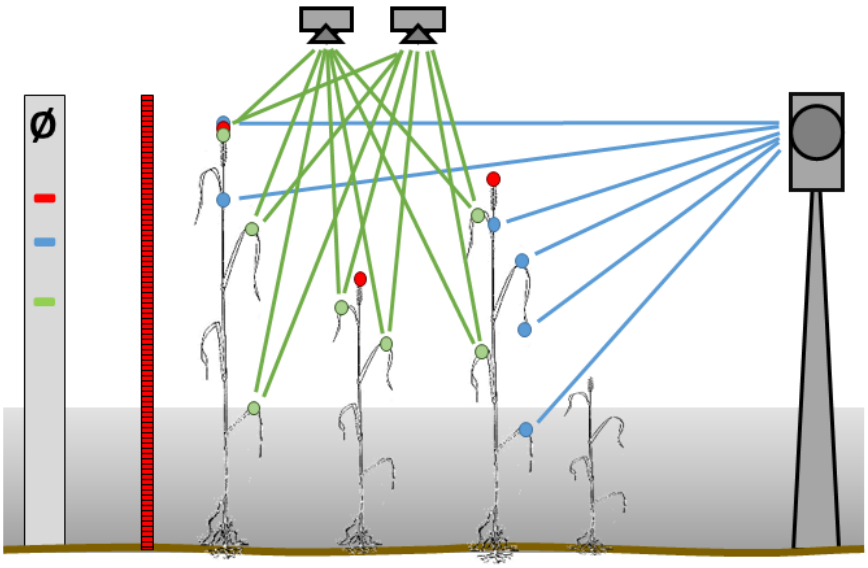

Figure 9.7 Schematic drawing of canopy height estimation with terrestrial laser scanning (blue), Structure from Motion (green) and manual ruler measurements (red) with the resulting average height (left). The shaded part of the canopy (gray background) can barely be captured by image-based approaches.

9.2.3 Canopy height

Measuring the plant height in the field is a difficult task. Already its definition is challenging. Heady (1957) defines the plant height as “the perpendicular distance from the soil at its base to the highest point reached with all parts in their natural position”. He reports three measurement methods that have been applied: ruler measurements alongside the plant in its natural position, ruler measurements of the plant stretched to its full length (eliminating the natural position), and ocular measurements that average the plant height based on the ‘mind’s-eye’. For an individual plant, the first described

measurement method aligns well with the Heady's definition of the PH. However, for canopies both a definition and the choice of an appropriate method become more difficult. Manual measurements are only suited to derive a few discrete measurements within an area to characterize the height. However, a canopy might be highly heterogeneous. Thus the question arises: which plant and which part of the plant to measure, since its inflorescence might stand out from the canopy, for example. And how, then, should these measurements be translated into the canopy height of dense cereal for a certain area? For forests different definitions exist, which estimate the canopy height using different metrics derived from the maximum heights of the individual trees within a stand (Nakai et al., 2010). For cereals, a definition besides that for a maximum canopy height could not be found in the literature. The manual ruler measurements of all datasets within this thesis followed a similar approach as that for forests considering 10 discrete PH measurements at randomly selected spots within a plot. However, this results in a canopy height which is calculated from maxima within the canopy, since most of the leaf surface is below the measured plant height (Figure 9.7, red).

Although remotely sensed data mostly consist of discrete measurements, very high-resolution methods generate quasi continuous data. UAV sensing systems and TLS capture the surface from a close-to-nadir and oblique angle, respectively. Thus, in contrast to the manual measurements, TLS and SfM not only capture the highest points within the canopy but also the height of the other elements within the canopy (c.f. Subsection 9.2.2). Additionally, due to the three-dimensionality of the data, several points at different heights might be captured for the same 2D coordinate (e.g. along a stem). During the generation of a DSM, the dimensionality of the 3D point cloud is reduced to what is often referred to as 2.5D, where one height value is assigned to a cell in x-y space (c.f. Section 2.2). This assignment is based on a specific rule such as averaging. Depending on the applied rule, the resulting value represents a canopy height different from that of the manual measurements. These considerations are visualized in Figure 9.7. The schematic drawing on the right shows the points in the canopy which are resolved by the different techniques. When these points are averaged to derive the height for the cell, they result in different heights (Figure 9.7, left). Additionally, as discussed in Subsection 9.2.2, the density of a point cloud both for SfM and TLS is variable throughout a scene or for different campaigns and might influence the derived height. Crommelinck and Höfle (2016) found that very low point densities (8 points per 0.01 m^2) result in a slight underestimation of the crop height. But overall, the estimated plant height appears to be quite robust against reduced densities. Additionally, no trend was found between the measurement error and the distance (of up to 150 m) to a TLS system when a similar workflow as in Tilly et al. (2015, Chapter 6) was used. However, it is likely that the necessary point density to achieve the required accuracy is related to the crop type and growth stage (Hämmerle and Höfle, 2014).

In addition to the quality of the acquired data, the algorithms used to process the point cloud also influence the result. In this thesis, the dense point cloud build within the SfM workflow was carried out in the depth-filtering mode 'aggressive'. This mode is recommended for aerial data processing (Agisoft LLC, 2016). However, it may classify small features (such as ears) as outliers, which are deleted and thus cannot be regarded later on. This may have increased the underestimation of the canopy height of the SfM approach in comparison to the manual measurements (c.f. Table 4.3). The TLS approach in Tilly et al. (2015, Chapter 6) showed a smaller offset. This might result from two reasons: as mentioned above, lower parts of the canopy are shaded by higher parts due to the oblique scan angle of the TLS. Additionally, the workflow for the TLS data included a maximum-point filter, which selected the maximum points within a given area before the canopy height model was generated (Tilly et al., 2015, Chapter 6). This results in a relative increase of high points and thus, in an increased estimate of the canopy height more similar to the manual measurements. These results are also comparable to those in Grenzdörffer (2014), where the maximum heights extracted from a SfM point cloud better matched the manual measured heights compared to the averaged heights.

As already seen in Subsection 9.2.2, the canopy structure may influence the derived data. During plant growth, the canopy structure changes. Aasen and Bolten (in review, Chapter 4) investigated the difference between the manual and SfM derived plot heights for four different growth stages. The SfM approach generated lower canopy height compared to the manual estimation and the difference continued to increase until the heading stage. For the development of fruit stage, the difference then decreased (Table 4.3). This aligns with the apparent heterogeneity within the canopy. Figure 9.8 shows oblique pictures from the booting, heading and development of fruit stage. In the booting stage, the non-erected leaves form a (more or less) closed canopy layer (Figure 9.8, top). In the heading, the inflorescences have emerged and stand out from the canopy (Figure 9.8, center). During the development of fruit stage, the weight of the grains cause the ears to bend and homogenize the canopy (Figure 9.8, bottom).

Overall, these results show that different quantities can and have been derived from the 3D data. Further research is needed to evaluate appropriate measurement procedure and processing workflow for desired quantities such as maximum or average canopy height. Additionally, these results underscore the challenges in the comparability between different methods that interact with the canopy structure. More studies are necessary to investigate these differences and establish a basis of comparison. In addition to technical solutions, consistent definitions to describe the 3D properties of dense cereal canopies are needed. In the studies within this thesis, the estimated height parameter was referred to as 'plant height' of the canopy. As outlined above, this referred to an average of the maxima of the plants within the canopy for the manual measurements and for the TLS estimation (with

the maximum filter). For the SfM method, this referred to an average of all points derived from the canopy. A proper definition of different metrics along with a deeper understanding of the techniques used would not only reduce the ambiguity of derived values, but would also allow for the development of more sophisticated metrics to estimate additional canopy parameters such as canopy density.

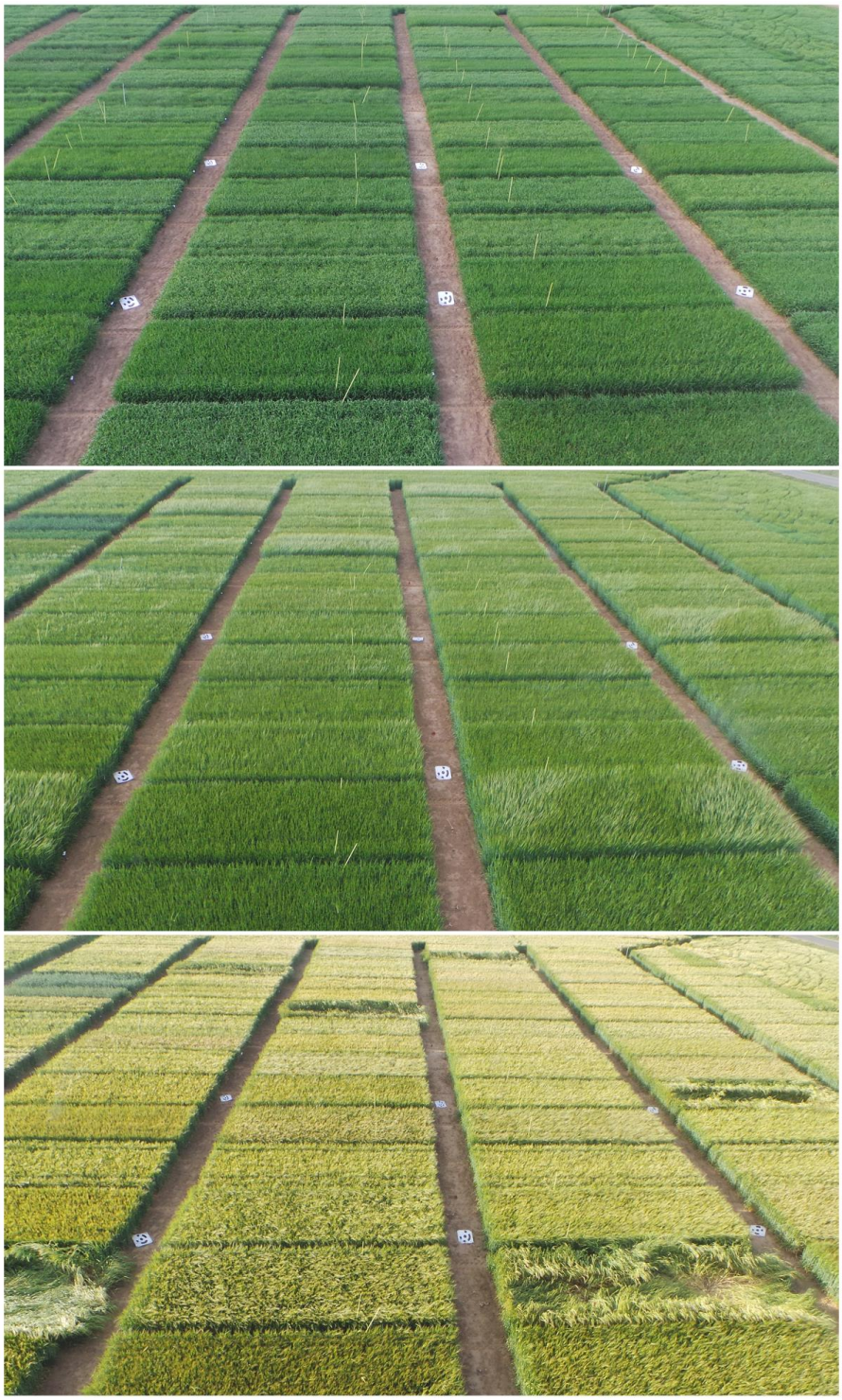

Figure 9.8 Oblique images (facing north) of the CROP.SENSe.net experiment at booting (top), heading (center) and development of fruit stage (bottom). Images are captured from a crop monitoring station (for details please refer to Brocks et al., in review).

9.2.4 Destructive measurements

Although this thesis is written in the context of precision agriculture, the CROP.SENSe.net field experiment was designed as a field-phenotyping experiment. The purpose of plant phenotyping is to produce a description of the plant's anatomical, ontological, physiological and biochemical properties (Guo and Zhu, 2014). Thus, from a technical point of view sensing methods for plant phenotyping and precision agriculture try to measure similar things. Traditionally, plot experiments are used to detect differences between different cultivars or treatments (Kling et al., 2004). Thus, sampling is carried out to determine differences among the plots. Since destructive measurements are both labor-intensive and expensive, only a few measurements are taken to characterize a plot. Such sampling is based on the assumption that the plants within a plot grow homogeneously. In case of the CROP.SENSe.net experiment, a 0.2 m by 0.2 m square of biomass was harvested at a random position within the destructive measurement part of a plot (c.f. Figure 2.10). Chlorophyll was measured from the top leaves of three plants and then averaged. These measurements were compared with spatially resolved spectral and PH data. Thus, data on different scales (leaf and canopy) and of different types (discrete manual and quasi continuous remote sensing measurements) were compared. To facilitate this comparison, the spatial dimension of the remote sensing data was reduced to one value per plot by means of the average (Aasen and Bolten, in review, Chapter 4; Bendig et al., 2015, Chapter 7; Tilly et al., 2015, Chapter 6). Figure 6.3 and Figure 4.9 show maps of the PH (from which the biomass was estimated) and the red edge inflection point (REIP; from which chlorophyll was estimated), respectively. These maps illustrate the heterogeneity within the plots and highlight the challenge of comparing an average value derived from spatially resolved remote sensing data with a destructive measurement at just one spot within the plot. While the latter might not represent the plot, the former is prone to the influences of the measurement techniques (c.f. Section 9.1 and Subsection 9.2.3). The issue of in-plot heterogeneity could (partly) be addressed by georeferencing the positions of the destructive measurements and establishing models based on only these points. On the other hand, if this position is affected by, for instance, vermin or small-scale soil variability and therefore does not represent the typical observable characteristics or physiological properties (phenotype) of a certain genotype under a specific treatment, the comparability of the results over time or with other trials might not be guaranteed based on the destructive sample. But georeferenced samples would decrease the uncertainty of remote sensing-based prediction models. These models could then be used to provide spatially resolved estimates for a certain parameter. To get estimates for a certain variety within a plot or an area within a field, zonal statistics (descriptive statistics to describe the pixel values within a certain area) could be calculated based on these pixel-wise estimates. This would lead to an increased sample size, since each could be regarded as a sample. Additionally, descriptive statistics such as the variance could be used to reflect parameters such as the growth heterogeneity. Finally, the

parameters derived from the remote sensing data could then be used to compare the different plant varieties.

For spectral measurements, additional considerations with regards to their comparability are needed. The apparent spectral reflectance is affected by many different factors as previously discussed (c.f. Section 9.1). Additionally, retrieval algorithms to estimate plant properties such as VIs may have been developed for a different scale (e.g. leaf scale) or sensor configuration than those to which they are applied (Aasen and Bolten, in review, Chapter 4). Besides, although the high spatial resolution of the data increases the apparent heterogeneity of the canopy it is still to coarse to comprehend individual plant organs and thus the interaction if the vegetation structure with the illumination. Due to these uncertainties, comparing this data to destructive ground validation measurements is difficult. The next generation of HSC systems with significantly increased spatial resolution have already been introduced to the market (e.g. UHD 258-Butterfly: Cubert GmbH, 2015). These may allow the segmentation of different parts of the canopy. Additionally, data products that incorporate 3D and spectral data, such as HS DSMs, may help to increase the traceability of the signal within the canopy and therefore increase the comparability between different types of measurements and should therefore be further investigated.

9.2.5 Conclusions on the comparability of hyperspectral digital surface models

Motivated by the diversification in remote sensing, this chapter discussed the comparability of the spectra and 3D data contained in HS DSMs derived with HSCs with data and data products from other devices and to destructive in-field measurements. In the following, the major issues are concluded and then summarized in Table 9.2 at the end of the section.

Three main aspects compromise the comparability of the spectral data. Different sensors produce different reflectance quantities (HDRF vs HCRF). These cannot be compared per se, since they are subject to different influences from differing angular properties, and subsequently angular effects, and may represent the objects within a scene differently (e.g. different soil - vegetation composition). Different measurement approaches (such as pushbroom and snapshot) also result in comparability issues. Since HS DSMs are composed by a multitude of images, the resulting data product is more complex to interpret. Furthermore, due to the two-dimensionality of the images, angular effects also appear in two dimensions in the resulting scene. At the same time, the processing workflow for HSCs is not as advanced as that of established pushbroom sensing systems. Sophisticated processing modules that could lead to a high degree of standardization within data products of HSCs are not yet available. The comparability of the color data within RGB DSMs, generated from uncalibrated consumer-grade RGB cameras, to HS DSMs is also questionable from a theoretical point of view. Therefore, the limitations of these approaches' comparability and reproducibility must be considered.

Several of the comparability issues for spectral data have a close relation to the influences discussed in Section 9.1. Specifically, influences related to measurement geometry play a significant role and underscore the need for research to better understand and handle these factors.

Four aspects compromise the comparability of the 3D data. These can be divided into issues related to the SfM workflow and its different implementations, differences between the sensing techniques LiDAR and SfM, and considerations on how a point cloud is transformed into canopy height. The major problem with SfM is its reliance on the features within the images and therefore on the objects which are to be measured. Although the objects stay constant, their representation as image features may vary due to changing illumination or camera specifications. Additionally, different implementations of SfM may result in different representations of the surface. Since the algorithms are complex and some software packages are 'black-boxes', these differences are hard to comprehend. As a result, comprehensive metadata about the software version and the chosen parameters should be stated in every study which uses SfM. Furthermore, data derived by different sensing techniques and different post-processing procedures has to be compared with care. Different measurement geometries and differences in the interaction with the canopy structure influence the visibility of features of a canopy and thus, its representation in the data product. Additionally, the workflow used to transform the point cloud into a DSM may strongly influence the derived canopy height. Further studies that investigate these differences and establish workflows which are appropriate for a desired parameter, such as canopy height, are needed. Together, with appropriate definitions of structural canopy properties and metadata that increase the transparency of a data product, the comparability of DSMs would be improved. Additionally, metrics for other structural parameters then canopy height should be developed which explore more of the potential information within the point clouds.

One of the major comparability issues is the correlation of the spatially resolved remote sensing data with destructive measurements at plot level. The sampling scheme of the destructive plant parameters was intended to investigate for differences between varieties and treatments. However, the remote sensing data revealed strong heterogeneities within the plots. This compromised the comparability of the data, since the position of the destructive sampling was not tracked. Ground observations should therefore be georeferenced in future studies, and match the sampling of a sensing system to reduce the uncertainty in the plant parameter estimation. Additionally, zonal statistics could improve the interpretability of the results and increase the benefits provided by remote sensing methods for agricultural applications.

Table 9.2 Summary of the issues related to the comparability of the data contained in HS DSMs to data from other sensing systems and destructive in-field measurements.

Comparability issue	Resulting limitation	Main reference
Spectral		
Measurement geometry and reflectance quantities	• Different angular properties in the data product • Differing representation of objects within the data	(Aasen and Bolten, in review, Chapter 4)
Data collection and processing workflows	• HSC data is more complex and affected by angular effects in 2D • HSC data processing modules are not yet able to generate standardized data	(Aasen and Bolten, in review, Chapter 4) Subsection 9.2.1
Calibration of the RGB data	• Uncalibrated data (e.g. in RGB DSMs) are not quantitatively comparable	Subsection 9.2.1
3D		
SfM approaches	• Different SfM tools derive different results • Differences are hard to comprehend since they may change with the software version and some software packages are a 'black-box'	Grenzdörffer (2014), Remondino et al. (2014)
Flight pattern and condition, sensor specification	• Flight pattern, image overlap, GCP position and image contrast might change between campaigns and influence the reconstruction • Image resolution and FOV influence the reconstruction	Aasen and Bolten (in review, Chapter 4), Subsection 9.2.2, Dandois et al. (2015)
Different sensing techniques	• In contrast to LiDAR, SfM is barely able to penetrate vegetation • Oblique TLS is more affected by obscuration than UAV SfM	Dandois et al. (2015) Subsection 9.2.2
Canopy height derivation	• Point cloud quality and processing algorithms influence the derived height • Derivation depends on the canopy structure	Subsection 9.2.3
Destructive measurements		
Data types	• Spatially resolved remote sensing data is compared to discrete values for each plot • Spectral retrieval algorithms may have been developed for different levels	Subsection 9.2.4, Aasen and Bolten (in review, Chapter 4)

9.3 Potentials of hyperspectral digital surface models acquired with UAV snapshot cameras

In the following, the potential of HS DSMs acquired with UAV snapshot cameras in support of site-specific crop management are discussed. During the discussion of the comparability of the data acquired with the different sensing systems, considerable differences were found (Section9.2). Thus, the first subsection within this research objective addresses the generality and transferability of the results of Chapter 6 to 8 to HS DSMs generated from HSCs.

9.3.1 For crop parameter estimation

In Tilly et al. (2015, Chapter 6) and Bendig et al. (2015, Chapter 7) VIs and RGB data were combined with PH to estimate biomass. The theoretical consideration to combine both types of information was that biomass would be a function of canopy volume (area x PH) and its density. It was assumed that the spectral response of the canopy could provide information about the density due its connection with e.g. the LAI (Broge and Leblanc, 2001; Haboudane et al., 2004). Both studies found PH to be the best predictor for dry biomass and to provide very good results for fresh biomass. A combination of PH and any VI or RGB information could barely increase the prediction. This might be explained by the known saturation of many VISNIR VIs at a certain LAI (for an in-depth discussion on the VIs please refer to Subsection 6.4.2). Although LAI was explicitly not considered, Tilly et al. (2015, Chapter 6) found that the VISNIR VIs saturated at approximately 150 g/m² dry biomass (Figure 6.5). This value was exceeded between the campaigns of DAS 49 and 64 in 2013 and DAS 41 and 56 in 2014. Similar observations could be made for the RGB indices GRVI and RGBVI, which saturated after DAS 39 (Figure 7.3). Overall, the two studies comprised data from DAS 25 to 89 (Bendig et al., 2015, Chapter 7) and DAS 34 to 97 (Tilly et al., 2015, Chapter 6), which greatly exceeded the unsaturated range of the RGB and VISNIR VIs. This limited the ability of the VIs to provide additional information. Future studies should investigate earlier growth stages where the VIs are still unsaturated. Additionally, most of the biomass gain after the tillering stage (DAS 49 and 54 in 2013 and 2014, respectively) happened in the stem (Figure 9.9). This also explains the very good performance of the PH, which can be assumed to be associated with stem growth. Beyond the two studies in this thesis, not many studies exist which investigate the potential of spectral and 3D information for crop monitoring. In alignment with the results of this thesis, Thenkabail and Marshall (2015) found that a combination of spectral and PH information could improve the prediction of fresh biomass for a variety of crops, while PH was the most important predictor. Aside from crops, a study by Schaefer et al. (2016) indicated that a combination of LiDAR and NDVI information was beneficial for pastures biomass estimation. In forest applications, the fusion of LiDAR and spectral information is already widely used e.g. for the classification of tree species

(Dalponte et al., 2012). As recently shown by Bareth et al. (2015b), similar approaches (with RGB data) can also be used to classify different plant communities, resulting from different nutrient availability, in grasslands. Such approaches should be further explored. Overall it can be concluded that biomass of cereals across several growing stages can be well predicted due to the good relationships with PH (Bendig, 2015; Ehlert et al., 2008; Tilly, 2015). Nevertheless, for precision agriculture applications estimations at a specific date are also needed. However, a model which is calibrated for a longer phase of the growing period might have variable success in predicting the biomass at a certain stage (Tilly, 2016).

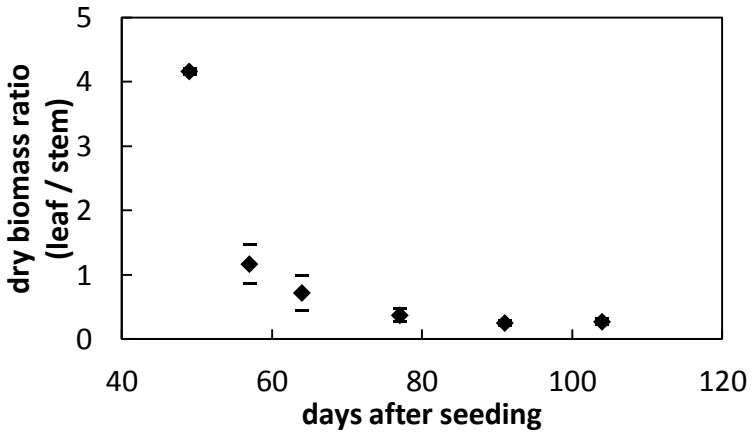

Figure 9.9 Ratio of the leaf and stem dry biomass of barley at different days after seeding (DAS) with standard deviation. Generated from data of the CROP.SENSe.net experiment in 2013. No stem was developed for dates prior to DAS 49.

To investigate the potential of the HS DSMs acquired with the UHD, PH was correlated with biomass for all available dates. Additionally, HyperCor was used to investigate an optimized combination of spectral bands and PH for the same reason. The optimization was based on the NDVI formula (c.f. Eq. 8.3). Table 9.3 shows the result. Only for DAS 70, PH was part of the optimized combination. At all dates besides of DAS 70, a combination of two spectral bands related best to fresh and dry biomass. Still, only low coefficients of determination ($R^2 < 0.5$) were found. In comparison, other studies with similar approaches found better results (Aasen et al., 2014, Chapter 8; Gnyp et al., 2014b; Marshall and Thenkabail, 2015). A major reason might be the sampling scheme of the biomass. As discussed in Subsection 9.2.4, the remote sensing observations suggested a high in-plot variability, which could not be captured by the destructive measurements. While such differences might be lost in the overall trend within a season, they considerably affect the results for single dates, due to the smaller range of biomass values. Additionally, different varieties have a different growth and a different structure (Munzert and Frahm, 2005). Biomass estimation with PH is based on an empirical relationship with the growing pattern of the plants. However, if the biomass accumulation pattern within a dataset differs because of the differences in growth of the varieties (e.g. different leaf count), this correlation is

weakened. Further studies need to investigate the transferability of models between different varieties. Besides, also the lack of the UHD to provide usable bands above 900 nm may have lowered the results since several studies found the NIR and SWIR domain to be important for the biomass estimation (Gnyp et al., 2014a; Koppe et al., 2010; Marshall and Thenkabail, 2015; Thenkabail et al., 2013; Tilly et al., 2015, Chapter 6). Finally, it is likely that the analysis approaches applied in this thesis are not optimally suited to combine spectral and PH data. A major issue is the different scaling and magnitude of the variables. While the reflection (0 to 100% reflection) and VIs (e.g. NDVI [-1,1], c.f. Aasen et al., 2014, Chapter 8, Eq. 8.3) have a normalized range, plant height has not. Additionally, the biomass gain throughout the growing season is neither linearly related with the plant height nor the spectral information (Tilly et al., 2015, Chapter 6). Thus, it is likely that simple linear and exponential regression models cannot fully exploit the potential of a combination of PH and spectral data. Thus in future, non-linear regression models potentially based on machine learning techniques should be applied to combine spectral and spatial information. Techniques such as random forest regression (Breiman, 2001) have a great potential for this purpose, since they can deal with the redundancy of hyperspectral bands, handle non-linear relations and variables of different types (Feilhauer et al., 2015; Shi and Horvath, 2006).

Table 9.3 Coefficient of determination (R^2) of the plant height (PH) and the optimized combination of spectral and PH data for the estimation of fresh and dry biomass at different days after seeding (DAS).

DAS		56	70	84	96
fresh biomass	PH	0.19	0.33**	0.01	0.05
	spectral and PH data	0.45	0.29	0.36	0.24
dry biomass	PH	0.23	0.43**	0.09	0.00
	spectral and PH data	0.42	0.23*	0.26	0.16

** For the dry biomass at DAS 70, the algorithm included PH into the best combination*
*** For DAS 70 only plots of the 70b case were regarded for the PH due to issues with the digital surface model (c.f. Aasen and Bolten, in review, Chapter 4)*

In Aasen and Bolten (in review, Chapter 4) chlorophyll was retrieved from HS DSMs based on published VIs. Although the results were variable for different dates, they were in the magnitude of results of other publications. The variable performance might be explained by variations in canopy structure (c.f. Figure 9.8) and the resulting angular effects (Subsection 9.1.1). Yu et al. (2014) supports these considerations and found that the optimal bands to estimate chlorophyll varies with the growth stage. Other studies report similar observations for other plant parameters (Aasen et al., 2014, Chapter 8; Gnyp et al., 2014b; Li et al., 2010). Besides, the applied VIs were developed for devices with a FOV different to the UHDs IFOVs (c.f. Subsection 4.3.2). Additionally, also the bandwidth configuration can influence the results of plant parameter retrieval (Hansen and Schjoerring, 2003; Li et al., 2014; Thenkabail et al., 2013, 2000). To validate if the growth stage and band configuration had an influence on the retrieval, HyperCor was used to derive optimized VIs based on the data acquired by the UHD.

To compare the results to the published VIs, the same date combinations as in Aasen and Bolten (in review, Chapter 4) were evaluated. With the growth stage and sensor specific band combinations the results could be considerably improved in comparison to the results achieved with the standard VIs (Table 9.4). Investigation of the correlation matrices revealed that the optimal bands differed from the wavelength of the VIs used in Aasen and Bolten (in review, Chapter 4). The upper triangular part of Figure 9.10 exemplary shows the correlations of chlorophyll with all band combinations for DAS 70. The best R^2 are found with combinations of bands around 500 nm and 600 nm. Similar observations can be found for all dates except DAS 56.

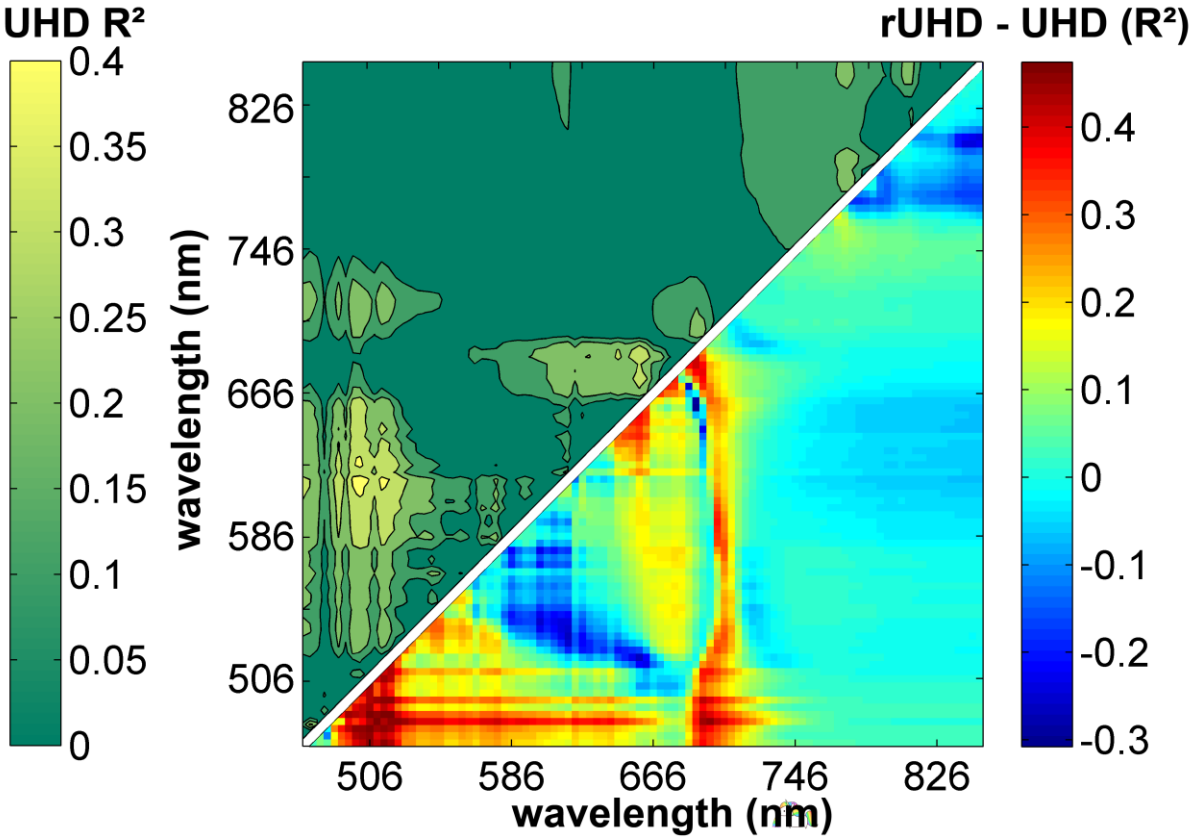

Figure 9.10 The upper triangular matrix shows the coefficient of determination (R^2) of all UHD band combinations with chlorophyll for DAS 70. The lower triangular matrix shows the difference of the result with spectral information of FS3 resampled to the UHD bands (rUHD) and the UHD data (rUHD - UHD).

In Subsection 4.2.1 the comparability with regard to different data products (HDRF vs HCRF) was discussed. To estimate this effect on the retrieval of the best bands, HyperCor was also used with data from the FS3 resampled to the UHDs band configuration (rUHD). The results can also be seen in Table 9.4. The comparison reveals that the correlations achieved with the UHD (HCRF) and rUHD (HDRF) data are similar. However, in every case the optimal band combination considerably differs. A further investigation based on the correlation matrices shows that not only individual band combinations differ but different patterns are obtained in large parts of the spectrum. The lower triangular part of Figure 9.10 exemplary shows this for DAS 70.

Table 9.4 Coefficients of determination (R^2) of different vegetation indices (VIs) with chlorophyll at different days after seeding (DAS) and for the same combinations of datasets as in Aasen and Bolten (in review, Chapter 4). UHD denotes the results of an optimized combination of UHD bands (denoted with its center wavelength in nm), rUHD for FS3 data resampled to UHD bands, VI for the best performing published VIs used in Aasen and Bolten (in review, Chapter 4, Table 4.2) and VIS for the spectral data resampled to the RGB bands in WorldView-3 configuration.

	UHD	rUHD	VI	VIS	UHD	rUHD	VI	VIS	UHD	rUHD	VI	VIS
DAS			**56**				**70**				**84**	
band 1	594	494	PRI550	B	614	462	REIP	B	706	502	MCARI /OSAVI	B
band 2	470	482		R	474	450		G	490	490		G
R^2	0.48	0.52	0.30	0.25	0.44	0.50	0.13	0.45	0.72	0.64	0.50	0.53
DAS			**96**				**70-96**				**84-96**	
band 1	694	498	REIP	B	586	774	REIP	B	602	702	REIP	B
band 2	478	482		R	486	746		G	490	474		G
R^2	0.61	0.60	0.60	0.36	0.6	0.51	0.55	0.41	0.66	0.69	0.64	0.64

Additionally, the examination of the correlation matrices also revealed promising band combinations for the retrieval of chlorophyll in the visible range of the spectrum. This region is covered by RGB cameras. Subsection 9.2.1 discussed the differences between spectral and RGB data and remarked issues due to uncertainties resulting from the missing reference to physically traceable units. Also in Bendig et al. (2015, Chapter 7) it was concluded that this might be a major source of uncertainty and Rasmussen et al. (2016) confirmed these considerations with regard to illumination conditions. However, some RGB cameras can record RAW data, which allows to radiometrically calibrate these cameras. Encouraged by the correlation matrices, the spectral information was resampled to the RGB bands of WorldView-3 (DigitalGlobe, 2016) and HyperCor generated optimized VIS VIs based on these three bands. As shown in Table 9.4, in many cases these VIS VIs correlated well ($R^2 > 0.5$) with chlorophyll. In particular for DAS 70, 84, and the combined dataset of DAS 84 and 96 these VIS VIs showed similar results as the hyperspectral data. These results have a high significance for practical applications. While several studies have shown the potentials of uncalibrated RGB data in combination with PH to estimate yield and biomass information (Bareth et al., 2015b; Bendig et al., 2015; Dandois and Ellis, 2013; Geipel et al., 2014) these results disclose the potential of calibrated VIS VIs for the estimation of chlorophyll. Since RGB cameras are considerably cheaper than hyperspectral sensors the potential of these systems should be further investigated. Still, it has to be noted that the results retrieved with the UHD data in this chapter are not cross-validated and thus, need to be handled with care. Overall, the discussion underlines the need to investigate sensor and growth stage specific retrieval approaches for spectral data. Besides of experimental studies, like in this thesis, this could also be addressed with modelling approaches. 3D canopy models, such as HySimCaR (Küster et al., 2014), can generate spectral data of virtual canopies for different growth stages. Such data could be

combined with End-to-End simulators (e.g. Vicent et al., 2016) to also comprehend how a sensing system and the subsequent image processing influences the results. Such an approach could help to understand the influence of sensing systems and different growth stages on the retrieved plant parameters.

Also PH can be derived with HSCs. While the difference between different sensing techniques have been discussed in Subsection 9.2.2, it can be concluded that PH can be derived quite reliably for individual dates and across different growth stages (Aasen and Bolten, in review, Chapter 4; Bendig et al., 2015, Chapter 7; Tilly et al., 2015, Chapter 6). Still, a DTM is necessary to calculate the PH as the difference between the DTM and the DSM. In most cases this DTM was generated with data acquired from the bare soil surface before the growing period. But sometimes, this might not be possible due to undersown crops or weeds, or because the sensing system is not available. The latter was the case in Aasen and Bolten (in review, Chapter 4). Problems with the sensor at the beginning of the growing season prevented the generation of a DTM. Thus similar to Geipel et al. (2014), patches of bare soil between the vegetated areas were used to interpolate a surface. However, this approach is rather not generic, since generally it cannot be assumed that patches of bare soil exist and the terrain is flat. Additionally, the soil might settle during the growing period. In airborne laser scanning it is common to generate a DTM based on the lowest points within a certain area (e.g. Wallace et al., 2012). For SfM such an approach might be compromised because of the reduced canopy penetration of the method (c.f. Subsection 9.2.2). Dandois and Ellis (2013) found that in case of forests SfM showed a large deviation from LiDAR DTMs under foliated trees. It is likely that similar problems occur in cereals due to the density of the canopy. Nevertheless, this should be investigated in future. Generally, future approaches should aim at exploiting the full potential of the 3D point cloud.

9.3.2 For site-specific crop management

Section 1.1 outlined the demand for timely information (revisit time of 5 – 10 days) in very-high spatial (~ 0.25 m and 0.01 m for the spectral and 3D data, respectively) and spectral resolution (< 10 nm) to support site-specific crop management. From its technical specifications the UHD is capable of acquiring information with the necessary spectral resolution (4 nm). Nevertheless, it has to be noted that this only specifics the spectral sampling of the camera. The FWHM is considerably higher (Figure 3.2). Additionally, results from one sensors might not be transferable to other sensors, even if the data is properly resampled (c.f. Subsection 9.3.1). Also, the impact of angular effects should be kept in mind for the application of spectral imaging sensors (c.f. Subsection 9.1.1). Thus, the retrieval of every parameter should be evaluated in a configuration that is matching a prospected application as close as possible. The spatial resolution within the HS DSMs complies with the precision of current agricultural machinery (< 0.25 m). However, it has to be noted that the flying altitude and the flying speed might

have to be increased to cover larger areas in real applications due to the limited flight time. But since the spatial resolution is linearly related to the flying altitude, this will come with a decreased resolution and it should be evaluated if it is still sufficient for a prospected application. The revisit time of UAV-based sensing systems is in theory limitless. Nevertheless, the spectral data acquisition is still limited by varying illumination conditions (c.f. Subsection 9.1.2). As long as this issue is not solved, spectral remote sensing with UAVs lose a large part of its advance to satellite systems. Still, PH information can be acquired quite independent from the illumination conditions (c.f. Subsection 9.2.3). Thus, the potential of the presented approach to meet the required revisit time depends on the parameter which needs to be acquired.

If farmers are asked about their reasons for applying new technologies, their answers mostly relate to an increase in yield and financial benefits (Stafford, 2007; and personal correspondence to farmers during the CROP.SENSe.net project). While yield is related to minimizing crop failures, e.g. due to pests, and optimized nutrient and water supply (Munzert and Frahm, 2005), the financial benefit is related to maximizing the yield and minimizing the input. Biotic stresses by plant diseases can be detected by changes in reflectance as early as four days after inoculation (Wahabzada et al., 2015) and can be uncovered by chlorophyll related VIs (Yu et al., 2013). Similar, chlorophyll related indices can also point out abiotic stresses such as water stress (Zarco-Tejada et al., 2012). The decent correlations ($R^2 > 0.48$) for the retrieval of chlorophyll with the UHD data at DAS 56, 84 and 96 (c.f. Table 9.4) suggest a potential for precision agriculture applications. Additionally, Mahlein et al. (2013) found that the most relevant wavelengths to detect diseased leafs were in the range of 450 to 950 nm, which is mostly covered by the UHD. Still, further studies are needed to evaluate the potentials for stress detection in in-field applications. Also PH can be an indicator for water stress (Samarah et al., 2009). Good correlations ($R^2 > 0.7$) were found for the UHD data for most growth stages and across different growth stages (Table 4.3). Due to the high reliability of remotely sensed PH, its potential for stress detection or fertilization should be further investigated. Since (in spring barley) fertilizer is commonly applied after seeding and at tillering stage, and plant protection and weed management is mostly carried out before stem elongation is completed (Figure 2.7), such studies should focus on the early growth stages including stem elongation. For these early growth stages also an advance can be expected in combination with spectral data, since PH increases majorly after tillering. To estimate yield, biomass can be used (Boukerrou and Rasmusson, 1990). Grain yield can be well estimated with dry green biomass until BBCH 75, while the best results are found at BBCH 25 and 39 (Kren et al., 2014). In this thesis, the biomass estimation in individual dates did not achieve satisfactory results. Nevertheless, the multi-date models predicted biomass very well (Tilly et al., 2015, Chapter 6, Table 6.6). Such approaches could be used to estimate the yield prior to harvest. Table 9.5 summarizes the results for

the retrieval of plant parameters (Subsection 9.3.1) and names potential applications in precision agriculture as outlined above.

Table 9.5 Quality of the retrieval (o: 0.48 < R^2 < 0.7) of different plant parameters from HS DSMs acquired with the UHD and potential applications in precision agriculture.

	Time frame		
Parameter	**Single date**	**Growing season**	**Reference**
Plant height	+	+	Aasen and Bolten (in review, Chapter 4)
Chlorophyll	o	o	Subsection 3.3.1
Biomass	-	+	Subsection 3.3.1, Bendig et al. (2015, Chapter 7) and Tilly et al. (2015, Chapter 6)
Potential application	Stress detection, fertilization	Yield estimation	

Already today, several optical sensing systems are commercially available to acquire information about the vegetation as the tractor drives along the field. Mostly, they are based on a few spectral bands and come with a calibration file for specific parameters and specific crops. The information gathered by these sensors can directly be used to control the output of crop treatments or stored for a later use (Whelan and Taylor, 2013). Compared to such solutions, UAV-based approaches have the potential to gather information prior to a startup of the machinery. Thus, a field only needs to be entered when necessary (e.g. after a stress is detected) and thus, soil compression is prevented and emissions and operating costs are reduced. Compared to satellite systems, UAV-based systems can overcome limitations due to cloud cover to a certain degree and eliminate issues of limited scene availability due to e.g. competing bookings. On the other hand, harsh winds and rain may prevent UAVs from flying (Eisenbeiß, 2009). Besides, stationary (Brocks et al., in review; Crommelinck and Höfle, 2016) and multi-stationary approaches (Tilly, 2015) are in current development or have been applied for precision agriculture applications. While both approaches can provide spatial information in very-high spatial and temporal resolution, they suffer from a limited flexibility. While mobile approaches, such as mobile laser scanning, can mitigate this disadvantage to a certain degree (Tilly, 2015), these platforms still might need to enter the agricultural area due to their operational range. Since UAVs are flying platforms, they overcome this issue and can cover large areas without disturbing the surface. Still, although the use of UAVs makes the presented approach quite flexible, it also brings disadvantages. Different countries have different and sometimes ambiguous legislations (Colomina and Molina, 2014). For example prohibits German legislation flights above 100 m and limits the flight radius to the line-of-sight of a pilot. Additionally, flight times of multi-rotor UAVs are still limited (< 25 min with the sensing system used in this thesis). Thus, remote sensing with UAVs always face the challenge of maximizing the coverage while retaining a suitable spatial resolution. In particular, this applies for spectral sensing

systems since spectral and spatial resolution competes during the design of a sensor (Aasen et al., 2015, Chapter 3). Still, in 2015 the sensing system used in this thesis was upgraded to permit a higher frame rate which allows the system to fly at 10 m/s, while still meeting the required image overlap. Thus a flight at 100 m above ground altitude could acquire the data to generate an HS DSM of approximately 20 ha with a spatial resolution of the spectral data of 0.7 m. With an average operated agricultural area per farm of 56 ha in Germany in 2010 (Statistische Ämter des Bundes und der Länder, 2011), an entire farm could be covered within about three flights. This relation changes, when farms approach the sizes of 175.6 ha, the average for the United States of America in 2012 (NASS, 2014). To cope with such farm sizes, satellite and UAV data could be combined as suggested by Gevaert et al. (2015). Besides, although an UAV was used to carry the HSC in this thesis, the method of generating HS DSMs is independent from the platform. Thus, it could also be applied to data captured from other carrier platforms such as small aircrafts.

Still, the biggest advantage of the approach presented in this thesis is that an HS DSM contains spectral and 3D information. As seen in Table 9.5, both types of information can complement each other for different applications. Besides of the method introduced in this thesis, almost no other remote sensing system is able to derive spectral and 3D spatial information at the same time with the same sensor. Although first attempts have been undertaken to exploit the radiometric information of LiDAR systems (Höfle, 2014; Junttila et al., 2015), these systems only acquire spectral information within a few bands and are not yet feasible to be frequently applied. As shown in Aasen and Bolten (in review, Chapter 4), HS DSMs can be used for the frequent multi-temporal acquisition of information of crops. Nevertheless, in the end it is likely that the profitability of a system decides if it is applied by a farmer. The sensing system used in this thesis cost around 60,000 €, while the UHD alone cost about 50,000 €. Such a system has to compete with spectral sensors such as the N-Sensor ALS (YARA, 2016), which cost about 39,700 € (dlz agrarmagazin, 2012) and high-resolution multispectral images e.g. from WordView-3 (DigitalGlobe, 2016), which cost around 3,100 € for 100 km² (e-geos, 2016). Besides, RGB cameras, which allow to derive PH with SfM cost a couple of 100 € and systems as the Phantom 4 even come as a package of UAV and RGB camera for about 1,500 € (DJI, 2016). While a calculation on the profitability of the different systems will be left for business economists, it is apparent that an HSC system such as the UHD is quite pricy. Additionally, this thesis also demonstrated that the data retrieval from HSCs is a quite complex process and data processing procedures are still of limited maturity (Subsection 9.1.3). Thus, on one hand it can be concluded that HS DSMs acquired with UAV snapshot cameras have a great potential to support site-specific crop management due to the combination of spectral and 3D information, the high resolution of the data and the potentially high revisit time. On the other hand, due to the complexity and costs it has to be concluded that camera systems such as the UHD are not yet suited for an application in precision agriculture. Nevertheless, recently more and

more low-cost systems have appeared on the market that are easy to use and acquire multispectral (e.g. SEQUOIA camera: Parrot SA, 2016) or even thermal data (FLIR XT camera: FLIR Systems Inc., 2016). This development will continue and the industry will be able to build sensing systems tailored for specific applications. HSC can support this development.

9.3.3 Prospects for hyperspectral snapshot cameras

This thesis demonstrated that the optimal variables (spectral band or PH) to predict a parameter may vary with growth stage and sensing system (Aasen et al., 2014, Chapter 8; Aasen and Bolten, in review, Chapter 4; Subsection 9.3.1). On the other hand, already some variables might be sufficient for an accurate prediction of a plant parameter (Thenkabail et al., 2004). The challenge, however, is to select suitable variables for a particular application at a particular time. As long as the entire path from particle to pixel cannot be simulated by a model, potential applications have to be validated with real sensing systems. HSCs provide a promising tool for this. Their data allows to identify the optimal hyperspectral information for a certain application. Moreover, since HSCs record HDRF like reflection quantities, results are also suited to be transferred to other imaging spectroscopy sensors such as satellites and support current and future satellite missions, e.g. by delivering data for calibration and validation activities. Last but not least, due to the simultaneous acquisition of spectral and 3D data, interactions of vegetation structure, illumination and the spectral signal can be investigated. This interaction has already caused misinterpretation of spectral data in the past (Knyazikhin et al., 2013; Morton et al., 2014) and should certainly be avoided in applications that can significantly threaten the environment, such as inappropriate use of fertilizer and pesticides (Skinner et al., 1997; van der Werf, 1996). HSCs offer a unique tool to further understand such effects and address one major source of uncertainty, and probably also information, in spectral remote sensing, namely angular effects (Subsection 9.1.4). Additionally, with the second generation of HSCs such as the newly announced UHD 258 – Butterfly X2 (Cubert GmbH, 2015), spectral data can be acquired with an 800 times higher spatial resolution compared to the camera used in this thesis. With these sensors hyperspectral point clouds can be generated that are suited for entirely new approaches in remote sensing. Overall, HSCs such as the UHD are likely to stay a tool for research due to their complexity and high costs. However, the outcome of studies like this thesis can identify challenges and potentials for a particular application and help to develop new, potentially more robust ways to exploit the data, for example for precision agricultural applications.

10. CONCLUSION

In this thesis, hyperspectral digital surface models (HS DSMs) acquired with UAV snapshot cameras were introduced and evaluated with regard to the quality of the contained spectral and spatial information. This also included an assessment of the comparability of the HS DSMs to data products from other sensing systems. Additionally, the potential of HS DSMs acquired with the hyperspectral snapshot camera (HSC*) UHD-185 Firefly* to support a site-specific crop management was discussed.

In many respects, HS DSMs have great potential. UAVs in combination with snapshot cameras allow to capture data in high spatial, spectral and temporal resolution. The spatial resolution allows estimation of canopy properties in more detail than with other spectral sensing systems. For site-specific crop management this enables the detection of small-scale heterogeneities. At the same time, data can be acquired with short revisit times due to the flexibility of UAVs. This is important as it enables rapid response to highly dynamic phenomena such as plant diseases. Additionally, with the spectral and 3D spatial information contained in HS DSMs, plant parameters such as chlorophyll, biomass and plant height, which relate to important crop traits, can be estimated within individual and across different growing stages.

However, the complexity of the remote sensing of vegetation is also apparent when working with HSCs. The spectral data captured by HSCs is influenced by angular effects. Currently, the different measurement geometries of the pixel within the HS DSMs cannot be compensated for and thus, the surface anisotropy affects the data. While this is not an error *per se*, it complicates the data interpretation. Additionally, HSCs measure hemispherical-directional reflectance factors while non-imaging devices such as field-spectrometers measure hemispherical-conical reflectance factors. The results of this thesis suggest that different measurement geometries and reflectance quantities influence the retrieval of plant parameters and a comparability of data derived with different devices might be hindered. Still, the method developed in this thesis to trace the properties of the individual pixel from an image into the HS DSM provides the necessary basis to approach these effects. Additionally, methods to reliably adapt for varying irradiance conditions are needed to utilize the benefit of UAVs to fly below clouds. Besides, several aspects influence the generation of the 3D data. Parameters such as image overlap and camera configuration have an impact on the 3D reconstruction with *Structure from Motion*. Additionally, different sensing techniques are able to ‘see’ different parts of the canopy. Together with the lack of proper definitions for parameters such as canopy height, the comparability of DSMs derived under different conditions or with different sensing systems is limited. Coupled with the diversification of sensing systems and processing workflows, efforts towards an increased comparability of different methods and standardized metrics are urgently needed.

Besides these challenges, new approaches could be facilitated using the data within the HS DSMs. The high resolution allows combination of the spectral and 3D spatial information of many pixels to characterize an area. This potentially allows to derive information about the variability of an area in addition to average values. Additionally, the exploration of the potential to combine spectral and 3D information is still in its infancy. Beyond new ways to estimate plant parameters such as biomass, the combination of spectral information with information about the vegetation structure could help comprehend and corrected for effects introduced by different measurement geometries. At the same time, HS DSMs are generated from overlapping images. Consequently, multi-angular measurements of the surface are commonly captured with every acquisition and also this information could be exploited to derive additional information about the canopy.

Overall, the insights of this thesis provide the foundation for further exploration of the spectral and 3D information within HS DSMs acquired by UAV snapshot cameras; although several challenges must be addressed as outlined above. Despite this, the new and exciting technologies within the diversification of remote sensing have the potential to revolutionize the way data about the environment is acquired and thus, support decisions on how resources are used. However, in the end humans will define how these decisions are made.

11. REFERENCES

Aasen, H., 2016. Influence of the viewing geometry on hyperspectral data retrieved from UAV snapshot cameras, in: ISPRS Annals of the Photogrammetry, Remote Sensing and Spatial Information Sciences. Presented at the XXIII congress of the International Society for Photogrammetry and Remote Sensing, Prague, Czech Republic.

Aasen, H., Bolten, A., in review. Multi-temporal monitoring of agricultural crops with high-resolution 3D hyperspectral digital surface models in comparison with ground observations.

Aasen, H., Burkart, A., Bolten, A., Bareth, G., 2015. Generating 3D hyperspectral information with lightweight UAV snapshot cameras for vegetation monitoring: From camera calibration to quality assurance. ISPRS J. Photogramm. Remote Sens. 108, 245–259. doi:10.1016/j.isprsjprs.2015.08.002

Aasen, H., Gnyp, M.L., Miao, Y., Bareth, G., 2014. Automated Hyperspectral Vegetation Index Retrieval from Multiple Correlation Matrices with HyperCor. Photogramm. Eng. Remote Sens. 80, 785–795. doi:10.14358/PERS.80.8.785

Agisoft LLC, 2016. Agisoft PhotoScan User Manual Professional Edition, Version 1.2. St. Petersburg, Russia.

Anderson, K., Dungan, J.L., MacArthur, A., 2011. On the reproducibility of field-measured reflectance factors in the context of vegetation studies. Remote Sens. Environ. 115, 1893–1905. doi:10.1016/j.rse.2011.03.012

ASD Inc., 2014. HandHeld 2: Hand-held VNIR Spectroradiometer [WWW Document]. HandHeld 2 Hand-Held Spectroradiometer Hand-Held Spectrometer ASD Inc. URL http://www.asdi.com/products/fieldspec-spectroradiometers/handheld-2-portable-spectroradiometer (accessed 5.4.16).

Atzberger, C., 2013. Advances in Remote Sensing of Agriculture: Context Description, Existing Operational Monitoring Systems and Major Information Needs. Remote Sens. 5, 949–981. doi:10.3390/rs5020949

Balmford, A., Green, R., Scharlemann, J.P., others, 2005. Sparing land for nature: exploring the potential impact of changes in agricultural yield on the area needed for crop production. Glob. Change Biol. 11, 1594–1605. doi:10.1111/j.1365-2486.2005.001035.x

Bareth, G., Aasen, H., Bendig, J., Gnyp, M.L., Bolten, A., Jung, A., Michels, R., Soukkamäki, J., 2015a. Low-weight and UAV-based Hyperspectral Full-frame Cameras for Monitoring Crops: Spectral Comparison with Portable Spectroradiometer Measurements. Photogramm. Fernerkund. Geoinformation 2015, 69–79. doi:10.1127/pfg/2015/0256

Bareth, G., Bolten, A., Hollberg, J., Aasen, H., Burkart, A., Schellberg, J., 2015b. Feasibility study of using non-calibrated UAV-based RGB imagery for grassland monitoring: Case study at the Rengen Long-term Grassland Experiment (RGE), Germany., in: DGPF-Proceedings. Presented at the DGPF Annual Conference'15, Cologne, Germany, pp. 55–62.

Bendig, J., 2015. Unmanned aerial vehicles (UAVs) for multi-temporal crop surface modelling (Dissertation). Universität zu Köln, Köln.

Bendig, J., Bolten, A., Bareth, G., 2013. UAV-based Imaging for Multi-Temporal, very high Resolution Crop Surface Models to monitor Crop Growth Variability. Photogramm. - Fernerkund. - Geoinformation 2013, 551–562. doi:10.1127/1432-8364/2013/0200

Bendig, J., Bolten, A., Bennertz, S., Broscheit, J., Eichfuss, S., Bareth, G., 2014. Estimating Biomass of Barley Using Crop Surface Models (CSMs) Derived from UAV-Based RGB Imaging. Remote Sens. 6, 10395–10412. doi:10.3390/rs61110395

Bendig, J., Yu, K., Aasen, H., Bolten, A., Bennertz, S., Broscheit, J., Gnyp, M.L., Bareth, G., 2015. Combining UAV-based plant height from crop surface models, visible, and near infrared vegetation indices for biomass monitoring in barley. Int. J. Appl. Earth Obs. Geoinformation 39, 79–87. doi:10.1016/j.jag.2015.02.012

Berni, J., Zarco-Tejada, P.J., Suarez, L., Fereres, E., 2009. Thermal and Narrowband Multispectral Remote Sensing for Vegetation Monitoring From an Unmanned Aerial Vehicle. IEEE Trans. Geosci. Remote Sens. 47, 722–738. doi:10.1109/TGRS.2008.2010457

Boukerrou, L., Rasmusson, D.D., 1990. Breeding for High Biomass Yield in Spring Barley. Crop Sci. 30, 31. doi:10.2135/cropsci1990.0011183X003000010007x

Breiman, L., 2001. Random forests. Mach. Learn. 45, 5–32. doi:10.1023/A:1010933404324

Brocks, S., Bendig, J., Bareth, G., in review. Towards an Automated Low-Cost 3D Crop Surface Monitoring System Using Oblique Stereo Imagery from Consumer-Grade Smart Cameras.

Broge, N.., Leblanc, E., 2001. Comparing prediction power and stability of broadband and hyperspectral vegetation indices for estimation of green leaf area index and canopy chlorophyll density. Remote Sens. Environ. 76, 156–172. doi:10.1016/S0034-4257(00)00197-8

Burkart, A., Aasen, H., Alonso, L., Menz, G., Bareth, G., Rascher, U., 2015. Angular Dependency of Hyperspectral Measurements over Wheat Characterized by a Novel UAV Based Goniometer. Remote Sens. 7, 725–746. doi:10.3390/rs70100725

Burkart, A., Cogliati, S., Schickling, A., Rascher, U., 2014. A Novel UAV-Based Ultra-Light Weight Spectrometer for Field Spectroscopy. IEEE Sens. J. 14, 62–67. doi:10.1109/JSEN.2013.2279720

Burney, J.A., Davis, S.J., Lobell, D.B., 2010. Greenhouse gas mitigation by agricultural intensification. Proc. Natl. Acad. Sci. 107, 12052–12057. doi:10.1073/pnas.0914216107

Campbell, J.B., Wynne, R.H., 2011. Introduction to remote sensing, 5th ed. Guilford Press, New York.

Campus Klein-Altendorf, 2010. Standort [WWW Document]. URL https://www.cka.uni-bonn.de/standort (accessed 12.1.16).

Casa, R., Jones, H., 2005. LAI retrieval from multiangular image classification and inversion of a ray tracing model. Remote Sens. Environ. 98, 414–428. doi:10.1016/j.rse.2005.08.005

Claverie, M., Demarez, V., Duchemin, B., Hagolle, O., Ducrot, D., Marais-Sicre, C., Dejoux, J.-F., Huc, M., Keravec, P., Béziat, P., Fieuzal, R., Ceschia, E., Dedieu, G., 2012. Maize and sunflower biomass estimation in southwest France using high spatial and temporal resolution remote sensing data. Remote Sens. Environ. 124, 844–857. doi:10.1016/j.rse.2012.04.005

Clevers, J.G.P.W., Jongschaap, R., 2003. Imaging spectrometry and vegetation science, in: van der Meer, F., de Jong, S.M. (Eds.), Imaging Spectrometry - Basic Principles and Prospective Applications, Remote Sensing and Digital Image Processing. Dordrecht, The Netherlands, pp. 157–200.

Cogliati, S., Rossini, M., Julitta, T., Meroni, M., Schickling, A., Burkart, A., Pinto, F., Rascher, U., Colombo, R., 2015. Continuous and long-term measurements of reflectance and sun-induced chlorophyll fluorescence by using novel automated field spectroscopy systems. Remote Sens. Environ. 164, 270–281. doi:10.1016/j.rse.2015.03.027

References

Colomina, I., Molina, P., 2014. Unmanned aerial systems for photogrammetry and remote sensing: A review. ISPRS J. Photogramm. Remote Sens. 92, 79–97. doi:10.1016/j.isprsjprs.2014.02.013

Congalton, R.G., 1991. A review of assessing the accuracy of classifications of remotely sensed data. Remote Sens. Environ. 37, 35–46. doi:10.1016/0034-4257(91)90048-B

Cracknell, A.P., 1998. Review article Synergy in remote sensing-what's in a pixel? Int. J. Remote Sens. 19, 2025–2047. doi:10.1080/014311698214848

Crommelinck, S., Höfle, B., 2016. Simulating an Autonomously Operating Low-Cost Static Terrestrial LiDAR for Multitemporal Maize Crop Height Measurements. Remote Sens. 8, 205. doi:10.3390/rs8030205

Cubert GmbH, 2016. UHD 185 – Firefly [WWW Document]. Hyperspectral Imaging UHD 185 - Firefly Cubert-GmbH. URL http://cubert-gmbh.de/uhd-185-firefly/ (accessed 4.21.16).

Cubert GmbH, 2015. Butterfly X2 announced [WWW Document]. Butterfly X2 Announc.-GmbH Cubert-GmbH. URL http://cubert-gmbh.de/2016/02/11/butterfly-x2-announced/ (accessed 4.10.16).

Dalponte, M., Bruzzone, L., Gianelle, D., 2012. Tree species classification in the Southern Alps based on the fusion of very high geometrical resolution multispectral/hyperspectral images and LiDAR data. Remote Sens. Environ. 123, 258–270. doi:10.1016/j.rse.2012.03.013

Damm, A., Guanter, L., Verhoef, W., Schläpfer, D., Garbari, S., Schaepman, M.E., 2015. Impact of varying irradiance on vegetation indices and chlorophyll fluorescence derived from spectroscopy data. Remote Sens. Environ. 156, 202–215. doi:10.1016/j.rse.2014.09.031

Dandois, J.P., Ellis, E.C., 2013. High spatial resolution three-dimensional mapping of vegetation spectral dynamics using computer vision. Remote Sens. Environ. 136, 259–276. doi:10.1016/j.rse.2013.04.005

Dandois, J.P., Ellis, E.C., 2010. Remote Sensing of Vegetation Structure Using Computer Vision. Remote Sens. 2, 1157–1176. doi:10.3390/rs2041157

Dandois, J.P., Olano, M., Ellis, E., 2015. Optimal Altitude, Overlap, and Weather Conditions for Computer Vision UAV Estimates of Forest Structure. Remote Sens. 7, 13895–13920. doi:10.3390/rs71013895

Datt, B., McVicar, T.R., Van Niel, T.G., Jupp, D.L.B., Pearlman, J.S., 2003. Preprocessing eo-1 hyperion hyperspectral data to support the application of agricultural indexes. IEEE Trans. Geosci. Remote Sens. 41, 1246–1259. doi:10.1109/TGRS.2003.813206

Descour, M., Dereniak, E., 1995. Computed-tomography imaging spectrometer: experimental calibration and reconstruction results. Appl. Opt. 34, 4817–4826.

DigitalGlobe, 2016. WorldView-3 Satellite Sensor [WWW Document]. WorldView-3 Satell. Imag. Satell. Sens. Specif. Satell. Imaging Corp. URL http://www.satimagingcorp.com/satellite-sensors/worldview-3/ (accessed 4.21.16).

DJI, 2016. Phantom 4 [WWW Document]. Phantom 4 - DJI's Smartest Fly. Camera Ever. URL http://www.dji.com/product/phantom-4 (accessed 4.25.16).

dlz agrarmagazin, 2012. So rechnen sich N-Sensoren. Pflanzenbau 36–39.

e-geos, 2016. Price List [WWW Document]. URL http://www.e-geos.it/images/Satellite_data/0416/prices.pdf (accessed 4.25.16).

Ehlert, D., Horn, H.-J., Adamek, R., 2008. Measuring crop biomass density by laser triangulation. Comput. Electron. Agric. 61, 117–125. doi:10.1016/j.compag.2007.09.013

Eisenbeiß, H., 2009. UAV photogrammetry, Mitteilungen / Institut für Geodäsie und Photogrammetrie an der Eidgenössischen Technischen Hochschule Zürich. ETH, Inst. für Geodäsie und Photogrammetrie, Zürich.

Eltner, A., Schneider, D., 2015. Analysis of Different Methods for 3D Reconstruction of Natural Surfaces from Parallel-Axes UAV Images. Photogramm. Rec. 30, 279–299. doi:10.1111/phor.12115

ESA, 2016. Sentinel-2 MSI - Resolutions [WWW Document]. User Guid. - Sentin.-2 MSI - Resolut. - Sentin. Online. URL https://sentinel.esa.int/web/sentinel/user-guides/sentinel-2-msi/resolutions/spatial (accessed 4.21.16).

FAO (Ed.), 2012. Economic growth is necessary but not sufficient to accelerate reduction of hunger and malnutrition, The state of food insecurity in the world. FAO, Rome.

FAO, OAA (Eds.), 2011. The state of the world's land and water resources for food and agriculture: managing systems at risk. Earthscan, Abingdon.

Feilhauer, H., Asner, G.P., Martin, R.E., 2015. Multi-method ensemble selection of spectral bands related to leaf biochemistry. Remote Sens. Environ. 164, 57–65. doi:10.1016/j.rse.2015.03.033

Fereres, E., Soriano, M.A., 2006. Deficit irrigation for reducing agricultural water use. J. Exp. Bot. 58, 147–159. doi:10.1093/jxb/erl165

Fischer, R.A., Byerlee, D., Edmeades, G.., 2014. Crop yields and global food security: will yield increase continue to feed the world? Australian Centre for International Agricultural, Canberra.

Fisher, P., 1997. The pixel: A snare and a delusion. Int. J. Remote Sens. 18, 679–685. doi:10.1080/014311697219015

FLIR Systems Inc., 2016. DJI Zenmuse XT [WWW Document]. DJI Zenmuse XT FLIR Syst. URL http://www.flir.com/suas/content/?id=73063 (accessed 4.30.16).

Foley, J.A., Ramankutty, N., Brauman, K.A., Cassidy, E.S., Gerber, J.S., Johnston, M., Mueller, N.D., O'Connell, C., Ray, D.K., West, P.C., Balzer, C., Bennett, E.M., Carpenter, S.R., Hill, J., Monfreda, C., Polasky, S., Rockström, J., Sheehan, J., Siebert, S., Tilman, D., Zaks, D.P.M., 2011. Solutions for a cultivated planet. Nature 478, 337–342. doi:10.1038/nature10452

Foody, G.M., 2002. Status of land cover classification accuracy assessment. Remote Sens. Environ. 80, 185–201.

Friedli, M., Kirchgessner, N., Grieder, C., Liebisch, F., Mannale, M., Walter, A., 2016. Terrestrial 3D laser scanning to track the increase in canopy height of both monocot and dicot crop species under field conditions. Plant Methods 12. doi:10.1186/s13007-016-0109-7

Gatebe, C.K., 2003. Airborne spectral measurements of surface–atmosphere anisotropy for several surfaces and ecosystems over southern Africa. J. Geophys. Res. 108. doi:10.1029/2002JD002397

Gege, P., Fries, J., Haschberger, P., Schötz, P., Schwarzer, H., Strobl, P., Suhr, B., Ulbrich, G., Jan Vreeling, W., 2009. Calibration facility for airborne imaging spectrometers. ISPRS J. Photogramm. Remote Sens. 64, 387–397. doi:10.1016/j.isprsjprs.2009.01.006

Geipel, J., Link, J., Claupein, W., 2014. Combined Spectral and Spatial Modeling of Corn Yield Based on Aerial Images and Crop Surface Models Acquired with an Unmanned Aircraft System. Remote Sens. 6, 10335–10355. doi:10.3390/rs61110335

Gerke, M., Przybilla, H.-J., 2016. Accuracy Analysis of Photogrammetric UAV Image Blocks: Influence of Onboard RTK-GNSS and Cross Flight Patterns. Photogramm. - Fernerkund. - Geoinformation 2016, 17–30. doi:10.1127/pfg/2016/0284

Gevaert, C.M., Suomalainen, J., Tang, J., Kooistra, L., 2015. Generation of Spectral-Temporal Response Surfaces by Combining Multispectral Satellite and Hyperspectral UAV Imagery for Precision Agriculture Applications. IEEE J. Sel. Top. Appl. Earth Obs. Remote Sens. 8, 3140–3146. doi:10.1109/JSTARS.2015.2406339

Gnyp, M.L., Bareth, G., Li, F., Lenz-Wiedemann, V.I.S., Koppe, W., Miao, Y., Hennig, S.D., Jia, L., Laudien, R., Chen, X., Zhang, F., 2014a. Development and implementation of a multiscale biomass model using hyperspectral vegetation indices for winter wheat in the North China Plain. Int. J. Appl. Earth Obs. Geoinformation 33, 232–242. doi:10.1016/j.jag.2014.05.006

Gnyp, M.L., Miao, Y., Yuan, F., Ustin, S.L., Yu, K., Yao, Y., Huang, S., Bareth, G., 2014b. Hyperspectral canopy sensing of paddy rice aboveground biomass at different growth stages. Field Crops Res. 155, 42–55. doi:10.1016/j.fcr.2013.09.023

Goetz, A.F.H., 2009. Three decades of hyperspectral remote sensing of the Earth: A personal view. Remote Sens. Environ. 113, S5–S16. doi:10.1016/j.rse.2007.12.014

Goetz, A.F.H., 1975. Portable field reflectance spectrometer, JPL Technical Report. California Jet Propulsion Laboratory, California Institute of Technology, Pasadena.

Goetz, A.F.H., Vane, G., Solomon, J.E., Rock, B.N., 1985. Imaging Spectrometry for Earth Remote Sensing. Science 228, 1147–1153. doi:10.1126/science.228.4704.1147

Gómez-Gutiérrez, Á., de Sanjosé-Blasco, J., de Matías-Bejarano, J., Berenguer-Sempere, F., 2014. Comparing Two Photo-Reconstruction Methods to Produce High Density Point Clouds and DEMs in the Corral del Veleta Rock Glacier (Sierra Nevada, Spain). Remote Sens. 6, 5407–5427. doi:10.3390/rs6065407

Green, R.O., Eastwood, M.L., Sarture, C.M., Chrien, T.G., Aronsson, M., Chippendale, B.J., Faust, J.A., Pavri, B.E., Chovit, C.J., Solis, M., Olah, M.R., Williams, O., 1998. Imaging Spectroscopy and the Airborne Visible/Infrared Imaging Spectrometer (AVIRIS). Remote Sens. Environ. 65, 227–248. doi:10.1016/S0034-4257(98)00064-9

Grenzdörffer, G.J., 2014. Crop height determination with UAS point clouds. ISPRS - Int. Arch. Photogramm. Remote Sens. Spat. Inf. Sci. XL-1, 135–140. doi:10.5194/isprsarchives-XL-1-135-2014

Gruen, A., 2012. Development and Status of Image Matching in Photogrammetry: Development and status of image matching in photogrammetry. Photogramm. Rec. 27, 36–57. doi:10.1111/j.1477-9730.2011.00671.x

Guo, Q., Zhu, Z., 2014. Phenotyping of Plants, in: Meyers, R.A. (Ed.), Encyclopedia of Analytical Chemistry. John Wiley & Sons, Ltd, Chichester, UK, pp. 1–15.

Haala, N., 2013. The Landscape of Dense Image Matching Algorithms. Presented at the Photogrammetric Week'13, pp. 271–284.

Haboudane, D., Miller, J.R., Pattey, E., Zarco-Tejada, P.J., Strachan, I.B., 2004. Hyperspectral vegetation indices and novel algorithms for predicting green LAI of crop canopies: Modeling and validation in the context of precision agriculture. Remote Sens. Environ. 90, 337–352. doi:10.1016/j.rse.2003.12.013

Hagen, N., Kester, R.T., Gao, L., Tkaczyk, T.S., 2012. Snapshot advantage: a review of the light collection improvement for parallel high-dimensional measurement systems. Opt. Eng. 51, 111702–1. doi:10.1117/1.OE.51.11.111702

Hakala, T., Honkavaara, E., Saari, H., Mäkynen, J., Kaivosoja, J., Pesonen, L., Pölönen, I., 2013. Spectral imaging from UAVs under varying illumination conditions. UAV-G2013 4–6 Sept. 2013 Rostock

Ger. Ed. G Grenzdörffer R Bill Int. Arch. Photogramm. Remote Sens. Spat. Inf. Sci. XL-1W2 Int. Soc. Photogramm. Remote Sens. ISPRS Doi 105194isprsarchives-XL-1-W2-189-2013.

Hakala, T., Suomalainen, J., Peltoniemi, J.I., 2010. Acquisition of Bidirectional Reflectance Factor Dataset Using a Micro Unmanned Aerial Vehicle and a Consumer Camera. Remote Sens. 2, 819–832. doi:10.3390/rs2030819

Hämmerle, M., Höfle, B., 2014. Effects of Reduced Terrestrial LiDAR Point Density on High-Resolution Grain Crop Surface Models in Precision Agriculture. Sensors 14, 24212–24230. doi:10.3390/s141224212

Hansen, P.M., Schjoerring, J.K., 2003. Reflectance measurement of canopy biomass and nitrogen status in wheat crops using normalized difference vegetation indices and partial least squares regression. Remote Sens. Environ. 86, 542–553. doi:10.1016/S0034-4257(03)00131-7

Harwin, S., Lucieer, A., 2012. Assessing the Accuracy of Georeferenced Point Clouds Produced via Multi-View Stereopsis from Unmanned Aerial Vehicle (UAV) Imagery. Remote Sens. 4, 1573–1599. doi:10.3390/rs4061573

He, L., Song, X., Feng, W., Guo, B.-B., Zhang, Y.-S., Wang, Y.-H., Wang, C.-Y., Guo, T.-C., 2016. Improved remote sensing of leaf nitrogen concentration in winter wheat using multi-angular hyperspectral data. Remote Sens. Environ. 174, 122–133. doi:10.1016/j.rse.2015.12.007

Headwall Photonics Inc, 2015. Micro-Hyperspec Airborne Sensors [WWW Document]. Micro Hyperspec. URL http://www.tetracam.com/Products-Mini_MCA.htm (accessed 4.16.16).

Heady, H.F., 1957. The Measurement and Value of Plant Height in the Study of Herbaceous Vegetation. Ecology 38, 313. doi:10.2307/1931691

Heuvelink, G.B.M., Burrough, P.A., Stein, A., 1989. Propagation of errors in spatial modelling with GIS. Int. J. Geogr. Inf. Syst. 3, 303–322. doi:10.1080/02693798908941518

Hirschmuller, H., 2008. Stereo Processing by Semiglobal Matching and Mutual Information. IEEE Trans. Pattern Anal. Mach. Intell. 30, 328–341. doi:10.1109/TPAMI.2007.1166

Höfle, B., 2014. Radiometric Correction of Terrestrial LiDAR Point Cloud Data for Individual Maize Plant Detection. IEEE Geosci. Remote Sens. Lett. 11, 94–98. doi:10.1109/LGRS.2013.2247022

Homolová, L., Malenovský, Z., Clevers, J.G.P.W., García-Santos, G., Schaepman, M.E., 2013. Review of optical-based remote sensing for plant trait mapping. Ecol. Complex. 15, 1–16. doi:10.1016/j.ecocom.2013.06.003

Honkavaara, E., Hakala, T., Markelin, L., Rosnell, T., Saari, H., Mäkynen, J., 2012. A Process for Radiometric Correction of UAV Image Blocks. Photogramm. - Fernerkund. - Geoinformation 2012, 115–127. doi:10.1127/1432-8364/2012/0106

Honkavaara, E., Saari, H., Kaivosoja, J., Pölönen, I., Hakala, T., Litkey, P., Mäkynen, J., Pesonen, L., 2013. Processing and Assessment of Spectrometric, Stereoscopic Imagery Collected Using a Lightweight UAV Spectral Camera for Precision Agriculture. Remote Sens. 5, 5006–5039. doi:10.3390/rs5105006

HORSCH Maschinen GmbH, 2016. Leeb GS - product leaflet.

Huete, A., Justice, C., Liu, H., 1994. Development of vegetation and soil indices for MODIS-EOS. Remote Sens. Environ. 49, 224–234. doi:10.1016/0034-4257(94)90018-3

Hunter, G.J., Bregt, A.K., Heuvelink, G.B.M., De Bruin, S., Virrantaus, K., 2009. Spatial Data Quality: Problems and Prospects, in: Navratil, G. (Ed.), Research Trends in Geographic Information Science. Springer Berlin Heidelberg, Berlin, Heidelberg, pp. 101–121.

Ishihara, M., Inoue, Y., Ono, K., Shimizu, M., Matsuura, S., 2015. The Impact of Sunlight Conditions on the Consistency of Vegetation Indices in Croplands—Effective Usage of Vegetation Indices from Continuous Ground-Based Spectral Measurements. Remote Sens. 7, 14079–14098. doi:10.3390/rs71014079

Itten, K.I., Dell'Endice, F., Hueni, A., Kneubühler, M., Schläpfer, D., Odermatt, D., Seidel, F., Huber, S., Schopfer, J., Kellenberger, T., Bühler, Y., D'Odorico, P., Nieke, J., Alberti, E., Meuleman, K., 2008. APEX - the Hyperspectral ESA Airborne Prism Experiment. Sensors 8, 6235–6259. doi:10.3390/s8106235

Jensen, J.R., 2007. Remote sensing of the environment: an earth resource perspective, 2nd ed. ed, Prentice Hall series in geographic information science. Pearson Prentice Hall, Upper Saddle River, NJ.

John Deere GmbH & Co. KG, 2016. Operations Center [WWW Document]. URL http://www.deere.com/en_US/products/equipment/ag_management_solutions/information_management/myjohndeere/myjohndeere.page? (accessed 4.20.16).

Jones, H.G., Vaughan, R.A., 2010. Remote sensing of vegetation: principles, techniques, and applications. Oxford University Press, Oxford ; New York.

Julitta, T., Corp, L., Rossini, M., Burkart, A., Cogliati, S., Davies, N., Hom, M., Mac Arthur, A., Middleton, E., Rascher, U., Schickling, A., Colombo, R., 2016. Comparison of Sun-Induced Chlorophyll Fluorescence Estimates Obtained from Four Portable Field Spectroradiometers. Remote Sens. 8, 122. doi:10.3390/rs8020122

Junttila, S., Kaasalainen, S., Vastaranta, M., Hakala, T., Nevalainen, O., Holopainen, M., 2015. Investigating Bi-Temporal Hyperspectral Lidar Measurements from Declined Trees—Experiences from Laboratory Test. Remote Sens. 7, 13863–13877. doi:10.3390/rs71013863

Kelcey, J., Lucieer, A., 2012. Sensor Correction of a 6-Band Multispectral Imaging Sensor for UAV Remote Sensing. Remote Sens. 4, 1462–1493. doi:10.3390/rs4051462

Kling, J.G., Hayes, P.M., Ullrich, S.E., 2004. BARLEY | Genetics and Breeding, in: Encyclopedia of Grain Science. Elsevier, pp. 27–38.

Knyazikhin, Y., Schull, M.A., Stenberg, P., Mõttus, M., Rautiainen, M., Yang, Y., Marshak, A., Carmona, P.L., Kaufmann, R.K., Lewis, P., others, 2013. Hyperspectral remote sensing of foliar nitrogen content. Proc. Natl. Acad. Sci. 110, E185–E192.

Koppe, W., Li, F., Gnyp, M.L., Miao, Y., Jia, L., Chen, X., Zhang, F., Bareth, G., 2010. Evaluating Multispectral and Hyperspectral Satellite Remote Sensing Data for Estimating Winter Wheat Growth Parameters at Regional Scale in the North China Plain. Photogramm. - Fernerkund. - Geoinformation 2010, 167–178. doi:10.1127/1432-8364/2010/0047

Koukal, T., Atzberger, C., 2012. Potential of Multi-Angular Data Derived From a Digital Aerial Frame Camera for Forest Classification. IEEE J. Sel. Top. Appl. Earth Obs. Remote Sens. 5, 30–43. doi:10.1109/JSTARS.2012.2184527

Kren, J., Klem, I., Svobodová, P., Mísa, P., Neudert, L., 2014. Yield and grain quality of spring barley as affected by biomass formation at early growth stages. Plant Soil Environ. 60, 221–227.

Kumar, L., Schmidt, K., Dury, S., Skidmore, A., van der Meer, F., de Jong, S.M., 2003. Imaging spectrometry and vegetation science, in: van der Meer, F., de Jong, S.M. (Eds.), Imaging Spectrometry - Basic Principles and Prospective Applications, Remote Sensing and Digital Image Processing. Dordrecht, The Netherlands, pp. 111–156.

Küster, T., Spengler, D., Barczi, J.-F., Segl, K., Hostert, P., Kaufmann, H., 2014. Simulation of Multitemporal and Hyperspectral Vegetation Canopy Bidirectional Reflectance Using Detailed Virtual 3-D Canopy Models. IEEE Trans. Geosci. Remote Sens. 52, 2096–2108. doi:10.1109/TGRS.2013.2258162

Large, A.R.G., Heritage, G.L., 2009. Laser Scanning– Evolution of the Discipline, in: Heritage, G.L., Large, A.R.G. (Eds.), Laser Scanning for the Environmental Sciences. Wiley-Blackwell, Oxford, UK, pp. 1–20.

Lee, W.S., Alchanatis, V., Yang, C., Hirafuji, M., Moshou, D., Li, C., 2010. Sensing technologies for precision specialty crop production. Comput. Electron. Agric. 74, 2–33. doi:10.1016/j.compag.2010.08.005

Li, F., Miao, Y., Hennig, S.D., Gnyp, M.L., Chen, X., Jia, L., Bareth, G., 2010. Evaluating hyperspectral vegetation indices for estimating nitrogen concentration of winter wheat at different growth stages. Precis. Agric. 11, 335–357. doi:10.1007/s11119-010-9165-6

Li, F., Mistele, B., Hu, Y., Chen, X., Schmidhalter, U., 2014. Optimising three-band spectral indices to assess aerial N concentration, N uptake and aboveground biomass of winter wheat remotely in China and Germany. ISPRS J. Photogramm. Remote Sens. 92, 112–123. doi:10.1016/j.isprsjprs.2014.03.006

Lillesand, T.M., Kiefer, R.W., Chipman, J.W., 2008. Remote sensing and image interpretation, 6th ed. ed. John Wiley & Sons, Hoboken, NJ.

Lintz, J., Simonett, D.S., 1976. Remote sensing of environment. Addison-Wesley, Reading, MA.

Lisein, J., Pierrot-Deseilligny, M., Bonnet, S., Lejeune, P., 2013. A Photogrammetric Workflow for the Creation of a Forest Canopy Height Model from Small Unmanned Aerial System Imagery. Forests 4, 922–944. doi:10.3390/f4040922

Lord, D., Desjardins, R.L., Dubé, P.A., 1985. Influence of wind on crop canopy reflectance measurements. Remote Sens. Environ. 18, 113–123. doi:10.1016/0034-4257(85)90042-2

Lowe, D.G., 2004. Distinctive image features from scale-invariant keypoints. Int. J. Comput. Vis. 60, 91–110. doi:10.1023/B:VISI.0000029664.99615.94

Lucieer, A., Malenovský, Z., Veness, T., Wallace, L., 2014. HyperUAS-Imaging Spectroscopy from a Multirotor Unmanned Aircraft System: HyperUAS-Imaging Spectroscopy from a Multirotor Unmanned. J. Field Robot. 31, 571–590. doi:10.1002/rob.21508

Luhmann, T., Robson, S., Kyle, S., Boehm, J., 2014. Close-range photogrammetry and 3D imaging, 2nd edition. ed, De Gruyter textbook. De Gruyter, Berlin.

Lunetta, R.S., Congalton, R.G., Fenstermaker, L.K., Jensen, J.R., McGwire, K.C., Tinney, L.R., 1991. Remote sensing and geographic information system data integration: error sources and research issues. Photogramm. Eng. Remote Sens. 57, 677–687. doi:-

Mac Arthur, A., MacLellan, C.J., Malthus, T., 2012. The Fields of View and Directional Response Functions of Two Field Spectroradiometers. IEEE Trans. Geosci. Remote Sens. 50, 3892–3907. doi:10.1109/TGRS.2012.2185055

Mac Arthur, A., Robinson, I., 2015. A critique of field spectroscopy and the challenges and opportunities it presents for remote sensing for agriculture, ecosystems, and hydrology, in: Neale, C.M.U., Maltese, A. (Eds.), . p. 963705. doi:10.1117/12.2201046

Mahlein, A.-K., 2016. Plant Disease Detection by Imaging Sensors – Parallels and Specific Demands for Precision Agriculture and Plant Phenotyping. Plant Dis. 100, 241–251. doi:10.1094/PDIS-03-15-0340-FE

Mahlein, A.-K., Rumpf, T., Welke, P., Dehne, H.-W., Plümer, L., Steiner, U., Oerke, E.-C., 2013. Development of spectral indices for detecting and identifying plant diseases. Remote Sens. Environ. 128, 21–30. doi:10.1016/j.rse.2012.09.019

Marshall, M., Thenkabail, P., 2015. Developing in situ Non-Destructive Estimates of Crop Biomass to Address Issues of Scale in Remote Sensing. Remote Sens. 7, 808–835. doi:10.3390/rs70100808

Mather, P.M., Natural Environment Research Council (Great Britain), British Aerospace (Firm) (Eds.), 1992. TERRA-1: understanding the terrestrial environment: the role of earth observations from space. Taylor & Francis, London ; Washington, DC.

Matson, P.A., 1997. Agricultural Intensification and Ecosystem Properties. Science 277, 504–509. doi:10.1126/science.277.5325.504

Meier, U., 2001. Growth stages of mono-and dicotyledonous plants. BBCH Monograph. Ger. Fed. Biol. Res. Cent. Agric. For. Berl.

Milton, E.J., 1987. Principles of field spectroscopy. Int. J. Remote Sens. 8, 1807–1827. doi:10.1080/01431168708954818

Milton, E.J., Schaepman, M.E., Anderson, K., Kneubühler, M., Fox, N., 2009. Progress in field spectroscopy. Remote Sens. Environ. 113, S92–S109. doi:10.1016/j.rse.2007.08.001

Moran, M.S., Inoue, Y., Barnes, E.M., 1997. Opportunities and limitations for image-based remote sensing in precision crop management. Remote Sens. Environ. 61, 319–346. doi:10.1016/S0034-4257(97)00045-X

Morton, D.C., Nagol, J., Carabajal, C.C., Rosette, J., Palace, M., Cook, B.D., Vermote, E.F., Harding, D.J., North, P.R.J., 2014. Amazon forests maintain consistent canopy structure and greenness during the dry season. Nature 506, 221–224. doi:10.1038/nature13006

Mulla, D.J., 2013. Twenty five years of remote sensing in precision agriculture: Key advances and remaining knowledge gaps. Biosyst. Eng. 114, 358–371. doi:10.1016/j.biosystemseng.2012.08.009

Munzert, M., Frahm, J. (Eds.), 2005. Pflanzliche Erzeugung: Grundlagen des Acker- und Pflanzenbaus und der Guten fachlichen Praxis, Grundlagen der Verfahrenstechnik, Produktions- und Verfahrenstechnik für Kulturpflanzen, Dauergrünland, Sonderkulturen, Nachwachsende Rohstoffe, Ökologischer Landbau, Naturschutz und Landschaftspflege, 12th ed, Die Landwirtschaft. BLV, München.

Nagol, J.R., Sexton, J.O., Kim, D.-H., Anand, A., Morton, D., Vermote, E., Townshend, J.R., 2015. Bidirectional effects in Landsat reflectance estimates: Is there a problem to solve? ISPRS J. Photogramm. Remote Sens. 103, 129–135. doi:10.1016/j.isprsjprs.2014.09.006

Nakai, T., Sumida, A., Kodama, Y., Hara, T., Ohta, T., 2010. A comparison between various definitions of forest stand height and aerodynamic canopy height. Agric. For. Meteorol. 150, 1225–1233. doi:10.1016/j.agrformet.2010.05.005

NASS, 2014. 2012 Census of agriculture United States - Summary and State Data (No. AC-12-A-51), Geographic Area Series. United States Department of Agriculture, Washington, D.C.

Nelson, A., Setiyono, T., Rala, A., Quicho, E., Raviz, J., Abonete, P., Maunahan, A., Garcia, C., Bhatti, H., Villano, L., Thongbai, P., Holecz, F., Barbieri, M., Collivignarelli, F., Gatti, L., Quilang, E., Mabalay, M., Mabalot, P., Barroga, M., Bacong, A., Detoito, N., Berja, G., Varquez, F., Wahyunto, E., Kuntjoro, D., Murdiyati, S., Pazhanivelan, S., Kannan, P., Mary, P., Subramanian, E., Rakwatin, P., Intrman, A., Setapayak, T., Lertna, S., Minh, V., Tuan, V., Duong, T., Quyen, N., Van Kham, D., Hin, S., Veasna, T., Yadav, M., Chin, C., Ninh, N., 2014. Towards an Operational

SAR-Based Rice Monitoring System in Asia: Examples from 13 Demonstration Sites across Asia in the RIICE Project. Remote Sens. 6, 10773–10812. doi:10.3390/rs61110773

Nicodemus, F.E., Richmond, J.C., Hsia, J.J., Ginsberg, I.W., Limperis, T., 1977. Geometrical considerations and nomenclature for reflectance. National Bureau of Standards, Washington DC, p. 67.

Nobel, P.S., 2005. Physicochemical and environmental plant physiology, 3rd ed. ed. Elsevier Academic Press, Amsterdam ; Boston.

Ouédraogo, M.M., Degré, A., Debouche, C., Lisein, J., 2014. The evaluation of unmanned aerial system-based photogrammetry and terrestrial laser scanning to generate DEMs of agricultural watersheds. Geomorphology 214, 339–355. doi:10.1016/j.geomorph.2014.02.016

Pajares, G., 2015. Overview and Current Status of Remote Sensing Applications Based on Unmanned Aerial Vehicles (UAVs). Photogramm. Eng. Remote Sens. 81, 281–330. doi:10.14358/PERS.81.4.281

Parrot SA, 2016. Parrot SEQUOIA [WWW Document]. URL http://www.parrot.com/usa/companies/sequoia/ (accessed 4.28.16).

Pearlman, J., Segal, C., Liao, L.B., Carman, S.L., Folkman, M.A., Browne, W., Ong, L., Ungar, S.G., 2000. Development and operations of the EO-1 Hyperion imaging spectrometer, in: International Symposium on Optical Science and Technology. International Society for Optics and Photonics, pp. 243–253.

Petrie, G., Toth, C.K., 2009. Introduction to Laser Ranging, Profiling, and Scanning, in: Shan, J., Toth, C.K. (Eds.), Topographic Laser Ranging and Scanning: Principles and Processing. CRC Press/Taylor & Francis Group, Boca Raton.

Pingali, P.L., 2012. Green Revolution: Impacts, limits, and the path ahead. Proc. Natl. Acad. Sci. 109, 12302–12308. doi:10.1073/pnas.0912953109

Pingali, P.L., 2007. Westernization of Asian diets and the transformation of food systems: Implications for research and policy. Food Policy 32, 281–298. doi:10.1016/j.foodpol.2006.08.001

Pinter, P.J.J., Hatfield, J.L., Schepers, J.S., Barnes, E.M., Moran, M.S., Daughtry, C.S.T., Upchurch, D.R., 2003. Remote Sensing for Crop Management. Photogramm. Eng. Remote Sens. 69, 647–664. doi:10.14358/PERS.69.6.647

Pix4D, 2016. Pix4D - simply powerfull [WWW Document]. Pix4D - Drone Mapp. Softw. URL https://pix4d.com/ (accessed 4.25.16).

Pontius, R.G., Millones, M., 2011. Death to Kappa: birth of quantity disagreement and allocation disagreement for accuracy assessment. Int. J. Remote Sens. 32, 4407–4429. doi:10.1080/01431161.2011.552923

Pretty, J., Bharucha, Z.P., 2014. Sustainable intensification in agricultural systems. Ann. Bot. 114, 1571–1596. doi:10.1093/aob/mcu205

Puliti, S., Olerka, H., Gobakken, T., Næsset, E., 2015. Inventory of Small Forest Areas Using an Unmanned Aerial System. Remote Sens. 7, 9632–9654. doi:10.3390/rs70809632

Ramankutty, N., Foley, J.A., Norman, J., McSweeney, K., 2002. The global distribution of cultivable lands: current patterns and sensitivity to possible climate change. Glob. Ecol. Biogeogr. 11, 377–392. doi:10.1046/j.1466-822x.2002.00294.x

Rao, R.N., Garg, P., Ghosh, S., 2006. The Effect of Radiometric Resolution on the Retrieval of Leaf Area Index from Agricultural Crops. GIScience Remote Sens. 43, 377–387. doi:10.2747/1548-1603.43.4.377

Rao, R.N., Garg, P.K., Ghosh, S.K., 2007. Evaluation of radiometric resolution on land use/land cover mapping in an agricultural area. Int. J. Remote Sens. 28, 443–450. doi:10.1080/01431160600733181

Rascher, U., Alonso, L., Burkart, A., Cilia, C., Cogliati, S., Colombo, R., Damm, A., Drusch, M., Guanter, L., Hanus, J., Hyvärinen, T., Julitta, T., Jussila, J., Kataja, K., Kokkalis, P., Kraft, S., Kraska, T., Matveeva, M., Moreno, J., Muller, O., Panigada, C., Pikl, M., Pinto, F., Prey, L., Pude, R., Rossini, M., Schickling, A., Schurr, U., Schüttemeyer, D., Verrelst, J., Zemek, F., 2015. Sun-induced fluorescence - a new probe of photosynthesis: First maps from the imaging spectrometer *HyPlant*. Glob. Change Biol. 21, 4673–4684. doi:10.1111/gcb.13017

Rasmussen, J., Ntakos, G., Nielsen, J., Svensgaard, J., Poulsen, R.N., Christensen, S., 2016. Are vegetation indices derived from consumer-grade cameras mounted on UAVs sufficiently reliable for assessing experimental plots? Eur. J. Agron. 74, 75–92. doi:10.1016/j.eja.2015.11.026

Remondino, F., Del Pizzo, S., Kersten, T.P., Troisi, S., 2012. Low-Cost and Open-Source Solutions for Automated Image Orientation – A Critical Overview, in: Ioannides, M., Fritsch, D., Leissner, J., Davies, R., Remondino, F., Caffo, R. (Eds.), Progress in Cultural Heritage Preservation. Springer Berlin Heidelberg, Berlin, Heidelberg, pp. 40–54.

Remondino, F., El-Hakim, S., 2006. Image-based 3D Modelling: A Review. Photogramm. Rec. 21, 269–291. doi:10.1111/j.1477-9730.2006.00383.x

Remondino, F., Spera, M.G., Nocerino, E., Menna, F., Nex, F., 2014. State of the art in high density image matching. Photogramm. Rec. 29, 144–166. doi:10.1111/phor.12063

Richter, R., Schläpfer, D., 2002. Geo-atmospheric processing of airborne imaging spectrometry data. Part 2: Atmospheric/topographic correction. Int. J. Remote Sens. 23, 2631–2649. doi:10.1080/01431160110115834

RIEGL GmbH, 2010. LMS-Z420i datasheet [WWW Document]. URL http://riegl.com/uploads/tx_pxpriegldownloads/10_DataSheet_Z420i_03-05-2010.pdf (accessed 10.9.15).

Rowley, J., 2007. The wisdom hierarchy: representations of the DIKW hierarchy. J. Inf. Sci. 33, 163–180. doi:10.1177/0165551506070706

Roy, D.P., Borak, J.S., Devadiga, S., Wolfe, R.E., Zheng, M., Descloitres, J., 2002. The MODIS land product quality assessment approach. Remote Sens. Environ. 83, 62–76. doi:10.1016/S0034-4257(02)00087-1

Salamí, E., Barrado, C., Pastor, E., 2014. UAV Flight Experiments Applied to the Remote Sensing of Vegetated Areas. Remote Sens. 6, 11051–11081. doi:10.3390/rs61111051

Samarah, N.H., Alqudah, A.M., Amayreh, J.A., McAndrews, G.M., 2009. The Effect of Late-terminal Drought Stress on Yield Components of Four Barley Cultivars. J. Agron. Crop Sci. 195, 427–441. doi:10.1111/j.1439-037X.2009.00387.x

Sandmeier, S.R., Itten, K., others, 1999. A field goniometer system (FIGOS) for acquisition of hyperspectral BRDF data. Geosci. Remote Sens. IEEE Trans. On 37, 978–986. doi:10.1109/36.752216

Schaefer, M., Lamb, D., 2016. A Combination of Plant NDVI and LiDAR Measurements Improve the Estimation of Pasture Biomass in Tall Fescue (Festuca arundinacea var. Fletcher). Remote Sens. 8, 10. doi:10.3390/rs8020109

Schaepman, M.E., Jehle, M., Hueni, A., D'Odorico, P., Damm, A., Weyermann, J., Schneider, F.D., Laurent, V., Popp, C., Seidel, F.C., Lenhard, K., Gege, P., Küchler, C., Brazile, J., Kohler, P., De Vos, L., Meuleman, K., Meynart, R., Schläpfer, D., Kneubühler, M., Itten, K.I., 2015. Advanced radiometry measurements and Earth science applications with the Airborne Prism Experiment (APEX). Remote Sens. Environ. 158, 207–219. doi:10.1016/j.rse.2014.11.014

Schaepman-Strub, G., Schaepman, M.E., Painter, T.H., Dangel, S., Martonchik, J.V., 2006. Reflectance quantities in optical remote sensing—definitions and case studies. Remote Sens. Environ. 103, 27–42. doi:10.1016/j.rse.2006.03.002

Schläpfer, D., Richter, R., 2002. Geo-atmospheric processing of airborne imaging spectrometry data. Part 1: Parametric orthorectification. Int. J. Remote Sens. 23, 2609–2630. doi:10.1080/01431160110115825

Schläpfer, D., Richter, R., Feingersh, T., 2015. Operational BRDF Effects Correction for Wide-Field-of-View Optical Scanners (BREFCOR). IEEE Trans. Geosci. Remote Sens. 53, 1855–1864. doi:10.1109/TGRS.2014.2349946

Semyonov, D., 2011. Algorithms used in Photoscan [WWW Document]. URL http://www.agisoft.com/forum/index.php?topic=89.0 (accessed 4.12.16).

Shi, T., Horvath, S., 2006. Unsupervised Learning With Random Forest Predictors. J. Comput. Graph. Stat. 15, 118–138. doi:10.1198/106186006X94072

Skinner, J.A., Lewis, K.A., Bardon, K.S., Tucker, P., Catt, J.A., Chambers, B.J., 1997. An Overview of the Environmental Impact of Agriculture in the U.K. J. Environ. Manage. 50, 111–128. doi:10.1006/jema.1996.0103

Smith, G.M., Milton, E.J., 1999. The use of the empirical line method to calibrate remotely sensed data to reflectance. Int. J. Remote Sens. 20, 2653–2662. doi:10.1080/014311699211994

Snavely, N., 2016. Bundler: Structure from Motion (SfM) for Unordered Image Collections [WWW Document]. Bundler - Struct. Motion SfM Unordered Image Collect. URL http://www.cs.cornell.edu/~snavely/bundler/ (accessed 4.3.16).

Snavely, N., Seitz, S.M., Szeliski, R., 2008. Modeling the World from Internet Photo Collections. Int. J. Comput. Vis. 80, 189–210. doi:10.1007/s11263-007-0107-3

Stafford, J.V. (Ed.), 2007. Precision agriculture '07. Wageningen Academic Publishers, The Netherlands.

Statistische Ämter des Bundes und der Länder, 2011. Agrarstrukturen in Deutschland - Einheit in Vielfalt. Stuttgart.

Suomalainen, J., Hakala, T., Peltoniemi, J., Puttonen, E., 2009. Polarised Multiangular Reflectance Measurements Using the Finnish Geodetic Institute Field Goniospectrometer. Sensors 9, 3891–3907. doi:10.3390/s90503891

Szeliski, R., 2011. Computer Vision, Texts in Computer Science. Springer London, London.

TETRACAM Inc, 2015. Tetracam's Miniature Multiple Camera Array [WWW Document]. Tetracam Mini-MCA. URL http://www.tetracam.com/Products-Mini_MCA.htm (accessed 4.16.16).

Thenkabail, P.S., Enclona, E.A., Ashton, M.S., Van Der Meer, B., 2004. Accuracy assessments of hyperspectral waveband performance for vegetation analysis applications. Remote Sens. Environ. 91, 354–376. doi:10.1016/j.rse.2004.03.013

Thenkabail, P.S., Lyon, J.G., Huete, A., 2012. Advances in Hyperspectral Remote Sensing of Vegetation and Agricultural Croplands, in: Thenkabail, P.S., Lyon, J.G., Huete, A. (Eds.), Hyperspectral Remote Sensing of Vegetation. CRC Press, Boca Raton, FL, pp. 3–38.

Thenkabail, P.S., Mariotto, I., Gumma, M.K., Middleton, E.M., Landis, D.R., Huemmrich, K.F., 2013. Selection of Hyperspectral Narrowbands (HNBs) and Composition of Hyperspectral Twoband Vegetation Indices (HVIs) for Biophysical Characterization and Discrimination of Crop Types Using Field Reflectance and Hyperion/EO-1 Data. IEEE J. Sel. Top. Appl. Earth Obs. Remote Sens. 6, 427–439. doi:10.1109/JSTARS.2013.2252601

Thenkabail, P.S., Smith, R.B., De Pauw, E., 2000. Hyperspectral Vegetation Indices and Their Relationships with Agricultural Crop Characteristics. Remote Sens. Environ. 71, 158–182. doi:10.1016/S0034-4257(99)00067-X

Tilly, N., 2016. In season estimation of barley biomass with plant height derived by terrestrial laser scanning, in: Proceedings of the 13th International Conference on Precision Agriculture. Presented at the 13th International Conference on Precision Agriculture, St. Louis, Missouri USA.

Tilly, N., 2015. Terrestrial laser scanning for crop monitoring - Capturing 3D data of plant height for estimating biomass at field scale (Dissertation). Universität zu Köln, Köln.

Tilly, N., Aasen, H., Bareth, G., 2015. Fusion of Plant Height and Vegetation Indices for the Estimation of Barley Biomass. Remote Sens. 7, 11449–11480. doi:10.3390/rs70911449

Tilly, N., Hoffmeister, D., Cao, Q., Huang, S., Lenz-Wiedemann, V., Miao, Y., Bareth, G., 2014. Multitemporal crop surface models: accurate plant height measurement and biomass estimation with terrestrial laser scanning in paddy rice. J. Appl. Remote Sens. 8, 83671. doi:10.1117/1.JRS.8.083671

Tilman, D., Balzer, C., Hill, J., Befort, B.L., 2011. Global food demand and the sustainable intensification of agriculture. Proc. Natl. Acad. Sci. 108, 20260–20264. doi:10.1073/pnas.1116437108

TOPCON, 2004. HiPer Pro Operators Manual.

Triggs, B., McLauchlan, P.F., Hartley, R.I., Fitzgibbon, A.W., 2000. Bundle Adjustment — A Modern Synthesis, in: Triggs, B., Zisserman, A., Szeliski, R. (Eds.), Vision Algorithms: Theory and Practice. Springer Berlin Heidelberg, Berlin, Heidelberg, pp. 298–372.

Turner, D., Lucieer, A., Wallace, L., 2014. Direct Georeferencing of Ultrahigh-Resolution UAV Imagery. IEEE Trans. Geosci. Remote Sens. 52, 2738–2745. doi:10.1109/TGRS.2013.2265295

Ullman, S., 1979. The Interpretation of Structure from Motion. Proc. R. Soc. B Biol. Sci. 203, 405–426. doi:10.1098/rspb.1979.0006

Ustin, S.L., Gitelson, A.A., Jacquemoud, S., Schaepman, M., Asner, G.P., Gamon, J.A., Zarco-Tejada, P., 2009. Retrieval of foliar information about plant pigment systems from high resolution spectroscopy. Remote Sens. Environ. 113, S67–S77. doi:10.1016/j.rse.2008.10.019

van der Wal, T., Abma, B., Viguria, A., Prévinaire, E., Zarco-Tejada, P.J., Serruys, P., van Valkengoed, E., van der Voet, P., 2013. Fieldcopter: unmanned aerial systems for crop monitoring services, in: Stafford, J. (Ed.), Precision Agriculture ’13. Wageningen Academic Publishers, pp. 169–175.

van der Werf, H.M.G., 1996. Assessing the impact of pesticides on the environment. Agric. Ecosyst. Environ. 60, 81–96. doi:10.1016/S0167-8809(96)01096-1

Verrelst, J., Muñoz, J., Alonso, L., Delegido, J., Rivera, J.P., Camps-Valls, G., Moreno, J., 2012. Machine learning regression algorithms for biophysical parameter retrieval: Opportunities for Sentinel-2 and -3. Remote Sens. Environ. 118, 127–139. doi:10.1016/j.rse.2011.11.002

Verrelst, J., Schaepman, M.E., Koetz, B., Kneubühler, M., 2008. Angular sensitivity analysis of vegetation indices derived from CHRIS/PROBA data. Remote Sens. Environ. 112, 2341–2353. doi:10.1016/j.rse.2007.11.001

Vicent, J., Sabater, N., Tenjo, C., Acarreta, J.R., Manzano, M., Rivera, J.P., Jurado, P., Franco, R., Alonso, L., Verrelst, J., Moreno, J., 2016. FLEX End-to-End Mission Performance Simulator. IEEE Trans. Geosci. Remote Sens. 1–9. doi:10.1109/TGRS.2016.2538300

von Bueren, S.K., Burkart, A., Hueni, A., Rascher, U., Tuohy, M.P., Yule, I.J., 2015. Deploying four optical UAV-based sensors over grassland: challenges and limitations. Biogeosciences 12, 163–175. doi:10.5194/bg-12-163-2015

Vosselman, G., Maas, H.-G. (Eds.), 2011. Airborne and terrestrial laser scanning, repr. ed. Whittles, Dunbeath.

Wahabzada, M., Mahlein, A.-K., Bauckhage, C., Steiner, U., Oerke, E.-C., Kersting, K., 2015. Metro Maps of Plant Disease Dynamics—Automated Mining of Differences Using Hyperspectral Images. PLOS ONE 10, e0116902. doi:10.1371/journal.pone.0116902

Wallace, L., Lucieer, A., Watson, C., Turner, D., 2012. Development of a UAV-LiDAR System with Application to Forest Inventory. Remote Sens. 4, 1519–1543. doi:10.3390/rs4061519

Weyermann, J., Damm, A., Kneubuhler, M., Schaepman, M.E., 2014. Correction of Reflectance Anisotropy Effects of Vegetation on Airborne Spectroscopy Data and Derived Products. IEEE Trans. Geosci. Remote Sens. 52, 616–627. doi:10.1109/TGRS.2013.2242898

Whelan, B., Taylor, J., 2013. Precision agriculture for grain production systems. CSIRO Publishing, Collingwood, Vic.

White, J., Stepper, C., Tompalski, P., Coops, N., Wulder, M., 2015. Comparing ALS and Image-Based Point Cloud Metrics and Modelled Forest Inventory Attributes in a Complex Coastal Forest Environment. Forests 6, 3704–3732. doi:10.3390/f6103704

Yao, H., Tang, L., Tain, L., Brown, R.L., Bhatnagar, D., Cleveland, T.E., 2012. Using Hyperspectral Data in Precision Farming Applications, in: Thenkabail, P.S., Lyon, J.G., Huete, A. (Eds.), Hyperspectral Remote Sensing of Vegetation. CRC Press, Boca Raton, FL, pp. 591–608.

YARA, 2016. N-Sensor [WWW Document]. N-Sens. Yara. URL http://www.yara.de/pflanzenernaehrung/tools-und-services/n-sensor/ (accessed 4.22.16).

Yu, K., Lenz-Wiedemann, V., Chen, X., Bareth, G., 2014. Estimating leaf chlorophyll of barley at different growth stages using spectral indices to reduce soil background and canopy structure effects. ISPRS J. Photogramm. Remote Sens. 97, 58–77. doi:10.1016/j.isprsjprs.2014.08.005

Yu, K., Leufen, G., Hunsche, M., Noga, G., Chen, X., Bareth, G., 2013. Investigation of Leaf Diseases and Estimation of Chlorophyll Concentration in Seven Barley Varieties Using Fluorescence and Hyperspectral Indices. Remote Sens. 6, 64–86. doi:10.3390/rs6010064

Zapryanov, G., Ivanova, D., Nikolova, I., 2012. Automatic White Balance Algorithms for Digital Still Cameras – a Comparative Study. Inf. Technol. Control X. doi:-

Zarco-Tejada, P.J., Diaz-Varela, R., Angileri, V., Loudjani, P., 2014. Tree height quantification using very high resolution imagery acquired from an unmanned aerial vehicle (UAV) and automatic 3D photo-reconstruction methods. Eur. J. Agron. 55, 89–99. doi:10.1016/j.eja.2014.01.004

Zarco-Tejada, P.J., González-Dugo, V., Berni, J.A.J., 2012. Fluorescence, temperature and narrow-band indices acquired from a UAV platform for water stress detection using a micro-hyperspectral imager and a thermal camera. Remote Sens. Environ. 117, 322–337. doi:10.1016/j.rse.2011.10.007

References

Zhao, F., Li, Y., Dai, X., Verhoef, W., Guo, Y., Shang, H., Gu, X., Huang, Y., Yu, T., Huang, J., 2015. Simulated impact of sensor field of view and distance on field measurements of bidirectional reflectance factors for row crops. Remote Sens. Environ. 156, 129–142. doi:10.1016/j.rse.2014.09.011

APPENDIX A: EIGENANTEILE

Chapter 3

Title: Generating 3D hyperspectral information with lightweight UAV snapshot cameras for vegetation monitoring: From camera calibration to quality assurance.

Authors: Helge Aasen, Andreas Burkart, Andreas Bolten, Georg Bareth

Journal: ISPRS Journal of Photogrammetry and Remote Sensing

Year: 2015

Volume: 108

Status: Published

Contributions:

- Concept and design of the study
- Data analysis
- Preparation of the manuscript
- Field data collection (major)

Chapter 4

Title: Multi-temporal monitoring of agricultural crops with high-resolution 3D hyperspectral digital surface models in comparison with ground observations.

Authors: Helge Aasen, Andreas Bolten

Journal: Remote Sensing of Environment

Year:

Issue:

Status: Under review

Contributions:

- Concept and design of the study
- Data analysis
- Preparation of the manuscript
- Field data collection (major)

Chapter 5

Title: Angular Dependency of Hyperspectral Measurements over Wheat Characterized by a Novel UAV Based Goniometer

Authors: Andreas Burkart, Helge Aasen, Luis Alonso, Gunter Menz, Georg Bareth, Uwe Rascher

Journal: Remote Sensing

Year: 2015

Volume (Issue): 7 (1)

Status: Published

Contributions:

- Concept and design of the study (major)
- Data analysis (major)
- Preparation of the manuscript (major, equally contribution authorship)

Chapter 6

Title: Fusion of Plant Height and Vegetation Indices for the Estimation of Barley Biomass

Authors: Nora Tilly, Helge Aasen, Georg Bareth

Journal: Remote Sensing

Year: 2015

Volume (Issue): 7 (9)

Status: Published

Contributions:

- Concept and design of the study (minor)
- Data analysis (major)
- Preparation of the manuscript (major)
- Field data collection (major)

Chapter 7

Title: Combining UAV-based plant height from crop surface models, visible, and near infrared vegetation indices for biomass monitoring in barley

Authors: Juliane Bendig, Kang Yu, Helge Aasen, Andreas Bolten, Simon Bennertz, Janis Broscheit, Martin L. Gnyp, Georg Bareth

Journal: International Journal of Applied Earth Observation and Geoinformation

Year: 2015

Volume: 39

Status: Published

Contribution:

- Spectral and field data analysis (major)
- Preparation of the manuscript (minor)
- Field data collection (minor)

Chapter 8

Title: Automated Hyperspectral Vegetation Index Retrieval from Multiple Correlation Matrices with HyperCor

Authors: Helge Aasen, Martin L. Gnyp, Yuxin Miao, Georg Bareth

Journal: Photogrammetric Engineering & Remote Sensing

Year: 2014

Volume (Issue): 80 (8)

Status: Published

Contributions:

- Concept and design of the study
- Data analysis
- Preparation of the manuscript (major)

APPENDIX B: ERKLÄRUNG

Ich versichere, dass ich die von mir vorgelegte Dissertation selbständig angefertigt, die benutzten Quellen und Hilfsmittel vollständig angegeben und die Stellen der Arbeit − einschließlich Tabellen, Karten und Abbildungen −, die anderen Werken im Wortlaut oder dem Sinn nach entnommen sind, in jedem Einzelfall als Entlehnung kenntlich gemacht habe; dass diese Dissertation noch keiner anderen Fakultät oder Universität zur Prüfung vorgelegen hat; dass sie − abgesehen von unten angegebenen Teilpublikationen − noch nicht veröffentlicht worden ist, sowie, dass ich eine solche Veröffentlichung vor Abschluss des Promotionsverfahrens nicht vornehmen werde.

Die Bestimmungen der Promotionsordnung sind mir bekannt. Die von mir vorgelegte Dissertation ist von Prof. Dr. Georg Bareth betreut worden.

Köln, den 26.08.2016